DISSERTATION

USING LABORATORY AND AIRBORNE MEASUREMENTS TO INVESTIGATE THE ROLE OF ICE NUCLEATING PARTICLES IN ICE AND MIXED-PHASE CLOUDS

Submitted by

Ryan John Patnaude

Department of Atmospheric Science

In partial fulfillment of the requirements

For the Degree of Doctor of Philosophy

Colorado State University

Fort Collins, Colorado

Fall 2023

Doctoral Committee:

Advisor: Sonia M. Kreidenweis
Co-Advisor: Paul J. DeMott

Susan C. van den Heever
J. Christine Chiu
Megan D. Willis

Copyright by Ryan Patnaude 2023

All Rights Reserved

ABSTRACT

USING LABORATORY AND AIRBORNE MEASUREMENTS TO INVESTIGATE THE ROLE OF ICE NUCLEATING PARTICLES IN ICE AND MIXED-PHASE CLOUDS

Ice may be present in the atmosphere either in cirrus or mixed-phase cloud regions, each with their own distinctly different characteristics and formation mechanisms. The former is characterized by the presence of only ice crystals at temperatures < -38 ºC, while the latter includes the coexistence of both supercooled liquid cloud droplets and ice crystals between temperatures of 0 ºC and -38 ºC. Cirrus clouds represent an important cloud type as they are ubiquitous in the atmosphere and their radiative effects depend upon their microphysical properties. Their formation mechanisms may proceed via homogeneous or heterogeneous nucleation, and whether one or the other or both occur determines the size and number of ice crystals.

The ocean represents one of the largest sources of aerosols into the atmosphere, and sea spray aerosols (SSA), if they are lofted to the upper troposphere, may act as ice nucleating particles (INPs) to initiate heterogeneous nucleation under cirrus conditions. Although a number of previous studies have investigated the ice nucleating behavior of SSA proxies such as sodium chloride (NaCl), or SSA generated from commercially-available artificial seawater products, ice nucleation under cirrus conditions of SSA generated from natural seawater had not been examined at the inception of this research program. Additionally, whether secondary marine aerosols (SMA), which form via the gas-to-particle conversion of ocean-emitted gas-phase species, may act as an INP in cirrus clouds is currently unknown. The first half of this

dissertation highlights two laboratory studies that investigated the role and characteristics of SSA and SMA to act as INPs at cirrus cloud temperatures.

The first study compared ice nucleation results for submicron SSA and NaCl particles and examined whether particle size affected the low temperature ice nucleation. Results showed that both SSA and NaCl initiated heterogeneous nucleation strongly at temperatures below 220 K, and that the size of the particles did not affect the ice nucleating ability of SSA. The similarities between the freezing behaviors of SSA and NaCl particles suggested the salt components were controlling heterogeneous ice nucleation. The second study used a more realistic aerosol generation method, utilizing a Marine Aerosol Reference Tank (MART) that was filled with natural seawater, and investigated the effects of atmospheric oxidation on SSA using an oxidation flow reactor (OFR), which was also used to generate SMA from gaseous emissions released in the MART. SMA alone were also examined for their ice nucleation behavior at cirrus temperatures. Results from this study indicated that atmospheric oxidation did not hinder low temperature ice nucleation of SSA, and that SMA are not efficient ice nucleating particles at cirrus temperatures, but could participate in homogeneous nucleation. Finally, the similarities between the findings from the two studies indicated that the generation method of SSA, and any impacts on SSA organic aerosol content, did not affect the ice nucleating behavior of SSA at cirrus temperatures.

Ice in mixed-phase clouds (MPCs), on the other hand, forms initially via heterogeneous nucleation at a wide range of temperatures and relative humidity conditions, depending on the abundance and characteristics of available INPs. Secondary ice production (SIP) may follow heterogeneous nucleation in MPCs, where new ice crystals form either during the heterogeneous freezing event, or through subsequent interactions between the pre-existing liquid cloud droplets

and ice crystals. SIP may lead to enhanced ice crystal number concentrations via a number of proposed mechanisms, especially in convective environments. Despite decades of study toward developing better understanding of ice formation in MPCs, the freezing pathways of ice crystals over the course of cloud lifetimes, and the conditions that favor the various proposed SIP pathways, are not fully resolved.

The third study in this dissertation reports and interprets observations of INPs during an airborne campaign over the U.S. Central Great Plains during the Secondary Production of Ice in Cumulus Experiment (SPICULE) campaign that primarily sampled cumulus congestus clouds. Coincident measurements of INP and ice crystal number concentrations in cumulus congestus clouds were used to infer the ice formation pathway, either through heterogeneous nucleation or SIP. Warmer cloud base temperatures and faster updrafts were found to facilitate environmental conditions favorable for SIP. Further, the fragmentation of freezing droplets (FFD) SIP mechanism was found to be critical in the enhancement of observed ice crystal number concentrations during the earliest stages of the cloud lifetime. Numerical model simulations of an idealized, single congestus cloud, designed to mimic the clouds sampled during SPICULE, were conducted with newly-implemented SIP mechanisms, added to the existing Hallet-Mossop (HM) rime-splintering mechanism. The model results indicated that HM dominated the production of ice crystals, but without the FFD and ice-ice collisional breakup (BR) SIP mechanisms, the model could not accurately resolve ice crystal number concentrations compared to observations. Competing results in the dominant SIP mechanisms underscore the need for improved mechanistic understanding of these SIP processes, either through laboratory or observational studies, in order to close this gap between model prediction and observations.

The final portion of this dissertation describes airborne observations of INPs during a field campaign along the U.S. Gulf Coast, also aimed at investigating the impacts of various aerosol-cloud interaction mechanisms on development of convective clouds. During this campaign, a widespread and prolonged Saharan Air Layer (SAL) event took place and INP characteristics during this event are reported and contrasted with INP characteristics prior to the arrival of the SAL. The INP concentrations at temperatures below -20 ºC were enhanced by 1–2 orders of magnitude compared to the flights prior to the dust intrusion, and showed good agreement with one previous study of Saharan dust near Barbados, but lower INP concentrations than another study off the coast of western Africa. The INP concentrations in the SAL also generally overlapped with or exceeded INP concentrations during SPICULE, but only for INPs active temperatures < -25 ºC. These observations were the first airborne measurements in nearly two decades tagging INP concentrations to North African dust that had been transported all the way to the United States. Further, they provide the most comprehensive description of these INPs yet recorded, and suggest a common natural INP perturbation in the southeastern U.S. and Gulf regions in early summer, with implications for cloud processes that warrant further study.

ACKNOWLEDGEMENTS

I would like to start by acknowledging my brilliant team of advisors Drs. Paul DeMott and Sonia Kreidenweis, who accepted me into the program in the Fall of 2020, and helped me navigate through the first year of my PhD during a challenging time. You both have inspired me to continue following my interests in aerosol-cloud interactions, and provided me with the opportunities to participate in multiple airborne field campaigns and laboratory studies. Paul, I will always feel especially grateful that I was the final student that you accepted to advise, and it has been such a privilege to have worked with you at the end of your great career. Sonia, I will always cherish our conversions that weave between the off topics of the day, to the in-depth and detailed topics of aerosol and cloud physics, which we both find so interesting. I owe you both a great debt of gratitude for guiding me through this PhD, and setting me up for success with my future career.

I would like to acknowledge my committee members Dr. Susan van den Heever, Dr. Christine Chiu and Dr. Megan Willis who have each contributed their own unique expertise to this dissertation and I have been fortunate to work with them throughout my PhD. Additionally, the contributions to this work from Sue and her group members cannot be overstated. Sue helped arrange a number of meetings with herself and members of her modelling group to guide me through learning, running, and trouble-shooting the RAMS model and without her help, a good portion of Chapter 4 of this dissertation would not have been possible.

The laboratory studies outlined in Chapters 2 and 3 and the scientific papers that were produced from these experiments were largely impacted by the contributions of my fellow group members Dr. Russell Perkins and Kathryn Moore. Much of the experimental setup for both of

the laboratory experiments were constructed by the two of them and I gained so much valuable knowledge and experience from each of their contributions. I also want to specifically thank Dr. Russell Perkins who spent countless hours training me on both the lab and aircraft CFDCs, and has been a great mentor for me at CSU. Thank you to Dr. Thomas Hill and Kevin Barry for training me on the ice spectrometer, not to mention many, many laughs along the way. I would also like to acknowledge the Center of Aerosols Impacts on the Chemistry of the Environment (CAICE), and the members of CAICE who helped make the laboratory studies possible. Thank you to Drs. Paul DeMott, Sonia Kreidenweis, Russell Perkins, and Thomas C. Hill and Kathryn Moore who contributed their input to the scientific findings of these two studies. To my fellow Kreidenweis research group members Kevin Barry, Drs. Thomas Hill and Marina Nieto, Carson Hume, Brian Heffernan and Kathryn Moore, thank you for the friendships during my time at CSU.

I would like to acknowledge my many collaborators, PIs, program managers, and flight crews during the two field studies. I would like to thank Dr. Pavel Romashkin and Cory Wolff for excellent planning and coordination during the Secondary Production of Ice in Cumulus Experiment (SPICULE) campaign. In addition, Kathryn Moore and Dr. Russell Perkins acted as CFDC operators and collected INP data during a number of SPICULE flights, which was critical for a large portion of this dissertation. Thank you to Adriana Raudzens Bailey for her help with the CVI data, and I want to specifically thank Dr. Paul Lawson who shared much of his knowledge and analysis tools, which were so important for Chapter 4 of this dissertation. I would like to thank Drs. Greg McFarquhar and Pavlos Kollias for leading the Experiment of Sea Breeze Convection, Aerosols, Precipitation, and Environment (ESCAPE) campaign and program managers Cory Wolff and Peisang Tsai. A special thank you to my fellow members of the

"A(erosol)-Team" Drs. Christina McCluskey, Greg Roberts, and Paul DeMott which was coined during the ESCAPE campaign. They convinced me to act as the Lead Scientist during the second aerosol focused research flight during ESCAPE, an experience I will not soon forget. For their invaluable help with running the RAMS model, I want to thank Steve Saleeby, Drs. Sue van den Heever and Leah Grant, and Ben Ascher and Gabrielle Leung, who answered countless emails with my many questions. Finally, I would like to thank the members of the CSU ATS department staff including Sarah Tisdale, Amanda Davey, Heidi Hammon and Adam Finefrock for their support during conferences and field campaigns.

Graduate is a long and arduous process and it would not have been a reality without the support from my family and friends, especially my parents Paul and Michele, my sister Claire, and my fiancé Samantha during the last five years of graduate school. You have all kept me motivated, encouraged me when I wanted to give up, and I attribute so much of my success to the love and support you all gave me. Thank you also to Duke (the dog) for staring at me until I would go for a walk, giving me those brief periods of relief, and reminding me that it is okay to take breaks during the hardest of times.

Finally, I would like to gratefully acknowledge the funding for this work from the National Science Foundation (NSF) through the Center for Aerosol Impacts on Chemistry of the Environment (CAICE) grant number CHE-1801971 for the laboratory studies, and NSF grant numbers #1917519 for SPICULE and #2019947 for ESCAPE.

TABLE OF CONTENTS

ABSTRACT ii

ACKNOWLEDGEMENTS vi

Chapter 1: Introduction 1

1.1 Ice Crystals in the Atmosphere 1

1.2 Description of Cirrus Cloud Formation Mechanisms and Characteristics 1

1.3 Ice in Mixed-Phase Clouds 4

1.4 Objectives and Overview 7

Chapter 2: Sea Spray Aerosols as a Source of Ice Nucleating Particles in Cirrus Clouds 12

2.1 Background on Cirrus Cloud INPs 12

2.2 Experimental Description 15

2.2.1 CFDC Setup 15

2.2.2 Description of Aerosol Generation and Phase State 19

2.2.3 Ice Nucleation Detection 24

2.3 Results of SSA Ice Nucleation 25

2.4 Discussion and Atmospheric Implications 33

Chapter 3: A Second Laboratory Study on the Low Temperature Ice Nucleation of Sea Spray and Secondary Marine Aerosols 41

3.1 Background on Marine Aerosols 41

3.2 Experimental Setup 44

3.2.1 Seawater Collection and Preparation 45

3.2.2 Aerosol Generation and Characteristics 46

3.2.3 Ice Nucleation Detection using the CFDC 52
3.3 Results and Discussion 56
3.3.1 Particle Size Distributions and Alteration via OFR Oxidation 56
3.3.2 Analysis of Ice Nucleation Results 60
3.4 Conclusions 68
Chapter 4: Airborne Ice Nucleating Particles and Ice Formation Processes in Cumulus Congestus Clouds 72
4.1 Background on the Ice Phase in Mixed-Phase Clouds 72
4.1.1 INPs in Mixed Phase Clouds 72
4.1.2 In Situ Observations of Ice Crystal Concentrations in MPCs 73
4.1.3 Modelling Primary Nucleation and Secondary Ice Production in MPCs 74
4.2 Description of Tools and Methods 76
4.2.1 SPICULE Project Overview 76
4.2.2 Aircraft Instrumentation 77
4.2.3 Airborne Observations of INPs 78
4.3 Configuration of Numerical Simulations 81
4.3.1 Model Initialization 81
4.3.2 Implementation of SIP Mechanisms into RAMS 86
4.4 Observational Results 88
4.4.1 INP Concentrations from SPICULE 88
4.4.2 Aircraft Cloud Passes and Estimating Ice Concentrations 92
4.4.3 Observations of Primary Nucleation and SIP 97
4.5 Evaluation of SIP Mechanisms in RAMS 105

4.6 Summary and Conclusions 108
Chapter 5: Characteristics of Ice Nucleating Particles from the Long-Range Transport of Saharan Dust 114
5.1 Mineral Dust Sourced from the Saharan Desert 114
5.2 ESCAPE Research Campaign 115
5.2.1 Aircraft Campaign Overview 115
5.2.2 Measurement of Aerosols and INPs during ESCAPE 116
5.3 Saharan Air Layer during ESCAPE 117
5.4 INP measurements of Saharan Dust 119
5.5 Comparison to the SPICULE campaign 125
5.6 Summary and Implications 127
Chapter 6: Conclusions 130
6.1 Summary of Studies 130
6.2 Implications and Future Work 134
References 138
Appendices 157
Appendix 1 157
A1.1 Flow Calculation Introduction 157
A1.2 Annular Forced Flow 157
A1.3 Annular Convective Flow 158
A1.4 Volume to Mass Flow Conversion 163
A1.5 Annular Water Vapor Profiles 165
A1.6 Comparisons to Previous Calculations 166

A1.7 Additional Figures 168

Appendix 2 172

A2.1 Estimate of Condensation Sinks in OFR 172

Appendix 3 177

CHAPTER 1: INTRODUCTION

1.1 Ice Crystals in the Atmosphere

Ice crystals are found in clouds across the globe at temperatures below 0 ºC. At temperatures below -38 ºC, cirrus clouds are composed entirely of ice (except at haze droplet sizes), while mixed-phase clouds (MPCs) occur at warmer temperatures between 0 and -38 ºC and contain both supercooled liquid droplets and ice crystals. The formation of ice crystals differs depending on the atmospheric conditions and the presence of ice nucleating particles (INPs). Sections 1.2 and 1.3 will describe the characteristics and formation mechanisms for cirrus and MPCs, respectively, and describe the importance of the ice-phase in global precipitation and the radiative balance.

1.2 Description of Cirrus Cloud Formation Mechanisms and Characteristics

Cirrus clouds are ubiquitous and play a significant role in the global radiative balance (Baker 1997; Liou 1986; Lynch 1996). Composed entirely of ice at temperatures < 235 K (-38 ºC), their formation in the atmosphere is controlled by upper tropospheric dynamical processes and the interplay between two basic ice nucleation pathways, homogeneous freezing and heterogeneous ice nucleation, which determines the size and number of ice crystals, and consequently can determine the warming or cooling effect of the clouds (Jensen et al. 1994; Zhang et al. 1999). Homogeneous freezing of condensed water is the process that will ultimately occur for the dissolved solute particles that constitute the major aerosol population capable of acting as cloud condensation nuclei (CCN), unless heterogeneous nucleation on a more specialized subset of aerosols intervenes to glaciate clouds before the relative humidity (RH) and solute dilution conditions required for homogeneous freezing can occur (Heymsfield et al. 2017;

Hoose and Möhler 2012), as discussed further below. Heterogeneous freezing requires an INP that catalyzes a freezing event by lowering the required energy in the activation process. Depending on environmental factors such as temperature and relative humidity, heterogeneous freezing may proceed via several different nucleation modes (Vali et al. 2015; Kanji et al. 2017; Hoose and Möhler 2012; Heymsfield et al. 2017). Firstly, immersion freezing is described by an INP becoming "immersed" in an aqueous solution or water droplet, with the presence of the particle surface initiating freezing. Often included in the immersion mode, as experimentally indistinguishable, condensation freezing describes the simultaneous uptake of liquid water on an INP and freezing. In contrast, deposition nucleation does not require any liquid water phase formation, instead forming ice directly from the supersaturated vapor onto an INP. However, it has been posited that this mechanism actually proceeds via a pathway wherein cavities on the surface of an INP fill with liquid water due to the reverse Kelvin effect, and that water subsequently freezes (pore condensation freezing, PCF) (Marcolli 2014; Campbell et al. 2017; David et al. 2019).

Homogeneous freezing of nearly pure water in the form of dilute cloud droplets depends on droplet size (volume) and temperature, but typically occurs by 235 K as clouds cool, and this temperature roughly brackets the highest temperature end of cirrus cloud formation. At lower temperatures, solution droplets (unactivated CCN) formed when the RH exceeded that required for deliquescence, freeze according to the solution water activity and the ambient temperature (Koop et al. 2000a). As a consequence, relatively high ice supersaturation (SS_i, equal to relative humidity with respect to ice (RH_i) minus 100%) must be achieved for homogeneous freezing to occur (DeMott et al. 2003a). Heterogeneous nucleation via condensation/immersion freezing can occur across the full range of tropospheric temperatures, primarily within dilute cloud droplets at

higher temperatures characteristic of mixed phase clouds, but progressively within more concentrated solution droplets at the lower temperatures that are characteristic of cirrus clouds. Whereas a freezing temperature can be stated to characterize where a particular ice nucleating particle type begins to freeze strongly via immersion freezing in dilute cloud droplets at mixed phase cloud temperatures, a water or ice relative humidity condition may be used to characterize the conditions for heterogeneous cirrus nucleation, reflecting solute compositional impacts on freezing (Zuberi et al. 2002; Archuleta et al. 2005).

During cirrus cloud formation, both heterogeneous and homogeneous nucleation may be active, or the former may dominate. The active nucleation mechanisms are determined by the number concentrations of INPs, their freezing onset characteristics, and the maximum relative humidity achieved, the latter of which depends on the strength and persistence of vertical motions that increase supersaturation against water vapor consumption by growing ice crystals (DeMott et al. 1997; Gierens 2003; Haag et al. 2003; Kärcher and Lohmann 2003). Homogeneous freezing will ensue when the RH_i exceeds the homogeneous freezing threshold (140 – 150 %, depending on temperature) (Krämer et al. 2009). Recent studies have attempted to group cirrus clouds in two categories, liquid origin and in situ, that are based on their dominant formation mechanism and the strength of vertical motions (Krämer et al. 2016, 2020; Luebke et al. 2016). Liquid origin cirrus are driven by deep convection, including contributions of heterogeneously frozen drops from the mixed phase regime and homogeneously frozen droplets that persist to cirrus levels, while in situ origin cirrus form entirely below 235 K via homogeneous and heterogeneous nucleation. Liquid origin cirrus generally contain high ice water content and ice crystal number concentrations, with the opposite for clouds of in situ origin (Krämer et al. 2016). Both cirrus origins may occur under either fast or slow updraft conditions

that largely determine the nucleation mechanism, where the former scenario likely leads to a dominance of homogeneous freezing and the latter proceeds via heterogeneous nucleation (albeit still debated in the literature). Meteorological scenarios where in situ cirrus may occur are synoptic scale systems (slow updraft) and gravity waves induced by jet streams, mesoscale convective systems and anvils (fast updrafts) (Krämer et al. 2016, 2020). One study inferred that cirrus have predominantly heterogeneous nucleation origins, based on the ice residuals (IR) that indicated the presence of INPs and the lower saturation requirement for nucleation in sub-tropical and tropical cirrus clouds (Cziczo et al. 2013). However, the dominant process of cirrus formation remains more broadly unresolved (Heymsfield et al. 2017), and likely varies depending on the particular aerosol and cloud dynamical scenario.

1.3 Ice in Mixed-Phase Clouds

Ice particle formation in the troposphere plays an important role in the physical processes of mixed-phase and ice clouds. MPCs are characterized by the presence of both supercooled liquid droplets and ice particles at temperatures between 0 and -38 ºC and have been found to occur from the tropics to polar regions across all times of the year (Korolev et al. 2017). Ice particles are particularly important in MPCs, firstly because they may control the supercooled liquid water content (LWC) through the Wegener–Bergeron–Findeisen process (Korolev, 2007), whereby ice crystals grow via vapor deposition at the expense of liquid droplets. However, this process may have limited importance in convective MPCs with strong updrafts where the vapor pressure in the clouds exceeds the saturation vapor pressure with respect to both liquid and ice (Korolev, 2007). Secondly, a significant fraction of continental precipitation initiates from the ice phase (Mülmenstädt et al. 2015), and hence processes that control ice formation will have impacts on the hydrological cycle and on cloud lifetimes.

The formation of ice in MPCs strongly depends on the presence of INPs, a specialized type of aerosol that facilitates the freezing process by lowering the required energy to overcome the initial formation of a critical ice embryo. In clouds forming entirely in the mixed-phase regime, heterogeneous nucleation represents the primary ice nucleation process. Heterogeneous nucleation may proceed via a number of different freezing pathways as described in the previous section. In the mixed-phase regime, the immersion freezing pathway should dominate heterogeneous nucleation, and it is assumed deposition freezing is not a significant freezing pathway, especially in convective updrafts when the ambient water RH is > 100 %. Heterogeneous nucleation will ultimately occur over a wide range of atmospheric conditions, generally at near water saturation, humidities that are frequently observed in MPCs (Korolev and Isaac 2006).

Secondary ice production (SIP) represents another source of ice particles in MPCs, where new ice crystals form through initial INP activation or through subsequent interactions between existing ice- and liquid-phase hydrometeors. SIP is generally believed to be the source of the observed discrepancy between the concentrations of INPs and ice crystals in many clouds (Pruppacher and Klett 1997; Field et al. 2017). Six mechanisms of SIP have been identified: 1) fragmentation of freezing droplets (FFD), 2) Hallett-Mossop rime-splintering (HM), 3) breakup from ice-ice collisions (BR), 4) ice fragmentation due to thermal shock, 5) fragmentation of sublimating ice and 6) the activation of INPs in supersaturated regions around freezing drops (Korolev and Leisner 2020). The Hallett-Mossop (HM) mechanism, or rime splintering, occurs over a relatively small range of temperatures (-8 ºC to -3 ºC) and relies on the presence of cloud droplets < 13μm and > 24 μm (Hallett and Mossop 1974), as well as the occurrence of larger frozen particles such as graupel. Because this mechanism requires specific cloud droplet sizes,

and is strongly linked to an active coalescence process, it may be affected by increased aerosol concentrations producing more numerous small cloud droplets (Twomey 1977). For example, Phillips et al. (2001) simulated the effects of CCN concentrations on the HM process, and showed that higher CCN concentrations decreased the average sizes of supercooled cloud droplets and greatly suppressed the HM process, due to the limitations on meeting the requirement of cloud drops with diameters > 24 μm. That same study also examined the effects of cloud base temperature (T_{CB}), and found when the T_{CB} was < 10 ºC, the mean droplet size decreased and suppressed SIP. The heterogeneous freezing and fragmentation of larger droplets (drizzle or rain), with the inclusion of an INP or ice crystal, may occur at a much broader temperature range and produce fragmented ice particles on freezing, when the ice shell around the liquid forms and expands, building up the internal pressure and sometimes leading to cracking, shattering and jetting of small ice particles (Korolev and Leisner 2020; Wildeman et al. 2017). In laboratory experiments with stagnant airflow, Lauber et al. (2018) showed ejection and breakup of 85 and 300 μm droplets upon freezing that occurred most frequently between -10 ºC and -20 ºC. Under free-fall flow velocity in moist air, Keinert et al. (2020) showed that freezing frequencies of 300 μm droplets increased and could stimulate SIP events at temperatures as high as -5 ºC. Thus far, in situ observations of tropical and continental cumulus congestus clouds suggest that a warmer T_{CB} > 10 ºC facilitated strong coalescence processes leading to large enough drops (> ~200 μm) that may initiate FFD below -10 ºC (Lawson et al. 2015; 2017; 2022). Lawson et al. (2015) speculated that their observations of ice at temperatures between -8 ºC and -12 ºC in tropical cumulus clouds may be represented by FFD since none of the observed ice were faceted, which would be expected for ice forming via vapor deposition. Droplets with diameters smaller than ~50 μm were found not to shatter upon freezing between -10 ºC and

-15 ºC (Pruppacher and Klett 1997; Wildeman et al. 2017). Much less is known or has been observed regarding the remaining three SIP mechanisms.

1.4 Objectives and Overview

Broadly, this dissertation is primarily focused on the improved understanding of the role of INPs in cirrus and mixed-phase clouds using both laboratory experiments and in situ airborne observations. Two laboratory studies, described in Chapters 2 and 3, were conducted to better understand the role of sea spray aerosols (SSA) under cirrus cloud conditions. Chapters 4 and 5 report observations of INPs from airborne platforms.

Chapter 2[1] reports the first laboratory experiment that was conducted to investigate the ice nucleating ability at temperatures below 235 K of particles generated from natural seawater. Lab-generated aerosols were probed using a continuous flow diffusion chamber (CFDC) (Archuleta et al. 2005; DeMott et al. 2009a; Rogers, 1988) that had been modified to reach temperatures below 200 K. While a number of previous studies have investigated the low temperature ice nucleation of SSA proxies such as NaCl or artificial seawater products (Schill and Tolbert 2014; Wagner et al. 2018; Wise et al. 2012), SSA generated from natural seawater had yet to be studied. Therefore, the ice nucleation characteristics of natural seawater-derived particles were compared to pure NaCl particles, and the impact of particle size on ice nucleation behavior was also investigated.

[1]This study is titled "Is Ice Formation by Sea Spray Aerosols at Cirrus Temperatures Controlled by Crystalline Salts? (Patnaude, R. J., Perkins, R. J., Kreidenweis, S. M., DeMott, P. J., 2021b), published in ACS Earth and Space Chemistry

Chapter 3[2] reports on the findings from the second laboratory study examining SSA as a source of cirrus cloud INPs, which expanded upon the work in Patnaude et al. (2021b) described in Chapter 2. Firstly, we examined the low temperature ice nucleating ability of SSA, generated using a Marine Aerosol Reference Tank (MART, Stokes et al. (2013)) that was designed to realistically represent ocean–atmosphere emissions of SSA and potentially gaseous emissions from seawater, compared to the very simple aerosol generation mechanism in Patnaude et al. (2021b). In contrast to the study in Chapter 2, which focused on freshly created particles, this laboratory study used an Aerodyne potential aerosol mass oxidation flow reactor (OFR) to examine the impact of atmospheric oxidation on the freezing behavior of primary SSA at cirrus temperatures. This was motivated by the fact that as the SSA particles are generated and during the pathway to the upper troposphere, SSA and any other emitted species are exposed to atmospheric oxidation, which can lead to addition or modification of organic coatings on the particle surface and subsequently impact ice nucleation. Secondly, the low temperature freezing behavior of secondary marine aerosols (SMA) produced during oxidation of gas-phase emissions from seawater was investigated. We compared primary SSA and SMA generated from real seawater and an artificial seawater product to infer the roles of the organic material and inorganic sea salts on heterogeneous ice nucleation at cirrus temperatures. In summary, the objectives of these two laboratory studies were as follows:

[2]This study is titled "Low Temperature Ice Nucleation of Sea Spray and Secondary Marine Aerosols Under Cirrus Cloud Conditions" (Patnaude, R. J., Moore, K. A., Perkins, R. J., Hill, T. C., DeMott, P. J., Kreidenweis, S. M., 2023) is conditionally accepted, pending revision in Atmospheric Chemistry and Physics

1) *Advance our understanding of the characteristics of SSA (i.e., phase state, particle size) that contribute to their low temperature ice nucleation, and the atmospheric implications.*
2) *Better understand the effects of atmospheric oxidation on the ice nucleating behavior of SSA at cirrus temperatures.*
3) *Determine whether SMA may act as a source of cirrus cloud INPs*

The next two chapters will move from laboratory studies to in situ field observations to understand other types of ambient INPs, and seeking experimental evidence of SIP in clouds. Chapters 4[3] presents in situ observations collected from the Secondary Production of Ice in Cumulus Experiment (SPICULE) campaign. The SPICULE campaign targeted ascending cumulus congestus clouds over the U.S. Central Great Plains. A major advancement made in this study was to design flight strategies to develop a more complete dataset of cloud microphysical, thermodynamic and dynamic measurements, as well as coincident measurements of in situ aerosol, INP and ice crystal number concentrations, than what was previously available in the literature. Ice crystal and INP concentrations were measured in young convective updrafts and were compared to infer whether SIP was active in updrafts early in cumulus congestus cloud life cycles. Although the theoretical processes of ice formation in convective clouds are well understood, observing these processes from aircraft observations is extremely difficult. This is in part due to the physical processes in clouds occurring faster than an aircraft can penetrate them. Therefore, in situ observations only capture a snapshot in time. Idealized numerical model

[3]This study is titled "On the Role of Airborne Ice Nucleating Particles in Primary and Secondary Ice Formation in Convective Midlatitude Clouds" (Patnaude, R. J., Moore, K. A., Perkins, R. J., Lawson, P., Raudzens Bailey, A., DeMott, P. J., van den Heever, S. C., Saleeby, S.M., Chiu, J. C., Bian, Q., Kreidenweis, S. M., 2023) in preparation, to be submitted to the Journal of Atmospheric Sciences

simulations, guided by the observations, were conducted to fill in these gaps, with a particular focus on exploring whether the inclusion of additional SIP mechanisms, besides the Hallet-Mossop rime-splintering mechanism, led to improved representation of the observed ice phase in young congestus updrafts. The analysis in this chapter is ongoing and the findings may change following additional simulations and deeper analysis of the observed ice crystal habits. The objectives of this chapter are as follows:

4) *Present a method for using in situ observations of INPs and ice crystal number concentrations to infer the ice formation mechanisms in congestus clouds.*
5) *Elucidate the relationship between environmental and cloud conditions and the onset of SIP in cumulus congestus clouds.*
6) *Improve our understanding of the chain of events in the formation of ice and relevant mechanisms over the course of the early lifetime of cumulus congestus clouds.*

Chapter 5[4] presents INP observations during a Saharan Air Layer (SAL) event that occurred during the Experiment of Sea Breeze Convection, Aerosols, Precipitation, and Environment (ESCAPE) campaign, keying on another important atmospheric aerosol type, the mineral dust aerosolized and transported from major desert regions around the globe. Until this study, with the exception of one airborne study in 2003 over Florida, the majority of reported measurements of INPs sourced from the Saharan Desert were collected near the source region or generated in the laboratory from dust samples, and much less was known about INPs associated with this aerosol type after long-range transport to the U.S. The SAL event was present during

[4]This study is titled "Characteristics of Ice Nucleating Particles from the Long-Range Transport of Saharan Dust" (Patnaude, R. J., McCluskey, C. S., DeMott, P. J., McFarquhar, G. M., Kollias, P., Wolde, M., Kreidenweis, S. M., 2023) in preparation, to be submitted to Geophysical Research Letters

the last five research flights of the ESCAPE campaign, which allowed for direct measurements of INP concentrations from Saharan dust. The objectives of this chapter include:

7) *Quantify the ice nucleating particle concentrations from Saharan Dust transported across the Atlantic Ocean.*
8) *Compare INP characteristics of Saharan dust collected during ESCAPE to the previously reported observations of Saharan dust much closer to the source regions.*
9) *Contrast the coastal and SAL dominated INP concentrations from ESCAPE to the INP measurements collected further north and west during SPICULE.*

Finally, Chapter 6 provides a summary of the studies presented in this dissertation and concluding remarks. This section also includes the atmospheric implications from these studies and suggests recommended future work.

CHAPTER 2: SEA SPRAY AEROSOLS AS A SOUCRE OF ICE NUCLEATING PARTICLES IN CIRRUS CLOUDS

2.1 Background on Cirrus Cloud INPs

Despite significant efforts, the role of specific types of aerosol particles in the formation of cirrus clouds remains highly uncertain (Boucher et al. 2013). In limited and specialized in situ observations, particles such as mineral dust and metallic particles have been noted to make up the largest fraction of ice residuals (IR) in cirrus clouds (Cziczo et al. 2004, 2013; Cziczo and Froyd 2014). Black carbon and isoprene-derived secondary organic aerosols (SOA) are frequently observed in the upper troposphere (Froyd et al. 2010; Schill et al. 2020; Schwarz et al. 2017). While black carbon is known to contribute significantly to IR in contrails, observations mostly suggest that these particle types do not contribute strongly as ice nucleating particles (INPs) in cirrus clouds, even though pathways for such action involving processing of larger aggregates have recently been revealed (Mahrt et al. 2020). Certain SOA have been observed to freeze heterogeneously with low active fractions (Wolf et al. 2020a), but most SOA is expected to freeze via the homogeneous pathway. Sea spray aerosols (SSA) also deserve attention in this regard due to their abundance in the atmosphere (O'Dowd et al. 1997), and the fact that sea salt particles have been observed to make up a significant fraction of the IR in cirrus clouds over ocean regions, where deep convection lofts particles to the upper troposphere where they are detrained from the cloud itself and can persist at high altitudes (Cziczo et al. 2004, 2013; Twohy and Poellot 2005). While it has been assumed that the role of SSA on impacting cirrus formation would most likely come about via their dominant composition as soluble species (Kärcher and Lohmann 2003), their phase states when lofted to the upper troposphere could present scenarios

where their action as heterogeneous INPs should be considered. In the upper troposphere, SSA concentrations can range between 10^{-4} and 10^{-1} μg m^{-3}, based on in situ and satellite observations (Bian et al. 2019; Murphy et al. 2019). In terms of relative abundance, SSA are more scarce than sulfate particles, which have been reported to make up a large percentage of aerosols in the upper troposphere (Chen et al. 1998; Murphy et al. 1998). However, only a very small fraction of sulfate particles freeze heterogeneously at these temperatures (Abbatt et al. 2006), and therefore any heterogeneous freezing potential of SSA could prove significant. For example, in a case study of Hurricane Nora, the authors speculated that marine aerosols generated and lofted in the deep convective core seeded cirrus clouds over a spatially and temporally vast region (Sassen et al. 2003a). Thus, understanding the ice nucleating mode of SSA at cirrus temperatures deserves further attention.

SSA are generated during wave breaking by the bursting of small film and jet-drop bubbles at the sea surface microlayer (Wilson et al. 2015; O'Dowd and De Leeuw 2007). Their composition may broadly include organic materials such as lipids, amino acids, saccharides, phytoplankton cell fragments, and inorganic sea salts (Gantt and Meskhidze 2013; Prather et al. 2013). While dissolved, surface active, and particulate organic matter in SSA are known to serve as sources of low concentrations of immersion freezing INPs in the mixed-phase cloud regime (>-38 ºC) (McCluskey et al. 2018b, the propensity of these to freeze at cirrus temperatures still remains uncertain, especially since ice nucleation modes there may be more varied. A number of studies have attempted to elucidate the heterogeneous nucleation ability of SSA in cirrus conditions using commercially available synthetic seawater products (Ladino et al. 2016; Schill and Tolbert 2014; Wagner et al. 2018, 2021; Wolf et al. 2019), and produced inconsistent results on whether the organic material enhanced or suppressed nucleation. However, using

Prochlorococcus as a source of organic matter to mimic natural marine aerosols, polysaccharides and proteins were found to potentially enhance the efficiency of SSA nucleation, whereas lipids were ineffective INPs (Wolf et al. 2019). Of further consideration at cirrus temperatures, some previous studies have shown that aqueous particles containing organic material may transition into a highly viscous semi-solid or solid glassy state (Ignatius et al. 2016; Knopf et al. 2018; Zhang et al. 2019; Zobrist et al. 2008). One study using citric acid tested the role glassy aerosols may play in ice nucleation, and found that below 212 K a fraction of glassy aerosols can freeze at relative humidities below those at which homogeneous nucleation would be expected (Murray et al. 2010). The ability of glassy aerosols to nucleate ice has largely been determined by the glass transition temperature and hygroscopicity, both of which can be affected by chemical aging and size of the particles (Berkemeier et al. 2014). Despite this freezing behavior of glassy aerosol, it is still assumed they would freeze at low fractions similar to secondary organic aerosols (Wolf et al. 2020a).

In the last decade, a number of studies have also investigated the inorganic components of SSA for their role in ice nucleation (Kong et al. 2018; Ladino et al. 2016; Schill and Tolbert 2014; Wagner et al. 2018; Wagner and Möhler 2013; Wise et al. 2012; Wolf et al. 2019). As the major component of natural seawater, sodium chloride (NaCl) has frequently been used as a proxy for sea spray aerosol (Tang et al. 1997). The pathway of ice nucleation for NaCl has been found to be largely determined by the phase state of the salt particles, where the mode of freezing is dependent upon the competition between deliquescence and heterogeneous freezing (Ladino et al. 2016; Schill and Tolbert 2014; Wagner et al. 2018). One study using the AIDA cloud chamber showed that both anhydrous NaCl and NaCl dihydrate particles that were fully deliquesced froze via homogeneous freezing above 225 K when exposed to high ice

supersaturation (SS_i, equal to relative humidity with respect to ice (RH_i) minus 100%). However, near their deliquescence point and below about 225 K, NaCl particles formed an internally mixed liquid-solid phase with solid crystalline remnants and froze via the immersion mode (Schill and Tolbert 2014). NaCl particles below their deliquescence relative humidities (DRH) remained solid and were reported to freeze via the deposition mode (Kong et al. 2018; Wise et al. 2012). These prior studies used different particles sizes (~0.7 – 10 μm), and it is unclear how size affected heterogeneous nucleation of NaCl particles. Finally, effloresced aqueous NaCl at cirrus temperatures can form hydrated salts that have been reported to act as heterogenous INPs (Wise et al. 2012; Wagner and Möhler 2013). One study using air mass trajectory analysis showed that hydrated salt particles may be present 40–80 % of the time at temperatures between 180 and 220 K when lofted from the boundary layer and detrained in deep convective anvils (Wise et al. 2012). The extent to which the organic components or non-NaCl salt contents affect the ice nucleating ability of natural seawater has received only limited attention in the current literature and remains uncertain.

2.2 Experimental Description

2.2.1 CFDC Setup

Ice nucleation experiments were conducted with a CFDC at Colorado State University (CSU) based on previously described designs (Archuleta et al. 2005; DeMott et al. 2009a, 2015; Rogers et al. 2001) modified to measure ice nucleation at temperatures from 240 K to 190 K. The CFDC consists of two concentric cylinders, which are coated in a thin layer of ice. The inner and outer walls of the chamber are held at different temperatures, producing gradients in both temperatures and water partial pressure. This can be used to create relative humidity conditions above saturation with respect to either ice or water (Rogers, 1988). Sheath air flow is inserted

into the column allowing sample flow to enter the column and remain in a narrow, central lamina flow. Calculations are carried out to determine temperature and supersaturation conditions experienced by aerosol within the instrument. These calculations are based on those of Rogers (1988), but modified to more accurately represent instrument geometry and prevent breakdown of calculations at low temperatures and flow rates. A full derivation of the current calculations and discussion of measurement uncertainties can be found in Appendix 1. Prior to nucleation experiments, the column is chilled to 246 K and filled temporarily with deionized water to produce the ice coating along the column walls.

Some modifications to the physical design and mode of operation were made to the low temperature CFDC as compared to its previous configuration. First, flow rates were reduced through the 1.51 m chamber (Figure 2.1), resulting in longer residence time of aerosols to promote activated ice crystal growth. The residence time is increased by operating at lower flow rates of 1 LPM_v sample flow and 4 LPM_v sheath flow (volumetric flows measured at column conditions, not ambient) than have been used in the past, where typically a 10:1 sheath to sample flow ratio has been used. This additional residence time is helpful because ice crystal growth slows with decreasing temperature, as water partial pressures decrease for a given SS_i, and final aerosol size is used to distinguish between frozen and unfrozen aerosol, as discussed in Section 2.3. Additionally, the bottom section of the column has been plumbed to allow for operation either as an evaporation section (constant temperature walls, $RH_i \sim 100\%$ or slightly above), or as an additional growth section (walls held at the same temperature throughout the chamber). Evaporation sections are useful in situations at > 235 K where positive water supersaturations (SS_w, equal to relative humidity over water (RH_w) – 100 %) are required to activate water droplets prior to immersion freezing by a small subset of the particles. In that case, the

evaporation section at low SS_i causes water droplets to evaporate toward liquid aerosol sizes while ice crystals continue to slowly grow, such that only ice crystals sustain sizes far exceeding aerosol sizes and are thus detected as nucleated particles. Under the low temperature conditions of this study, however, the growth region is held below water saturation, where particles achieve at most haze sizes, so an evaporation section is not required. For all experiments described here, the bottom section of the column is used as additional growth section, allowing for extra residence time at growth conditions. This extra growth time allows for clearly distinguishing the nucleated ice crystal mode from the aerosol mode optically, as discussed later.

A second, and minor change to the laboratory CFDC configuration is the use of two ultra-low temperature circulating bath chillers (Thermo Scientific ULT-95) to control the fluid circulated to inner and outer walls of the chamber, extending the effective operating range beyond the ~211 K lower lamina temperature achieved in past studies. The bath fluid used is a low temperature, low viscosity, high thermal conductivity silicone oil (Syltherm XLT, Dow). This allows for lower temperature operation with very stable temperatures and negligible gradient across a given wall of the instrument.

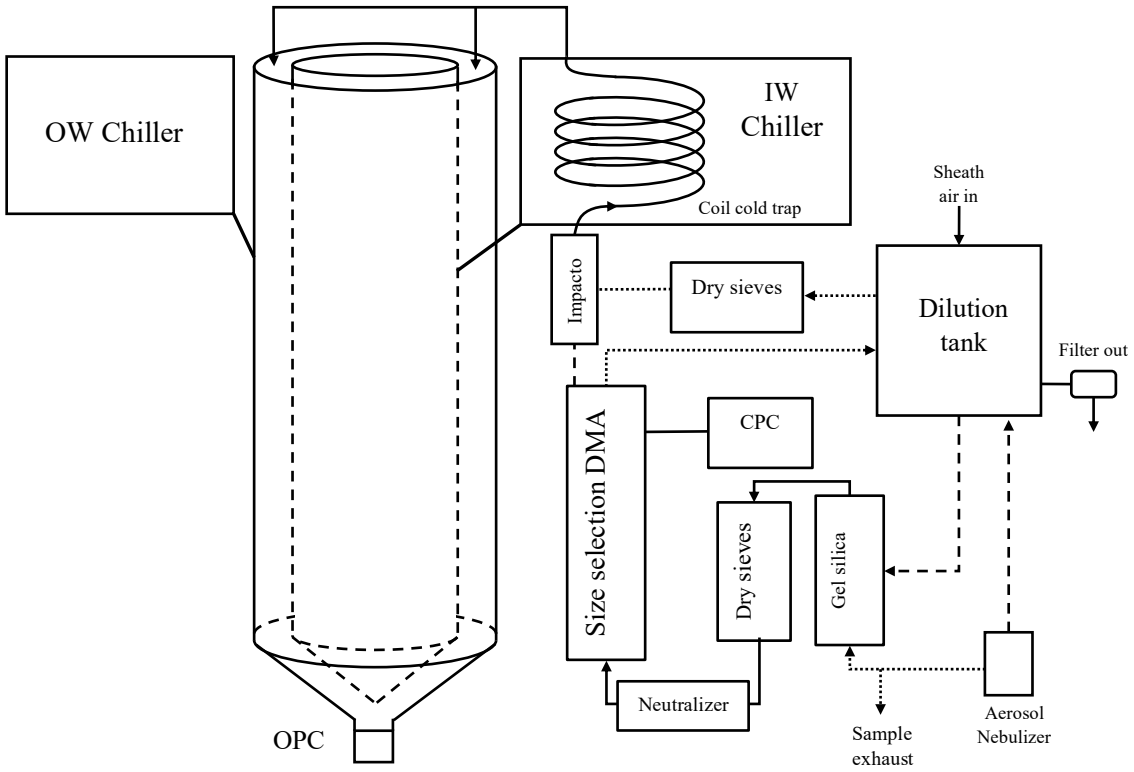


Figure 2.1. Diagram of the setup for SSA and NaCl generation, size selection, and flow configuration for CFDC experiments. Note, dashed and dotted lines indicate the pathway during experiments when selecting for 150 nm and 600 nm aerosols, respectively, and solid lines indicate the shared pathway for both aerosol sizes.

Finally, the sample and sheath air drying systems were modified from standard desiccant drying systems to cold traps. For low temperature operation, standard desiccants such as silica gel and molecular sieves do not provide sufficient drying. Molecular sieves, for example, can dry ambient air to a RH of ~1%. At 25 °C, this corresponds to a vapor pressure of about 0.31 mbar. If this same air mass is cooled to -65 °C this corresponds to a SS_w of ~3200 %, which would prevent meaningful instrument operation. Although such instant cooling and high SS_w are an extreme scenario, to avoid this problem, cold traps are installed in both the sheath and sample lines submerged in the cold wall chiller bath. These traps are simple coils of copper tubing, 3.4 and 2.2 m long for the sheath and sample traps, respectively. The bath is a few degrees colder than the cold inner wall of the instrument, which is always colder than the temperatures the

aerosol experience within the instrument. The trap will force the RH to ice saturation at the trap temperature, which will always be a lower vapor pressure than ice saturation under aerosol conditions in the growth region of the instrument. Hence all sample and sheath air entering the instrument will remain below ice saturation upon cooling. One additional consideration with this approach is that incoming sample air should be allowed to warm between the cold trap and introduction into the growth chamber to allow for transport of residual water off the aerosol particles. Given the small mass of aerosol relative to air, the effect on RH of water evaporating from the aerosol is negligible.

2.2.2 Description of Aerosol Generation and Phase State

Aerosol measurements and size distributions were obtained using a combination of a differential mobility analyzer (DMA, TSI model 3071A), a condensation particle counter (CPC, TSI model 3010), and an aerodynamic particle sizer (APS, TSI model 3321). In this study, natural seawater (SW) collected from the Scripps Pier in La Jolla, CA was used for SSA generation. The seawater was stored in the dark and flown at room temperature to CSU. It was then filtered through a 0.22 μm sterile PES filter to sterilize the seawater to prevent any microbial growth and remove additional insoluble material such as dust and sand that may be present. Following filtration, it was again stored in the dark until use. For comparison, we used a 3.5% by weight NaCl (certified ACS, Fisher Chemical) solution prepared with deionized water to mimic the salt content of seawater. Aerosols were generated using a B&F Medical Aeromist Nebulizer and dried at room temperatures using a silica gel diffusion dryer followed by a molecular sieve dryer. Particles were then size selected at either 150 nm or 600 nm using the DMA, operated with a sheath(sample) flow of 10(2) and 4(1) LPM_v, respectively. Aerosol concentrations were diluted to achieve concentrations in the range of 100 – 500 cm^{-3}, and

depending on the aerosol size, the configuration of the dilution tank and DMA was rearranged to control aerosol flow into the DMA. For example, for 150 nm particles the dilution tank was located upstream of the DMA, and the opposite for 600 nm (Figure 2.1). An additional molecular sieve dryer was required after the dilution tank for 600 nm particles as the sheath air contained small amounts of water vapor and would build up ice in the cold trap during experiments. Finally, particles size selected at 600 nm were passed through a 2.5 μm aerodynamic impactor before entering the CFDC, in order to limit larger particles that would have made discerning small, activated ice crystals difficult at the slow growth rates present at cirrus temperatures.

Previous studies have shown that two crystalline structures can form via efflorescence of NaCl, i.e., anhydrous NaCl and NaCl dihydrate ($NaCl \bullet 2H_2O$), where the former is the stable phase above ~273 K and the latter below ~273 K (Martin 2000). For this study, since NaCl particles are dried beyond their efflorescence RH of ~45 % at room temperature, it is assumed the particles entering the CFDC have an anhydrous NaCl structure (Koop et al. 2000b) (see trajectory phase state diagram, Figure 2.2). Although injection of the seed particles into the CFDC system occurred at temperatures below 273 K, dry NaCl particles remained below the eutectic (Koop et al. 2000a) and thus likely retained the anhydrous NaCl form, compared to scenarios where some aqueous particles that effloresced below 252 K formed $NaCl \bullet 2H_2O$ (Wise et al. 2012). Therefore, we discounted the possibility that the experimental results reflected sampling of $NaCl \bullet 2H_2O$ in this study. The structure of the SSA particles is more complex to characterize at low temperatures. Although very low RHs are achieved during aerosol drying after generation and before introduction into the CFDC, prior work has demonstrated that it is likely that SSA particles retain liquid water, due to the presence of ions other than sodium and chloride and varying organic components (Koop et al. 2000b; Peckhaus et

al. 2016b; Tang et al. 1997). The range of organic mass fractions in submicron SSA particles may vary but previous studies generally show an increase with decreasing particle size (Prather et al. 2013; Bertram et al. 2018). We assume the SSA particles in this study would exhibit similar characteristics but cannot rule out some differences due to varying generation methods. Additionally, it is possible for small amounts of other salts (i.e., magnesium and calcium) in SSA to precipitate prior to the NaCl contents(Tang and Munkelwitz 1993).

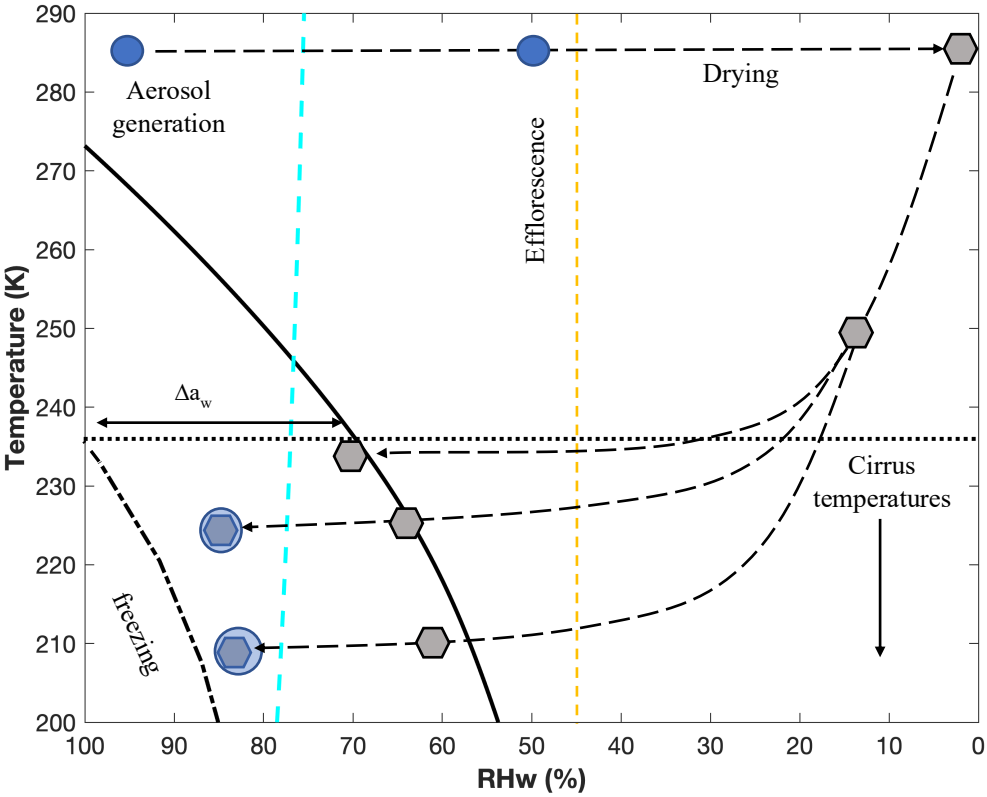


Figure 2.2. Expected trajectory and phase state of the NaCl and SSA particles for CFDC experiments. Cyan and orange dashed lines are the expected deliquescence and efflorescence lines, respectively, for NaCl based on the parameterization of anhydrous NaCl and extrapolated to cirrus temperatures(Tang and Munkelwitz 1993). The long dashed black line follows the path of aerosol particles as through drying, cooling, and CFDC scans at different temperatures. The blue circle represents aqueous NaCl and SSA solution, gray hexagons represent effloresced aerosols, and the light blue circles with embedded hexagon represents deliquesced particles. Lines indicating ice saturation and predicted homogeneous freezing conditions are also denoted. The gray hatched region indicates ice supersaturated conditions with dry aerosols, and the dotted region represents conditions where aerosol particles experience ice supersaturated conditions and relative humidities that exceed their deliquescence point.

Figure 2.3 shows the combined size distributions from the SMPS and APS for SSA and NaCl after drying but before size selection. The blue diamonds denote SMPS data with a measurement range of 12 – 615 nm and cyan circles denote APS data with a measurement range of 520 nm – 20 μm. The black solid line represents the best fit line averaged for 4 separate scans from the SMPS and APS. APS measurements were converted to true diameter from aerodynamic diameter using equation (2.1):

$$D_t = D_a \sqrt{\frac{\chi}{\rho_p}} \tag{2.1}$$

where D_t is the true diameter, D_a is the aerodynamic diameter, χ is the dynamic shape factor, and ρ_p is dry particle density. For dynamic shape factor, we used 1.08 and 1.05 for NaCl and SSA, respectively(Zieger et al. 2017) and estimated particle densities for SSA and NaCl of 2.2 g m^{-3} (Brock et al. 2019), and 2.16 g m^{-3}, respectively. The resulting corrections shifted APS data towards slightly smaller sizes. In general, the distributions of both SSA and NaCl had peaks ~100 nm. The SSA distribution indicated an increase in number concentrations of particles < 1 μm of almost five times that obtained for NaCl, and also showed a broader distribution of particles > 1 μm, consistent with previous studies using a similar method combining SMPS and APS data for SSA (Quinn et al. 2015; Collins et al. 2014).

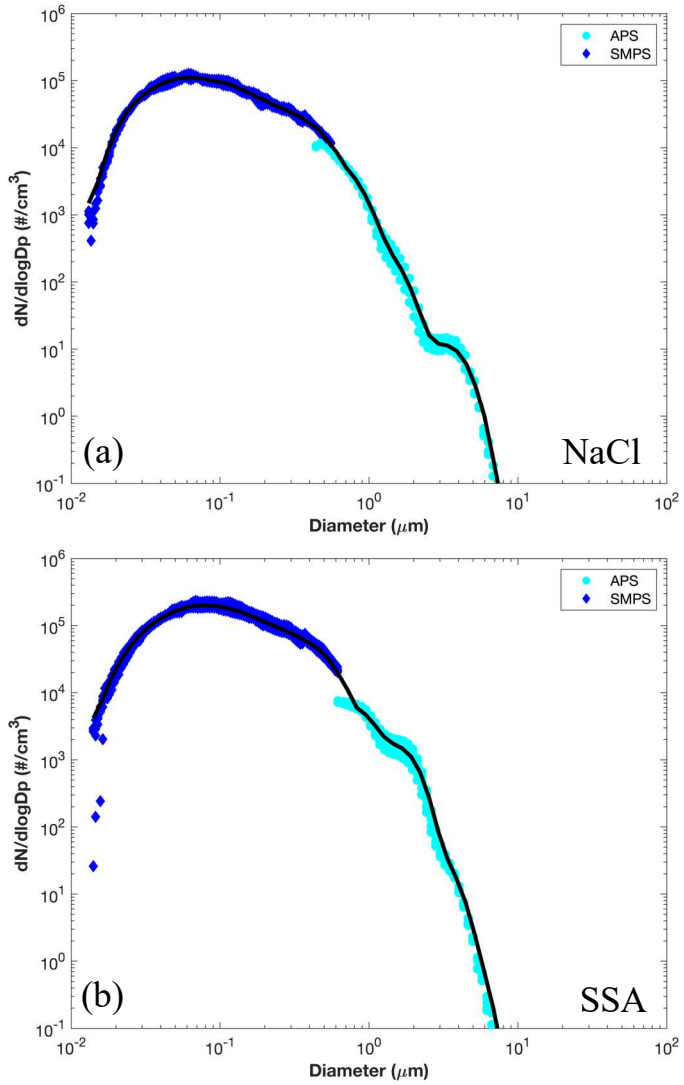


Figure 2.3. Combined particle size distributions for (a) NaCl and (b) SSA particle by combining measurements from a SMPS (blue diamonds) and an APS (cyan circles). The solid black line is the best fit from four measurement scans from the SMPS and APS.

Figure 2.4 shows the fraction of different sized particles predicted to be present after size selection at 150 and 600 nm with the DMA. For SSA (NaCl), a +1 charge represents 74% (76%) of the sample after applying the fractional contributions of the monodisperse aerosol population for 150 nm, and 86 % (92 %) for 600 nm, based on their respective size distributions. Larger, multiply-charged particles were present in sufficient numbers that we must consider their effects

in detection of frozen particles, as discussed below, and explicitly account for their contributions to aerosol surface area, as discussed in Section 3.

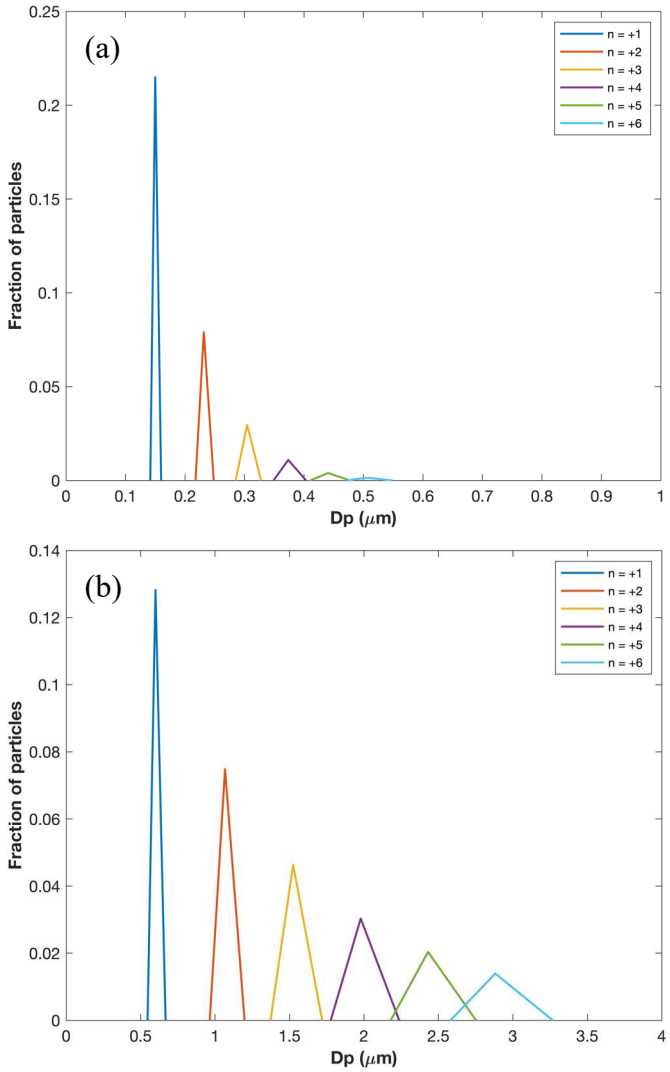


Figure 2.4. The fraction of particles represented by a given DMA multiplet, ranging from charges of +1 up to +6 for a monodisperse aerosol distribution of (a) 150 nm and (b) 600 nm particles.

2.2.3 Ice nucleation Detection

For detection of ice, an optical particle counter (OPC) located immediately downstream of the CFDC column detects particle sizes. Aerosol particles that do not freeze or deliquesce will not change size appreciably. Frozen particles, however, will grow rapidly, only constrained by

the rate of diffusional growth and residence time in the instrument. To distinguish between frozen and unfrozen particles, we introduce a size bin cutoff in OPC response. This size cutoff is determined by analyzing the distribution of seed particles from the OPC against the distribution of particles at conditions where a high frozen fraction was observed, and is different for 150 nm and 600 nm particles but identical between temperatures. The size bin cutoff is chosen such that no ice nucleation is detected for NaCl samples at higher temperatures where ice nucleation is not expected to occur. This approach essentially accounts for impacts of larger multiply charged particles passing through the DMA, ensuring that those large particles are not counted as frozen particles unless they have actually frozen.

2.3 Results of SSA Ice Nucleation

For ice nucleation experiments, the procedure for the CFDC involves "scans", while sampling the aerosol stream, where RH_w and RH_i increase over time at a quasi-steady laminar temperature, which is achieved by incrementally increasing the outer wall temperature (T_{OW}) while holding the inner wall temperature (T_{IW}) constant. Once a fraction of ice of 10 % is reached, the T_{IW} is stepped down 5 K and the T_{OW} is decreased incrementally until the fraction of ice is < 0.1 %. The cycle is generally repeated 4 – 6 times until temperatures reach < 220 K. For each aerosol type and size, two CFDC scans were conducted, one beginning at ~228 K and one at ~223 K, totaling eight experiments. The time series in Figure 2.5 represent scans for 150 nm NaCl particles at different temperatures producing different freezing results. For example, Figure 2.5a shows two subsequent CFDC scans that began at 228 K and 223 K. In the first case, there was no ice formation until the SS_i reached nearly 50 %, and there was a sudden increase in the number of ice particles (Figure 2.5a, cyan line). This scan illustrates a case of homogeneous freezing, where no ice is formed until the SS_i reaches the homogeneous freezing threshold and

nearly all the aerosol particles freeze. A similar trend was observed as RH was increased again beginning at 223 K, where in this particular case the SS_i reached even higher values (~55 %) before ice formation began. This observation is consistent with results from expansion chamber experiments using anhydrous NaCl particles starting at 235 K (Wagner et al. 2018), wherein particles passed their DRH and subsequently froze via homogeneous freezing. In addition, the ~5% increase in RH_i between 228 and 223 K follows closely with the expected homogeneous freezing conditions for fully dissolved particles (Koop et al. 2000a).

For CFDC scans of NaCl starting at colder temperatures (Figure 2.5b), ice nucleation behavior was considerably different. In the first scan starting at 218 K, ice formation was observed at SS_i as low as 30 %, with a gradual increase in the number of ice particles with increasing SS_i up to ~40 % before RH was reset to a lower value. Note the scans reset when the temperature (red line) dropped 5 K, and produced a modest increase in supersaturations due to the T_{IW} decreasing faster than the T_{OW}. The second scan starting ~214 K showed a similar trend and SS_i only reached 38% before the ice fraction reached 10 % and the RH was brought back down. This SS_i was well below the highest SS_i that was reached during scans at warmer temperatures. These cases illustrate NaCl freezing through an apparent heterogeneous nucleation process since the onset of freezing occurred at ~30 % SS_i, well below the threshold expected for homogeneous freezing. The ice nucleating behavior of SSA for 150 nm particles produced very similar trends as observed for NaCl (Figure A1.4).

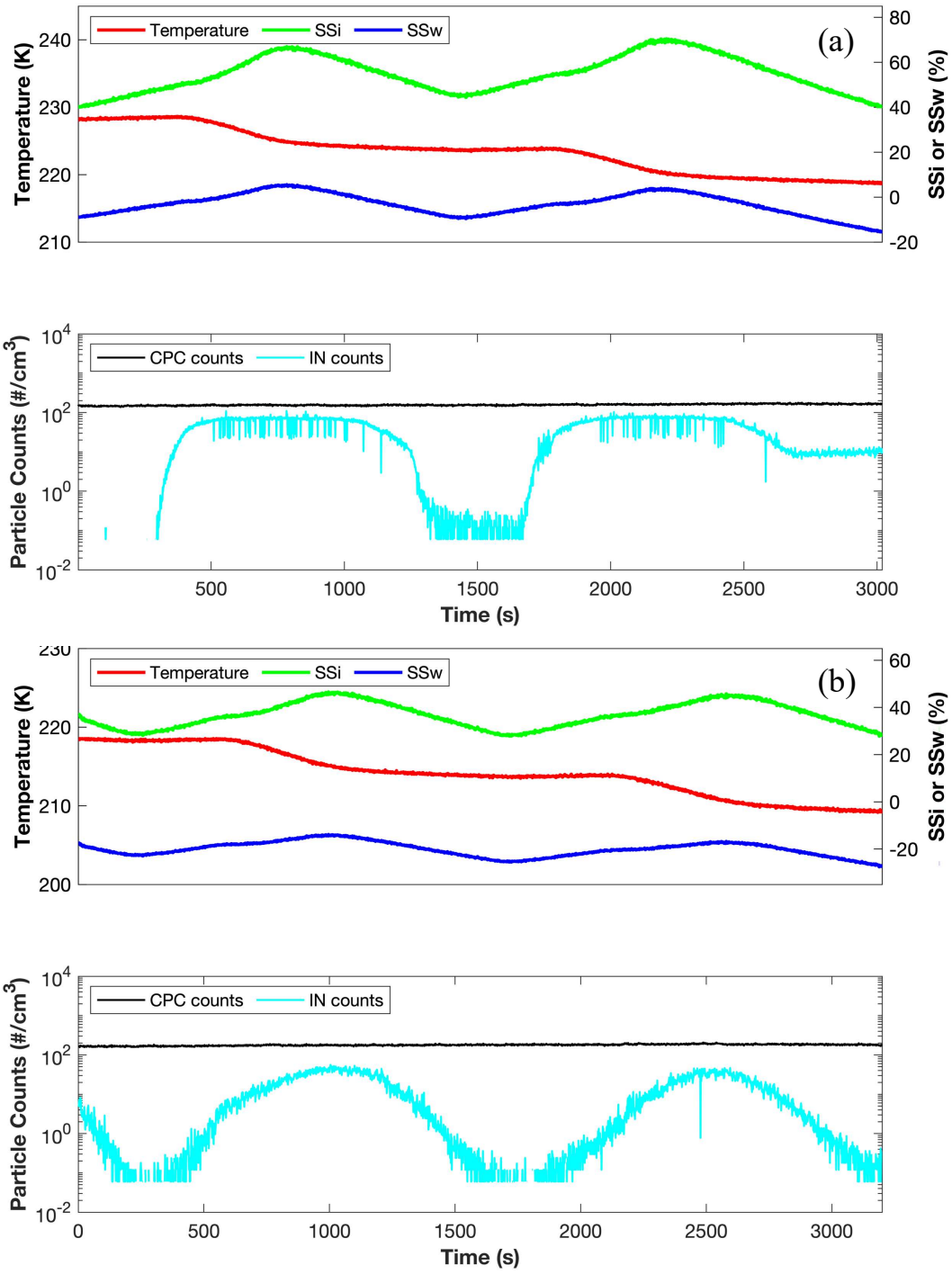


Figure 2.5. CFDC time series for NaCl experiments at (a) ~228 K and 223 K, and experiments at (b) ~218 K and 214 K. Red line indicates temperature and blue and green lines indicate water and ice supersaturations, respectively. Black and cyan lines indicate the number of particles from the CPC and ice nucleating particles, respectively.

To elucidate the ice nucleating behaviors of differing aerosol sizes, Figure 2.6 shows the ice fraction of 1 % and 10 % freezing in T – RH_w space for both sizes of SSA and NaCl at temperatures < 230 K. The fraction freezing is based on ice concentrations divided by total CPC counts rather than OPC counts. Using the CPC provided a more reliable total aerosol count since the OPC may not have captured the smallest aerosols that were not deliquesced, particularly for the 150 nm experiments. Results using total aerosol counts from the OPC can be found in Figure A1.5. The color and shape of markers indicate the size and ice active fraction of the particles, where open markers denote 150 nm and filled denote 600 nm particles. Black solid and dashed lines denote ice saturation and the predicted homogeneous freezing threshold (Koop et al. 2000a), respectively. The majority of NaCl particles froze near the homogeneous freezing line above 222 K. The 10 % ice fraction observations above the homogeneous freezing line were within the range of uncertainties for the RH_w calculations (4 %) (Richardson 2009). Below 222 K there was a large decline in the required RH_w for 1 % and 10 % ice frozen fractions for both aerosol sizes shown in Fig. 6a. For example, 1 % freezing for both 150 and 600 nm NaCl particles occurred at ~80 % RH_w, at 218 K, significantly lower than the 95 % RH_w observed at 225 K. The onset of freezing for both sizes also occurred within proximity (~1–3 %) to the DRH line for anhydrous NaCl extrapolated to lower temperatures (Tang and Munkelwitz 1993) (dashed cyan line). In general, our NaCl freezing results agreed well with results from previous lower temperature studies, all of which observed a shift from homogeneous freezing to heterogeneous nucleation as temperature decreased below 225 K (Ladino et al. 2016; Schill and Tolbert 2014; Wagner et al. 2018).

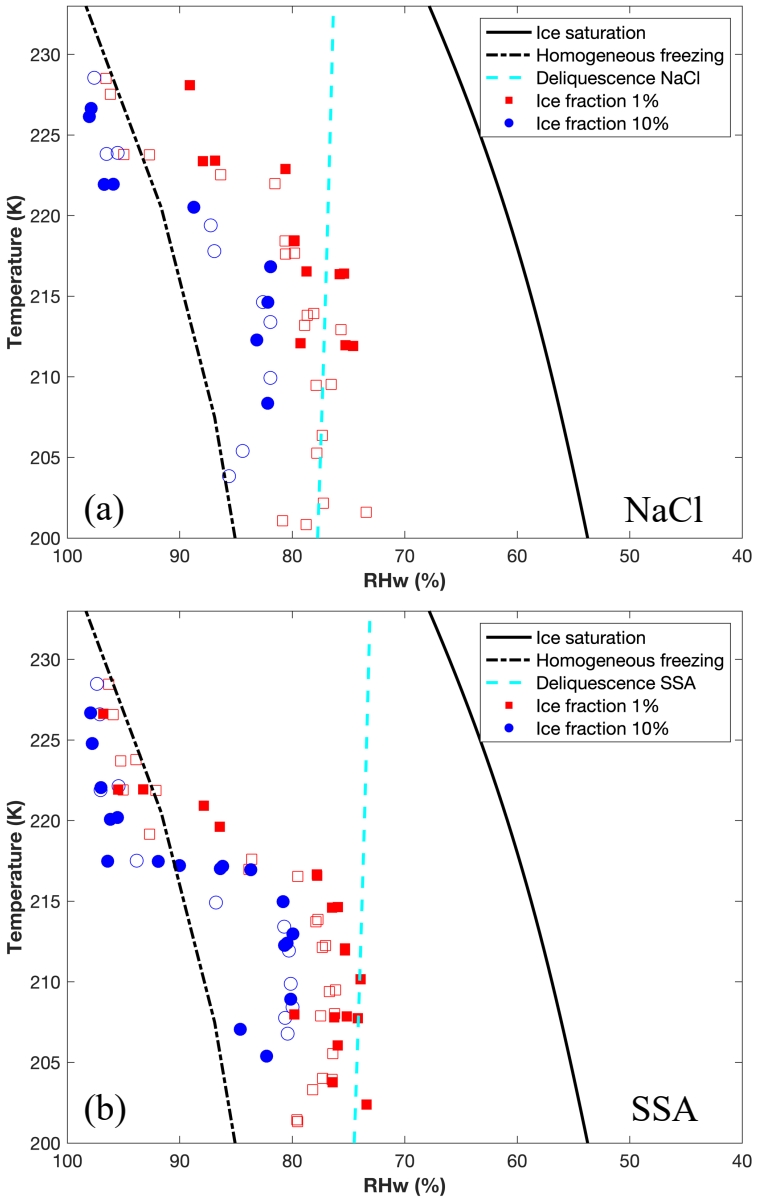


Figure 2.6. Ice fractions for (a) NaCl and (b) SSA generated particles. Blue and red markers denote 10% and 1% frozen fraction, respectively, where filled markers represent 600 nm particles and open markers for 150 nm particles. The dashed cyan line represents the predicted deliquescence for NaCl(Tang and Munkelwitz 1993), and was lowered by 4% RH_w for SSA. Black solid and dashed lines denote ice saturation and expected homogeneous freezing (Koop et al. 2000a), respectively.

Similar to NaCl, SSA showed a transition from homogeneous freezing to heterogeneous nucleation (Figure 2.6b). However, the temperature at which this transition was observed, ~217 K, was nearly 5 K lower than observed for NaCl, similar to observations made in a previous

study comparing NaCl and SSA (Wagner et al. 2018). The 5 K decrease in heterogeneous freezing onset for NaCl and SSA is likely a result of the lower DRH of SSA (Tang et al. 1997). Because the eutectic point falls on the DRH line, this leads to a lower eutectic temperature for SSA by about the same amount (~5 K) compared to pure NaCl particles (Martin 2000). Ice fractions of 1 % and 10 % below 215 K were observed 1–3 % RH_w lower than for NaCl particles at the same temperature. In general, SSA heterogeneous freezing at a 10% ice fraction aligned above the extrapolated DRH line, which was lowered by 4 % RH_w for SSA, similar to the observed DRH in a previous study using synthetic seawater at low temperatures (Wagner et al. 2018), and 1% freezing conditions aligned near the DRH line, within RH_w uncertainty. This ice nucleating behavior of SSA demonstrating freezing onsets at slightly lower RH than NaCl has been shown in previous studies (Schill and Tolbert 2014; Wagner et al. 2018), one of which used synthetic seawater and another that used a 1:1 synthetic sea salt and sucrose mixture. However, those studies differed on the inferred mode of heterogeneous freezing: the former attributed findings to possible deliquescence and immersion freezing since freezing occurred at the point where the liquid–solid transition was expected to initiate, and the latter inferred deposition freezing well below the DRH as the active mechanism. Particle sizes were different in those studies than used in this work, employing polydisperse distributions or supermicron particles.

Previous studies focusing on heterogeneous nucleation have used the ice nucleation active surface site density (n_s) as a parameter to determine the ice nucleation efficiency of aerosol particles for a given temperature and SS_i, normalized by the surface area (Connolly et al. 2009; Wagner et al. 2018; Hoose and Möhler 2012). Therefore, we calculated n_s for SSA and NaCl for both aerosol sizes, as shown in Figure 2.7. Average surface area concentrations per

particle (S_a) for both aerosol sizes also accounted for DMA multiply-charged particles using equation 2.2.

$$S_a = \sum_{i=1}^{6}(\pi N_i Dp_i^2) / \sum_{i=1}^{6} N_i \quad (2.2)$$

In Eq. 2.2., N_i denotes the number concentration for each diameter with ϵ positive charges, and Dp_i is the expected diameter with i positive charge. Values of n_s were then calculated by dividing the number of ice particles (N_{ice}) by the product of S_a and the total number of aerosols from the CPC (N_a) as shown in equation 2.3.

$$n_s(T, SS_i) = \frac{N_{ice}}{S_a N_a} \quad (2.3)$$

The inclusion of N_a serves as a scaling factor for S_a to the aerosol concentrations used in the experiments, since S_a was based on the generated size distributions, in which the aerosol concentrations were higher (Figure 2.3) due to the lack of dilution. In this manner, S_a still accounts for multiplet distributions and can be applied to the N_{ice} and N_a during experiments. While it is possible that the largest multiply charged particles freeze first due to thermodynamic considerations, that is both beyond the scope of the n_s framework and unsupported by our experimental data.

Figure 2.7 shows n_s magnitudes for SSA and NaCl, where circles represent 150 nm particles and squares represent 600 nm particles for 1 % ice fraction. Magnitudes of n_s for 10 % ice fraction are shown in Figure A1.6. In general, SSA and NaCl particles produced very similar (within a factor of 5) n_s magnitudes for each aerosol size, and the data suggested that higher n_s magnitudes were required for smaller particles to produce the same frozen fraction. The upper limit of 600 nm n_s magnitudes of ~1×10^{10} m^{-2} also agreed well with previous n_s calculated values for 800 nm particles (Wagner et al. 2018). The most interesting feature of these results is the fact that ice onset was nearly the same regardless of the n_s values. Or, alternately, a strict

association with total particle surface area would have suggested that freezing onsets for the 600 nm particles would occur for the same n_s values as for 150 nm particles. This result implies that the n_s concept was not relevant for ice nucleation for SSA in our study, either because features controlling freezing were not consistently distributed as a function of size or through a different mechanism. In other words, the process driving freezing of SSA particles at low temperature occurred with the same efficiency regardless of the aerosol size or apparent geometric surface area.

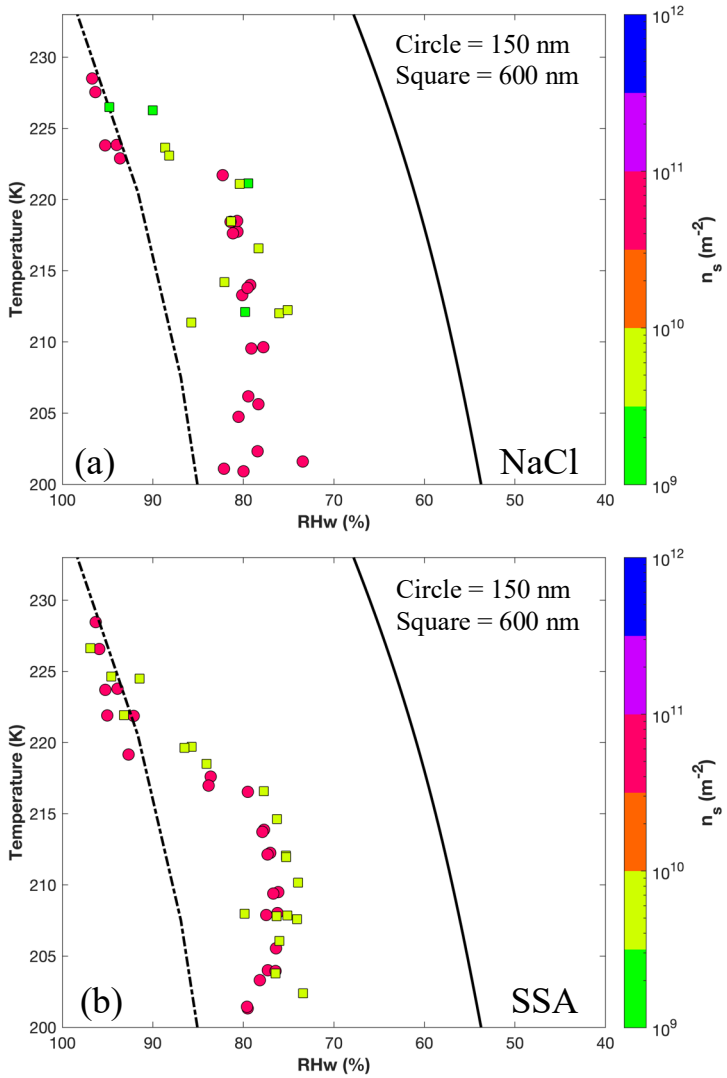


Figure 2.7. Ice active surface site density (n_s) magnitudes for a given RH_w and temperature for (a) NaCl and (b) SSA at 1 % ice fraction. Circle and square markers indicate 150 nm and 600 nm

particles, respectively. The black solid line indicates ice saturation and the dashed line represents expected homogeneous freezing conditions (Koop et al. 2000a).

2.4 Discussion and Atmospheric Implications

It is clear from this study that SSA generated from natural seawater can initiate heterogeneous nucleation, and the similarities between NaCl and SSA for both aerosol sizes indicate that the freezing behavior may be dominated by the crystalline salts. The freezing behavior of NaCl and SSA as well as the n_s calculations from this study indicate that the size of lofted salt particles may not be an important factor for initiating heterogeneous nucleation. Based on our results, regardless of the surface area and site density, conditions supporting the onset of freezing for SSA and NaCl particles remained largely the same. The higher n_s values for 150 nm particles at the same freezing onsets as 600 nm particles clearly violate the concept of active site density, and suggest it is not applicable for NaCl and SSA. Instead, these results suggest little to no size dependence on the heterogeneous freezing behavior of SSA and NaCl, but rather dependence on the particle composition and thermodynamic conditions.

It remains difficult to determine what mode of freezing is controlling the onset of heterogeneous nucleation, and the reason for the abrupt onset below a certain temperature threshold that differs between SSA and NaCl particles. Deposition nucleation is an unlikely pathway for the SSA particles that freeze (in 1 % frozen fraction) at below the DRH line since the initial water uptake of the additional salt components of SSA would likely begin to occur at RH_w well below the DRH (Tang et al. 1997; Wagner et al. 2018), therefore discounting deposition as a nucleation mechanism. We consider two possible pathways for heterogeneous freezing for NaCl and SSA at cirrus conditions, as outlined in Figure 2.8. We simplify the discussion by including only 150 nm data at 1 % frozen fraction. First, the immersion freezing mode, which is depicted as a required Δa_w with respect to the ice line, following previous

application of the water activity concept of homogeneous freezing to the heterogeneous freezing of mixtures of dissolved or partially dissolved particles (Zuberi et al. 2002; Archuleta et al. 2005). It is possible to set a constant Δa_w, and thus nucleation rate, to align more or less with the data (short dashed line, with uncertainties indicated by the blue shading). For classical immersion freezing, the temperature threshold could be understood as the impact of the kinetic competition between full deliquescence and freezing, where at higher temperatures, deliquescence would occur at progressively lower RH_w values with respect to the onset RH_w for freezing, favoring full dissolution and homogeneous freezing. The long black dashed lines in Figures 2.8a and 2.8b indicate the transition point between homogeneous and heterogeneous freezing for NaCl and SSA, respectively, near the intersection of the lower bound of the immersion freezing envelope and the DRH line.

Pore condensation freezing (PCF) is another potential mechanism that might be insensitive to particle size or surface area, explaining the existence of both the onset of heterogeneous freezing with decreasing temperature, and the RH_w onsets at a given temperature. In Figure 2.8, the solid green line represents the parameterized RH_w for expected condensation of liquid water in a 11.5 nm and 10 nm pore (Marcolli 2014) for NaCl and SSA, respectively, relevant to onset conditions of PCF, and the intersection of this condition with the DRH boundary becomes the controlling factor in governing the onset conditions of freezing. We note that the transition point between homogeneous and heterogeneous freezing does reasonably align with the intersection of the PCF (for the pore size chosen) and the DRH lines. If the PCF RH_w is above the DRH at a particular temperature, the pore freezing site is likely to be dissolved before it can activate heterogeneous freezing. If PCF RH_w is below DRH, freezing may occur prior to dissolution. SSA and NaCl particles produced from drying of aqueous solutions are suspected to

be highly porous, with observations of supermicron single particles suggesting that SSA is even more likely to form porous aggregates than NaCl (Weis and Ewing 1999; Peckhaus et al. 2016b). In addition, dry submicron NaCl aerosols were found to retain more water at low RH_w than could be explained by solid crystalline NaCl morphologies (Weis and Ewing 1999). That study states that their analysis is consistent with porous NaCl particles containing NaCl solution (rather than adsorbed water), although the exact morphology could not be identified. Another study examined water uptake in pores filled with soluble material, which may be similar to the water uptake behavior of pores formed in soluble material (Sjogren et al. 2007). Freezing behavior of solution filled pores will depend not only on pore size but also solution concentration (Koop et al. 2000a). At sufficiently low temperatures, however, it seems reasonable to expect that if a sufficiently large pore activates and fills with solution it will subsequently freeze. In this regime, pore size is the controlling factor on the RH_w where freezing occurs.

This PCF framework is a possible mechanism for the freezing of NaCl particles, and may explain the transition temperature between homogeneous and heterogeneous freezing and the lack of differences between onset freezing conditions for the two sizes. However, PCF would require the particles to be fully dry, which is unlikely for SSA at these temperatures. The additional calcium and magnesium salts in SSA, which have lower deliquescence points (Tang et al. 1997), as well as the presence of organics, would allow for partial deliquescence at lower RH_w than for the NaCl core. In addition, previous studies have shown that even after efflorescence, SSA particles may retain up to 5-10 wt % of residual water (Cziczo and Abbatt 2000; Koop et al. 2000b; Tang et al. 1997). The more likely scenario is the development of a brine layer for SSA as the RH_w approaches the DRH, which has been observed in two previous studies using inorganic SSA particles (Schill and Tolbert 2014; Wagner et al. 2018). Schill and

Tolbert (2014) were able to visually observe a brine layer encompassing an inorganic sea salt particle at 59 % RH_w, and using laser light scattering intensity and linear depolarization ratio, Wagner et al. (2018) also concluded the presence of a brine layer on SSA. Therefore, PCF is not a viable freezing mechanism under these circumstances because the surface pores would dissolve and inhibit freezing via this pathway. Instead, both previous studies concluded the formation of a brine layer helped initiate immersion freezing. However, one difference was that Schill and Tolbert (2014) observed much lower freezing onsets ~68 % RH_w for their 1:1 ratio sucrose to synthetic sea-salt particles compared to SSA particles in Wagner et al. (2018). This may indicate that the dissolution of the particles is dictated by the organics present, and it is unclear whether a sucrose mixture is representative of the organic components of SSA. The onset freezing results from this study are most consistent with the previous work of Wagner et al. (2018) on heterogeneous freezing of SSA, confirming immersion freezing as the likely pathway for SSA below 220 K. The lack of size effects must be explained by the concentration of solution on the particle surface controlling the immersion freezing, but would require further inspection of the rates of dissolution and dilution in different size classes and probing of their relative compositions. This result may also explain why the surface area normalization does not work for SSA because the dry surface area is not relevant for a partially dissolved salt crystal acting as the freezing site. It is presently unclear the reason for the similar heterogeneous freezing behavior between NaCl and SSA and seemingly very different freezing mechanisms, which will warrant future study.

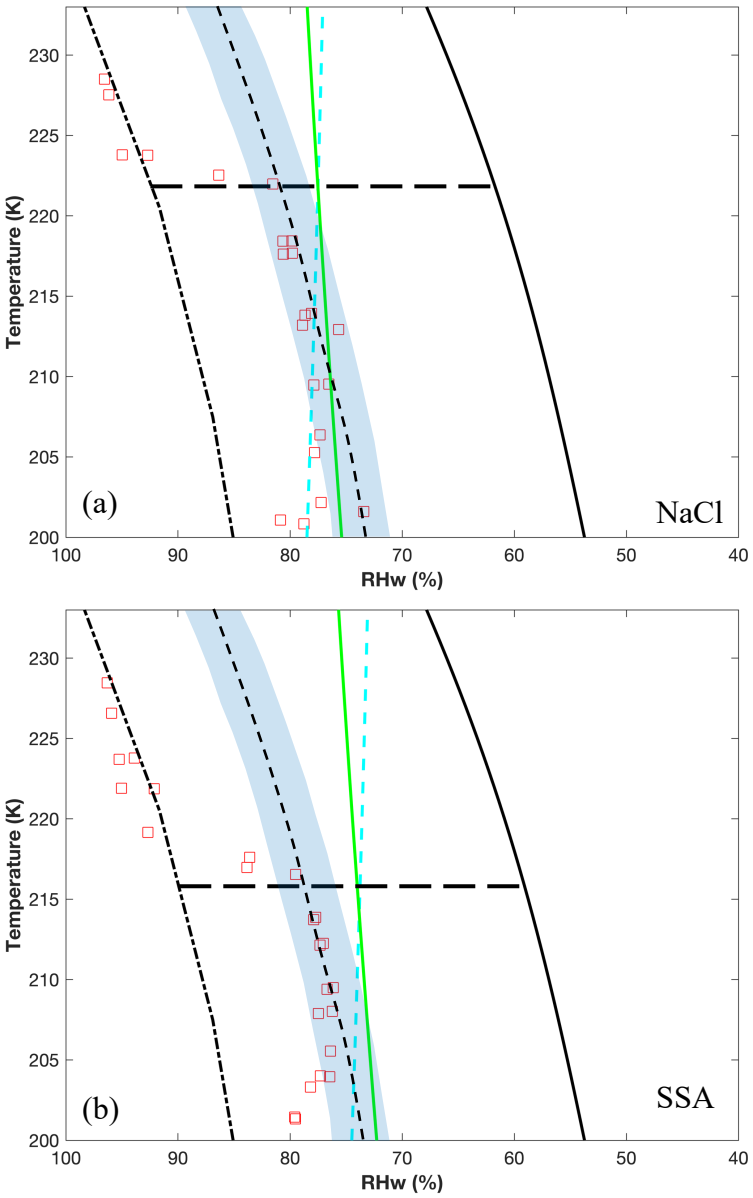


Figure 2.8. Conceptual diagram illustrating the competition between immersion freezing and pore-condensation freezing (PCF). Included are 1 % frozen fraction for 150 nm particles denoted by the open squares. Solid green line indicates the parameterized RH_w for the onset of condensation into a 11.5 nm pore and 10 nm pore (Marcolli 2014) for NaCl and SSA, respectively. The dashed cyan line indicates the deliquescence relative humidity (DRH) for NaCl, extrapolated to cold temperatures, and shifted towards slightly lower RH_w for SSA. The dashed black line indicates a constant Δa_w with uncertainties represented by the shaded blue region. The long dashed black line indicates the intersection of the PCF and DRH lines, indicative of the transition from homogeneous to heterogeneous nucleation.

In this study we found that particles produced from natural SW spray froze via heterogeneous nucleation at conditions similar to those reported in previous studies (Schill and

Tolbert 2014; Wagner et al. 2018). We have demonstrated the ability to replicate and augment heterogeneous freezing results of NaCl particles and SSA from the AIDA cloud chamber (Wagner et al. 2018) in easily conducted scans using a CFDC. An advantage to this instrument and the scanning procedure employed is that the nature of the CFDC allows for study of particle response over a full profile of RH_w up to water saturation for any temperature (i.e., the limitations imposed by ice formation depleting water vapor in an expansion cloud chamber do not exist), which allows for studies relevant to cirrus cloud ice nucleation over a wide range of environmental conditions. The method could be extended to measurements on ambient particles, for which there exists a dearth of data for freezing behaviors at these temperatures and humidities.

Our results illustrate the potential of SSA to be a significant source of INPs in the cirrus regime. For both aerosol sizes, up to 10 % of the SSA population froze below 80 % RH_w at temperatures < 225 K. SSA concentrations in the upper troposphere range from $10^{-4} – 10^{-1}$ μg m^{-3}, and assuming a density of 2.2 g cm^{-3} (Brock et al. 2019), the upper and lower bounds of 150 and 600 nm particles could be in the range $10^{-1} – 10^{4}$ L^{-1}. Since average ice crystal number concentrations in cirrus clouds range between 0.01 – 10 L^{-1} depending on latitudinal location (Krämer et al. 2009, 2020; Patnaude et al. 2021a), the projected population of SSA-derived INPs would represent a significant source of heterogeneous INPs for cirrus clouds. In the absence of significant numbers of other efficient INPs, such as mineral dusts, one could expect SSA to be strongly competing or dominating ice formation. In addition, size distributions of SSA above 4 km were found to be dominated by sizes < 400 nm (Murphy et al. 2019). Therefore, the aerosol sizes chosen in this study may be more representative of the sizes of SSA active in the cirrus regime as opposed to previous studies that used aerosols 800 nm or larger (Schill and Tolbert

2014; Wagner et al. 2018, 2021). These results represent a strong case for explaining the observations of SSA as a cirrus INP in previous studies of cirrus IR over the tropical and subtropical oceans (Cziczo et al. 2013). Although that study concluded that the dominant sources of cirrus INPs were mineral dust and metallic particles, the flights that took place over the ocean were located predominantly downstream of major sources of dust and pollution, and SSA still made up substantial fractions of IR when in direct competition with efficient INPs like mineral dust. It is unclear what fraction of IR would be sea salts if flights occurred over more pristine ocean regions, and this may warrant future exploration.

When discussing SSA as a source of heterogeneous INPs it is important to address the origin of the cirrus, liquid versus in situ origin, as this could determine by which nucleation mechanism SSA would initiate freezing (i.e., homogeneous versus heterogeneous freezing). SSA in liquid origin cirrus would likely remain as aqueous solutions and initiate homogeneous freezing. However, SSA may be present at cirrus levels in effloresced crystalline structures and initiate heterogeneous nucleation to form in situ origin cirrus. There are a number of different scenarios where the latter case may occur. Firstly, SSA is lofted to cirrus temperatures via deep convective updrafts and detrained in anvils, specifically in the tropics where cirrus are most frequently observed (Sassen et al. 2008). However, it would require the SSA particles to encounter dry air and effloresce; understanding how often this particular scenario occurs is beyond the scope of this study. Secondly, warm conveyor belts associated with lofting of air in frontal systems are known to be the most frequent source of in situ cirrus (Krämer et al. 2016, 2020), which may occur over some ocean regions and bring SSA to high altitudes and lower temperatures. An example of this scenario may be large storm tracks over the Northern Atlantic

where in situ origin cirrus can be present ~70 % and > 50 % of the time above 200 hPa or below 220 K (Gasparini et al. 2018; Wernli et al. 2016), respectively.

We have shown that SSA have the potential to initiate heterogeneous nucleation at temperatures below 220 K. It is known that cirrus clouds have the potential to warm or cool the atmosphere depending on their formation mechanism and origin type. Heterogeneous nucleation of SSA would drive the formation of the in situ origin type cirrus, that are shown to produce a net positive radiative forcing (Krämer et al. 2020). This illustrates a potentially significant indirect effect of SSA in the cirrus regime. Since SSA concentrations are strongly modulated by sea-surface temperatures (Liu et al. 2021), as well as surface winds, changes in SSA generation and lofting to the upper troposphere may represent an important aerosol-cloud interaction that should be studied in assessing atmospheric response in a warming future climate.

CHAPTER 3: A SECOND LABORATY STUDY ON THE LOW TEMPERATURE ICE NUCLEATION OF SEA SPRAY AND SECONDARY MARINE AEROSOLS

3.1 Background on Marine Aerosols

Marine aerosols are generally separated into primary sea spray aerosols (SSA) and secondary marine aerosols (SMA). Primary SSA are produced by wind stress on the ocean surface, which causes wave breaking and the production of bubble-bursting film and jet drops, comprised of inorganic sea-salt and organic matter (O'Dowd and De Leeuw 2007). SMA, on the other hand, may be produced via gas-to-particle conversion of the gas phase species that are emitted from the ocean, which includes dimethyl sulfide (DMS), a biproduct of marine phytoplankton, and other volatile organic compounds (VOCs) (Fitzgerald 1991; O'Dowd and De Leeuw 2007). DMS and VOCs may also alter the composition of primary SSA via condensation onto existing particles. SMA have been shown to be comprised primarily of non-sea-salt (nSS) sulfates and other secondary organic species, produced primarily from the oxidation of DMS, which can dominate the total submicron aerosol mass (Fitzgerald 1991; O'Dowd et al. 2004). However, observations in the North Atlantic showed wide variability in the submicron organic mass depending on season (Saliba et al. 2020). SMA may play an important role in cloud formation in oceanic regions, specifically by modulating the cloud condensation nuclei (CCN) concentrations. CCN concentrations in marine environments have been found to be directly related to DMS emissions (Pandis et al. 1994; Berresheim et al. 1993). Ship based measurements in the Southern Ocean found higher concentrations of CCN containing more biogenic sulfates and organics closer to Antarctica, where there is a greater source of biogenic emissions during austral summer (Sanchez et al. 2021). More recently, laboratory studies have focused on the

impact of ocean emissions on atmospheric chemistry (Mayer et al. 2020a; Prather et al. 2013) and have utilized oxidation flow reactors (OFRs) (Peng and Jimenez 2020) to study the formation of SMA and the aging processes of the primary SSA. For example, Mayer et al. (2020b) found that SMA generated from natural seawater using an OFR plays a dominant role in the formation of cloud droplets, compared to primary SSA. Despite the attention given to studying the impact of SMA on CCN concentrations and the formation of liquid clouds, the ability of SMA to take part in ice nucleation in cirrus clouds is not well understood.

In contrast to SMA, the ice nucleating ability of primary SSA at cirrus temperatures has received more attention in recent years. A number of laboratory studies have observed heterogeneous nucleation behavior of NaCl, synthetic sea-salt, and SSA generated from real seawater at temperatures < 235 K (Schill and Tolbert 2014; Wagner et al. 2018; Wagner and Möhler 2013; Wise et al. 2012). Most significantly, the inorganic components of SSA have been found to freeze heterogeneously at high fractions (~10 %) below 225 K (Patnaude et al. 2021b; Wagner et al. 2021), high enough to potentially compete with more conventionally effective ice nucleating particles (INPs) (i.e., mineral dust). In Patnaude et al. (2021b) we posited that our ice nucleation results for simpler model SSA were a result of the competition between full deliquescence and immersion freezing. Those freezing results at temperatures > 220 K were characteristic of homogeneous freezing, in agreement with other previous studies (Schill and Tolbert 2014; Wagner et al. 2018), which was likely due to the full deliquescence of the salt components around ~75 % RH_w, as defined by Tang and Munkelwitz, (1993) that occurred prior to the onset of immersion freezing. Below 220 K, SSA particles have been found to initiate heterogeneous nucleation at/near the range of deliquescence relative humidities (DRHs) for NaCl and SSA. Both Schill and Tolbert (2014) and Wagner et al. (2018) concluded that at

temperatures below 220 K, the phase state of their SSA particles was characterized by a solid core with a brine layer shell, and speculated that heterogeneous freezing proceeded via the immersion pathway. Patnaude et al. (2021b) further discussed the reason for the transition between homogeneous and heterogeneous pathways around 220 K, which also happened to occur at the intersection of the DRH and PCF freezing parameterization from Marcolli (2014) for a specific pore size. However, due to the lower DRHs for the additional salt components such as magnesium and calcium (Tang et al. 1997) the PCF pathway is less likely. The exact heterogeneous freezing mechanism of SSA and cause of the transition between freezing pathways remains unresolved.

While the nSS components of primary SSA have been shown to act as heterogeneous INPs in the mixed-phase regime ($\gtrsim$ 235 K, presence of liquid and ice) (McCluskey et al. 2018a; Ickes et al. 2020), until recently less was known regarding the freezing of nSS components at cirrus temperatures. Possible types of primary marine organics may include bacteria, fatty acids, proteins, and saccharides (Wolf et al. 2019). A few recent studies have investigated the ice nucleating behavior of organic material at cirrus temperatures and found particles with a higher organic carbon fraction were more likely to freeze via heterogeneous nucleation below 235 K (Wolf et al. 2019, 2020b; Wagner et al. 2021). Additionally, Wagner et al. (2021) speculated on whether organic rich particles present in seawater would be aerosolized with a more realistic generation method and thus have the potential to act as heterogenous INPs. The inclusion of additional organic components in primary SSA may have implications for ice nucleation both below and above 220 K. Clearly, organics from seawater that are contained in primary SSA, and/or those added to the aerosol through atmospheric processing of SSA, are responsible for a major proportion of the ice nucleation activity of SSA in the mixed-phase cloud regime

(McCluskey et al. 2018a), and a question has remained as to how effective these organics are as INPs at below 238 K. Organic aerosols have been shown to form a glassy state under cirrus cloud conditions (Berkemeier et al. 2014; Ignatius et al. 2016; Knopf et al. 2018; Koop et al. 2011; Murray et al. 2010) and depending on the glass transition temperature and DRH, these particles may have heterogeneous ice nucleating ability at temperatures > 220 K, where the salt components of SSA would have already dissolved. It is unknown how organic rich particles would compete with the salt components of SSA below 220 K, but based on the results in Kasparoglu et al. (2022), the contribution of glassy SOA may be relatively minor. These studies illustrate the potential of the organic material and inorganic salts in seawater to initiate heterogeneous nucleation at cirrus temperatures. However, the pathway of SSA from the marine boundary layer to the upper troposphere where cirrus clouds reside would likely modify both the inorganic and organic components of these aerosols due to atmospheric oxidation. The question of whether atmospheric oxidation alters the ice nucleating ability of SSA at cirrus temperatures remains unanswered.

3.2 Experimental Setup

A general overview of the experimental setup is shown in Figure 3.1. The following sections provide descriptions of each component of the aerosol generation and processing instrumentation and the design of the experiments.

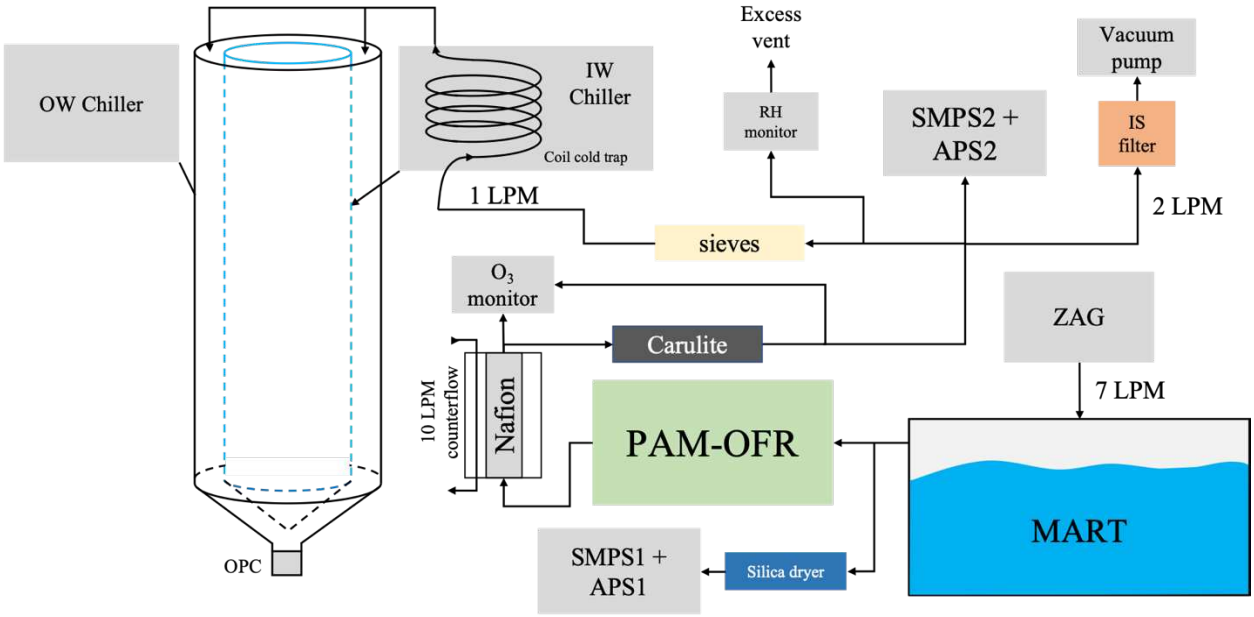


Figure 3.1. Schematic of the experimental setup for the MART studies. Flow configuration remained the same for all aerosol generation methods and water types.

3.2.1 Seawater Collection and Preparation

For this study, a Marine Aerosol Reference Tank (MART), originally developed by the NSF Center for Aerosol Impacts on Chemistry of the Environment (CAICE, Prather et al. (2013)), was used for generation of an atmospherically relevant size distribution of SSA by mimicking wave breaking in the ocean (Mayer et al. 2020a; Stokes et al. 2013). The MART was filled with 120 L of 1) natural seawater (SW) collected at the Scripps pier in La Jolla, CA, 2) Neomarine (Brightwell Aquatics), a commercially available artificial seawater (ASW) product (3.5 % by weight) or 3) deionized water (DI). The ASW was mixed outside of the MART in 5-gallon plastic (LDPE/LLDPE) cubitainers, filtered through a TOC+HEPA filter and into the MART, then recirculated through the filter using a peristaltic pump for ~24 hours to remove residual organic carbon. The seawater was shipped overnight at room temperature to Colorado State University in the same cubitainers, which had been acid washed prior to use in mixing the ASW, then thoroughly rinsed with deionized water before SW collection. During seawater

collection, the water was filtered through a 50-µm food-grade woven polyester mesh, which was pre-cleaned with methanol and 5 % hydrogen peroxide and rinsed with deionized water. Unlike the ASW, the SW was not filtered before being added to the MART in order to retain any biological material that may have been present. Since the MART was located indoors, it was equipped with a VIPARSPECTRA full spectrum aquarium grow light to provide broad spectrum light to the microorganisms inside the tank during experimental days and turned off at night. The grow light was set to a realistic PAR (photosynthetically active radiation) quantity of ~175 µmol m^{-2} to keep the microorganisms active and not stimulate a bloom. A hollow aluminum coil connected to a water-cooling bath was inserted into the MART to cool the seawater to ~15 ºC to mimic spring ocean temperatures in San Diego. However, during experiments the water warmed (< 5 ºC) due to the heat exhaust from the CFDC chillers located near the MART and cooled again overnight. The centrifugal pump used to recirculate and plunge the water in the MART can damage microorganisms due to strong pump shear (Mayer et al. 2020a) and this effect can be highly selective and may change the composition of the biologic community. It is unclear how this affects the microorganisms that are directly emitted as SSA and subsequent ice nucleating ability, but this impact has existed in prior MART studies of freezing by nascent SSA (McCluskey et al. 2018a). MART plunging was turned on shortly after the icing stage of the CFDC (discussed in section 2.3, about 30 minutes before measurement) to ensure aerosol concentrations had equilibrated in all the lines prior to the ice nucleation experiments.

3.2.2 Aerosol Generation and Characteristics

Aerosol generation from the MART is accomplished by intermittently plunging a sheet of water on top of the water surface, producing a plume of bubbles with a distribution similar to those measured in the ocean. The subsequent polydisperse aerosol size distribution produced

from the bursting of bubbles at the water surface closely resembles that which is produced from ocean wave breaking in the ambient environment (Mayer et al. 2020a). The sealed headspace of the MART containing both aerosols and any emitted gases was modestly pressurized by a zero-air generator (ZAG) pumping 7 liters per minute by volume (LPM_v) into the MART and forcing out the sample air.

The aerosol sample line was split in two after exiting the MART with one sample line sent through two silica gel diffusion dryers to the upstream set of sizing instruments to confirm the nascent SSA number size distributions produced by the MART. The other sample line was passed through the OFR, whether powered to produce oxidation or not (see below), for further processing and characterization of ice nucleation behavior, to ensure aerosol losses were consistent during all the experiments. The OFR generates high concentrations of O_3 and OH radicals to oxidize particles using two UV lamps at wavelengths $\lambda = 254$ nm and $\lambda = 185$ nm (Mayer et al. 2020b). The UV lamp type used in this study was GPH436T5L/VH/4P 90/10, which emits radiation of the 185 nm wavelength at 0.6 % of the intensity of the 254 nm wavelength (Rowe et al. 2020). The OH exposure in the OFR was calibrated using the change in carbon monoxide (CO) concentrations inside the OFR, using the same temperature and RH conditions as during the experiments. The change in CO versus light intensity of the lamps uses the CO + OH rate coefficient ($k_{OH+CO} \sim 1.48 * 10^{-13}$ cm^3 $molecules^{-1}$ s^{-1}). The residence time in the OFR was ~2.4 min and the average OH exposure was in the experiments was ~6.31 molecules sec/cm^3 which translated to ~4–6 days of aging under typical atmospheric conditions (OH = 1.5 *10^6 molecules cm-3). In addition, the RH inside the OFR was maintained > 60 % to ensure OH chemistry dominated the oxidation processes and minimize O-singlet reactions.

Because the air was humidified inside the OFR, the oxidation reactions that occurred would mimic those which occur in the marine boundary layer.

Sample air exiting the OFR first passed through a Nafion dryer, which used ~10 LPM_v of counter flow in its dry air circuit to dehydrate the sample air. After drying, sample air was passed through a diffusion dryer packed with Carulite, an O_3 destroying catalyst, to remove residual O_3 and then passed through a final 4-way split: 1) molecular sieves dryer and CFDC, 2) second set of sizing instruments, 3) ice spectrometer filter (IS), and 4) RH monitor and excess flow vent (Figure 3.1). The RH monitor confirmed the aerosol stream RH was generally <10 % for all experiments, so aerosol size distribution measurements and IS filter collections were considered to be dry. Prior to particles entering the CFDC they passed through a coil cold trap immersed in the inner wall chiller, which further chilled and dried particles and incoming sample air to a frost point at least 5 K below the CFDC measurement temperature, corresponding to an ambient temperature RH of ~0 % (see Kasparoglu et al. (2022)).

Three different aerosol types were generated and investigated for both natural and artificial seawater, depending on whether the MART plunging and OFR were active (see Table 3.1). The generation, oxidation, sizing and flow configuration was the exact same for both water types. The three aerosol types were 1) primary or freshly emitted SSA (pSSA), 2) “aged” (or oxidized) SSA and SMA (aSSA+SMA, henceforth), and 3) SMA (SMA-only). We hypothesize SMA is formed mostly through the oxidation of DMS, similar to Mayer et al. (2020b), who showed that sulfates contributed to > 50 % of the mass of SMA generated from real seawater in a MART. Two duplicate CFDC experiments were conducted for both pSSA and aSSA+SMA measurements, while only one experiment was conducted for SMA-only. Between the artificial and natural seawater experiments, the MART was cleaned and filled with DI water and a “blank”

experiment was conducted to test background contamination. This experiment was conducted the same as the SMA experiments where the MART plunging was turned off and only the MART headspace was sampled.

Table 3.1. Descriptions of experimental aerosol generated from the MART for each water type.

Generated aerosol types (Water type)	OFR lamp operation	MART plunging
pSSA (ASW, SW)	OFF	ON
aSSA+SMA (ASW, SW)	ON	ON
SMA only (ASW, SW, DI)	ON	OFF

Size distributions of the aerosol samples were measured using a combination of a Scanning Mobility Particle Sizer (SMPS, TSI models 3080, 3081, 3010; 12-600 nm) and an Aerodynamic Particle Sizer (APS, TSI model 3321; 0.52 – 20 μm). For this study, two sets of aerosol sizing instruments were used, one located upstream of the OFR, and one located downstream of the OFR, Nafion, and Carulite dryers (see Figure 3.1). Measurements from the downstream set were used to quantify the sample losses that occurred inside the OFR and dryers. Size distributions comparing both upstream and downstream sets of sizing instruments can be found in Figure A2.1 and represent an average of the SMPS and APS scans over the course of each ice nucleation experiment, ~4 hours. The APS measurements were converted from aerodynamic to geometric diameter using a dynamic shape factor and particle density of SSA of 1.05 and 1.9 g cm^{-3}, respectively, consistent with values from observations and those applied in previous studies (Zieger et al. 2017; Brock et al. 2019; Patnaude et al. 2021b).

The phase state of the particles before entering the CFDC remains uncertain and could affect the heterogeneous nucleating ability of the aerosol population. Several previous studies have analyzed the temperature- and humidity-dependent phase states of NaCl particles, since they are often used as a proxy for SSA. Previous studies have found that the phase state of NaCl after efflorescence depends on the temperature at which efflorescence occurred, with anhydrous

NaCl observed for efflorescence temperatures above 273 K (Koop et al. 2000b; Bartels-Rausch et al. 2021; Peckhaus et al. 2016b; Wagner et al. 2012). Since the majority of aerosol drying, including the efflorescence of the salt components of pSSA and aSSA+SMA, occurred at room temperature (Figure 3.2), it is believed the salts would be in the anhydrous form. However, the phase state and morphology of co-emitted organic particles or coatings on the pSSA and aSSA+SMA are less well understood at low temperatures, and the exact structure was uncertain in this study. This is especially difficult to know for the aSSA+SMA particles, due to the exposure to oxidation in the OFR. It is assumed that particles generated from SW contain high fractions of insoluble organic particles or salt particles mixed with organic carbon below 500 nm, similar to previous lab-generated SSA (Bertram et al. 2018; Kaluarachchi et al. 2022a; Prather et al. 2013). In addition, DeMott et al. (2023) showed particle morphologies generated from laboratory bubble-bursting production from seawater that include organic coatings in the submicron size range, both before and after similar use of an OFR for oxidation studies. The MART was demonstrated to produce substantially similar size distributions and compositions of SSA compared to a more natural wave breaking process for bubble bursting (Prather et al. 2013; Stokes et al. 2013), so no bias in organic content in comparison to natural SSA production is expected. During cooling, the RH_w would be low enough such that organic particles or coatings may form a glassy state (Ignatius et al. 2016; Knopf et al. 2018; Koop et al. 2011) as shown by the shaded green region in Figure 3.2, which represents the glass transition conditions for sucrose (Zobrist et al. 2008).

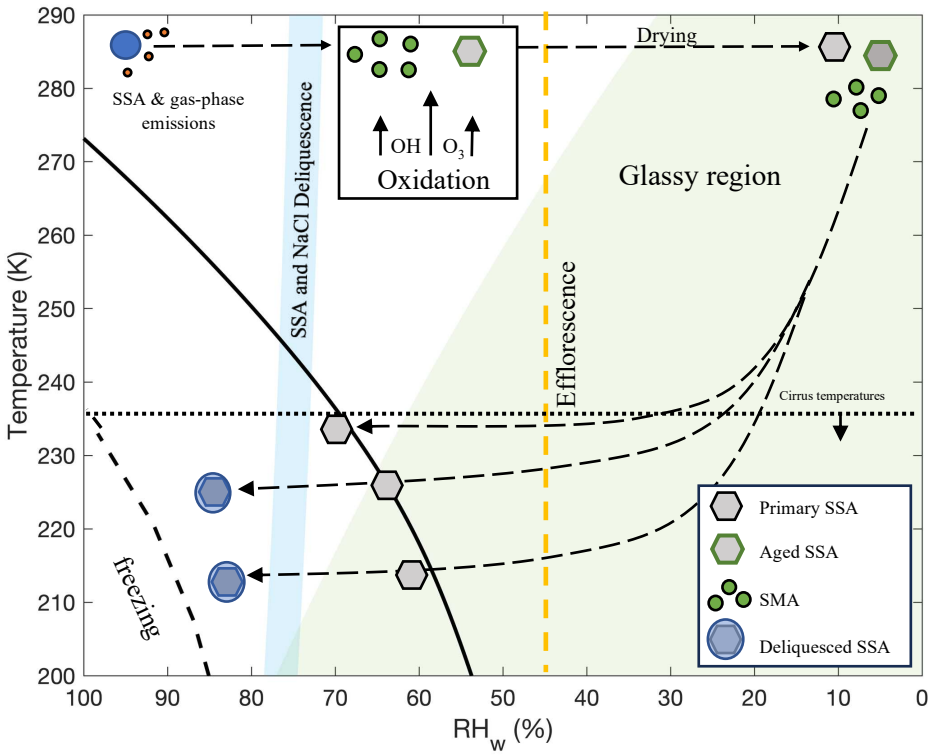


Figure 3.2. Expected trajectory and phase state of the pSSA, aSSA+SMA and SMA particles for CFDC experiments, modified from Patnaude et al. (2021b). Orange dashed line is the expected efflorescence line for NaCl on the basis of the parametrization of anhydrous NaCl and extrapolated to cirrus temperatures (Tang and Munkelwitz 1993). The blue shaded region represents the range of possible deliquescence RHs for NaCl and SSA, using the parameterization from Tang and Munkelwitz (1993) for NaCl extrapolated to colder temperatures as the upper bound and shifting it down 4 % RH_w for SSA similar to Wagner et al. (2018). The long dashed black lines follow the path of aerosol particles as through drying, cooling, and CFDC scans at different temperatures. The blue circles represent aqueous solutions, gray hexagons represent effloresced pSSA aerosols, and the light blue circles with embedded hexagons represent fully deliquesced particles. The gray hexagons with green outlines and green circles represent the aSSA+SMA and SMA particles, respectively. Lines indicating ice saturation and predicted homogeneous freezing conditions are also denoted. The dotted region represents conditions where aerosol particles experience ice supersaturated conditions and relative humidities that exceed their deliquescence point. The green shaded region represents conditions below the glass transition curve of sucrose from Zobrist et al. (2008).

Aerosols that contain organic material may either enhance heterogeneous nucleation (Wilson et al. 2012; Adler et al. 2013) or have no effect (Kasparoglu et al. 2022). For example, organic coatings on mineral dust particles have been shown to suppress heterogeneous nucleation to higher RH at cirrus temperatures (Möhler et al. 2008), depending also on the coating thickness or the fractional coverage of the particles, while another study found organic coatings on mineral

dust had no effect on immersion freezing between 233–253 K regardless of the coating thickness (Kanji et al. 2019). At warmer temperatures > 233 K, organic coatings may be in a less viscous or liquid-like phase state, while at colder temperature may become semi-solid or glassy (Charnawskas et al. 2017), which may explain the differences in ice nucleation behavior of particles with organic coatings in those studies. Specifically, the inclusion of glassy coatings on the pSSA or aSSA+SMA particles may inhibit water uptake and delay dissolution of the salt components until higher RH_w is reached.

3.2.3 Ice Nucleation Detection using the CFDC

Detection of low temperature ice nucleation for all experiments was carried out using a CSU CFDC, which had been modified from the design used in previous studies (Archuleta et al. 2005; DeMott et al. 2015; DeMott et al. 2009a) to reach temperatures down to 190 K. A full description of the modifications made to the CFDC to reach lower temperatures, and a complete derivation of calculations and measurement uncertainties can be found in Patnaude et al. (2021b). The CFDC is made up of two vertically-oriented concentric cylinders consisting of a "cold" inner wall and "warm" outer wall. The chamber temperature and RH are controlled by holding the inner and outer walls at different temperatures, producing temperature and water partial pressure gradients. This approach can produce a very broad range of RH conditions as low as 0 % with respect to ice and up to double digit supersaturations with respect to water (Rogers 1988). The walls are covered with a thin layer of ice by chilling the column to 246 K and filling, then draining, the column with deionized water prior to ice nucleation experiments. The flow rates during experiments were 4 LPM_v sheath flow and 1 LPM_v sample flow (calculated in the CFDC interior). The low sample flow translates to a longer residence time inside the CFDC, allowing for more ice crystal growth and thus less ambiguous optical detection

of ice crystals versus much smaller unfrozen aerosol particles. An optical particle counter (OPC) is located immediately downstream of the CFDC column at its base and freezing of aerosol particles is distinguished by analyzing the number of particles, presumed to be ice crystals, above a certain size.

In these experiments, the CFDC was operated to perform RH_w "scans" wherein the column temperature was held constant and the RH_w gradually increased until a specified frozen fraction was achieved, in this case 10 %. During an individual scan the inner wall temperature (T_{IW}) was held constant while the outer wall temperature (T_{OW}) was gradually raised, increasing the column supersaturation. Once 10 % frozen fraction was reached, the T_{IW} was raised 5 K and the T_{OW} was lowered until the frozen fraction dropped below 0.1 %, and the cycle was repeated. The thresholds of ice fraction for the RH_w scans required 10 continuous seconds above 10 % or below 0.1 % in order to reset the scans. Note these activation fractions were calculated based on particle counts in channels above a selected OPC channel to define ice counts during the experiments, as opposed to a more accurate method for calculation of ice fraction that accounted for the background aerosol distribution (described below). Using 10 % and 0.1 % as endpoints of the RH_w scans resulted in a broad range in RHs being covered. By the time 10 % of the particles were nucleating, the RHw would be at/above homogeneous freezing conditions (Koop et al. 2000a) and it was not necessary to conditions raising the RH_w. The lower threshold of 0.1 % for 10 continuous seconds was sufficient to reset the scans as the RH_w was well below the deliquescence RH_w for NaCl and SSA (~74 %; Tang and Munkelwitz, (1993)), with the exception of RH_w at warmer temperatures > 225 K, where the RH scans did not reach below ~75 % but we did not expect heterogeneous freezing conditions.

Careful attention was given to the challenging identification of slow-growing ice crystals, without incorrectly classifying large aerosols as ice, when using a polydisperse aerosol size distribution and without the presence of an aerosol impactor upstream of the CFDC to remove large particles from the sample stream. In this study, it was not sufficient to only use a single OPC cut size at all temperatures for identifying ice crystals for two reasons: 1) the larger salt particles may undergo significant hygroscopic growth into the size range of ice crystals at RHs above their deliquescence point, and 2) Patnaude et al. (2021b) demonstrated the lack of size dependence on the freezing of SSA, meaning the smaller salt particles would likely freeze along with the larger particles and may not be counted if they are below the OPC cut size. Instead, we analyzed the OPC size distributions for increasing RHs, as shown in Figure 3.3, and identified the background aerosol distributions when the RH is lower, but after deliquescence has likely occurred. Figure 3.3a shows the OPC size distributions at -45 ºC for pSSA generated from SW and shows little change in the distribution until the RH reaches 99 % (green line) where a significant number of larger particles emerged, signifying ice nucleation was occurring. At the lower RHs (< 95 %) the salt particles in the seawater would have already deliquesced and taken up water, and therefore these distributions represent the background aerosol population that would need to be removed to count the total number of ice crystals. The lack of change in the size distributions between 80–90 % may be due to smaller SSA growth factors below 95 % (Tang et al. 1997), or kinetic limitations at these temperatures. Figure 3.3b shows another example of the OPC distributions for measurements at -68 ºC. In this case, there was a much more considerable shift in the distributions with increasing RH, more likely due to ice nucleation and to a lesser extent from hygroscopic growth. Figure A2.3 shows a timeline of the particle counts from lower OPC channels, similar to Figure 3 from Kong et al. (2018) but does not show

the sharp step where deliquescence occurred. This may be due to several reasons, such as the lower vapor pressures at a colder temperature (213 K versus 233 K in Kong et al. (2018)), or that in this study we used a polydisperse aerosol distribution so smaller particles taking up water would shift into the same OPC channels that larger particles should be shifting out of toward larger sizes. However, both the pSSA and aSSA+SMA did show some decrease in the number of particles as the RH_w increase above the deliquescence RH (~74 %) indicating more gradual water uptake and slower deliquescence transition at lower temperatures.

When comparing the two temperatures (Figures 3.3a and b), the distributions in Figure 3.3b below 75 % (blue and red lines) closely match the lower RH distributions in Figure 3.3a, indicating they are likely the background aerosols at this temperature and that the additional shift to larger sizes for RHs > 75 % was a result of particles freezing. Based on this analysis we used bin channel 40 on the OPC as the lower (more conservative) threshold for ice, which from previous calibrations represents particles ~2 μm for a flow rate of 5 LPM_v, where roughly 0.1 % of the dry aerosol particles are present (see Figure A2.1). Therefore, the total number of ice crystals is calculated as the difference between the OPC spectra and background aerosol distributions summed above channel 40 (denoted by the blue shaded region in Figure 3.3). This method considers both the nucleation of smaller particles and eliminates larger particles that have not nucleated ice. The inferred mechanisms of freezing at these temperatures will be discussed below.

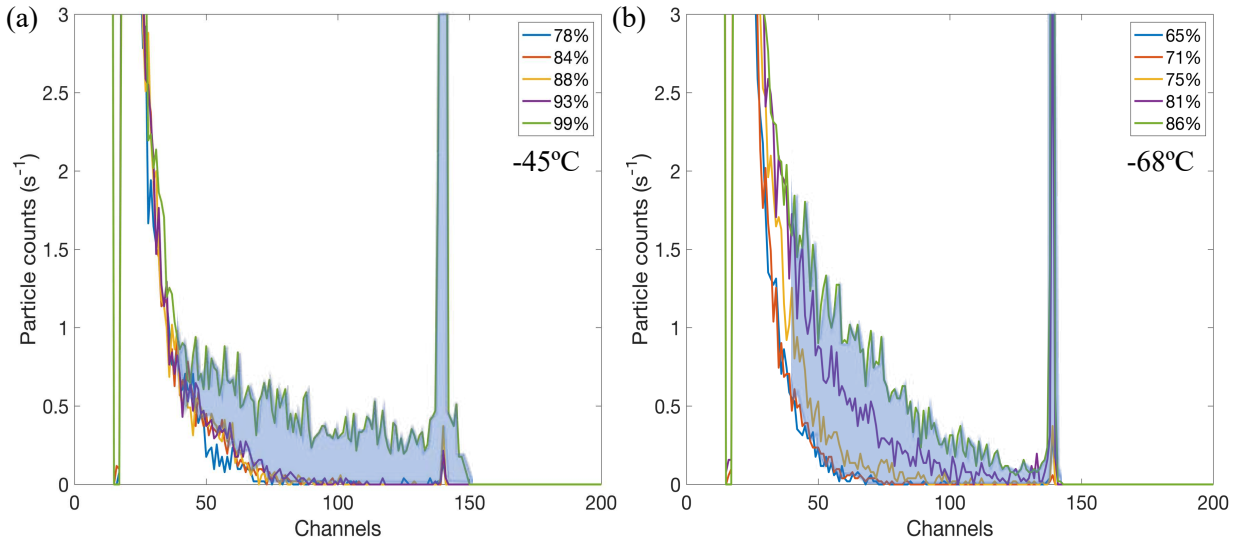


Figure 3.3. CFDC OPC size distributions of pSSA for increasing RH at (a) -45 ºC and (b) -68 ºC during the first of two real seawater experiments. The blue shaded region represents the difference between OPC counts at higher RHs and counts of background aerosol distributions at lower RHs above channel 40, denoting what would be distinguished as ice particles.

3.3 Results and Discussion

3.3.1 Particle Size Distributions and Alteration via OFR Oxidation

Data from the SMPS and APS downstream of the OFR were merged into a complete size distribution, as shown in Figure 3.4 for all experiments. The solid lines indicate aerosols generated from real seawater and the dashed lines are those generated from artificial seawater. For sizes < 200 nm that the aSSA+SMA distributions were dominated by secondary particle formation, as indicated by their similarity to the SMA-only experiment. This is consistent with previous work that showed only a small fraction of the submicron aSSA+SMA number distribution generated from a MART originated from the pSSA (Mayer et al. 2020b; Prather et al. 2013). Mayer et al. (2020b) also suggested that new particle nucleation was favored over condensation in the OFR due to the high OH concentrations and fast oxidation rates. The SW size distributions had higher concentrations of aSSA+SMA than the ASW < 100 nm, which may indicate additional gas phase emissions capable of oxidizing to condensable species. In general,

both aSSA+SMA distributions agree with the pSSA distributions at larger sizes, however this occurs at different aerosol diameters for the ASW and SW, where the distributions begin to converge at ~200 nm and 1 µm for the ASW and SW, respectively. In addition, the higher concentration of aSSA+SMA compared to pSSA from natural SW between 200 nm and 1 µm (Figure 3.4b) suggests some modification of the pSSA. This could occur through a number of different factors, including gas-phase condensation, changes to the seawater microbial activity altering emissions, or minor changes to particle generation due to surface tension or temperature.

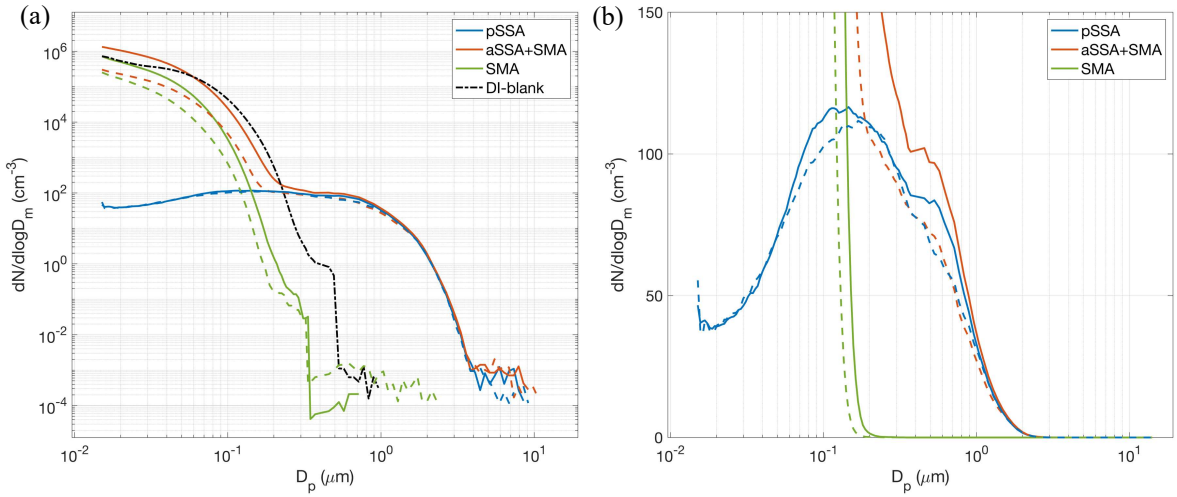


Figure 3.4. (a) Particle size distributions combined from the SMPS and APS measured downstream of the OFR and (b) the same as (a) but zoomed in a linear axis. The solid lines denote aerosols generated from SW and the dashed lines from ASW. The DI-blank experiment is denoted by the black dashed-dotted line. Size distributions represent a time-average of the SMPS and APS scans measured throughout the entire ice nucleation experiment.

Although there were higher number concentrations of aSSA+SMA between 200 nm and 1 µm, there was not a discernable shift towards larger sizes, which would be expected after condensation from the gas phase onto the pSSA. In addition, the low concentrations of pSSA would limit condensation of organics in the OFR and would favor new particle formation. The estimated condensation sink timescales were calculated and shown in the supplemental material, indicating that the condensation sink timescale for the nucleation mode aerosols (SMA-only) was

~3 minutes compared to ~11 minutes for the pSSA. Therefore, it is likely the nucleation mode particles scavenged the majority of the condensable material in the OFR and minimized condensation onto the pSSA. However, prior OFR studies for similar pSSA loadings indicated modest increases in organic volume fractions in pSSA as detected by atomic force microscopy (AFM) following similar oxidation exposures using the same OFR (Kaluarachchi et al. 2022b). These changes were accompanied by modifications in particle phase state in the water subsaturated regime, as well as hygroscopicity, for submicron pSSA. (DeMott et al. 2023) discussed how similar OFR studies on laboratory generated pSSA led to apparent changes in organic functionalization, at least as determined by AFM for submicron particles. Raman spectroscopy did not detect functional changes following oxidation in that study, but this was inferred to be a consequence of the emphasis on the 1 μm and larger particle regime for the Raman spectroscopic studies, for which organic volume fractions are already quite small and signal to noise becomes an issue. Finally, DeMott et al. (2023) noted that OFR processing of pSSA led to a decrease in INP concentrations by a factor of a few times in the temperature regime >243 K, where heterogeneous ice nucleation has been shown to be initiated by the organic components in very small fractions of pSSA. It has been unknown if this alteration of ice nucleation in very small fractions of pSSA at higher temperatures translates to impacts at cirrus temperatures. Further, it is also not known whether changes induced by oxidization of the organics present in the pSSA, or the changes in ice nucleating activity due to organics added via condensation or functional alteration might affect the heterogeneous nucleation process that was inferred to be stimulated by crystalline salts at temperatures below 220 K (Patnaude et al. 2021b).

Both pSSA size distributions showed peaks around 100 nm, in agreement with other studies that generated SSA in laboratory settings (Collins et al. 2014; Quinn et al. 2015; Patnaude et al. 2021b). However, there was a slight secondary mode at ~800 nm that only occurred during the real seawater experiments (Figure 3.4b). These two aerosol modes at 100 nm and 800 nm likely represent particles generated from film and jet drops, respectively, consistent with a previous laboratory study that generated aerosol particles from real seawater (Hill et al. 2023). Prather et al. (2013) showed that the fraction of biological particles increased for particles > 1 μm, and can make up to ~20 % for particles > 2 μm. Therefore, this apparent mode for particles ~800 nm may represent additional aerosolized biologic material such as bacteria, gels and viruses, that may be enriched with organic particles (Hill et al. 2023), would not exist in the ASW, and may explain lower concentrations in the aSSA+SMA generated from ASW compared to SW between 200 nm and 1 μm. The differences in the ~800 nm mode could also be due to modifications in droplet generation mechanisms, through small differences in temperature, RH, and surfactant content (Stokes et al. 2013).

For the blank (background) tests, in which the MART was filled with only DI water and the OFR was turned on but MART plunging turned off (black line), it was found that there was also secondary particle formation, likely a result of VOCs emitted from the acrylic material of the MART walls. It is likely that the outgassing of acrylic tank materials, and subsequent aerosol formation from those compounds in the OFR, occurred in all oxidation experiments. The outgassing may have varied with water temperature, which increased throughout each experimental day, and could contribute to some of the differences observed in the aSSA+SMA and SMA-only size distributions. For example, during the pSSA and aSSA+SMA experiments, particle concentrations below 100 nm were higher later in the day due to the warming of the

water with time (Figure A2.2). During the blank test the water was not pre-cooled as in the SW and ASW experiments due to time constraints, which likely led to higher VOC emissions and secondary particle concentrations observed during the blank measurements. Hence, the proportion of secondary particles or condensable material formed in the SMA-only and aSSA+SMA cases that was contributed from direct gas-phase emission from the SW and ASW, compared to other organics from the acrylic outgassing, cannot be determined. Future studies will need to probe SMA ice nucleation by using non-plastic materials. We will nevertheless assume the role of SMA can be interpreted from the ice nucleation experiments, as will be discussed in the subsequent results sections.

3.3.2 Analysis of Ice Nucleation Results

Figure 3.5a shows a time series of CFDC scans for a pSSA experiment. The first three scans, which occurred below 220 K showed a gradual increase in ice particle counts (light blue markers) with increasing RH_w starting around 65 %. The final three scans beginning ~218 K and above, showed a more modest increase in ice particle counts until the RH_w reached nearly 100 %, resulting in a very sharp increase in ice particle counts. The first three scans indicate particles freezing via heterogeneous nucleation due to the slow and gradual increase of ice particles, with the initial formation of ice particles below 75 % RH_w. In contrast, the last three scans showed very few ice particles below 85 % RH_w, but then had a sudden and dramatic spike in ice particles when the RH_w was > 90 %. The fourth scan may be at/near the transition between the two freezing mechanisms, as there were some increased ice particles counts at RH_w < 80 %, but we also observed the sharp spike in ice particles when the RH_w was near water saturation. These results were broadly consistent with previously reported freezing behaviors of NaCl particles at temperatures between 205 K and 235 K (Patnaude et al. 2021b; Wagner et al. 2018) who showed

time series of freezing indicative of heterogeneous freezing below ~218 K and homogeneous freezing above 218 K. Ice nucleation experiments illustrating CFDC scans for SMA-only generated from sampling the headspace over real seawater are shown in Figure 3.5b. In this case, all the scans showed little ice formation (< 1 L^{-1}) until the RH_w reached > 100 %, where there was a sudden and rapid onset of freezing of nearly all the aerosol particles. These cases illustrate that SMA froze through a homogeneous freezing mechanism, as there was almost no ice formed until the RH_w exceeded conditions for expected homogeneous freezing (Koop et al. 2000a). The CFDC RH_w scanning procedure was modified for the SMA cases and is the reason for the slower increase in RH_w after ice is initially formed. Additionally, most of the SMA particles formed are below the minimum size of detection of the OPC (~300 nm), therefore the sharp increase in total particles (black line) is mostly a result of the particles freezing and growing to sizes that can be detected by the OPC.

The ice nucleating ability of pSSA and aged aSSA+SMA generated from the MART is examined in Figure 3.6. The fractions of frozen particles at 1 % and 5 % are shown in T – RH_w space. The frozen fraction was calculated by dividing the CFDC OPC-measured ice concentrations (discussed previously) by the integrated total particle counts measured in the second set of sizing instruments (post-OFR losses). The sizing instruments provided a total aerosol count, since the OPC may not have detected the smallest particles at its lower size bound (~0.3 microns) even at RH exceeding expected deliquescence RH, particularly for the SMA experiments. Note when using this method, 10 % ice fration was no longer observed in any of the experiments and is the reason for presentation of 5 % instead. For calculations of frozen fraction for the aSSA+SMA experiments, the pSSA size distributions were used with the assumption that pSSA would freeze first. The colored markers denote 1 % (blue) and 5 %

(green) frozen fraction, where the filled and open markers denote the SSA generated from natural and artificial seawater, respectively. The reference lines indicate ice saturation (black dashed), homogeneous freezing calculated from (Koop et al. 2000a) (black solid), and the estimated pore condensation RH for an 11 nm pore size (Marcolli 2014) (yellow solid), as in Patnaude et al. (2021b).

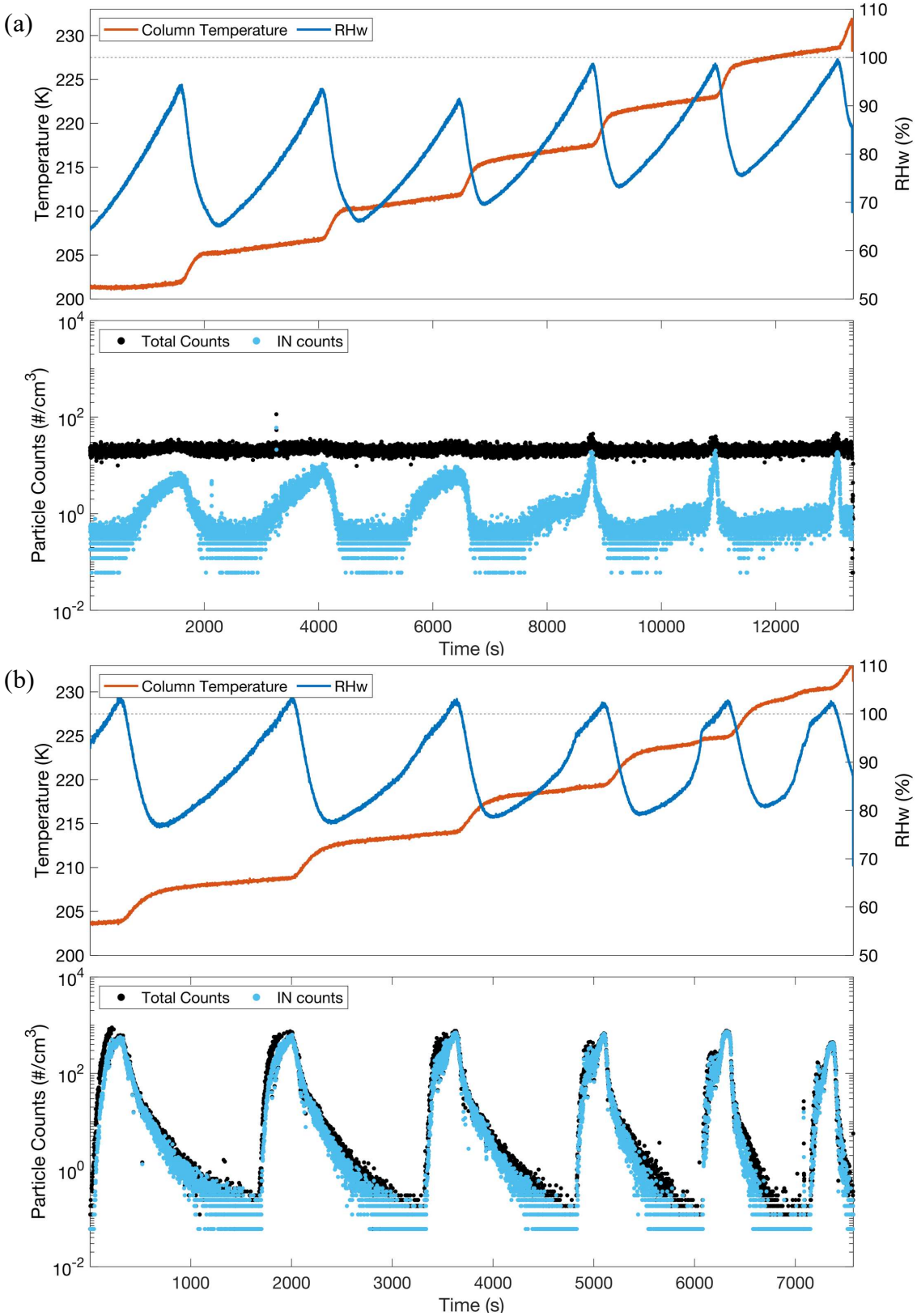


Figure 3.5. Time series of CFDC scans for (a) pSSA and (b) SMA experiments generated from real seawater beginning at 204 K. The CFDC column temperature is represented by the red lines,

and the blue lines represent the RH_w. The black and light blue markers indicate the numbers of total particles counted in the OPC and those that are considered ice crystals, respectively. The black dotted horizontal lines in the top panels of (a) and (b) represent water saturation.

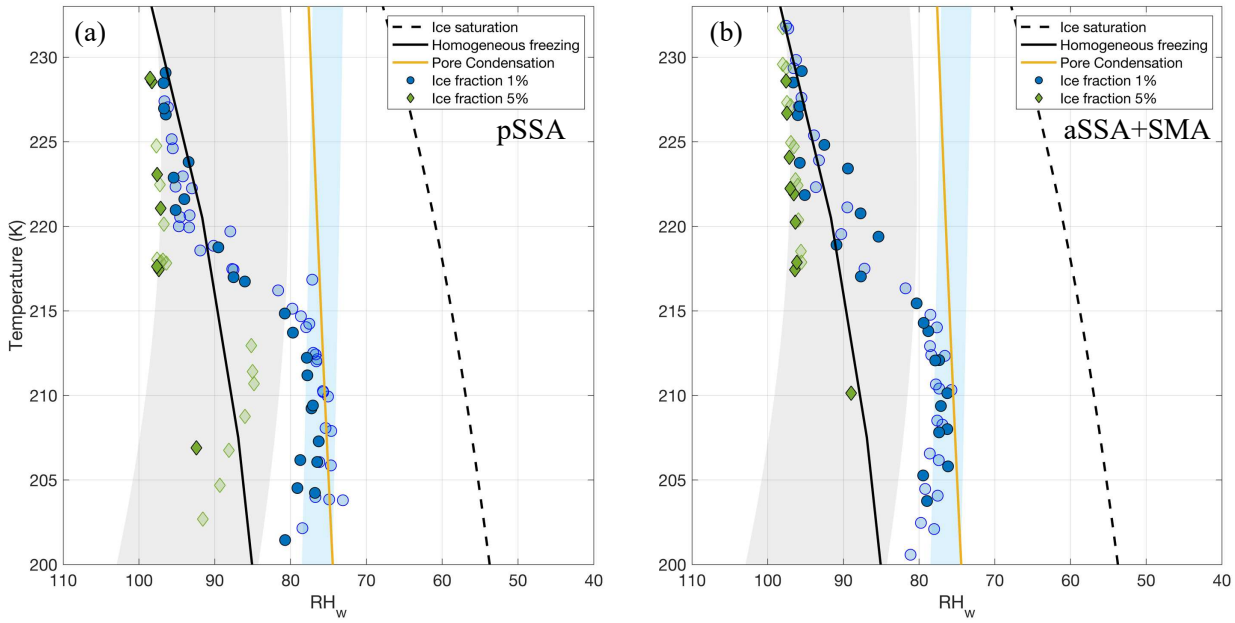


Figure 3.6. Fraction of frozen particles for (a) pSSA and (b) aSSA+SMA particles. The filled markers denote particles generated from the real seawater and the open markers from the artificial seawater. The blue and green markers indicate 1 %, and 5 % frozen fractions, respectively. The reference lines indicate ice saturation (black dashed), the parameterized RH_w for pore condensation in an 11 nm pore (Marcolli 2014) (solid yellow), and the expected threshold for the onset of homogeneous freezing (Koop et al. 2000a) (solid black). The blue shaded region represents the range of possible deliquescence RHs for NaCl and SSA, using the parameterization from Tang and Munkelwitz (1993) for NaCl extrapolated to colder temperatures as the upper bound and shifting it down 4 % RH for SSA similar to Wagner et al. (2018). The gray shaded region represents the range of uncertainty for the homogeneous freezing parameterization for aqueous sulfuric acid particles as presented in Schneider et al. (2021).

For temperatures > 218 K, the majority of both pSSA and aSSA+SMA particles froze at conditions near the threshold expected for homogeneous freezing (Koop et al. 2000a). Interestingly, both 1 % and 5 % frozen fractions of pSSA, and 5 % frozen fraction of aSSA+SMA, closely follow the upper bound of the expected homogeneous freezing parameterizations for aqueous sulfuric acid particles (Schneider et al. 2021) as temperatures decrease from 230 K to 217K. 1 % frozen fractions of aSSA+SMA particles followed the Koop et al. (2000a) average homogeneous freezing conditions more closely, within the range of

uncertainties for calculation of RH_w in the CFDC (4 %) (Richardson 2009). It should be noted that this is not a random uncertainty, that if there is error in the calculated RH_w it will be the same for all measured points. Results for 0.1 % frozen fraction (A2.4) indicated that a small fraction of the aerosol population still froze via heterogeneous nucleation at temperatures warmer than 218 K, with RH_w ~5–10 % lower than the 1 % observations. However, they still fell within the lower uncertainty bounds suggested by Schneider et al. (2021) for freezing of aqueous sulfuric acid. The 0.1 % frozen fraction for particles generated from natural seawater also occurred at lower RH_w (by up to 5 %) than for those from artificial seawater, perhaps indicating the inclusion of a more active subset of organic INPs in the real seawater. One might expect these more effective immersion freezing INPs to be present in concentrations that could be inferred from higher temperature freezing data, and if contained within the overall SSA population, their freezing conditions should parallel homogeneous freezing conditions but with a water activity offset (Archuleta et al. 2005).

During the pSSA experiments the total aerosol concentrations were ~150 cm^{-3}, therefore 0.1 % of the aerosol population would be 150 L^{-1}. When extending the immersion freezing line to water saturation (water activity = 1), as shown in Figure A2.5, the number of INPs per liter from the IS spectra at those temperatures, ~0.005 L^{-1} at 251 and ~0.5 L^{-1} at 245 K for SW and ASW, respectively, was much lower than reflected by 0.1 % freezing of all particles at lower temperatures. Therefore, we did not observe the expected number of heterogeneous freezing INPs based on the ice spectrometer spectra (not shown). We do not understand the exact mechanism for the freezing of the lower fractions of particles in the temperature regime where homogeneous freezing dominates. In other words, the 0.1 % frozen fraction is not consistent (higher than) the expected contribution of immersion freezing of the more specialized INPs that

are present in SSA for mixed-phase temperatures (when using the water activity freezing concept).

Below 218 K, the onset of freezing for both pSSA and aSSA+SMA occurred at much lower RH_w, ~70 %, for both the artificial and real seawater experiments. This shift from homogeneous freezing to heterogeneous freezing for the major proportion of particles at temperatures below ~220 K was consistent with several previous experiments investigating the freezing of NaCl and SSA particles (Ladino et al. 2016; Patnaude et al. 2021b; Schill and Tolbert 2014; Wagner et al. 2018; Wolf et al. 2019; 2020a). Additionally, for both water types, the onset of heterogeneous freezing occurred near the estimated deliquescence RHs of NaCl and the full deliquescence of SSA (blue shaded region), similar to the results in previous studies (Patnaude et al. 2021b; Wagner et al. 2018, 2021). The deliquescence RH of NaCl was estimated for colder temperatures from Tang and Munkelwitz (1993), and was lowered ~4 % RH for SSA following Wagner et al. (2018) with the assumption that the additional salts in seawater would deliquesce at a lower RH. The observations in Figure 3.6 also demonstrated that the alteration of the pSSA via oxidation (either through condensed organics or modification of the functional groups) did not modify the ice heterogeneous ice nucleation of pSSA. Both the pSSA and aSSA+SMA results showed that a transition from primarily homogeneous freezing to heterogeneous nucleation occurred at ~218 K.

Similar to Patnaude et al. (2021b), the pathway for heterogeneous nucleation and the transition between homogeneous and heterogeneous below 220 K remains unresolved. Deposition freezing remains an unlikely freezing pathway for pSSA and aSSA+SMA (at 1 % frozen fraction) at/near the DRH as water uptake of minor salt constituents would begin at lower RHs (Schill and Tolbert, 2014; Tang et al. 1997; Wagner et al. 2018). The competition between

full deliquescence and immersion freezing or PCF to explain this transition in freezing pathways was also discussed in Patnaude et al. (2021b) but bears repeating. While the 1% frozen fraction of both pSSA and aSSA+SMA occurred at near the PCF line, we do not believe this to be the likely freezing pathway for two reasons: 1) the PCF line shown in Figure 6 was approximated for an 11 nm pore size, and there is little evidence this is an realistic size for SSA and 2) the SSA particles would need to be fully dry to retain surface pores, which was not likely the case at 75 % RH_w where 1 % frozen fraction occurred. At temperatures above ~220 K, particle deliquescence would occur at a lower RH_w than the expected value for immersion freezing (see Patnaude et al. (2021b) Figure 8), thus favoring full dissolution and homogeneous nucleation at much higher RHs. At lower temperatures (< 220 K), the particles may have developed a brine layer, which has been observed in two previous studies (Schill and Tolbert, 2014; Wagner et al. 2018), and ice nucleation may have proceeded via the immersion pathway. Therefore, the most likely heterogeneous freezing pathway for pSSA and aSSA+SMA was immersion freezing.

In contrast to the ice nucleation results for pSSA and aSSA+SMA, the SMA generated by sampling and oxidizing the gases in the headspace of the MART, over both artificial and natural seawater samples, showed no indication of heterogeneous nucleation at any temperature (Figure 3.7; 1 % frozen fraction shown). For SMA generated from a combination of emissions and acrylic VOCs from both water types, 1 % frozen fraction did not occur until RH_w had almost reached water saturation, well above the expected freezing threshold for homogeneous nucleation. Due to the rapid onset of ice particle formation as the RH_w was increased beyond the homogeneous freezing threshold, 1 % was the lowest fraction that could be reliably detected by the OPC. These results support the conclusion that pure SMA does not freeze via heterogeneous

nucleation at cirrus temperatures, similar to previous studies that analyzed the ice nucleating ability of non-marine SOA in the cirrus regime (Kasparoglu et al. 2022).

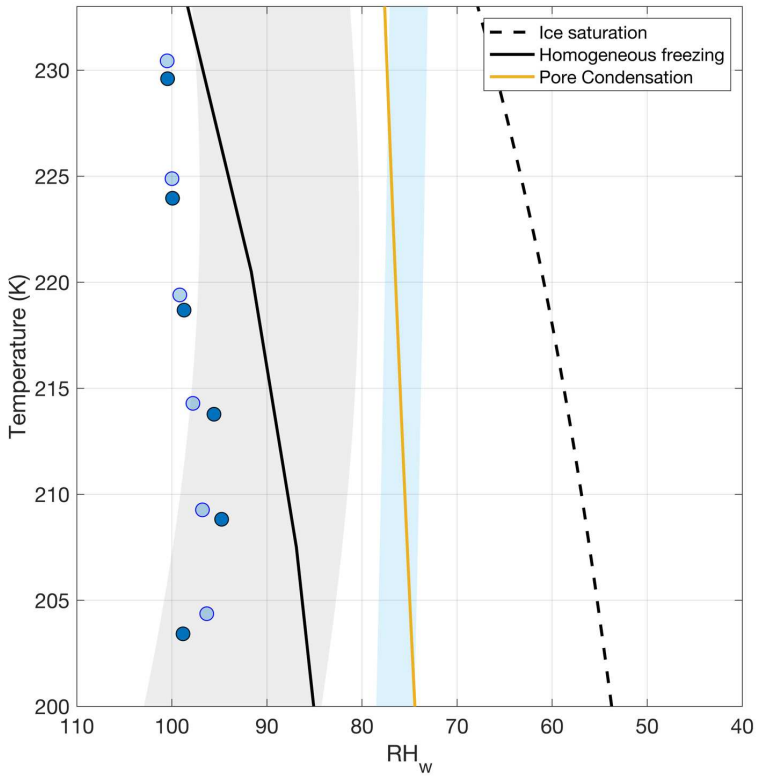


Figure 3.7. Similar to Figure 3.6, but only showing 1 % frozen fraction of SMA particles, where the filled and open markers denote SMA generated by sampling the headspace over real and artificial seawater, respectively.

3.4 Conclusions

In this study, a MART provided a representative method for generating polydisperse SSA for comparison to our prior studies of monodisperse NaCl and SSA particle freezing at cirrus temperatures (Patnaude et al. 2021b). Despite the added complexity from generating a polydisperse SSA distribution, the impact on heterogeneous ice nucleation behavior was minimal. This was illustrated by the striking similarities in ice nucleation results between the pSSA from this study and the results from Patnaude et al. (2021b), which both determined heterogeneous ice formation with activated fractions above 1 % only occurred at temperatures of 218 K or below. The results from this current study also corroborate the association of the

transition from homogeneous to heterogeneous nucleation at these cirrus temperatures with the presence of crystallized (undissolved) salts in pSSA, and with no demonstrated size dependence. Based on the similarities between freezing results in this study and Patnaude et al. (2021b) and Wagner et al. (2018), the dominant heterogeneous freezing mechanism below 218 K was likely the immersion freezing pathway.

The results in this study specifically address questions raised by Wagner et al. (2021): will a higher number of ice-active particles be generated from a sea spray chamber where highly organic particles may be formed (Wilson et al. 2015; Wolf et al. 2020b); or, if highly organic-rich particles are present, would these particles be aerosolized when generated in a more realistic manner? It is possible that organic particles in the pSSA from real seawater may contribute a small additional subset of the INP population and freeze more efficiently at warmer temperatures, as shown by the observed 0.1 % frozen fraction at much lower RH_w above 220 K than the 1 % or 5 % frozen fractions (Figure A2.5). Additionally, the 0.1 % frozen fraction from natural SW has RH_w up to 5 % lower than the 0.1 % results from ASW, which may also be a result of organic enrichment. Organic-rich particles may not deliquesce until higher RHs (>80 %), allowing for heterogeneous nucleation under these conditions, whereas pure salt particles would be fully dissolved and would not freeze until the homogeneous freezing threshold is reached. However, even if these are organic-enriched or internally mixed particles and represent a subset of the INPs in marine aerosols at cirrus levels, they are vastly outnumbered by the inorganic salt particles that appear to dominate heterogeneous ice nucleation at these temperatures.

No prior studies have investigated how atmospheric aging may impact SSA ice nucleation at cirrus temperatures. This study showed that the freezing pSSA particles after

undergoing atmospheric aging and the formation of an additional SMA population via new particle formation (simulated by use of an OFR) was not changed compared to the freshly emitted pSSA particles, as demonstrated by the similar results obtained with both pSSA and aSSA+SMA. There are a few possible reasons for the similar freezing behaviors between these two particle types: 1) the newly formed particles scavenged the majority of condensable material produced in the OFR and only modest amounts of secondary organics condensed to the pSSA, 2) the air stream remained humidified when entering the OFR and the pSSA particles were thus likely in an aqueous state. Whether oxidation of their organic content could proceed in the wetted or partially wetted state, and whether changes to the pSSA organic content would be similar to that observed when processed in a dry crystalline state is unknown, or 3) the addition of SMA coatings to the pSSA and/or alteration of organic components of the pSSA did not alter the crystallization behaviors, nor did they hinder the water uptake by the inorganic salts. Nevertheless, the inclusion of organic material on the pSSA would likely only hinder the heterogeneous nucleation ability that remains dominated by the crystalline salts. Future studies using more realistic or at least slower atmospheric aging processes, such as what may occur in a typical smog chamber, may better represent the possible organic coatings on pSSA. Additionally, oxidation of pSSA at cold temperatures (< 233 K) and after efflorescence may produce different freezing results than this study due to oxidation under different phase states and morphologies. These results also indicate that secondary particle formation from the gas-phase emissions of natural seawater does not generate effective INPs at cirrus temperatures, as the SMA-only case did not reach 1 % frozen fraction until the RH_w had almost reached water saturation. Thus, SMA may only be considered a relevant source for ice nucleation in cirrus clouds if they are exposed to a pathway that begins via activation as a CCN into cloud droplets at lower altitudes, lofted to

cirrus temperatures in deep convection, and then freeze homogeneously (liquid-origin cirrus, see Krämer et al. (2020) and Luebke et al. (2016)).

This study could not distinguish whether the experiments were affected by any of the following: changes to the phase state or morphology of the pSSA particles following oxidation; whether fragmentation of aerosol-phase organic compounds occurred; or if glassy states were induced. Exploring these possibilities would require that associated compositional studies be aligned with similar experiments (Mayer et al. 2020b; Prather et al. 2013; DeMott et al. 2023; Kaluarachchi et al. 2022a,b) but these results suggested that the strongest heterogeneous freezing behaviors noted at temperatures below 218 K were dominated by the salt components even after atmospheric aging. One remaining caveat to this study regarding the SMA and aSSA+SMA results is the uncertainty of the contribution from the seawater versus outgassing from the MART to the mass of secondary material produced, which should be addressed by future studies that might also include compositional and phase state data.

We have shown SSA can nucleate ice via heterogeneous nucleation below 220 K. Airborne observations have found concentrations of sea salt between 10^{-4} – 10^{-1} μg m^{-3} in the upper troposphere (Murphy et al. 2019; Bian et al. 2019), and based on the results shown herein a large proportion of those salt particles should retain their ice nucleating ability even after the atmospheric aging that would occur during their ascent to cirrus levels. Cirrus clouds are ubiquitous in the upper troposphere and represent a large source of uncertainty in determining Earth's radiative budget. In addition, cirrus clouds that form via heterogeneous nucleation have also been shown to represent a net positive radiative forcing (Krämer et al. 2020), thus demonstrating a potential indirect radiative effect of SSA on our climate system.

CHAPTER 4: AIRBORNE ICE NUCLEATING PARTICLES AND ICE FORMATION PROCESSES IN CUMULUS CONGESTUS CLOUDS

4.1 Background on the Ice Phase in Mixed-Phase Clouds

4.1.1 INPs in Mixed-Phase Clouds

Numerous studies have been conducted in recent decades to characterize the types of aerosols that may act as heterogeneous ice nucleating particles (INPs) in mixed-phase clouds (MPCs). Mineral dust, primarily sourced from deserts, represents one of the most important and commonly observed INPs in the mixed-phase regime, readily initiating ice formation below -15 ºC over a range of relative humidity (RH) conditions (Hoose and Möhler 2012; Hiranuma et al. 2014; Wex et al. 2014; Boose et al. 2016; DeMott et al. 2003b; Tobo et al. 2019; Price et al. 2018; Niemand et al. 2012; Sassen et al. 2003b). Soil dust from arable regions (grazed and agricultural lands) have ice nucleation properties associated with their contained organic matter and may be especially important as an INP source over continental regions, having the ability to impact MPCs at temperatures as high as -6 ºC (Conen et al. 2011; DeMott et al. 2018; Hill et al. 2016; Testa et al. 2021; Tobo et al. 2013). Biological aerosols, primarily from terrestrial sources, represent another important source of INPs in MPCs and may be variously composed of plant fragments, pollen, bacteria, and fungal spores (Murray et al. 2012; Patade et al. 2021). In contrast to mineral dust, it has been shown that biological INPs are highly active at temperatures > -15 ºC (Testa et al. 2021; Petters and Wright 2015; Tobo et al. 2013) based on the near complete disruption of the INP activity in this temperature range after treatment with 95 ºC heat for a short period (Christner et al. 2008; Hill et al. 2014). Patade et al. (2022) simulated a midlatitude convective system with specific inclusions of biological INPs and found few changes to the

warm-phase microphysical properties and ice crystal number concentrations. Despite this, uncertainties remain regarding the role of biological INPs in ice formation during the early stages of cloud development. Biomass burning has also been shown to be a source of atmospheric INPs, with enhanced INP concentrations found inside of wildfire plumes (Barry et al. 2021a; McCluskey et al. 2014).

4.1.2 In Situ Observations of Ice Crystal Concentrations in MPCs

An early study collecting in situ observations of ice crystal number concentrations (N_{ice}) was reported in Heymsfield et al. (1979) who suggested that ice particles in cumulus congestus clouds form mainly through primary (heterogeneous) nucleation at temperatures > -15 ºC. They posited that this finding applied to undiluted updraft cores, but fails when once there are intermixed up- and downdrafts in more mature clouds. Additionally, that study detected ice crystals at sizes > 100 μm using a camera system in a slow moving sailplane, therefore the artificial ice crystal enhancement due to shattering on the cloud probe tips (Korolev et al. 2011) was not an issue. Years later, Prenni et al. (2007) compared INP and ice crystal number concentrations in anvil cirrus formed from deep convection and found relative agreement, within a factor of 2–3, when ice crystals were > 30 μm. However, they found a larger disagreement between INP concentrations and N_{ice} when comparing smaller sized hydrometeors between 3.5 – 58 μm, and attributed this difference to homogeneous freezing or secondary ice production (SIP). A key advancement in Prenni et al. (2007) was the deployment of a counterflow virtual impactor (CVI) located upstream of a continuous flow diffusion chamber (CFDC) allowing for measurement of INPs from the residual particles of evaporated cloud hydrometeors for direct comparison with N_{ice}. In orographic wave clouds, where thermodynamic and dynamical conditions are simpler than non-orographic cloud types due to the relatively predictable airflow

structure, and impacts from SIP are not expected (Cooper and Vali 1981; Field et al. 2001), in situ observations of N_{ice} were found to correlate with residual INP concentrations, as well as with the number concentrations of particles with diameters > 100 and 500 nm (Eidhammer et al. 2010; Twohy et al. 2010). In contrast, cumulus and convective clouds are more thermodynamically and dynamically complex than orographic clouds, and very few studies exist that include coincident measurements of INPs concentrations and N_{ice}. More commonly, INP parameterizations are applied to measured aerosol number concentrations to estimate INP concentrations and are compared to N_{ice} in convective environments (Crawford et al. 2012; Ladino et al. 2017; Stith et al. 1994). These studies found that N_{ice} in the environment greatly exceeded the estimated number concentrations of INPs and attributed this difference to either SIP or vertical mixing and/or sedimentation. However, which SIP mechanism is active, and the conditions required for the onset of SIP, are not well understood. More recently, Korolev et al. (2022), using in situ observations, found evidence of SIP present at temperatures lower than those necessary for HM, and suggested fragmentation of freezing droplets (FFD) as the most likely SIP mechanism. Korolev et al. (2020) described environmental conditions most frequently associated with clouds where SIP was present as the presence of liquid droplets, active convective updrafts, and aged rimed particles. Despite these findings, their conclusions were not based on direct measurements of INPs, which is fundamental for accurate estimation of the number of ice crystals formed via primary nucleation and establishing whether SIP are active or not.

4.1.3 Modelling Primary Nucleation and Secondary Ice Production in MPCs

Despite significant attention to better understanding the ice phase in MPCs, representation of ice processes in numerical models remains challenging (Seinfeld et al. 2016). Predicting primary ice nucleation is difficult due to the wide variability in the types of INPs and

the corresponding conditions at which they will nucleate ice. Additionally, the ice nucleating ability of aerosol particles may vary significantly depending on particle size and morphology, and chemical composition (Archuleta et al. 2005; Wex et al. 2014; Möhler et al. 2008; Marcolli 2014). Commonly used parameterizations for primary ice nucleation predict ice crystal numbers as a function of ice supersaturation, temperature, aerosol surface area, or composition (DeMott et al. 2010; Meyers et al. 1992; Niemand et al. 2012; Phillips et al. 2008). Subsequent studies have applied parameterizations to specific aerosol types such as desert dust or biological INPs and found better agreement than when solely relating INPs to total aerosol concentrations > 500 nm (DeMott et al. 2015; Tobo et al. 2013). Ultimately, primary nucleation in numerical simulations is highly dependent upon which parameterization is used and whether primary ice nucleation is dominated by a certain type of particle.

Representation of SIP adds another level of complexity in simulating ice in numerical models. Many models to this day only include the Hallet-Mossop (HM) mechanism, however in recent years additional SIP mechanisms such as FFD and breakup from ice-ice collisions (BR) have been implemented into numerical models (Phillips et al. 2017, 2018; Sullivan, et al. 2018b, 2018b; Yano et al. 2016). The addition of these SIP mechanisms has led to improved representation of N_{ice} in tropical (Huang et al. 2022; Qu et al. 2022) and continental (Waman et al. 2022) convection, and cold frontal (Sullivan et al. 2018b) and polar (Sotiropoulou et al. 2021) MPCs. Yet many of these studies focused on the processes contributing over the total lifetime of the clouds, which may last several hours, in order to analyze the contributions of a specific SIP mechanism. For convective clouds, which may develop on the order of tens of minutes, it is important to understand the chain of events of ice formation, and when and if a specific SIP

mechanism will trigger. These are important considerations for the onset of precipitation, cloud lifetime, as well as updraft intensity, and remain for the most part unanswered.

4.2 Description of Tools and Methods

4.2.1 SPICULE Project Overview

In situ aircraft observations were obtained during SPICULE in May and June 2021 over the U.S. Central Great Plains (Figure 4.1). The airborne platforms for SPICULE were the National Science Foundation (NSF)–National Center for Atmospheric Research (NCAR) Gulfstream V (GV) and the Stratton Park Engineering Company (SPEC) Inc. Learjet model 35J. The two aircraft flew in coordination to target convective turrets in the early stage of development, with the GV and Learjet targeting the warm- (> 0 ºC) and cold- (< 0 ºC) phase regions of the clouds, respectively. Typically, the GV would sample sub-cloud aerosols in the area of clouds and then penetrate varied levels above the cloud base, while the Learjet would attempt to capture ascending cloud top regions. Once the clouds reached a deeper convective stage or lightning was present, the aircraft moved on to a new target. The GV and Learjet were equipped with and air motion sensors as well as thermodynamic and cloud particle measurements. The GV also included aerosol instrumentation, as discussed below.

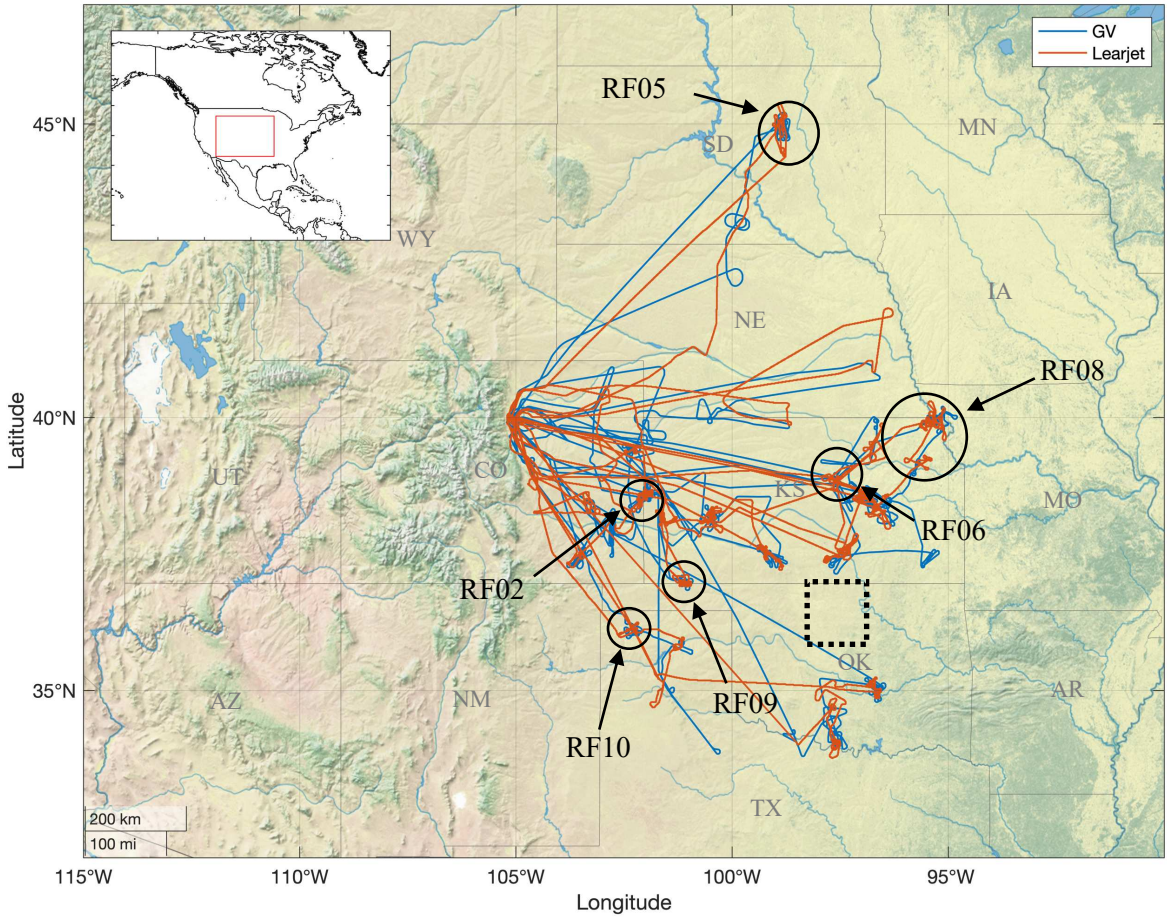


Figure 4.1. Flight tracks during SPICULE of the GV and Learjet denoted by the blue and red lines, respectively. Circled clusters of the GV and Learjet flight tracks denote the geographical location of the cloud passes used in this analysis. The black dashed square represents the model domain for the RAMS simulations.

4.2.2 Aircraft Instrumentation

For this study, a number of different cloud probes aboard both aircraft were used to measure the entire range of liquid and ice hydrometeors. This includes the Fast Cloud Droplet Probe (FCDP) measuring cloud droplet size distribution and concentrations between 1.5 – 50 µm aboard the Learjet. The GV was instead equipped with a Cloud Droplet Probe (CDP) measuring between 2 – 50 µm. Both aircraft included wingpod-mounted two-dimensional stereo (2DS) probes, which have 128 diode arrays with a measurement range of 10 – 3000 µm with a 10 µm resolution and the High Volume Precipitation Spectrometer (HVPS) with a measuring range of

150 μm – 2 cm, with 150 μm resolution. Cloud probes are equipped with anti-shattering tips (Korolev et al. 2011), therefore, the effects of shattering are assumed to be insignificant in this study. High-resolution cloud images (2.3 μm pixel size) were captured using a cloud particle imager (CPI) (Lawson et al. 2001; Woods et al. 2018). Cloud liquid and total water contents between 0 and 4 g m^{-3} were measured using a Sky Tech Nevzorov Probe. Both aircraft were equipped with a Rosemount temperature probe with a measurement range and accuracy of 50 ºC to -50 ºC and 0.5 ºC, respectively. Measurements of aerosol concentrations were collected aboard the GV using a Passive Cavity Aerosol Spectrometer Probe (PCASP) with 30 size bins between 0.1 – 3 μm. Condensation nuclei (CN) were collected using a butanol condensation nucleus counter which can measure particles > ~11 nm. An upward- and downward viewing Ka-band probe radar (KPR) (Pazmany and Haimov 2018) was also installed on the Learjet. Measurements aboard both aircraft were collected at 1 Hz. The special analysis of cloud probe measurements to determine ice crystal concentrations is detailed in the Results section 4.4.2.

4.2.3 Airborne Observations of INPs

Real-time observations of INPs were obtained using the Colorado State University (CSU) CFDC (Barry et al. 2021a; Rogers, 1988) which was installed aboard the GV and was configured similarly to a previous study sampling over the Southern Ocean (McCluskey et al. 2018b). The CFDC provided high-temporal resolution INP measurements primarily in the immersion freezing mode. The CFDC consists of two temperature controlled concentric walls coated in a thin layer of ice. Temperature and water vapor gradients between the two walls determine the supersaturation within the column with respect to liquid and ice. Sample air from outside the aircraft flows through the chamber at ~1.5 liters per minute (LPM) and is contained in narrow lamina in the annular region by inserted dry sheath air (~8.5 LPM). During operation, the CFDC

was held at a constant temperature between -20 ºC and -30 ºC while maintaining supersaturation with respect to water (SS_w, RH with respect to water (RH_w) minus 100%) conditions ~3–7 % within the aerosol lamina, encapsulating sampled aerosol particles in water droplets. DeMott et al. (2017) have shown these conditions lead to INP concentrations comparable to those obtained in immersion freezing measurements. Total residence time during which ice nucleation occurs inside the column is ~5 s. As droplets containing INPs freeze, the crystals grow quickly and preferentially compared to the liquid droplets due to the high supersaturations. The lowest section of the column acts as the evaporation region where the wall temperatures are the same, producing ice supersaturated and water subsaturated ($SS_w < 0$) conditions causing liquid droplets to evaporate but allowing for further growth of the nucleated ice crystals. Ice particles are then detected downstream of the column by an optical particle counter (OPC), which determines the number of frozen particles based on the differences in sizes between aerosol and ice crystals. An aerodynamic impactor, located upstream of the column and sample inlet, was used to remove large particles so they are not detected as frozen particles. An impactor with a 50 % cut-size of 2.5 μm was used in this study. During operation, 10-minute sampling periods were alternated with 5-minute filter periods where sampled air was passed through HEPA filters to provide background counts. These background filter periods were accounted for in correcting raw integrated CFDC ice counts during sampling periods and in determining confidence intervals of corrected INP concentrations (Moore et al. 2023). INP concentrations are reported at standard conditions (STP; 0 ℃ and 1013 kPa).

Offline INP analyses were also conducted for the determination of the number of INPs active in the immersion freezing mode (Hiranuma et al. 2015). Ambient aerosols were collected onto 0.2 μm pore Nuclepore polycarbonate filter membranes loaded into two pre-cleaned 47 mm

in-line aluminum filter units on top of the CFDC rack. Collection on the filters was powered by an air pump pulling ambient aerosol particles into the cabin through the aircraft aerosol inlet at a rate of ~10 LPM. (Hiranuma et al. 2015). Preparation of the filters to minimize contamination, which involves cleaning the filters via ultrasonication in methanol and rinsing with deionized water, is described in Barry et al. (2021b). Collected particles were resuspended into liquid and the extracts analyzed using the CSU Ice Spectrometer (IS) to determine the number of INPs per liter of air as a function of temperature (Barry et al. 2021b; Vali 1971). Before every other research flight (RF), "blank" filters, which are loaded and then immediately removed from the filter units, were collected and processed using the same methods as the other filters, and the data subsequently used to remove background contamination. The average INP spectra from the blank filters and the best fit line used for background removal are shown in Figure A3.1. Filter collections were conducted for a minimum of ~20 minutes during level legs in the boundary layer (BL) and up to but below cloud base in an effort to directly collect INPs that were likely to be entering clouds.

Sampling INPs during SPICULE occurred both in- and out of clouds. Ambient (out of cloud) sampling of aerosols used the HIAPER Modular Inlet (HIMIL). The HIMIL passing efficiency is near 100% for 1 μm particles and decreases to ~90 % for 10 μm particles. The HIMIL provided sampled air to the CFDC and to the filters via separate lines. For in-cloud measurements with the CFDC, cloud hydrometeors were sampled using a Counterflow Virtual Impactor (CVI) similar to previous configurations (Levin et al. 2019; Prenni et al. 2007), which collected those cloud hydrometeors with sufficient inertia to overcome the counterflow into the inlet while rejecting unactivated particles (Twohy et al. 1997). During all SPICULE RFs, the mean (± 1 standard deviation) 50 % penetration cut size for the CVI was 6.61 ± 0.55 μm in

diameter. Cloud droplets and ice crystals were melted and evaporated in the heated sample line, allowing for the sampling of the residual particles that are present in the hydrometeors. Due to the concentrations by virtual impaction of a higher volume of air being swept up by the CVI inlet into the lower passed flow rate, particles concentrations are enhanced within the CVI. Enhancement factors were averaged for each cloud segment during all RFs and used to normalize the CFDC measurements when in cloud and sampling on the CVI. The mean (± 1 standard deviation) CVI enhancement factor during all SPICULE RFs was 12.48 ± 2.5. A final correction to in-cloud particle concentrations also includes estimating the efficiency of hydrometeors captured in the CVI inlet. This involves calculating the ratio of total concentrations from the CDP wing probe to the total residual concentrations behind the CVI when in-cloud. This efficiency factor was ~3, and is multiplied by the aerosol and INP measurements downstream of the CVI. "In cloud" conditions were selected for CDP number concentrations > 10 cm^{-3} or CVI cloud water contents > 0.01 g m^{-3}.

4.3 Configuration of Numerical Simulations

4.3.1 Model Initialization

Model simulations were carried out using the Regional Atmospheric Modelling system (RAMS) version 6.3.02 (Cotton et al. 2003; Saleeby and van den Heever 2013). RAMS predicts the mass mixing ratio and number concentration of eight hydrometeor classes using a bin-emulating bulk microphysics scheme. The current version of RAMS simulates a number of different ice nucleation processes including homogeneous freezing (DeMott et al. 1994), contact freezing (Meyers et al. 1992), secondary ice production (Hallett and Mossop 1974) and collection of cloud droplets by ice crystals via riming (Saleeby and Cotton 2008). A summary of

the model configuration, initial conditions, and experimental simulations used in this study is shown in Table 4.1.

Table 4.1. Summary of RAMS model configuration, initialization, and list of experimental simulations used in this study.

Model Aspect	**Setting**
Domain	Arakawa C Grid
	600 x 600 points, $\Delta x = \Delta y = 100$m
	Centered on 36.6ºN, -97.5ºW
	80 stretched vertical levels, Δz = 100–300 m, 1.015 stretch ratio
Time	2.5-hour simulation, Δt = 1s
	16 May 2021, 22:00:00 UTC – 17 May 2021, 00:30:00 UTC
Initialization	Horizontally homogeneous thermodynamic and dynamic profile using radiosonde from Lamont, Oklahoma on 16 May 2021
	Gaussian potential temperature perturbation 10-km wide in the lowest 2 km of the domain, with a maximum perturbation of 2 K and centered in the domain at x = y = 10 km
Boundary conditions	Periodic in zonal and meridional directions
Microphysics scheme	Two-moment bin-emulating bulk microphysics for eight hydrometeor species (Meyers et al. 1997; Saleeby and Cotton 2004) Heterogeneous nucleation (DeMott et al. 2015)
Aerosol treatment	Max concentration defined at the surface; profile decreases defined by fit from SPICULE observations
	Aerosol sources and sinks and tracking of CCN and IN (Saleeby and van den Heever 2013)
Numerical Experiments	
Simulation name	**Ice formation**
Primary only (PR-only)	N_i = PR, DeMott et al. (2015)
Fragmentation of freezing droplets (FFD)	N_i = PR+FFD, Sullivan et al. (2018b)
Ice breakup (BR)	N_i = PR+BR, Sotiropoulou et al, (2021)
Rime-splintering (HM)	N_i = PR+HM, Hallet and Mossop (1974)
All-SIP	N_i = PR+HM+FFD+BR

The model domain was centered over north-central Oklahoma (black dashed square Figure 4.1) and was 60- by 60-km wide with 100 m grid spacing in the horizontal. The geographical location of the domain was in the same general area of the SPICULE flights and centered around the radiosonde used for initialization (discussed below). The domain had 80

vertical grids with 100 m vertical spacing at the surface stretched (1.015 stretch ratio) to a maximum vertical spacing of 300 m towards the top of the domain ~15 km, which was sufficiently high enough to ensure there were no interactions between the cloud tops (7-8 km) and top of the domain. The thermodynamic profile was initialized using a radiosonde from May 16, 2021 over Lamont, Oklahoma shown in Figure 4.2, and was set up as horizontally homogeneous at the start of the simulations. The date and location were chosen to be shortly before and in the same general area as the SPICULE campaign, and represented a day with elevated CAPE ~2700 J kg^{-1} (red shaded region), which was generally representative of the environmental conditions during SPICULE. The forcing mechanism for the congestus cloud was applied just at the start of the simulations and was generated by inducing a 10-km wide gaussian shaped temperature perturbation with a maximum of 2 K, between the surface and ~2 km aloft. This initiated the cloud development and apart from this initial buoyant forcing, the clouds were allowed to evolve freely without any additional forcing. These simulations were intended to represent an idealization of the microphysical and dynamic processes occurring in the early-growth cumulus congestus clouds observed in SPICULE. The model was initialized starting at 2200 UTC and the results reported in this study only focus on a short period of the cloud development (~2340 UTC) when the simulation produced a consistent updraft from near the surface up to ~7 km aloft, similar to the maximum vertical extent of the observed clouds (Table 4.2).

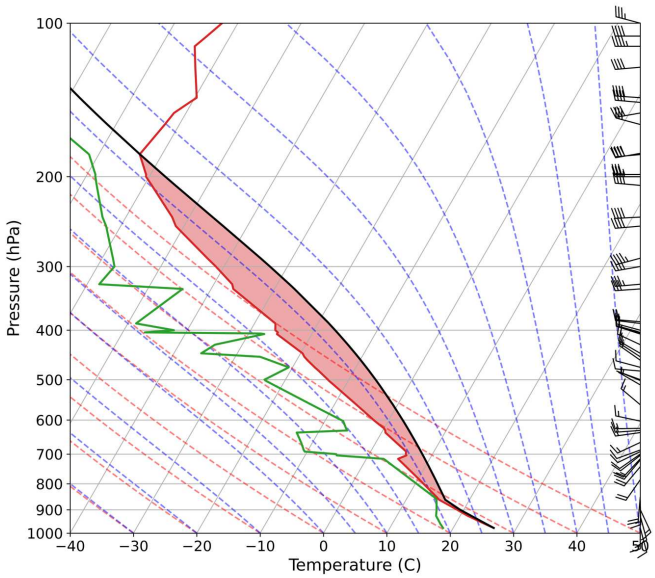


Figure 4.2. Radiosonde from Lamont, Oklahoma on May 16, 2021 used to initialize the initial thermodynamic profile in the RAMS simulations. The red and green lines represent the environmental temperature and dewpoint, respectively, and the black line represents the trajectory of a hypothetical buoyant air parcel. The dashed blue and red lines represent the moist and dry adiabats, respectively. The red shaded region denotes the convective available potential energy (CAPE). Wind barbs indicate the wind speed (knots) and direction.

The model initialized the aerosol field as horizontally homogeneous across the domain at the start of the simulations, similar to previous RAMS experiments (Leung et al. 2023; Saleeby et al. 2016; Saleeby and van den Heever 2013) and are described below. There were no additional aerosol sources during the duration of the simulations, however the particles were allowed to advect though the grid boxes. For all simulations, the cloud condensation nuclei (CCN) particles had a solubility fraction of 0.9 and followed a lognormal distribution with a geometric mean diameter of 180 nm and a standard deviation σ_g of 1.8; number concentrations were specified by the input profile and then evolved through the simulation. The vertical profiles of the number concentrations of CCN were initialized to mimic the observed number concentrations of aerosol particles > 100 nm from SPICULE (Figure 4.3a). The observed number concentrations shown in Figure 4.3 were obtained from the merged size distributions from the PCASP and CDP probes during clear sky periods. The model did not track the aerosol-radiation

interactions as it was unlikely to affect the cloud evolution. However it did track aerosols through the categories of un-activated, activated, wet-deposited and regenerated aerosols (Saleeby and van den Heever 2013). Heterogeneous ice nucleation of INPs followed the dust parameterization from DeMott et al. (2015) (D15 henceforth). The number of INPs in the simulations were calculated from the aerosol number concentrations > 500 nm (Figure 4.3b) via D15. The D15 scheme was chosen as it had better agreement with the in-cloud CFDC and IS measurements than the DeMott et al. (2010) scheme when applying a fixed number of aerosols of 2.5 cm^{-3} (Figure A3.2), taken from the low-level RAMS profile in Figure 4.3b.

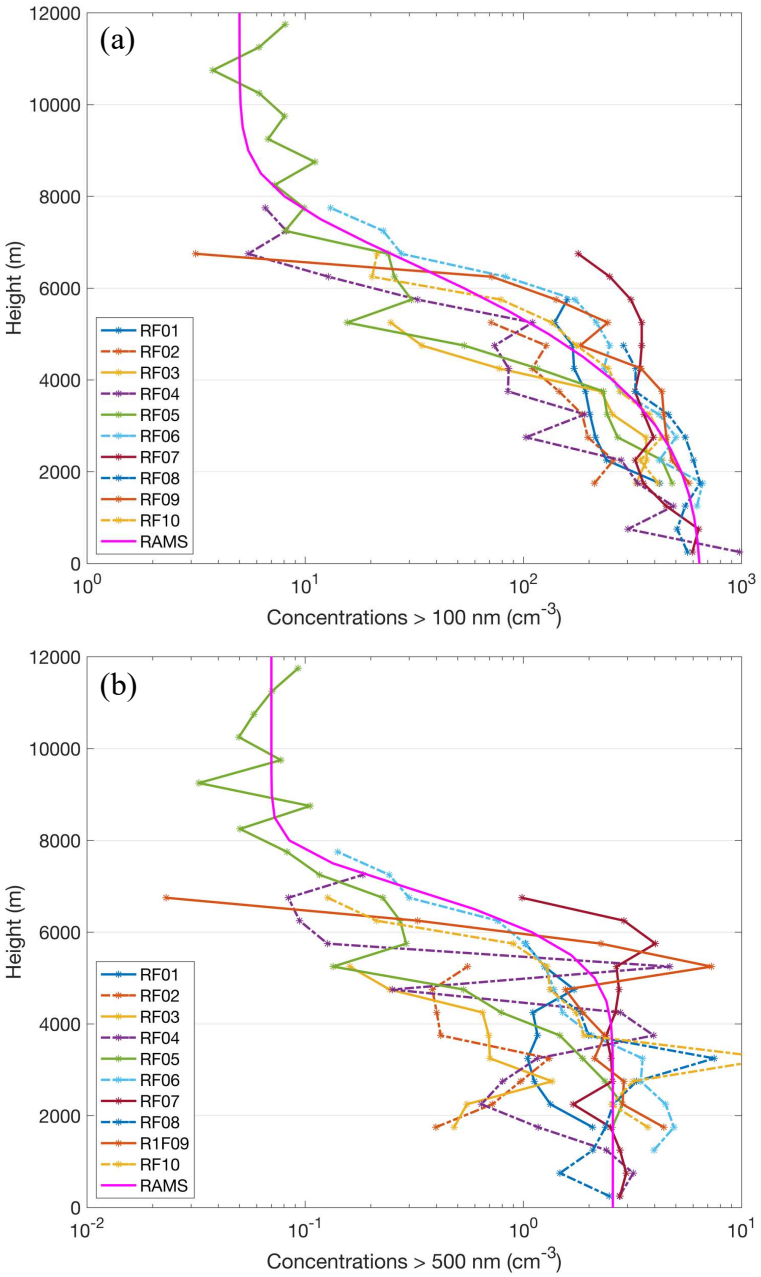


Figure 4.3. Vertical profiles of aerosol number concentrations (a) > 100 nm and (b) > 500 nm for each RF from SPICULE and the fitted profile for aerosols that may act as cloud condensation nuclei (CCN) or INPs, respectively in (a) and (b) for RAMS initialization (pink lines). The PCASP number concentrations were corrected to standard conditions (0 ºC and 1013.15 hPa).

4.3.2 Implementation of SIP Mechanisms into RAMS

Previously, the HM rime-splintering mechanism was the only SIP mechanism included in RAMS. The RAMS parameterization for rime-splintering is a simple empirical formula based on

Mossop (1978) and depends upon the number concentrations of cloud droplets > 24 μm and < 13 μm. The scheme used a simple scaling factor that linearly increases from 0 to 1 from -8 ºC to -5 ºC and linearly decreases from 1 to 0 from -5 ºC to -3 ºC, SIP is inactive at all other temperatures (Cotton et al. 2003). This study introduced representations for two new SIP mechanisms, FFD and BR, into RAMS and evaluated the effects of the various SIP mechanisms on ice formation. FFD was introduced into RAMS using the parameterization from Sullivan et al. (2018b) which uses a temperature-dependent fragmentation probability with a maximum fragmentation probability of 40 % (their equations 1–3), where the fragmentation probability follows a normal distribution centered at 261 K with a standard deviation of 5 K. The maximum probability and standard deviation were chosen as they produced a probability distribution (Figure A3.3) that best fits the laboratory observations of droplet fragmentation in moist airflow from Keinert et al. (2020). A constant number of ejected fragments of 10 was used similar to Sullivan et al. (2018b). The freezing of droplets was calculated using a stochastic model from Bigg (1953) and predicted the freezing of droplets based on the number and mean mass of raindrops and an empirically derived heterogeneous nucleation coefficient J_{het} shown by equation (4.1).

$$J_{\text{het}} = b_{\text{het}} \exp\left(a_{\text{het}} \Delta \text{T} - 1\right) \tag{4.1}$$

where a_{het} and b_{het} were set to 0.65 K^{-1} and 0.2 $\text{kg}^{-1}\,\text{s}^{-1}$ respectively, and ΔT is supercooling (Sullivan et al. 2018b; Seifert and Beheng 2006). This parameterization does not explicitly relate droplet freezing with an INP, but rather was based on a stochastic interpretation of droplet freezing using laboratory samples of distilled water droplets. The application of the Bigg (1953) formulation was only for the addition of the FFD mechanism. The freezing of raindrops without the FFD mechanism turned on was handled separately in RAMS and only allows freezing via contact with existing ice particles.

Implementation of the BR mechanism into RAMS was based on the parameterization from Sotiropoulou et al. (2021). In this scheme, ice breakup was allowed following the collision of ice hydrometeors. In RAMS, this involved collisions of pristine ice, aggregates, and snow, but not graupel and hail. The collisions of pristine ice particles were dependent upon the collection efficiency E_{col}, set to 10%, which is the percent chance that a pristine ice crystal will collect with another pristine ice crystal. The pristine ice crystals that did collect were transferred to aggregates. The remaining 90% of collisions resulted in ice particle breakup. The number of fragments resulting from ice-ice collisions was given by:

$$F_{\text{BR}} = 280(T - 252)^{1.2} e^{-(T-252)/5} \frac{D}{D_o} \tag{4.2}$$

where D was the size of ice crystals fracturing and D_o is 0.02 m. The collection efficiency between pristine ice and snow with aggregates was set to 50 % and also used equation 4.2 for the number of ice fragments produced.

Five RAMS simulations were run to examine the effects of each SIP mechanism on ice formation in a convective cloud (Table 4.1). All simulations initially formed ice via the heterogeneous nucleation of INPs, and subsequent ice formation was allowed to proceed via SIP, depending on which individual mechanism was turned on. A final simulation was conducted with all SIP mechanisms turned on.

4.4. Observational Results

4.4.1 INP Concentrations from SPICULE

INP concentrations measured by the CFDC during the SPICULE campaign ranged from ~0.1 to 100 L^{-1} at temperatures between -19 ºC and -29 ºC (Figure 4.4a), which were in the same range as other INP measurements collected in areas of agriculture harvesting or in a Saharan dust plume (Boose et al. 2016; Suski et al. 2018). There was wide variability in the INP

concentrations during a given RF. However, the ambient out-of-cloud (circles) and in-cloud (diamonds) measurements generally overlap and span nearly the same range in concentrations. This suggests the INPs out-of-cloud were likely being ingested into the clouds.

The timelines of INP concentrations active at temperatures between -13 and -29 ºC collected on the IS filters during SPICULE are shown in Figure 4.4b. The number of INPs active at -25 ºC ranged from ~0.1 L^{-1} to 10 L^{-1} depending on the RF. Interestingly, RFs in which multiple filters were collected, showed up to an order of magnitude difference in the number of INPs at nearly all temperatures. RF02 for example, showed an increase in the number of INPs at -17 ºC from < 0.01 to ~0.2 L^{-1} from the first filter collected to the second. In contrast, the number of INPs at temperatures ≥ -23 ºC from RF08 decreased from the first filter to the second while the number of INPs active below -23 ºC increased between the first and second filter. The variability between multiple filters collected during the same flight may be a result of the aircraft sampling across air mass boundaries (i.e., cold fronts or dry lines). For example, RF08 sampled congestus clouds along a strong cold front as it moved across central Kansas. During that flight, IS filters were collected both behind (NW) and ahead (SE) of the front. The differences may also have been due to differences in the duration of sample collection between filters that leads to varied volumes of air over different spatial regions being sampled. However, the implications of the variability in warm-active INPs (> -20 ºC) represents the determinant factor for the formation of primary ice in the clouds sampled during SPICULE, as all the cloud passes (CPs) analyzed in this study occurred at temperatures > -20 (discussed below).

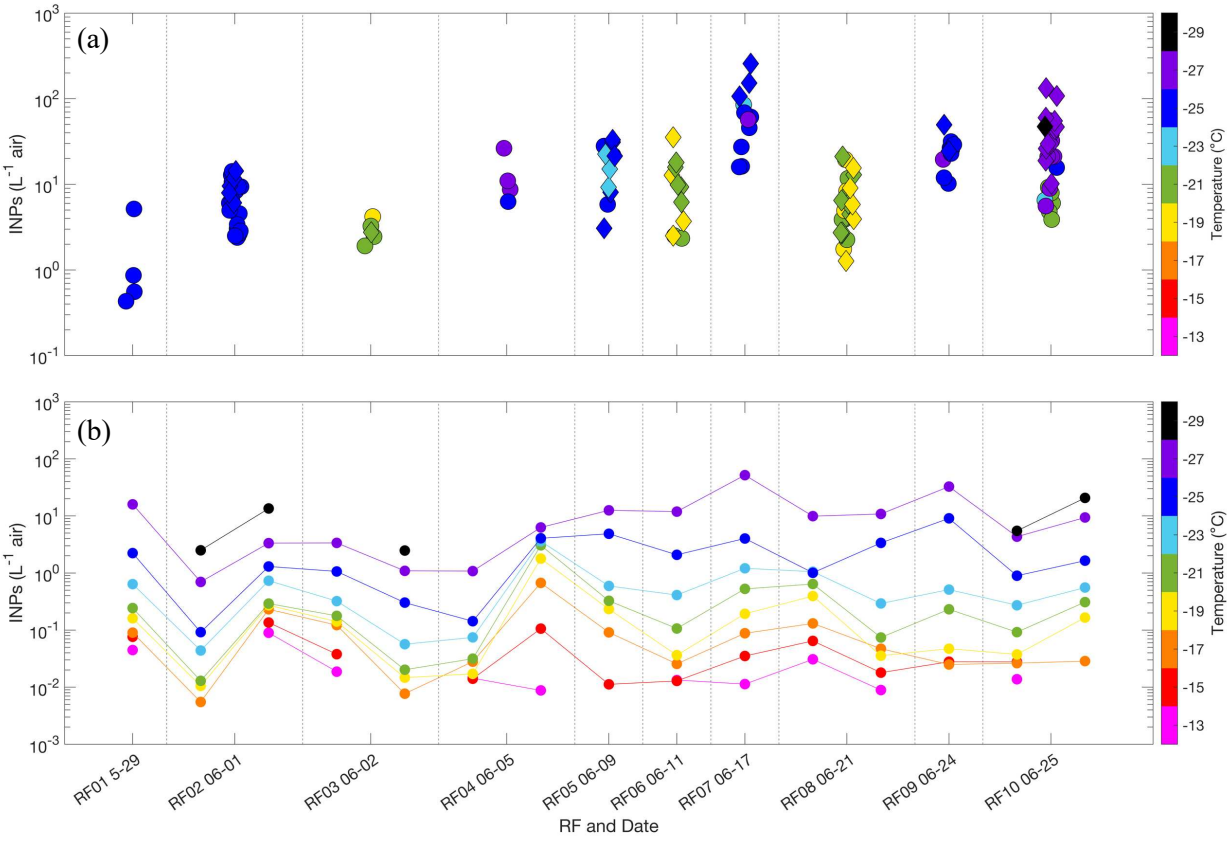


Figure 4.4. SPICULE timeline of INP concentrations collected (a) from the CFDC and (b) on polycarbonate filters and processed with the CSU IS. The marker colors denote the temperature for which the INPs froze. The circles and diamonds in (a) represent CFDC measurements when on the HIMIL and CVI inlets, respectively.

The cumulative spectra of INP number concentrations vs. temperature for all RFs during SPICULE, including both the CFDC and IS measurements, are shown in Figure 4.5. The number concentrations of INPs collected on the IS filters varied by ~2 orders of magnitude for a given temperature over the course of the SPICULE campaign. The CFDC measurements were also 0.5–1 orders of magnitude higher than the IS measurements, especially at temperatures > -25 ºC. This discrepancy between the number concentrations of INPs measured by the IS and CFDC was found in one previous airborne study (Barry et al. 2021a), but was not observed in another (Levin et al. 2019) and may be due to the CFDC measuring INPs at a higher time resolution, thus capturing small-scale variability. However, there was stronger agreement between the CFDC and

IS for colder temperatures < -25 ºC, as was true in all prior airborne studies. The majority of the data from the IS filters fell below the Fletcher (1962) approximation of INP concentrations (black dashed line) and the range of global INP concentrations from Pruppacher and Klett (1997), although those INP measurements were made at the surface. However, the CFDC measurements followed very closely and occasionally exceeded those ranges of INP concentrations. In contrast, the gray shaded region represents the range in airborne INP measurements collected on filters over the U.S. High Plains (Bowdle et al. 1985) and is in good agreement with the IS filter measurements. The IS filters generally followed a log-linear trend, with a few exceptions such as filters from RFs 1, 2 and 4 that showed the highest number of INPs at temperatures > -20 ºC. These filters had modest reductions in the INP activity at temperatures warmer than -20 ºC INPs when heat treated (Figure A3.4), indicative of the presence of biologic INPs. However, the remainder of INP spectra suggested a strong presence of dust-type INPs during SPICULE. A similar trend in INP spectra was observed for glacially (Tobo et al. 2019) and Saharan (Price et al. 2018) sourced dust particles. While the full range in INP variability could not be captured by a single exponential fit, as shown by the range in INP concentrations used for the Fletcher (1962) and Bowdle et al. (1985) approximations. The application of the D15 parameterization to represent the observed data, as introduced earlier in Figure A3.2, best captured the upper limit of the IS measurements and more generally agreed with the CFDC measurements, which was used for definition of the ice nucleation processes (discussed below).

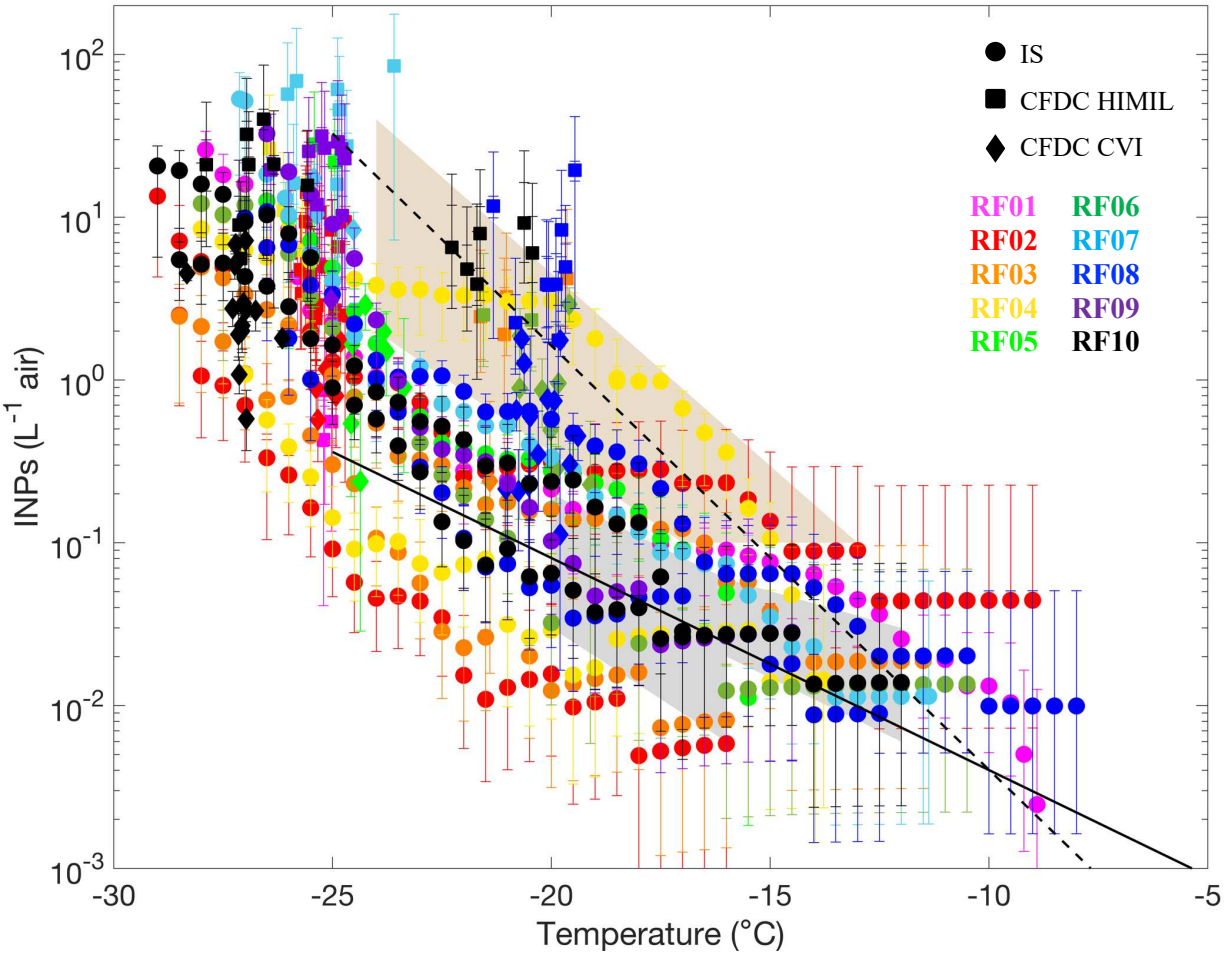


Figure 4.5. INP number concentration versus temperatures for the IS (circles) and CFDC when sampling on the HIMIL (squares) and CVI (diamonds) and colored by the research flight. Errors bars represent the 95% confidence intervals. The black dashed line represents the INP approximation from Fletcher (1962) and the tan shaded region represents the range in global INP concentrations from Pruppacher and Klett (1997). The solid black line and gray shaded region represent the modified INP approximation and range in INP measurements from Bowdle et al. (1985), respectively.

4.4.2 Aircraft Cloud Passes and Estimating Ice Concentrations

As mentioned previously, the Learjet and GV flew in coordination during SPICULE in order to capture the warm- and cold-phase regions of developing cumulus congestus clouds. The observational strategy is depicted in Figure 4.6. To determine whether primary nucleation or SIP were occurring in the young ascending updrafts, paired CPs between the two aircraft were selected based on three criteria: 1) a Learjet CP occurred within five minutes of a GV CP during

which a CFDC measurement on the CVI inlet was collected, 2) the horizontal distance between the two aircraft at the time of their respective CPs was < ~4 miles and 3) CPs were in an actively growing region of the cloud. This ensured the two aircraft were sampling the same cloud regions at roughly same time, with the assumption that the aerosol and INP measured from the GV would be transported vertically in the convective clouds as depicted in Figure 4.6. Isolating CPs that were defined as actively growing was intended to capture the onset of primary nucleation or SIP at the time of measurement. This was also done to minimize the contamination by ice crystals that may have nucleated previously at other vertical levels and settled into the CP region. Defining a cloud to be in a growth stage was accomplished by analyzing the radar velocities from the KPR and using visual images of the clouds from the Learjet forward- facing flight videos (Figure 4.7 and 4.8 a and b). If the clouds did not feature active updrafts or visually crisp cloud edges, or contained noticeable downdrafts, the CP data did not meet the criteria for inclusion. A total of 26 Learjet CPs from six research flights met these criteria. However, six of these CPs were later excluded as the estimated ice concentrations were below the detection limit (discussed below) and occurred at a temperature warmer than the warmest CP containing ice (-10 ºC, Table 4.2). CPs that occurred at lower temperatures (< -10 ºC) but did not include any ice particles were retained as no-ice cases. The aircraft flight information during the CPs used for this analysis is shown in Table 4.2, and Figure 4.1 denotes the geographical areas in which the CPs used in this study were sampled during each flight.

Table 4.2. List of aircraft flight information for the cloud passes from the Learjet and ***GV*** used in this study.

RF & CP#	Pass time (UTC)	Altitude (m)	Latitude	Longitude	Lear Temp (ºC)	Pass width (m)	Ice?
2.1	18:45:10, ***18:44:10***	5610.6, ***2791.2***	38.60, ***38.618***	-102.003, ***-101.966***	-15.7	1180	y
2.2	18:52:45, ***18:53:55***	5773.7, ***4049.7***	38.658, ***38.642***	-101.940, ***-101.975***	-16.4	456.6	y
2.3	18:55:20, ***18:53:55***	5981.2, ***4049.7***	38.657, ***38.642***	-101.938, ***-101.975***	-17.8	781.1	y
2.4	19:00:30, ***18:58:36***	5483.8, ***4360.6***	38.65, ***38.68***	-101.948, ***-101.945***	-13.5	999.95	y
5.1	21:38:00, ***21:37:44***	5766.3, ***3582.2***	45.09, ***44.918***	-98.860, ***-98.859***	-10	1616	y
5.2	21:49:30, ***21:52:51***	6566.5, ***4823.6***	45.0, ***44.831***	-98.931, ***-98.824***	-15.3	1090.67	y
5.3	21:58:20, ***21:59:08***	6163.9, ***3699***	45.01, ***44.930***	-98.910, ***-98.808***	-12.8	1094.87	y
6.1	19:59:35, ***19:58:05***	5997.7, ***2659.3***	38.567, ***38.637***	-96.951, ***-96.899***	-10.7	1156.16	y
6.2	20:40:50, ***20:40:35***	6602.3, ***2247.1***	39.47, ***39.17***	-96.770, ***-96.913***	-16.9	1688.5	y
6.3	20:47:20, ***20:46:10***	5994.5, ***2247.0***	39.659, ***39.534***	-96.654, ***-96.699***	-11.1	991.62	n
8.1	19:59:55, ***22:01:25***	6333.4, ***2260.2***	40.097, ***39.941***	-95.330, ***-95.473***	-12.8	849.9	y
8.2	22:06:45, ***22:05:33***	6396.7, ***3552.1***	39.959, ***39.987***	-95.331, ***-95.445***	-13.3	922.74	n
8.3	22:10:40, ***22:12:02***	6823.3, ***2363.2***	39.956, ***39.940***	-95.320, ***-95.279***	-17.3	1128.68	y
8.4	23:34:30 ***,23:32:55***	7134.2, ***2929.4***	38.639, ***38.923***	-96.316, ***-95.880***	-16.4	956.34	y
8.5	23:41:10, ***23:40:20***	7023.6, ***3092.5***	38.373, ***38.582***	-96.66, ***-96.243***	-17.3	504.84	n
9.1	22:14:05, ***22:14:23***	6131.80, ***4843.7***	37.010, ***36.973***	-101.085, ***-101.075***	-10.3	1948.44	y
9.2	22:16:40, ***22:18:38***	6118.6, ***4845.8***	37.020, ***37.019***	-101.067, ***-101.056***	-10.4	1554.1	y
10.1	21:33:50, ***21:32:48***	6663.3, ***4371.1***	36.140, ***36.058***	-102.3475, ***-102.413***	-11.7	493.44	n
10.2	21:34:38, ***21:35:03***	6730.7, ***4518.0***	36.130, ***36.162***	-102.246, ***-102.244***	-12.2	1110.9	y
10.3	21:52:30, ***21:51:41***	6989.8, ***4371.1***	36.050, ***36.162***	-102.600, ***-102.396***	-15.4	455.04	y

The CPs from the Learjet used in this study were between ambient temperatures of -10 ºC and -20 ºC (Table 4.2). In this temperature range, the low ice number concentrations may produce erroneous cloud probe data due to limitations in small sample volumes and difficulties distinguishing liquid from ice hydrometeors using automated methods. Therefore, 1-Hz cloud probe data of ice concentrations are untrustworthy without careful inspection of the imagery from various instrumentation. Instead, newer methods have been developed to phase separate the total concentrations of liquid- and ice-phase hydrometeors measured by the cloud probes. In this study, N_{ice} during CPs was estimated using methods developed by SPEC Inc. (Lawson et al. 2015, 2017). Composite size distributions for the complete size range of hydrometeors (2 μm to several millimeters) were first constructed from the FCDP, 2DS, and HVPS probes (Figure A3.5). The composite size distribution was then deconstructed by specifying a fraction of the total concentration in each size bin in the distribution to be either liquid or ice, creating two distinct but overlapping size distributions for the liquid and ice phases. The fractions of liquid and ice were determined by visually inspecting the CPI and 2DS cloud images (Figures 4.7 and 4.8 c and e). Both imaging probes were required for this analysis because the CPI images provided the highest-resolution imaging of the cloud hydrometeors, but were limited to a smaller sample volume and may under-sample ice particularly when concentrations of ice are low or when concentrations of liquid droplets are high, which was the case for SPICULE. The 2DS, on the other hand, has a much higher sample volume and provided better imaging during occurrences of low ice crystals concentrations but the 2DS does not provide high-resolution images of individual hydrometeors, making identification of small ice crystals challenging. The smallest ice crystals that were identified were ~50 and 100 μm from the CPI and 2DS, respectively, therefore under-sampling of small ice crystals at short times after nucleating was

possible. However, because the median effective radius of cloud droplets during all the CPs was 14 µm, and the growth rates of ice crystals at -20 ºC can be up to 2.5 µm/s (Bailey and Hallett 2004, 2012), newly formed ice particles would only require 15–35 s to reach sizes that would be interpretable cloud images. The estimated ice concentrations were calculated by integrating the ice-phase size distribution and represented the total ice concentration for that CP, as shown by Figures 4.7d and 4.8d. The minimum ice concentration estimated from all the CPs was 0.01 L^{-1} and occurred during RF08 CP1 at -12.8 ºC, representing the lower detection limit for this method. As mentioned above, there were six CPs that occurred at temperatures > -10 ºC where no ice crystals were observed. However, the INP concentrations at temperatures > -10 ºC were generally < 0.01 L^{-1} (Figure 4.5), therefore, it may be the case that there were very small concentrations of ice, but this method was not sensitive enough to detect the very few ice crystals that may have been present.

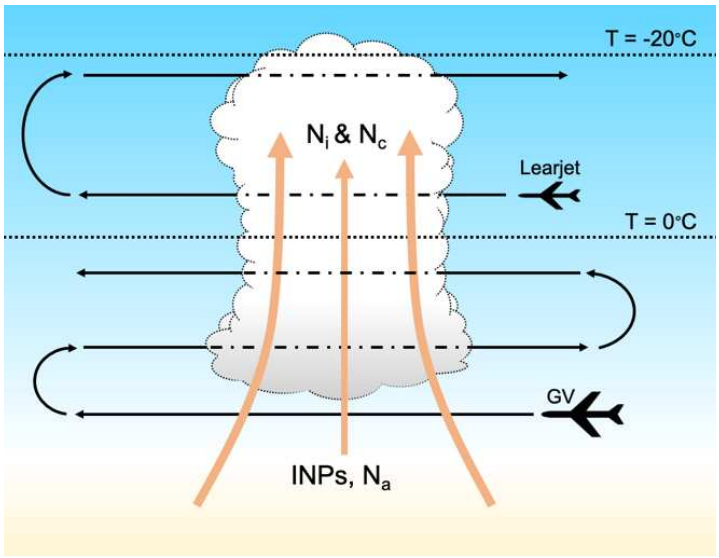


Figure 4.6. Diagram of aircraft coordination during SPICULE. The time cycle of the sampled clouds is not depicted in this diagram. In reality, the Learjet followed the cloud tops as they ascended to progressively lower temperatures.

For each CP in this analysis, a multiplication factor (MF) was calculated to determine the dominance of primary or secondary ice formation:

$$\mathrm{MF} = \frac{N_i}{\mathrm{upper}(N_{INPs})_{\mathrm{T}}} \tag{4.3}$$

where N_i is the estimated ice particle number concentration for a particular CP and upper$(N_{INPs})_T$ represents the upper uncertainty limit of the number of INPs at the temperature of the cloud pass determined from the INP spectrum (Figure 4.7f and 4.8f). The full INP uncertainties (shaded tan regions in Figures 4.7f and 4.8f) were based on the INP concentrations from both the IS filters and the in-cloud CFDC measurements for each CP. In addition, if a CFDC measurement exceeded the number of INPs from any IS INP measurement at a particular temperature, a best fit line was calculated for the IS measurements < -20 ºC and the INP uncertainty was then shifted up to the upper limit of the highest CFDC measurement (Figure 4.7f, for example). The INP uncertainties from RFs 5, 8, 9, 10 are shown in Figure A3.6. If the MF was ≤ 1 for a particular CP temperature, the number of ice crystals formed was less than the number of INPs and is indicative of ice formation via primary nucleation mechanisms. However, if the MF was > 1, the number of ice crystals exceeded the number of INPs and indicated SIP were active.

4.4.3 Observations of Primary Nucleation and SIP

Figure 4.7 shows an example CP from RF02 for a cloud pass temperature (T_{CP}) of -16.4 ºC and an estimated T_{CB} of 9 ºC. The Learjet penetration occurred within a few hundred meters of cloud top and encountered modest updrafts of ~4 m/s, and visually the cloud showed signs of growth with crisp and billowy cloud edges (Figure 4.7a and b). The estimated ice concentration in the cloud pass was 0.1 L^{-1}, while the number concentration of INPs at the temperature of the CP shown in Figure 4.7 was ~0.5 L^{-1}, resulting in a MF of ~0.2. This CP was classified as a case of ice forming through primary nucleation only. The CPI images indicated a few pristine ice crystals and larger aggregates along with many small cloud droplets, with the largest cloud droplets only ~ 150 µm. These observations of smaller cloud droplets supported the

hypothesis that lower T_{CB} (or higher cloud base) leads to smaller droplets and a suppression of FFD (Lawson et al. 2017). The very large ice crystal captured by the CPI showed signs of riming of the very small cloud droplets. The 2DS also observed only a few ice crystals and even fewer large droplets, and images were dominated by very small cloud droplets (Figure 4.7c). These conditions would normally meet the criteria for HM if the CP occurred at warmer temperatures (-8 to -3 ºC). However, with weaker updrafts, it was inferred that the few ice crystals that had formed at lower temperatures had not yet sedimented into the warmer supercooled temperatures where HM would have been active. Lawson et al. (2023) had a similar observation of only three ice crystals during a CP at -17.8 ºC, but did not estimate the ice concentrations during that CP. However, it is likely the number of ice crystals would also have been < 1 L^{-1} since RF08 CP1 contained more than three ice crystals and was the minimum ice concentration detected. This gives confidence in the classification of primary nucleation for this particular CP.

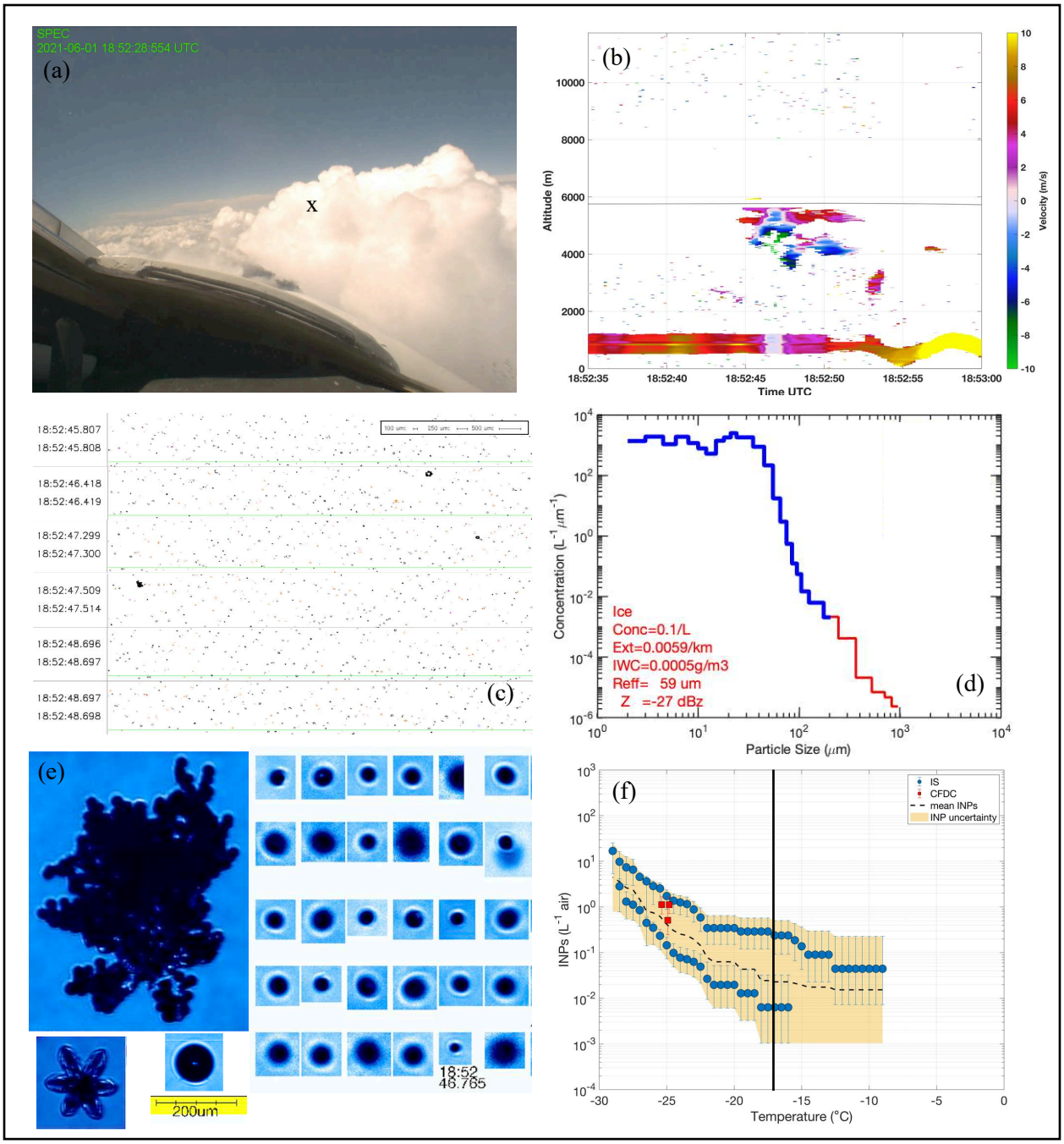


Figure 4.7. Observations from RF02 CP2 at -16.4 ºC showing (a) snapshot from the Learjet flight videos of the cloud before penetration, (b) radar velocities from the KPR and the flight altitude of the Learjet (black line), (c) 2DS images, (d) phase-separated size distribution of ice (red) and liquid (blue), (e) CPI images, and (f) INP concentrations from the IS (blue markers) and CFDC (red markers) and the INP uncertainty (shaded tan region) for a given temperature. The average INP concentrations are shown by dashed black lines in (f) and the black solid line denotes the CP temperature.

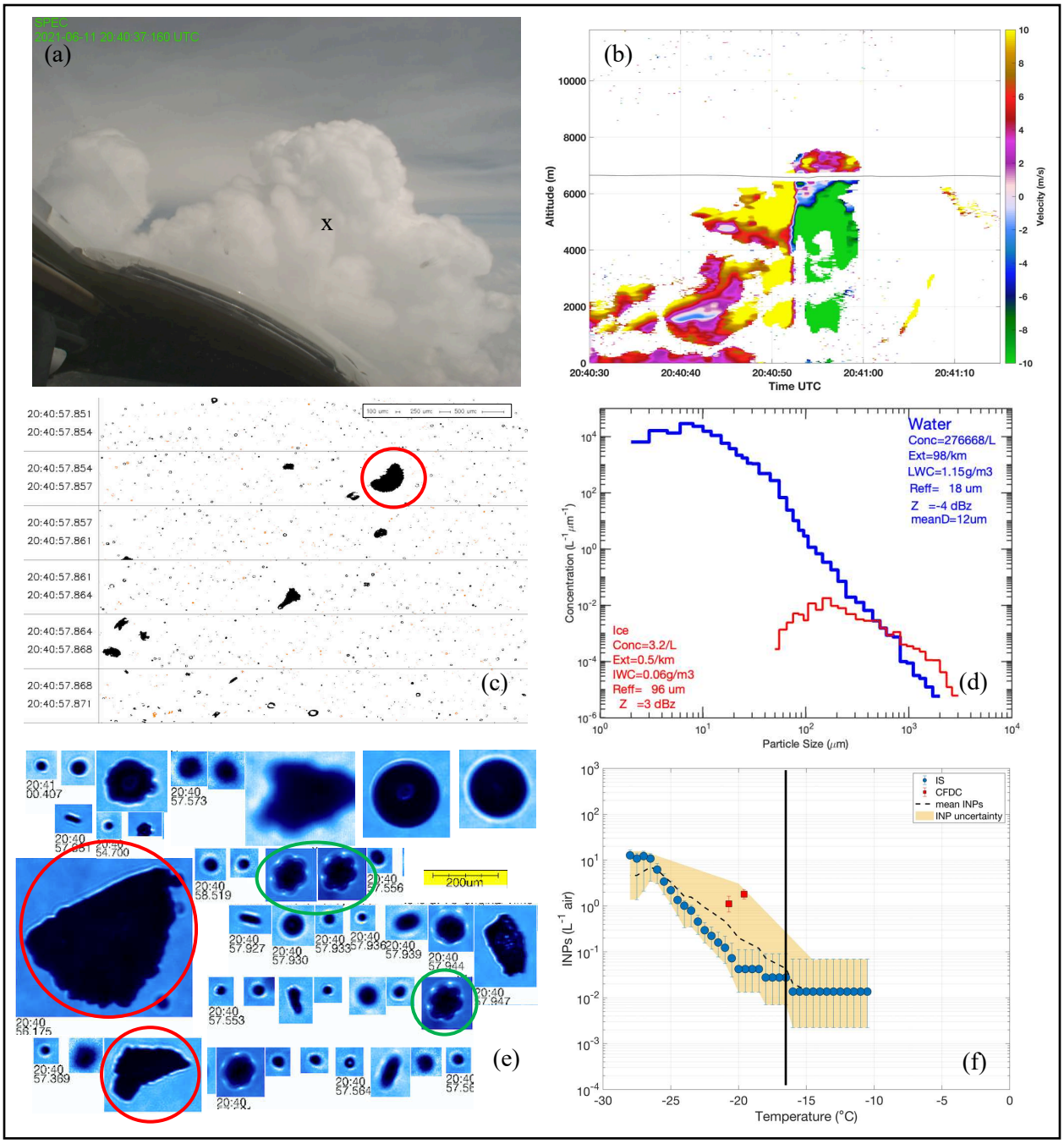


Figure 4.8. Similar to Figure 4.7 but for RF06 CP2 at -16.9 ºC.

Figure 4.8 shows another example CP that occurred during RF06 with a T_{CP} of -16.9 ºC and an estimated T_{CB} of 20 ºC, which would lead to a low cloud base and a deep warm phase region. Differences between this CP from the example shown in Figure 4.7 were 1) this CP occurred several hundred meters below the cloud top and 2) updrafts were very strong, with a

peak vertical velocity of 19 m/s. The estimated ice concentrations were 3.2 L^{-1} compared to an ice concentration of 0.56 L^{-1} producing a MF of 5.7. Therefore, this CP was classified as a case where SIP was active. Based on the phase-separated size distribution, cloud droplets during this CP reached sizes > 1 mm, which was likely a result of the much warmer T_{CB} and increased time for collision-coalescence processes. There were also higher concentrations of droplets (N_c) during RF06 CP2 compared to RF02 CP2 (606 and 283 cm^{-3}, respectively). The difference in altitudes between two aircraft (ΔH), a proxy used for the depth of the cloud, was ~4400 m compared to ~1800 m for RF02 CP2, further indicating the likelihood of additional coalescence processes. The 2DS and CPI images showed large ice crystals and aggregates as well as large cloud droplets > 200 μm. The green circled ice crystals in Figure 4.8e were pristine ice crystals formed from primary nucleation, while the red circled ice crystals in Figures 4.8c and 4.8e originated from fragmented frozen droplets, similar to images from Lawson et al. (2023). In addition, there were also examples of small needle-like ice crystals that may be spicules or fragments from FFD, or possibly ice crystals formed via HM at lower altitudes and lofted to colder temperatures. It appeared likely that the formation of the much higher concentrations of ice crystals compared to RF02 CP2 (Figure 4.7) was a result of SIP via the FFD mechanism but, we cannot discount the possibility that the fragmented ice crystals may also indicate contamination of ice crystals from other vertical levels, possibly from the HM mechanism. It was also unlikely that high concentrations of ice crystals would sediment from above, given the strong updrafts.

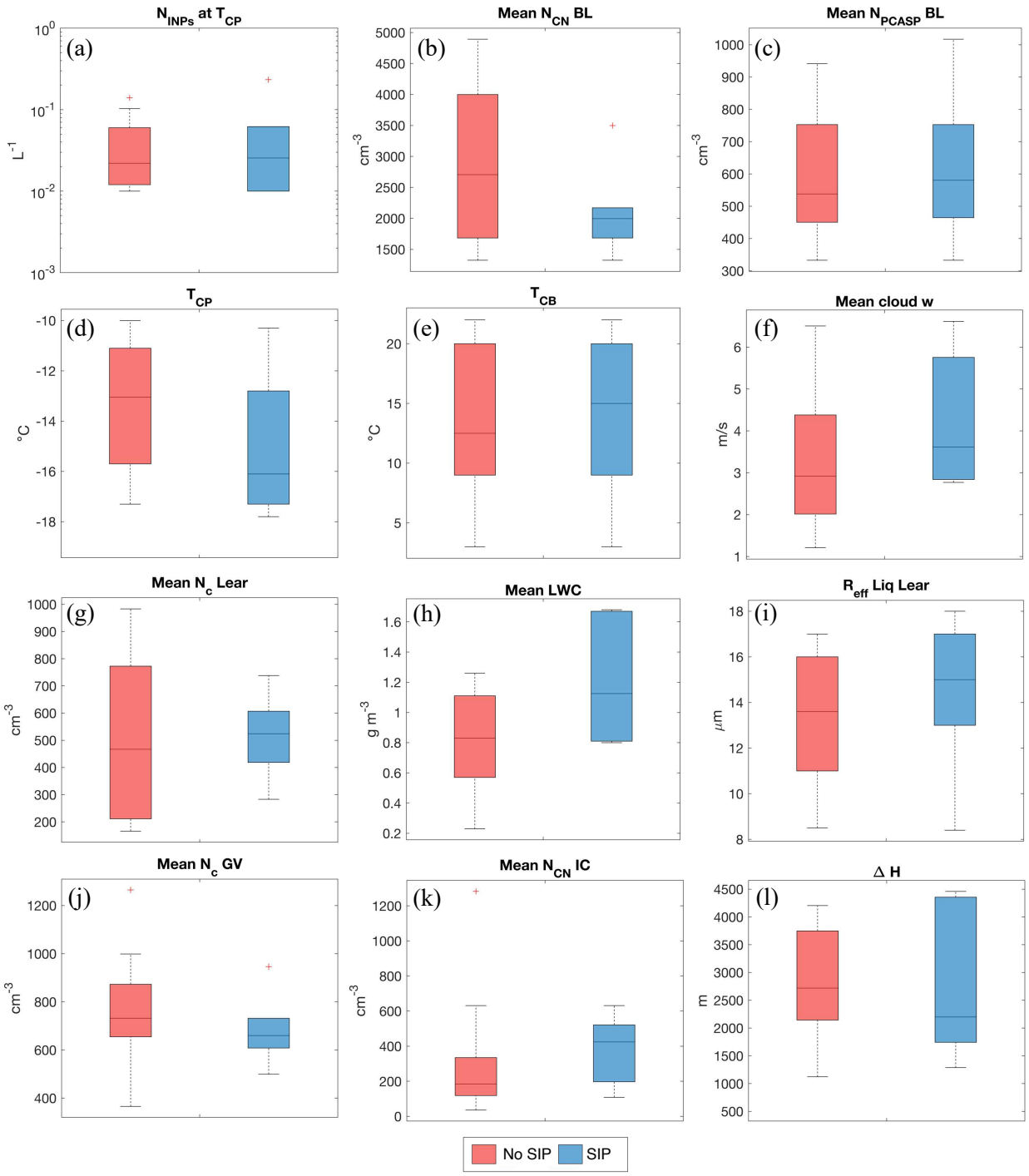


Figure 4.9. Boxplots and whiskers for cases of no SIP (red) and SIP (blue). The no SIP includes both CPs classified as no ice and primary nucleation. Panels a–c denotes the number of INPs at the cloud pass temperature (T_{CP}), boundary layer (BL) aerosol concentrations from the CN counter and PCASP, respectively, and were collected on the GV. The mean vertical velocity between the two aircraft is shown in (f). Panels g-i denote microphysical properties and were observed by the Learjet instrument package and represent a CP average. The mean number

concentration of cloud droplets (N_c) and nuclei (N_{CN}) when in-cloud (IC) are denoted by (j) and (k) and were observed on the GV. The difference in the sampling altitude between the two aircraft (ΔH) is shown in (l).

The cloud microphysical properties, aerosol and INP concentrations, and environmental conditions are summarized statistically in Figure 4.9, distinguishing cases with and without SIP. All of the CPs in Table 2 were analyzed similarly to the approach in the examples shown in Figures 4.7 and 4.8. The mean values reported in Figure 4.9 were also only calculated for in-cloud conditions and when updrafts were occurring (vertical velocity > 0). Figures 4.9 a–c and j–k show aerosol and INP concentrations and N_c for each ice category collected aboard the GV, while the rest of the panels show cloud microphysical and environmental conditions that were observed by instrumentation aboard the Learjet (Figure 4.9 d–e and g–i), or averaged between the two aircrafts (Figures 4.9 f and l). The color of each boxplot indicates the ice formation category based on the MF described above, as either no SIP or SIP. Of the 20 CPs analyzed, nine were classified as primary nucleation, seven were classified as SIP, and in four of the CPs no ice particles were observed. Therefore, no SIP includes both the no ice and primary nucleation CPs. The mean N_{CN} and N_{PCASP} (Figure 4.9 b and c) represent the mean aerosol concentrations from the CN counter and PCASP, respectively, collected during BL segments that occurred shortly before or after the CPs, to best estimate the aerosol distributions that would have been ingested into the clouds. The rest of the microphysical properties or environmental conditions represent an average value across the CP, with the exception of the T_{CB} which was determined from the Learjet flight notes. Finally, the N_{CN} shown in Figure 4.9k represents the in-cloud (IC) mean, and were observed at the same time as the INP measurements shown in Figure 4.9a.

There was little variability (< factor of ten) in the number of INPs at the T_{CP} for the no-SIP category, while the SIP category showed slightly higher median number of INPs (Figure 4.9a). This may be a result of the SIP category having a lower median T_{CP} (Figure 4.9d), but it is

an important point that the SIP classification was not merely a result of lower INP numbers at the T_{CP} that led to higher MF. The SIP cases had a higher median effective radius (R_{eff}) of liquid droplets and also a higher median T_{CB} than the no SIP CPs. The mean cloud vertical velocity, calculated as the mean updraft speed from both aircraft, was also higher for the SIP cases. Although the median ΔH (Figure 4.9l) was lower for the no-SIP cases, the SIP cases generally showed higher overall depths. The median N_c from the GV was lower for the SIP cases but had a slightly higher median N_c from the Learjet for the SIP cases. However, overall the highest N_c values from the Lear occurred in the no-SIP cases. Additionally, the median N_c was lower from the Learjet than the GV for both cases, likely a result of the coalescence processes. These results suggest that a higher T_{CB} deepened the warm-phase region of the cloud, leading to larger cloud droplets, and may have been aided by a more vigorous updraft. This corroborates previous findings on the dependence of large, supercooled droplets on the T_{CB} (Lawson et al. 2022, 2023) and suggests FFD as the dominant SIP mechanism in these cases due to the presence of larger droplets and T_{CP} well outside of the HM temperature range (-8 to -3 ºC).

Interestingly, there was a higher median BL N_{CN} for the no SIP cases compared to the SIP, but the opposite was true for the N_{PCASP}. Although CCN concentrations were not directly measured during SPICULE, the number of CCN would likely fit somewhere between these two measurements, since the PCASP only measured aerosols > 100 nm, likely missing some smaller aerosols that may have acted as a CCN for the expected supersaturations present in convective updrafts (>1 %). However, since the CN counter measured particles down to ~11 nm, it likely overestimated the number of particles that may have served as CCN. While the median BL N_{PCASP} was very similar between the no SIP and SIP cases, the SIP cases showed a slightly higher median value than the no SIP cases. The median IC N_{CN} measured in the GV was also

slightly higher for the SIP cases. The higher (lower) mean N_c from the GV for the no-SIP (SIP) cases agrees with the mean BL N_{CN} but not with the IC N_{CN} or BL N_{PCASP} providing uncertainty in the role of aerosols on the formation of cloud droplets and subsequently, SIP. The very high BL N_{CN} but lower mean IC N_{CN} for the no-SIP cases may be interpreted as the CVI was not able to capture the full cloud droplet distribution, or that the IC N_{CN} did not fully represent the aerosol concentrations that were seeding the clouds, since the N_c from the GV was also higher for the no-SIP cases. But this does suggest that the BL N_{CN} may provide some indication towards the CCN concentrations. Therefore, these results suggest that higher aerosol concentrations may have promoted smaller and more numerous cloud droplets and could have suppressed the onset of SIP. Despite this finding, the depth of the warm region of the clouds, a function of T_{CB}, and the updraft strength both appeared to be more important factors than aerosol concentrations in the formation of large liquid droplets at a given cloud pass temperature, and subsequently enhanced the probability of the occurrence of SIP.

4.5 Evaluation of SIP Mechanisms in RAMS

Vertical profiles of N_{ice} from the RAMS simulations are shown in Figure 4.10. The N_{ice} from RAMS represent an in-cloud horizontal average for updrafts > 1 m s^{-1} at each vertical level and were calculated at the first timestep when there was ice present at a temperature < -22 ºC. This criterion ensured the simulated cloud was present through a temperature of -20 ºC, similar to the SPICULE CPs. Additionally, the T_{CB} was 16.5 ºC, the mean updraft speed of the 3.5 m s^{-1} and the cloud base droplet number concentration was ~400 cm^{-3}, which were all also representative of the clouds that were sampled during SPICULE (Figure 4.9). At temperatures < -10 ºC, N_{ice} from the primary nucleation only (PR-only) simulation (Figure 4.10a, solid black line) was a factor of 2–5 lower than the predicted number of ice crystals from D15 (Figure 4.10a,

dashed black line) but were in better agreement near -5 ºC. The observed number concentrations of ice crystals from the CPs classified as primary nucleation (yellow diamonds) followed closely with the D15 line around -15 ºC but were ~5 times higher around -10 ºC. The difference between the N_{ice} from RAMS and the D15 predicted line was likely due to ice crystal aggregation, evaporation due to entrainment, and sedimentation. The cloud microphysical properties for the simulations with SIP turned on (discussed below) were similar to those for the no-SIP cases. Therefore, the conditions favorable for SIP to be active were present during the no-SIP simulation and would have likely initiated SIP had they not been turned off.

The vertical profiles from the RAMS experiments with each SIP mechanism turned on produced N_{ice} that exceeded the number concentrations of ice crystals predicted by the D15 scheme for each SIP mechanism, with the exception of the simulation with BR turned on (Figure 4.10c). In fact, the BR simulation (Figure 4.10c, red line) produced N_{ice} that closely resembled the results from the PR-only simulation, likely because concentrations of ice and aggregates were so low that they did not collide at sufficiently high rates to make meaningful amounts of secondary ice crystals at these timescales. Whether the BR simulation would produce higher N_{ice} if the cloud were allowed to reach a deeper and more mature stage, as shown in prior work in which a longer cloud life cycle was considered (Waman et al. 2022; Yano et al. 2016), is of interest but is beyond the scope of this study. The simulation with HM turned on (Figure 4.10c, green line) produced N_{ice} 1–2 orders of magnitude higher than the PR-only case, especially at temperatures between -10 ºC and -20 ºC, and generally predicted N_{ice} about a factor of 2–5 less than the observations. Similar to BR, the FFD simulation produced N_{ice} that were only slightly higher than the PR-only simulation and were well below the SPICULE SIP cases at all temperatures, suggesting it is less important than the HM mechanism at early stages of ice

development. The All-SIP simulation very closely followed but exceeded the HM simulation, suggesting HM was the most important SIP mechanism in the early stages of a convective cumulus cloud. In general, the All-SIP agreed well with the observations, and produced slightly higher ice concentrations compared to the HM, suggesting that without contributions from the FFD and BR mechanisms, the model would underpredict ice concentrations at this stage in cloud development. The peak at -5 ºC is likely caused by the active HM process as it only occurred in the HM and All-SIP simulation.

The results described above remained consistent when allowing the cloud to grow further as shown in Figures 4.10b and 4.10d, which show the vertical profiles of the same cloud two minutes later, when the cloud top reached temperatures below -30 ºC. The main difference between Figures 4.10c and 4.10d are that the All-SIP simulation produced higher concentrations of ice at warmer temperatures (> -10 ºC), likely a result of more active HM processes, as ice concentrations in the HM simulation were also higher at these temperatures. These results confirm the findings in Waman et al. (2022) that the HM mechanism appears to play the strongest role in ice crystal enhancement in the early stages of cloud development, but the FFD and BR mechanisms also produce additional contributions that resulted in improved representation of ice crystal number concentrations in RAMS.

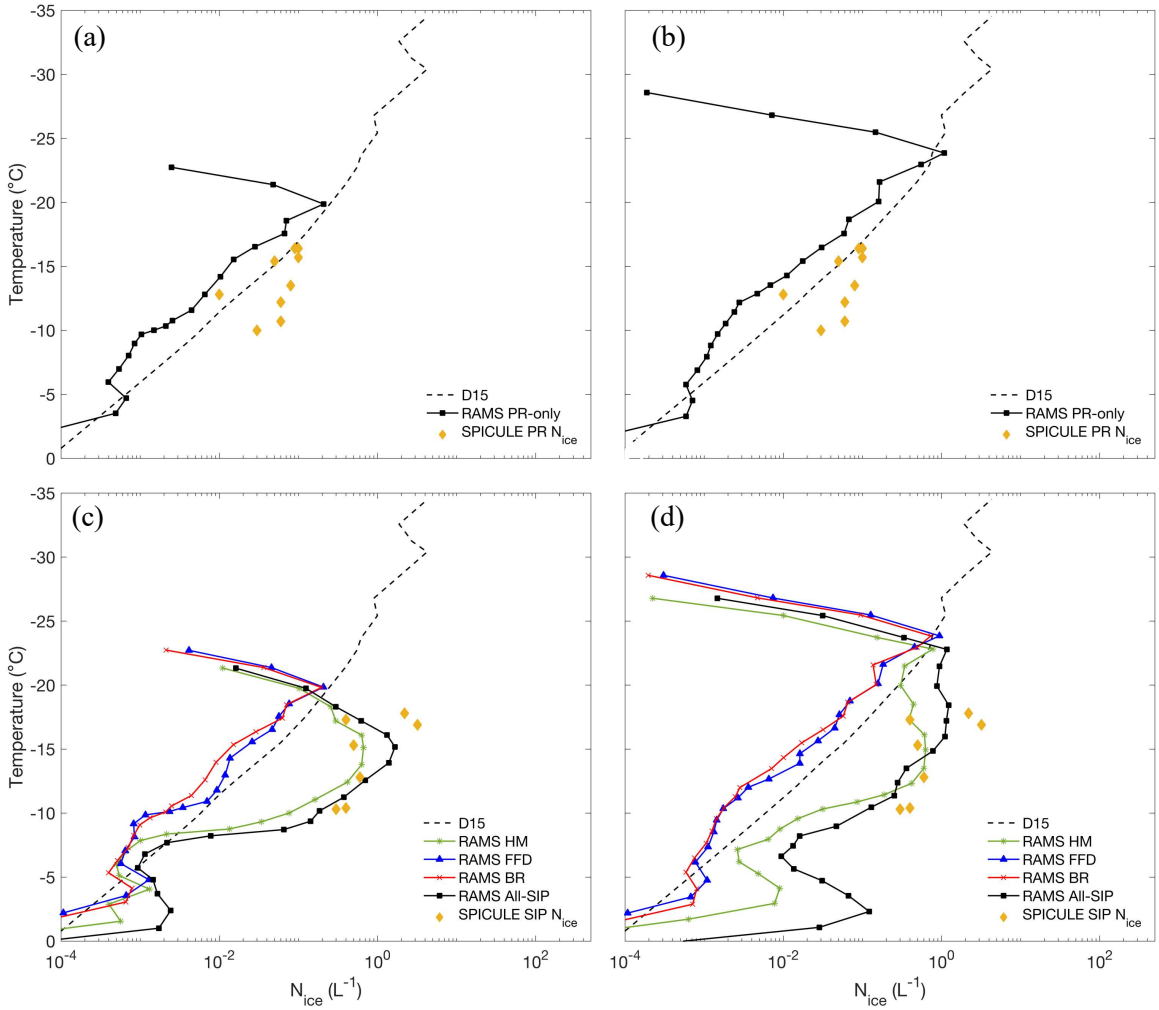


Figure 4.10. Simulated vertical profiles of ice crystal number concentrations (N_{ice}) versus temperatures for RAMS simulations of (a and b) primary nucleation only and (c) various SIP mechanisms turned on. The black dashed line in (a) denotes the number of ice crystals predicted by the DeMott et al. (2015) parameterization based on the number of aerosols initialized in RAMS (Figure 4.3b). The yellow diamonds denote the estimated number of ice crystals from SPICULE for cases of (a) primary nucleation and (c) SIP. The profiles shown in (b) and (d) are the same as (a) and (c) but for two minutes later in the simulations.

4.6 Summary and Conclusions

In situ observations of aerosol and INP concentrations, cloud microphysical properties, and environmental thermodynamic and dynamic conditions collected aboard the GV and Learjet aircraft during the SPICULE campaign are reported in this study. A major advancement in the SPICULE study design was the inclusion of coincident measurements of INP (below and in-

cloud) and ice crystal number concentrations in developing cumulus congestus clouds. These concurrent measurements allowed classification of CPs based on the inferred mechanism of ice formation, in turn enabling detailed analysis of the cloud microphysical properties and thermodynamic and dynamic conditions favorable for primary nucleation or SIP. Model simulations of an ascending cumulus congestus cloud provided additional clarity on the order of ice formation mechanisms active in these clouds during the early stages of development.

The results presented herein are some of first airborne INP measurements over the U.S. Central Great Plains in nearly 40 years and showed the wide variability in the number of INPs that can occur over a relatively short period of time and wide geographical area. The inclusion of the CVI upstream of the CFDC allowed for in-cloud INP measurements. The IS filters and the majority of the out-of-cloud CFDC measurements were collected in the BL with the intent of sampling the aerosols that were ingested into the clouds. INP measurements from the CFDC closely followed with global INP concentrations, while the IS measurements showed remarkable agreement with airborne filter measurements of INPs from a previous study over the U.S. High Plains (Bowdle et al. 1985). High concentrations of INPs from the IS filters during the first four flights at temperatures > -15 ºC and subsequent reductions after heat treatments provided some indication of biological-type INP activity during this period. Later in the campaign (after RF05), there was less influence of biological INPs and likely a stronger presence of dust INPs based on the steepness of the INP spectra below -20 ºC (Tobo et al. 2019; Price et al. 2018).

We present observations of N_{ice} in ascending cumulus congestus clouds that showed evidence of ice formation through primary nucleation and SIP. All of the CPs analyzed in this study occurred at temperatures below -10 ºC. As mentioned, there were six Learjet CPs that were not included as they did not show resolvable ice crystal concentrations present at temperatures >

-10 ºC. It was possible there were ice crystals forming via primary nucleation at these temperatures but were below the detection limit of the methods used for estimating ice concentrations ~0.01 L^{-1}, especially since the number of INPs at temperatures between -5 ºC and -10 ºC were between 0.01 L^{-1} and 0.001 L^{-1}. This is the temperature range where the HM mechanism has been shown to be active (Hallett and Mossop 1974), however if HM were active, it is likely ice concentrations would have exceeded the detection limit and would have shown ice crystals during the warmer temperature CPs. We also did not observe significant proportions of needle or small columnar crystals, which are indicative of HM (Pruppacher and Klett 1997), but rather more large and irregularly shaped aggregates. Therefore, the observations suggest that the HM mechanism was less of a contributor to total ice concentrations at the stages of the cumulus congestus clouds that were observed during SPICULE. Instead, the CPs classified as SIP cases showed higher T_{CB}, vertical velocities, and R_{eff} of cloud droplets and occurred at temperatures between -10 ºC and -20 ºC. These observations suggest the depth of the warm-phase region of clouds promotes collision-coalescence processes as described in Lawson et al. (2022). Additionally, the presence of larger cloud droplets met the criteria for the fragmentation of cloud droplets upon freezing (Keinert et al. 2020; Korolev and Leisner 2020; Lauber et al. 2018; Lawson et al. 2022). Therefore, the observations presented here provide evidence that the FFD mechanism was likely active and played an important role in the enhancement of N_{ice} during the early stages of cumulus congestus clouds.

The influence of aerosols and INP concentrations on SIP was also examined in this study. There were competing results when comparing the BL and IC N_{CN} to the N_c from the GV. This was attributed to a potential bias in the CVI sampling a higher proportion of the cloud droplet distribution when the aerosol loading was lower as was the case for the SIP cases. The no-SIP

cases had higher BL N_{CN} and N_c, which may indicate the BL N_{CN} was more representative of the aerosols concentrations that seed the clouds. This provides evidence that the higher aerosol concentrations lead to more numerous and smaller cloud droplets during the no-SIP cases. This enhancement of aerosol and cloud droplet number concentrations may have led to weaker coalescence and cloud droplet growth, shown by the smaller R_{eff} for the no-SIP cases, and suppressed the onset of SIP. The impact of INPs on the formation of SIP was less clear. While the SIP cases showed higher INP concentration than the no SIP cases, this is more likely due to the SIP cases occurring at lower T_{CP}. It may be possible that the presence of higher numbers of warm-active INPs such as biological INPs could initiate SIP mechanisms, such as HM or FFD, at warmer temperatures. However, in this study, the lack of warm-active INPs likely delayed ice formation until the clouds ascended to colder temperatures. Thus, there must be a time element to consider for the formation of SIP, that longer timescales and deeper clouds reaching colder temperatures promoted higher INP activation at the lower temperatures, and increased probability of FFD.

Numerical model simulations of an ascending and early-stage cumulus congestus cloud produced N_{ice} in the same range of the observed SIP CPs, driven primarily by the HM mechanism and minor contributions from the FFD and BR mechanisms. Previously RAMS had only included HM, however it has been shown in this study that ice concentrations are in better agreement with observations when FFD and BR are included. These findings agreed with the findings of Waman et al. (2022), who argued HM contributed over 90 % of the ice crystals in the first 5–10 minutes of cloud evolution as it reaches temperatures of -15 ºC. The convective cell simulated in this study likely fell somewhere between the second and third stages from Waman et al. (2022) (their Figure 15), as they found that when the cloud was allowed to grow further

(cloud top temperature < -30 ºC), the BR mechanism begins to dominate. Additionally, Yano et al. (2016) suggested that breakup following ice-ice collisions can cause explosive N_{ice} in convective systems. However, their findings are based on cloud systems that lasted over the course of several hours. They also suggest that BR may only require initial ice concentrations of 0.001 L^{-1}. Results from the RAMS simulation in this study contradicts this finding, as even ice concentrations of 0.1 L^{-1} did not appear to initiate BR. Based on the results in this study, BR is a less important mechanism than HM in very early stages of congestus cloud development. Interestingly, as the simulated cloud matured, additional contributions of N_{ice} emerged from the HM mechanism as the All-SIP simulation produced N_{ice} that exceeded the FFD simulation. Therefore, FFD and BR may remain important SIP mechanisms over the lifetime of a convective cloud, but are likely secondary to HM, based on the current representation of the HM process in RAMS.

Over the last decade, several modelling and observational studies have highlighted the importance of previously overlooked SIP mechanisms such as BR and FFD (Lawson et al. 2015, 2017, 2022a,b; Phillips et al. 2017, 2018; Sullivan et al. 2018a,b; Waman et al. 2022; Yano et al. 2016). This study provided observational evidence of FFD occurring in early stages of cumulus congestus clouds, outside of the temperatures range for expected HM, but could not rule out the possibility of contributions from HM from warmer temperatures due to limited observations in the temperature range for HM initialization. Numerical model simulations of an ascending early-stage cumulus congestus cloud with the inclusions of FFD and BR SIP mechanisms showed improved representation of N_{ice}, compared to the previous configurations with only HM, but demonstrated that HM was the most important SIP mechanism.

We cannot fully describe the reasons for the difference in inferred dominant SIP mechanism between the model simulations and observations in the early stages of cloud development. On the one hand, the model clearly predicted copious amounts of ice formed via HM at the lower levels and lofted them to colder temperatures, with fewer contributions from BR and FFD. It is possible the model overpredicted the number of ice crystals formed via HM as the number of splinters may vary by 1–2 orders of magnitude (Korolev and Leisner 2020), and have been shown to be a factor of 5 less for higher rimer velocities (Saunders and Hosseini 2001). The model may also have underpredicted the number of fragments from FFD, which have been shown to exceed 100 for mm sized droplets (Korolev and Leisner 2020). But on the other hand, we present only the observed environmental conditions that are assumed to be favorable for the onset of FFD, and assume that the ice crystals observed were formed at/near the T_{CP} rather than at lower levels. Future work is required to accurately predict the number of fragments via FFD and HM in convective environments, such as employing the same sampling strategies used during SPICULE which involved following the upward growth of congestus clouds and tracking the ice concentrations as the clouds ascend.

As mentioned above, this analysis is ongoing, and additional simulations may help resolve these seemingly conflicting results. However, accurate representation of the ice formation mechanisms in developing convective clouds will improve prediction of the onset of precipitation, as well as cloud lifetimes, structure and intensity, and facilitate better studies of aerosol effects on these properties. Furthermore, understanding the atmospheric conditions favorable for the formation of SIP in convective clouds will ultimately improve our understanding and representation of convective cloud evolution.

CHAPTER 5: CHARACTERISTICS OF ICE NUCLEATING PARTICLES FROM THE LONG-RANGE TRANSPORT OF SAHARAN DUST

5.1 Mineral Dust Sourced from the Saharan Desert

Mineral dust that originates from arid regions may act as one of the most efficient ice nucleating particles (INPs) in mixed-phase clouds (MPCs) (Boose et al. 2016; DeMott et al. 2003b; Hiranuma et al. 2014; Hoose and Möhler 2012; Niemand et al. 2012; Price et al. 2018; Tobo et al. 2019; Wex et al. 2014). North Africa, including the Saharan Desert and Sahel regions, represent the world's largest source of dust, generating > 100 Tg of mineral dust that can be transported across the Atlantic Ocean and seed clouds in the Americas (Kaufman 2005). A common mechanism for large-scale transport of Saharan dust is the Saharan Air Layer (SAL), which generally occurs above the BL (typically 3-4 km aloft) and is described as a layer of hot and dry air with significant loadings of dust that is lofted in convective activity over North Africa (Carlson and Prospero 1972). Several laboratory studies have attempted to quantify the number of INPs from mineral dust using representative soil and clay samples (Atkinson et al. 2013; Niemand et al. 2012; Peckhaus et al. 2016a) to better understand the characteristics of dust-sourced INPs that may be present in the SAL. Much fewer in situ studies exist quantifying the number of INPs in airborne Saharan dust and are generally conducted off the coast of West Africa (Price et al. 2018; Boose et al. 2016; Welti et al. 2018). Even fewer studies have observed INPs in air layers originating from the Saharan Desert that have also been transported across the Atlantic Ocean.

One of the first in situ observations of INP concentrations attributable to Saharan dust was reported in DeMott et al. (2003b, 2009b) during flights over Florida as part of the

CRYSTAL-FACE campaign. These authors reported INP concentrations as high as 300 L^{-1} at temperatures warmer than homogeneous freezing conditions. Following this, DeMott et al. (2015) collected INP measurements with a CFDC in an elevated SAL during the Ice in Clouds Experiment – Tropical (ICE-T) campaign and found INPs concentrations in the SAL were ~10 times higher than in the marine boundary layer (MBL), achieving nearly 100 L-1 active at -25 ºC. Much more recently, INP measurements during a SAL event were reported in Harrison et al. (2022) over Barbados. The number concentrations of INPs measured in Harrison et al. (2022) were much lower than what was parameterized from the data on soils samples, and they argued that K-feldspar defined the ice nucleating ability of their Saharan dust observations. The ability of Saharan-sourced dust to act as INPs has been well documented. However, with the exception of measurements collected during CRYSTAL-FACE, the vast majority of studies have sampled close to source or at surface sites, and very little is known about the ice nucleating behavior and influence of Saharan dust that has been transported to North America. Characterizing the INPs that are transported across the Atlantic may have implications on cloud processes over the Gulf Coast and Southern Great Plains, regions that are frequently impacted by long-range-transported dust plumes. In this study, we present observations of airborne INP concentrations during a SAL event that took place during the Experiment of Sea Breeze Convection, Aerosols, Precipitation, and Environment (ESCAPE) campaign between June 12th and 17th, 2022 over the U.S Gulf Coast.

5.2 ESCAPE Research Campaign

5.2.1 Aircraft Campaign Overview

In situ observations were collected during the ESCAPE campaign aboard the National Research Council of Canada (NRC) Convair-580 research aircraft. One of the goals of the

ESCAPE campaign were to better understand the kinematic and thermodynamic characteristics of sea-breeze convection under varying aerosol environments around the Houston metropolitan area. Research flights (RFs) targeted sea-breeze convection that initiated near the coastline, and missions flew perpendicular to the coastline to capture the aerosol gradients that may have been present between the land and ocean interface. The Convair-580 research aircraft was equipped with air-motion and thermodynamic sensors, cloud microphysical probes and aerosol instrumentation which will be described in detail in section 5.1.2.

5.2.2 Measurement of Aerosols and INPs during ESCAPE

Measurements of INPs during the ESCAPE campaign, both in real-time and offline, were conducted in the same manner as in the SPICULE campaign and described in Chapter 4. Similar to SPICULE, the Convair-580 was equipped with a CVI-inlet, located upstream of the CFDC allowing for measurement of INPs from cloud residuals. However, ambient sampling of aerosols and INPs used an isokinetic (ISK) inlet. The mean (± 1 standard deviation) CVI enhancement factor during all ESCAPE RFs was 6.29 ± 0.5, and we assume a 50% cutsize of ~ 10 μm based on a mean true air speed and added sample flow of ~94 m/s and ~19 liters per minute, respectively (Shingler et al. 2012). In addition, with very warm cloud base temperatures (> 22 ºC) during the ESCAPE campaign deep warm phase regions occurred, and coalescence was a common feature and cloud droplet sizes nearly always exceeded 10 μm (personal communication with Greg McFarquhar and Saurabh Patil). Therefore, it was assumed the CVI captured the majority of the cloud droplet distribution and the CVI efficiency factor described in Chapter 4.2.3 was not applied to the in-cloud INP measurements during ESCAPE. Collection of INPs on filters for post-processing with the CSU ice spectrometer (IS) used the ISK. During ESCAPE, a total of 26 IS filters were collected, primarily in the boundary layer. Heat treatment

was also performed on some of the IS filters for analysis of the biological INP activity. Details for the heat treatment of IS filters can be found in Suski et al. (2018). Total aerosol concentrations were collected using an Ultra-High Sensitivity Aerosol Spectrometer (UHSAS) that has 99 logarithmically spaced bins between 60 nm and 1 μm. Coarse mode aerosols (> 1 μm) were measured using the CDP under clear sky conditions, which were defined by the Nevzorov LWC < 0.01 g m^{-3} and CDP LWC < 0.001 g m^{-3}. Aerosol measurements are reported at standard conditions (STP; 0 ℃ and 1013 kPa).

5.3 Saharan Air Layer during ESCAPE

During the ESCAPE campaign, a prolonged and widespread SAL advected into the Gulf Coast region, beginning during RF09 and lasting through the remainder of the airborne campaign. The presence of the SAL was evident in the large increase in the coarse mode aerosol optical depth (AOD) measured at four different Aerosol Robotic Network (AERONET) sites across the region, one of which the Convair-580 flew directly over (Figure 5.1b). During this period, two RFs (9 and 10) were focused primarily on sampling the Saharan dust and urban aerosols around the Houston region, while the remaining flights targeted sea-breeze convection over SW Louisiana (Figure 5.1a). In general, the highest coarse mode AOD was measured at the Smith Point site, and the ARM Laporte site followed closely with Smith Point. This suggested that some of the highest concentrations of Saharan dust were located in the airborne sampling region. Although the NEON LENO site measured lower AOD during this period, that site still had elevated values during this period, showing how widespread this SAL event was, spanning much of the Gulf Coast. The highest AOD measured at the Sequin, TX site occurred two days after the peak values observed at the Smith Point site, indicating the SAL continued to progress further over land with time. In addition to the elevated values of coarse mode AOD, a two-week

ensemble of HYSPLIT back trajectories ending on June 14th was conducted as shown in Figure 5.2. All but one of the back trajectories originated over western Africa, providing additional confidence that the dust layer originated over the Saharan Desert or Sahel region.

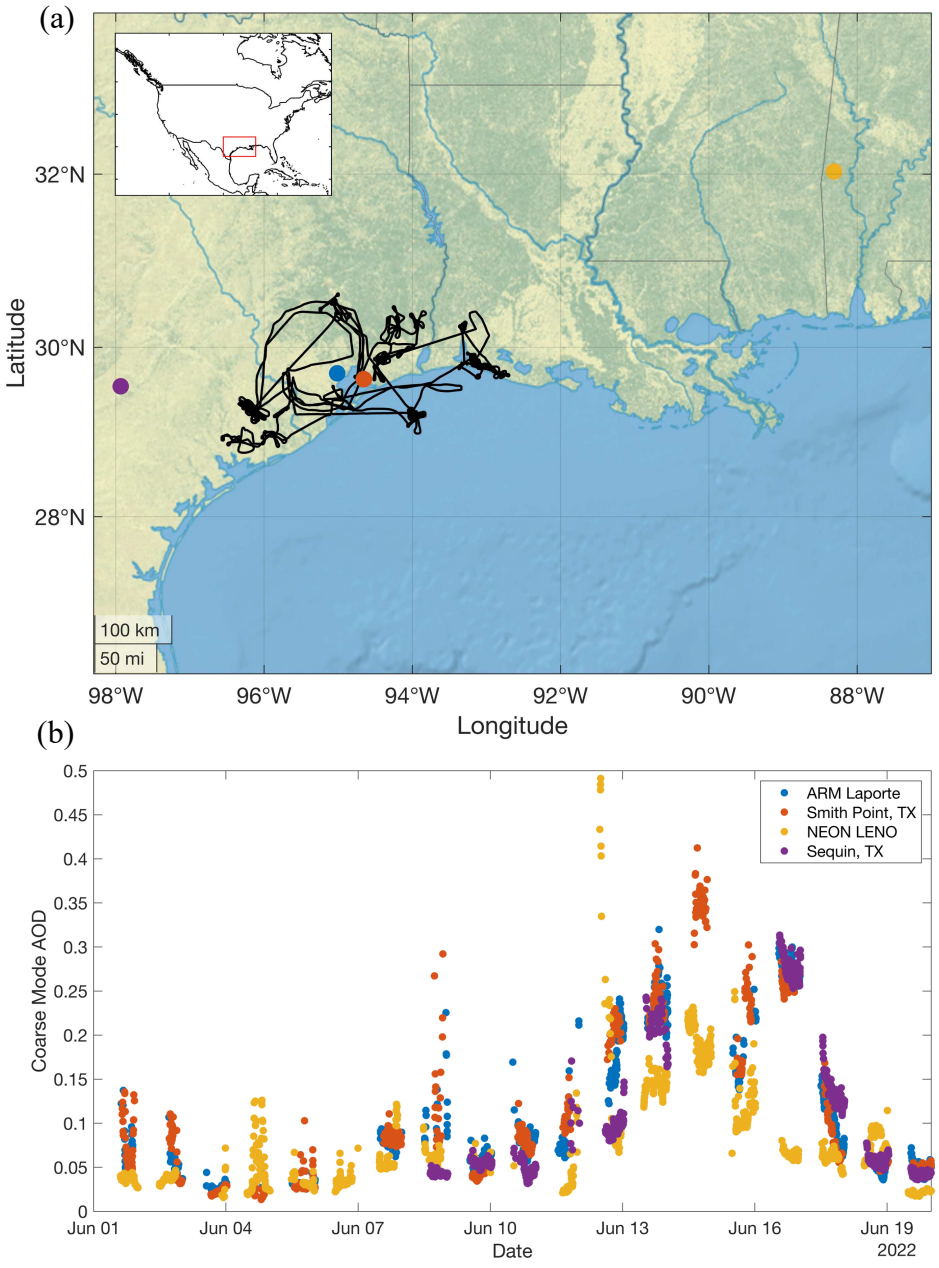


Figure 5.1. (a) Flight tracks of the Convair-580 during research flights 9–13 of the ESCAPE campaign. The colored markers in (a) denote the AERONET sites and the colors correspond to the markers of coarse mode aerosol optical depth (AOD) shown in (b).

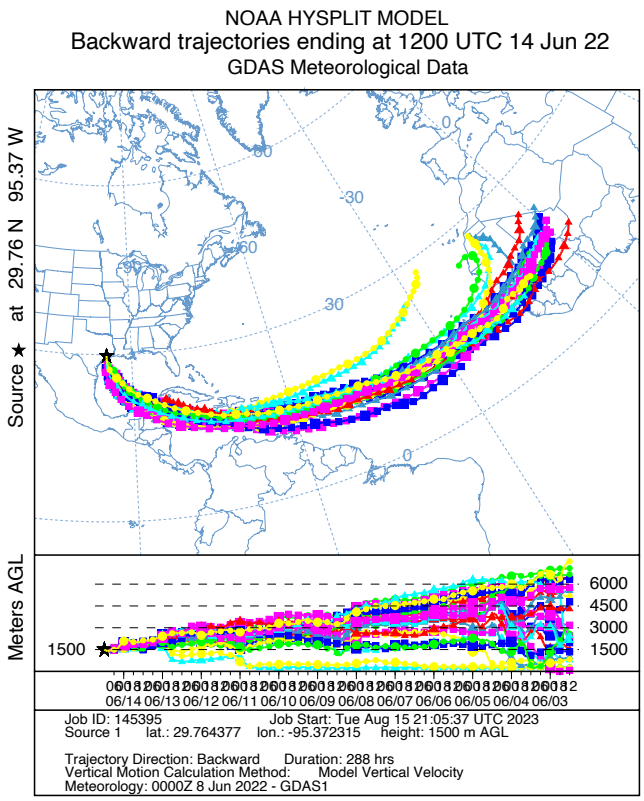


Figure 5.2. Two-week ensemble HYSPLIT back trajectories ending on June 14th over Houston, TX at approximately 1500 m.

5.4 INP measurements of Saharan Dust

Figure 5.3 shows the timeline of INP concentrations measured by the CFDC and active between temperatures -16 ºC and -32 ºC during the ESCAPE campaign. The number of INPs ranged from ~1 to 800 L^{-1} and generally varied by 1–2 orders of magnitude during a given flight. Prior to the SAL event (shaded tan region in Figure 5.3) the highest number concentration of INPs measured at -26 ºC was ~40 L^{-1}. However, as the SAL moved into the region, the peak concentrations of INPs during RF09, measured from the CFDC at -26 ºC were much higher, nearly 300 L^{-1}. The INP concentrations were even higher during RF10, where the highest concentrations of INPs observed during that flight were ~300 L^{-1} at a temperature of -24 ºC (Figure 5.3a). The remaining flights (RFs 11–13) still showed elevated INP concentrations compared to the RFs prior to the SAL event, but were lower than the previous two flights. For

example, the highest number concentrations of INPs at -26 ºC during RF11 and RF13 was ~90 L^{-1} and ~50 L^{-1}, respectively, which was still higher than any INP measurement at -26 ºC before RF09. These very high INP concentrations, especially during RF09 and RF10, correspond to the same time period as the elevated values from the AERONET sites, which also occurred between June 12th and 17th.

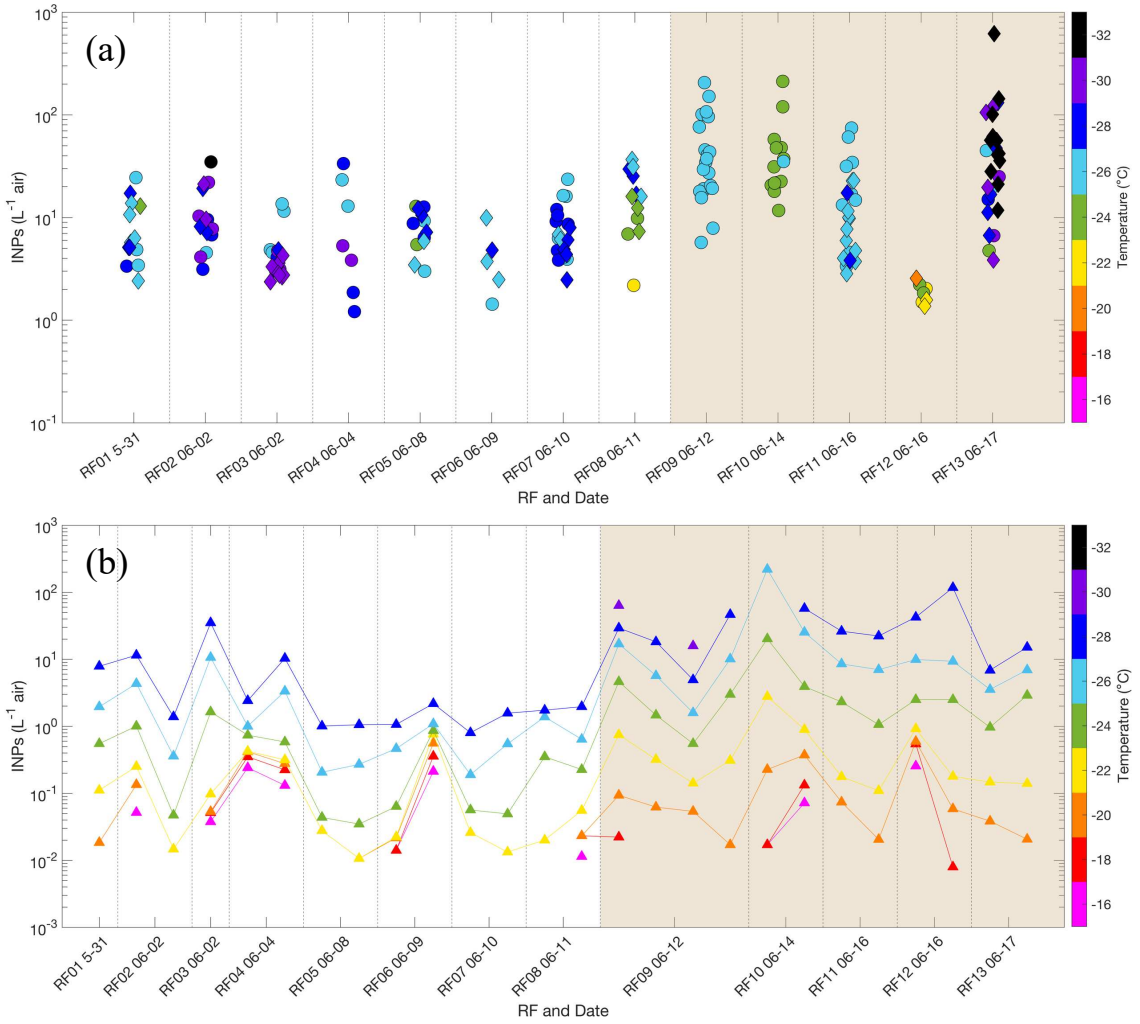


Figure 5.3. ESCAPE timeline of INP concentrations collected (a) from the CFDC and (b) on polycarbonate filters and processed with the CSU IS. The marker colors denote the temperature for which the INPs froze. The circles and diamonds in (a) represent CFDC measurements sampling from the ISK and CVI inlets, respectively. The tan shaded region represents the period during which the SAL advected over Houston. All concentrations have been expressed in standard liters of air.

The timelines of INP concentrations determined from IS measurements during ESCAPE (Figure 5.3b) had a similar trend during the SAL event as the CFDC measurements (Figure 5.3a). For example, the INP concentration between -24 ºC and -28 ºC increased by ~2 orders of magnitude between RF08 and RFs 9 and 10. Similar to the CFDC measurements, the INP concentrations at -24 ºC and -26 ºC during RFs 9–13 remained elevated compared to RFs 1–8. However, in contrast to the INP concentrations active at temperatures below -20 ºC, INP concentrations at warmer temperatures (> -20 ºC) did not show a consistent enhancement during the SAL period. This suggests that the INPs measured in the SAL were predominantly Saharan dust and did not include biological INPs that are active at warmer temperatures (Testa et al. 2021; Petters and Wright 2015; Tobo et al. 2013). Heat treatment on the first filter collected during RF10, shown in Figure 5.4, appears to validate this conjecture. The INP spectra at temperatures < -20 ºC showed very little reduction in the INP activity, with a consistent reduction in INP concentrations by a factor of two or less. Similarly, Harrison et al. (2022) performed similar heat treatments on their INP measurements and reported no substantial decrease in the ice nucleating activity. In contrast to the first filter collected during RF10, the first filter collected during RF12 showed much higher INP concentrations at temperatures > -20 ºC that were subsequently almost completely removed after heat treatment. The filter collected during RF12 likely captured a distinct aerosol population, such as locally sourced bio-INPs, in addition to sampling the Saharan dust, since RF12 primarily sampled over SW Louisiana and this particular filter was collected at a relatively low altitude of ~4000 ft. In contrast, the first filter collected during RF10, shown in Figure 5.4, was collected SW of Houston at an altitude of 7000 ft and the flight specifically targeted sampling in the SAL. The only other filter that was collected above the BL inside of the SAL was RF09 filter 3 (Figure

5.3), and showed lower INP concentrations than the first filter collected during RF10. This indicates two points: 1) the Saharan dust was likely present in elevated layers when it first advected over the region as the highest concentrations of INPs were measured well above the BL and 2) particles present in the SAL also settled down to lower altitudes later on and became mixed with the aerosol population present in the boundary layer.

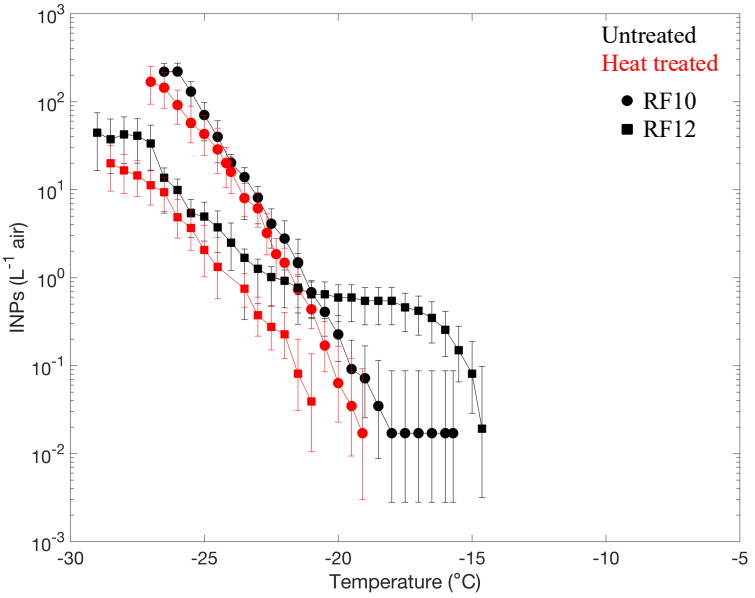


Figure 5.4. INP spectra as functions of temperature for untreated (black) and heat treated (red) IS filters, where circles and squares denote the first filters collected during RF10 and RF12, respectively.

During this period of ESCAPE when the SAL advected over the region, the INP concentrations had a very steep log-linear profile between temperatures of -20 ºC and -32 ºC, as shown in Figure 5.5a. The highest INP concentrations measured by the CFDC were between 200–300 L^{-1} between temperatures of -24 ºC and -26 ºC. These very high INP concentrations agreed with lower temperature range measurements of Saharan dust reported in Price et al. (2018) (gray shaded region in Figure 5.5a), which were INP observations from filter samples collected from an airborne platform just off the coast of western Africa. Most of the ESCAPE INP concentrations were lower than those in Price et al. (2018). However, the majority of CFDC

and IS measurements of INP from ESCAPE overlapped well with the range of INP measurements from Harrison et al. (2022) (light blue shaded region). The INP measurements from Harrison et al. (2022) were collected in the MBL near Barbados, and were reported as African mineral dust. These INP concentrations during ESCAPE were also in good agreement with measurements during CRYSTAL-FACE, where airborne INP concentrations were between 50 – 300 L^{-1} at -24 ºC. As discussed earlier, the high INP concentrations from RF12, that also overlap with the Price et al. (2018) observations were likely from a second, distinct aerosol population, not Saharan dust. However, these results suggest that the SAL can still contain high concentrations of INPs that would be active in convective storms at temperatures below -20 ºC after long-range transport to the U.S., and the agreement between the observations from ESCAPE and Harrison et al. (2022) and DeMott et al. (2003b, 2009b) suggests the majority of the loss of higher temperature INPs occurred during transport over the Atlantic Ocean. It is also possible that differences with Price et al. (2018) are attributable to different sources over Africa, but the similarity of results to Harrison et al. (2022), which included close comparison to earlier ICE-T results (DeMott et al. 2015) suggest that the INP temperature spectrum observed in ESCAPE is common for SAL dust reaching North America.

In order to quantify the ice nucleating ability of the Saharan dust collected during ESCAPE, the active surface-site density (n_s) was derived as a function of temperature (Figure 5.5b). The n_s values were calculated using the equation below:

$$n_s = INPs/SA \tag{5.1}$$

Where *SA* denotes the aerosol surface area concentration, which was calculated based on the integrated aerosol size distributions combining both the UHSAS and CDP and averaging over the course of each of the five flights that took place during the SAL event. Aerosol

concentrations were restricted to clear sky conditions and below the maximum altitude sampled in the SAL, ~9500 ft.

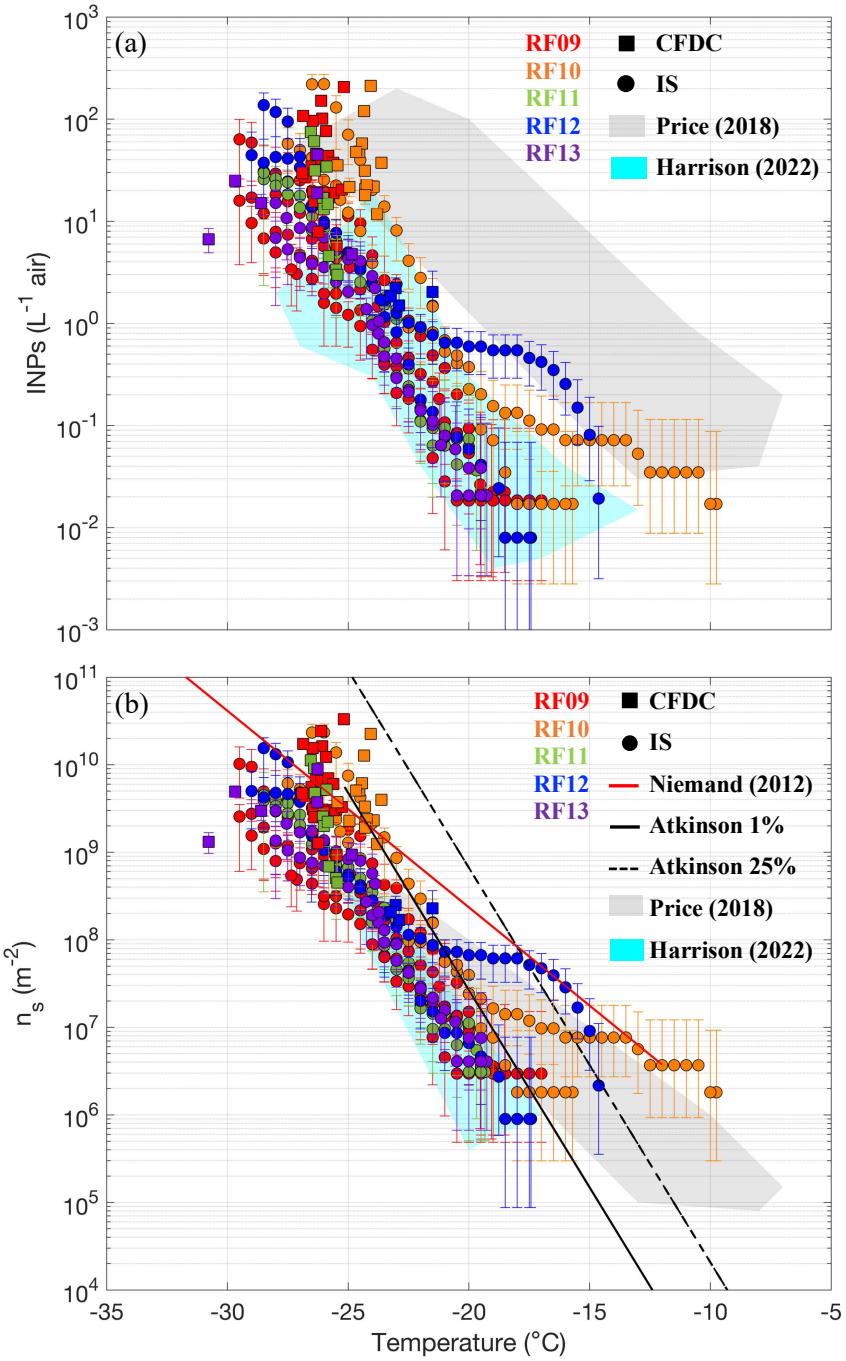


Figure 5.5 (a) INP number concentration (per standard liter of air) and (b) active surface site density (n_s) values versus temperature for the IS (circles) and CFDC (squares) and colored by the research flight during ESCAPE. Errors bars represent the 95% confidence intervals. The black solid and dashed line represents the n_s for 1 % and 25 % scaled K-feldspar parameterizations (Atkinson et al. (2013), respectively. The red line represents the n_s parameterization from

Niemand et al. (2012). The light blue and gray shaded regions represent the range in (a) INP concentrations and (b) n_s values from two studies sampling airborne Saharan dust (Price et al. 2018; Harrison et al. 2022).

Similar to the INP concentrations shown in Figure 5.5a, the n_s values generally fall below the range in n_s values from Price et al. (2018) but show very good agreement with Harrison et al. (2022). Apart from a small number of samples, the majority of n_s values in this study also fell below the parameterizations from Niemand et al. (2012) and Atkinson et al. (2013). The former study was based on measurements of desert dust in the AIDA cloud chamber and the latter were from laboratory measurements of dusts containing different surface area fractions of K-feldspar. The slope of the majority of n_s values from ESCAPE followed very closely with the 1 % Atkinson et al. (2013) line, suggesting there may have been slightly lower (< 1 %) fractions of K-feldspar in the Saharan dust sampled during ESCAPE, if indeed the feldspar content is the salient factor in describing their activity. Harrison et al. (2022) attributed some of the lower ice nucleating activity in their dust measurements to be from the mixing of dust and sea-salt, which may also have also been the case for the ESCAPE measurements. Despite this, these results suggest that the INPs that are sourced from the Saharan Desert and make it to the U.S. may still remain highly active as heterogeneous INPs.

5.5 Comparison to the SPICULE campaign

The cumulative spectra of INP concentrations as a function of temperature collected during all flights of the ESCAPE campaign are shown in Figure 5.6. As described previously, the INP concentrations during the SAL event were generally 1–2 orders of magnitude higher than the concentrations from the previous flights. However, the INP concentrations collected during ESCAPE generally fall within the range of INP concentrations from the SPICULE campaign (gray shaded region in Figure 5.6). Only the very high INP concentrations during the SAL event at temperatures < -24 ºC exceeded the highest INP concentrations from SPICULE. In addition,

the lowest INP concentrations from ESCAPE at temperatures < -20 ºC fall below the lower bound of INP concentrations from SPICULE. The lowest INP concentrations active at temperatures < -20 ºC may suggest coastal marine influences dominating the INP population early in the ESCAPE campaign. The INP concentrations active at temperatures > -20 ºC for all flights during ESCAPE fall within the SPICULE envelope.

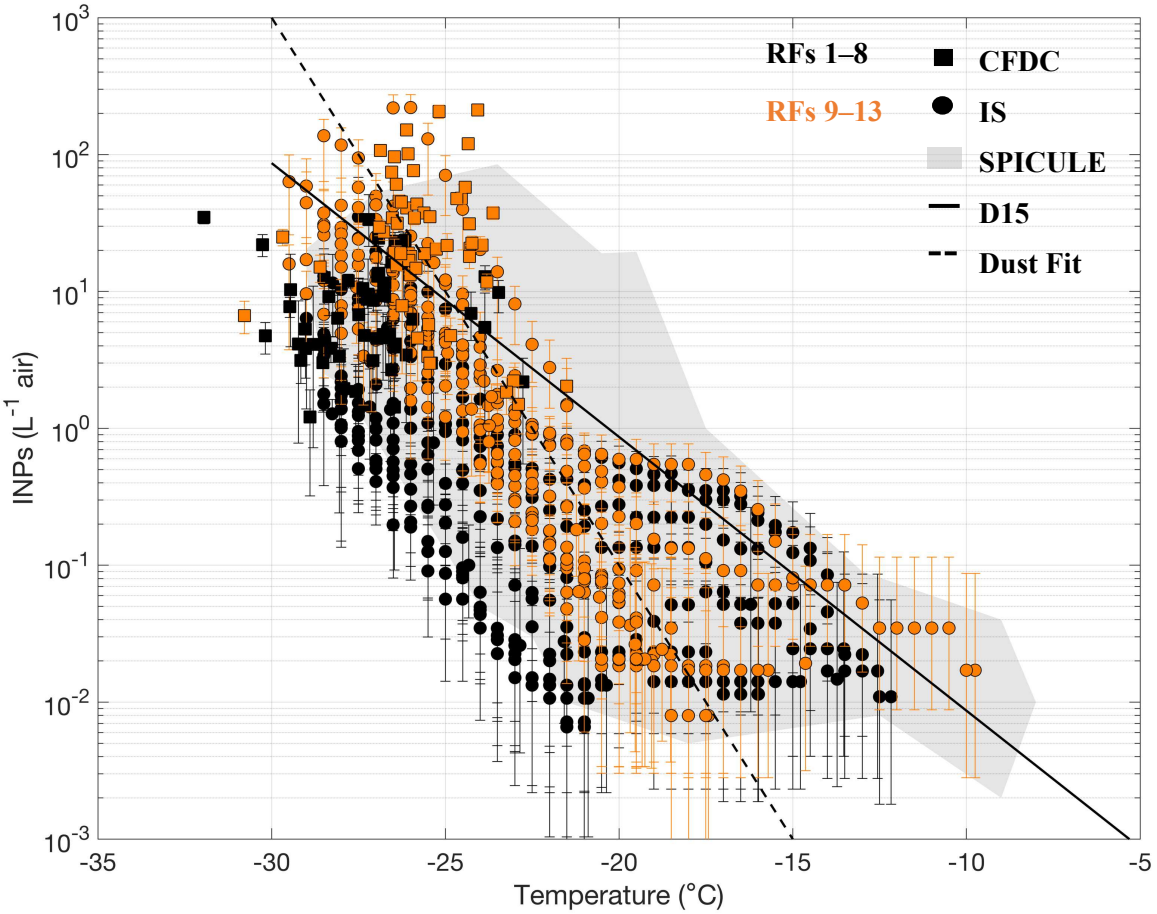


Figure 5.6. INP concentrations as a function of temperature from the ESCAPE campaign, where the black markers denote RFs 1–8 and the orange markers denote RFs 9–13, representative of the SAL event. The square and circle markers denote INP concentrations measured by the CFDC and the IS filters, respectively. The gray shaded region represents the range in INP concentrations collected during SPICULE and the black solid line denotes the INP parameterization from DeMott et al. (2015) (D15) used to initialize the model simulations in Chapter 4. The black dashed line denotes a best fit line for the SAL INP measurements.

The INP parameterization from DeMott et al. (2015) (D15), used to initialize the SPICULE INP concentrations in RAMS (black solid line, described in section 4.3.1), and the

best fit line of the INP concentrations in the SAL (dashed black line) meant to represent the number of INPs that may be initialized for an African dust-only simulation are shown in Figure 5.6. The slope of the dust line is much steeper than the D15 line from SPICULE, which results in a greater number of INPs at lower temperatures (< -25 ºC) but much fewer at warmer temperatures (> -15 ºC). Model simulations using the dust fit to initialize the INP concentrations would likely predict fewer ice crystals forming via primary nucleation early in the cloud development compared to the D15 parameterization used for the SPICULE simulations. This would lead to secondary feedbacks such as a delayed onset of SIP, specifically the HM mechanism due to the limited number of ice crystals at temperatures between -3 ºC and -8 ºC, and a modification to the cloud evolution.

5.6 Summary and Implications

Airborne measurements of INP concentrations from the SAL that occurred during the ESCAPE campaign are reported in this study. While few studies have collected INP measurements of Saharan dust on the west side of the Atlantic Ocean (Harrison et al. 2022; DeMott et al. 2003b; Lasher-Trapp et al. 2016), never before have they been documented as far from the source region as the U.S. Gulf Coast.

The INP concentrations measured during ESCAPE showed a large increase during the SAL event compared to the flights made prior to the event. The INP measurements from both the CFDC and the IS filters showed INP concentrations between 10–50 times higher at -24 ºC, but showed no discernable difference in INP concentrations at temperatures > -20 ºC, indicating the Saharan dust was only active at colder temperatures. This findings agrees well with that of Boose et al. (2016), who sampled Saharan dust off the coast of Africa, and observed higher INP concentrations at temperatures < -25 ºC but found no significant ice nucleating behavior at

-20 ºC. In general, the INP concentrations also agreed well with previously reported airborne measurements of Saharan dust from the eastern Caribbean (Harrison et al. 2022), and were only ~1–2 order magnitude lower than INP concentration sampled off the coast of western Africa (Price et al. 2018). These results suggest that, if the differences in INP concentrations in the Price et al. (2018) and Harrison et al. (2022) studies represent the influence of a loss process for INPs, that loss occurs primarily during the transport across the Atlantic, and there is much less loss of INP number concentrations during transport across the Caribbean and Gulf of Mexico. These processes remain to be investigated.

Previous studies, at least outside of the laboratory, have not reported the results of treatments on the INP spectra of Saharan dust collected at cloud altitudes, making these measurements the first reported heat treatments of airborne Saharan dust. The heat treatment on the INP spectrum from RF10 showed very little reduction in the ice nucleating activity, suggesting Saharan dust is not sensitive to heat treatment, similar to the findings for other mineral dusts. However, treatment of the filter from RF12 induced a substantial reduction in the number concentrations of INPs at temperatures > -20 ºC, indicating the SAL had likely mixed with a second, distinct INP-containing aerosol population later in the dust incursion.

We quantified the ice nucleating activity of Saharan dust by calculating the n_s values and comparing them to previous airborne observations that were sampled much closer to the source region. We found good agreement with previously reported n_s values, suggesting the INPs in the SAL remain highly active during transport after atmospheric oxidation of the particles has likely occurred. The atmospheric oxidation of dust particles may produce an organic coating that one study showed could suppress heterogeneous nucleation at mixed-phase temperatures (0 to -38 ºC) (Möhler et al. 2008), while others have found these coatings do not affect the ice nucleating

behavior of dust particles (Wex et al. 2014; Kanji et al. 2019). Whether these dust particles measured during ESCAPE had coatings is not known, but the results presented herein suggest they were still highly active at initiating heterogenous freezing at temperatures < -20 ºC. Cloud processing during transport across the Atlantic Ocean, which may represent an additional sink, and may also modify the ice nucleating activity of transported dust, but has yet to fully explored.

While these types of long-range dust events are not unusual, measurements of the INP concentrations over the U.S. are very rare. The SAL events that episodically transport high concentrations of dust aerosol over the U.S. may act as a natural INP perturbation that will likely have implications for cloud processes and evolution. To better understand this, we compared the INP concentrations from the ESCAPE campaign to the observations collected in SPICULE, as described in Chapter 4 (Figure 5.6) and assessed the implications on cloud processes for model simulations. The very low INP concentrations active at temperatures > -20 ºC during the SAL suggest a potential delay in ice formation for simulated convective clouds, as the clouds would need to reach colder temperatures for higher concentrations of ice crystals to form via primary nucleation. The clouds would also likely have an even stronger dependence on the FFD SIP mechanism for ice crystal enhancement later in cloud evolution. The very low INP concentrations at temperatures where the HM mechanism is active may shut down this mechanism until there was sufficient ice formation at higher altitudes to sediment down and trigger HM later in the cloud development. Future study using both in situ observations and model simulations would be required to fully understand the impacts of the SAL on cloud microphysical properties and cloud evolution.

CHAPTER 6: CONCLUSIONS

6.1 Summary of Studies

Both cirrus and mixed-phase clouds play important roles in influencing global precipitation and radiative balance. With regard to cirrus clouds, the mechanisms of ice formation, homogeneous and heterogeneous nucleation, have been extensively studied. However, knowledge of the types of aerosols that may act as ice nucleating particles (INPs) to initiate heterogeneous nucleation in cirrus clouds remains incomplete. This gap is in part due to limited direct observations of cirrus cloud INPs as a result of the difficulty in sampling cirrus cloud residual particles from airborne platforms, and a limited number of campaigns that have ever flown to sample INPs at cirrus levels (DeMott et al. 1998; Rogers et al. 1998). Therefore, much of our understanding of heterogeneous nucleation under cirrus cloud conditions is based upon laboratory studies. Similarly, a theoretical understanding of the various pathways of ice formation in mixed-phase clouds (MPCs) is well documented. Despite this, uncertainties remain linking INPs and ice crystal concentrations during cloud evolution, specifically what triggers the transition from primary nucleation to SIP during the early stages of convective clouds.

The overarching goals of this dissertation were to 1) elucidate whether sea spray aerosol (SSA) and secondary marine aerosol (SMA) produced during atmospheric oxidation of marine emissions may act as significant sources of INP in cirrus clouds and the subsequent atmospheric implications, 2) improve our understanding of the pathways of ice formation in congestus clouds during the early stages of the cloud lifetime, and 3) characterize a natural INP perturbation from African dust that may have implications for cloud processes over the U.S. Gulf Coast and

Southern Great Plains. These goals were accomplished using a combination of carefully conducted laboratory studies and targeted airborne research campaigns.

The goals of the first study of this dissertation (Chapter 2) were to elucidate the ice nucleating behavior of SSA under cirrus cloud conditions. This was accomplished with a laboratory study using SSA particles generated from natural seawater collected at the Scripps Pier in La Jolla, CA and a CFDC for detection of ice nucleation. To better understand the characteristics of SSA that influence ice nucleation, two particle sizes (150 and 600 nm) were generated from natural seawater and from a NaCl solution. The major findings of this study included: 1) SSA generated from natural seawater initiated heterogeneous nucleation (at potentially significant fractions ~10 %) at temperatures < 220 K, 2) the onset of ice nucleation for both NaCl and SSA particles was independent of particle size, and 3) the similarities between the ice nucleating behavior of SSA and NaCl suggested that the salt components of SSA determine the ice nucleating behavior. Outstanding questions remain regarding the transition between homogeneous and heterogeneous nucleation, which consistently occurred at/near 220 K, and will be discussed in section 6.2.

The second study in this dissertation (Chapter 3) was motivated by the experiments discussed in Chapter 2, and expanded upon those results to further advance our understanding of the ice nucleating behavior of SSA. In this study, we employed a more complex and realistic aerosol generation method using a MART, which generates SSA by cascading a sheet of water over the water surface, producing bubble distributions (and hence SSA distributions) that are similar to those produced by ocean wave breaking. The first goal of this study was to examine how atmospheric oxidation (or aging), will impact the ice nucleating behavior of SSA under cirrus cloud conditions. This was accomplished by exposing generated SSA to a strongly

oxidizing environment by passing the sample through an oxidation flow reactor (OFR), located directly downstream of the MART. The second goal of this study was to determine the ice nucleating behavior of SMA, formed via the oxidation of the gas-phase species emitted from the MART. The major findings of this study included: 1) the similarities between ice nucleation behaviors of SSA with and without the OFR turned on indicate that the oxidation of pSSA did not hinder the ice nucleating ability of pSSA at low temperatures, suggesting the contributions of condensed organics onto the pSSA or the alteration of the functional groups in pSSA following atmospheric aging did not significantly delay water uptake of the inorganic salts and 2) ice nucleation of SMA did not occur until the relative humidity was elevated well above water saturation at most cirrus temperatures, which indicated that SMA is unlikely to act as a potential source of cirrus cloud INPs.

The motivation of the third study, described in Chapter 4 was to elucidate the pathways of ice formation during the early stages of cumulus congestus clouds. In this study, we presented coincident measurements of in situ INP and ice crystal number concentrations observed in convective clouds, the first report of this kind in many decades. This study, SPICULE, was successful largely due to the excellent coordination between two aircraft, one of which sampled in the boundary layer in the vicinity of developing cumulus congestus clouds and near cloud base, and the other which sampled in the growing tops of the same clouds. This strategy provided a diverse and comprehensive dataset of aerosol and INP measurements, cloud microphysical properties, and thermodynamic and kinematic observations. The number concentrations of INPs during SPICULE cloud passes, compared with observed ice crystal number concentrations, were used to classify the ice formation mechanism as either primary nucleation or secondary ice production (SIP). A final component of this study comprised idealized model simulations of a

congestus cloud, set to resemble the clouds in SPICULE, to provide additional understanding regarding the sequence of ice formation mechanisms during the earliest stages of congestus clouds. The major findings of this study included: 1) airborne INP measurements indicated wide variability over the U.S. Central Great Plains and the presence of different INP types, 2) in situ observations of cloud microphysical properties indicated that the most important SIP mechanism in the early stages of congestus clouds is fragmentation of freezing drops (FFD), 3) warmer cloud base temperatures (T_{CB}) and higher vertical velocities were important environmental factors that produce cloud microphysical properties favorable for the onset of FFD and 4) numerical simulations confirm that HM is the major SIP mechanism and but without contributions of FFD and BR, the model would likely underestimate ice concentrations during the early stages of cloud development.

The goal of the analysis described in Chapter 5 was to present airborne INP observations collected during a Saharan air layer (SAL) event over the U.S. Gulf Coast region. Mineral dust from desert sources is well-known as a source of INPs active at the colder end of mixed-phase cloud temperatures, however, direct measurements aloft of transported Saharan dust are limited in the literature. During the ESCAPE campaign, a prolonged and widespread Saharan Air Layer (SAL) event was present during five of the thirteen RFs, and INP measurements were collected throughout the boundary layer up to ~3 km. The major findings from this study include: 1) INP concentrations were enhanced by 1–2 orders of magnitude at temperatures below -20 °C in the SAL compared to urban and background INP concentrations sampled prior to the SAL event, and 2) Saharan dust likely retains much of its ice nucleating ability and remained highly active even after long range transport across the Atlantic Ocean, 3) comparison of the INP concentrations in the SAL generally overlapped, but sometimes exceeded, those measured during

the SPICULE campaign and 4) the slope of the INP spectra of the transported dust suggested implications for cloud processes in model simulations.

6.2 Implications and Future Work

The findings presented in Chapters 2 and 3 of this dissertation served to advance our understanding of the characteristics that influence low temperature ice nucleation of SSA and SMA. These findings were based on controlled laboratory studies, however there remain outstanding questions that require additional laboratory studies. Firstly, the transition between homogeneous and heterogenous nucleation that occurred at 220 K was consistent for the NaCl, the primary-sourced SSA, and the oxidized SSA+SMA. However, both studies were only able to speculate on the mechanism for this transition. We speculated that there was competition between deliquescence and immersion freezing and pore condensation freezing (PCF), and switches between mechanisms coincided with the intersection of the DRH of NaCl and the PCF line for a specific pore size of 11 nm. However, the intersection of the DRH and PCF lines was for an arbitrary selected pore size, and we had no direct evidence that PCF occurred. Thus, there are still remaining questions, including: What specifically is causing the transition between homogeneous and heterogeneous freezing around 220 K? What are the sizes of the pores or cracks on SSA if they are present? How do surface features such as pores and cracks affect this transition? To answer these questions, future studies could include RAMAN microscopy, as in Schill and Tolbert (2014), electron microscopy, or high-temporal resolution cameras, to better examine the phase state and morphology of the particles at the time of freezing.

Secondly, Chapter 3 illustrated that future studies exploring oxidation of emissions from authentic seawater must use a water reservoir and reaction chamber consisting of materials that do not produce VOCs. Although the study reported in Chapter 3 found that the oxidation of SSA

and any volatile emissions from the tank did not affect the ice nucleating behavior of the particles, the blank experiments with DI water showed that new particle formation occurred in the OFR. The nucleated particles were attributed to oxidation products of the VOCs released from the acrylic material of the MART, and their presence led to uncertainties in the composition of the SMA particles and coatings. Future studies that include an OFR for oxidation of aerosol particles must be careful with the materials used for aerosol generation to avoid such issues and the role of marine-sourced VOCs, and direct oxidation of SSA can only be clarified after eliminating this artifact. Another consideration for future study would be to address atmospheric aging process on pSSA particles under upper tropospheric conditions. In this study, the air stream remained humidified in the OFR, therefore would mimic the oxidation reactions that occur in the marine boundary layer. Therefore, the salt components of pSSA would be in an aqueous state during oxidation and the contributions of condensed organics may have been different than if the salt particles were in the crystalline state. Since the most probable pathway for SSA to reach the upper troposphere involves deep convection and detrainment from anvils, the role of cloud processing of SSA in affecting its ice nucleating ability is of interest and remains unresolved. Finally, the findings from both of these studies strongly supports the relevance of SSA as an important global aerosol for cirrus cloud formation. Estimates of 1 % and 10 % frozen fractions of global SSA concentrations ranged between 10^{-1} – 10^{4} L^{-1}, depending on particle size, which were in the same range as average ice crystal number concentrations in cirrus clouds. Thus, SSA may represent an important aerosol type to initiate heterogeneous freezing at cirrus cloud temperature, especially in a warming climate, where SSA emissions may increase along with increasing global temperatures.

The main significance of the conclusions from Chapter 4 was to serve as a blueprint for future in situ observations of SIP. Determination of the ice formation mechanisms from in situ observations has always been challenging due to cloud processes occurring faster than aircraft can capture them. Targeted cloud passes between two coordinating aircraft during SPICULE allowed for coincident measurements of ice crystal and INP number concentrations at different levels of the clouds. Future studies should build off the targeted approach used in SPICULE in order to gain much larger datasets of cloud microphysical properties and aerosol and INP measurements to better characterize the ice formation processes in convective clouds. Specific next steps suggested by this work include: How might this targeted approach for ascending congestus clouds be applied with only one aircraft instead of two? What types of aircraft maneuvers would best capture the ice formation processes? What are the most dominant SIP mechanisms in non-convective clouds and how could this strategy be adapted to answer that question? How would the results from this study change for convective clouds sampled over different regions?

Finally, Chapter 5 described observations of INP concentrations during a SAL that occurred during the ESCAPE campaign and showed that the INP concentrations were enhanced during the SAL compared to the earlier flights, where INP concentrations were generally low. When comparing the initialized INP concentrations used for the numerical simulations in Chapter 4 and the best fit line of the INP concentrations during the SAL event showed that the slope of the dust fit was much steeper than what was used from SPICULE. Future modelling studies could use the ESCAPE dataset, initialized using INP concentrations in the SAL, to better understand how these natural INP perturbations affect cloud microphysical properties and evolution. Based on the findings in Chapter 4, there would likely be impacts on the formation of

ice in early-stage convective clouds as the clouds would need to reach colder temperatures for higher rates of ice crystal formation via primary nucleation. Additionally, under these conditions, convective clouds would likely have a stronger dependence on the FFD mechanism, as the HM mechanism would be effectively shut off with so few INPs present at the temperatures where HM is most active (-3 to -8 ºC). Therefore, the sequence of ice formation pathways may remain the same as described in Chapter 4 under the SAL scenario, but the contributions of all the SIP mechanisms over the course of the cloud lifetime is currently unknown.

REFERENCES

Abbatt, J. P. D., S. Benz, D. J. Cziczo, Z. Kanji, U. Lohmann, and O. Möhler, 2006: Solid Ammonium Sulfate Aerosols as Ice Nuclei: A Pathway for Cirrus Cloud Formation. *Science* (80-.)., 313, 1770–1773, https://doi.org/10.1126/science.1129726.

Adler, G., T. Koop, C. Haspel, I. Taraniuk, T. Moise, I. Koren, R. H. Heiblum, and Y. Rudich, 2013: Formation of highly porous aerosol particles by atmospheric freeze-drying in ice clouds. *Proc. Natl. Acad. Sci.*, 110, 20414–20419, https://doi.org/10.1073/pnas.1317209110.

Archuleta, C. M., P. J. DeMott, and S. M. Kreidenweis, 2005: Ice nucleation by surrogates for atmospheric mineral dust and mineral dust/sulfate particles at cirrus temperatures. *Atmos. Chem. Phys.*, 5, 2617–2634, https://doi.org/10.5194/acp-5-2617-2005.

Atkinson, J. D., and Coauthors, 2013: The importance of feldspar for ice nucleation by mineral dust in mixed-phase clouds. *Nature*, 498, 355–358, https://doi.org/10.1038/nature12278.

Bailey, M., and J. Hallett, 2004: Growth rates and habits of ice crystals between - 20° and -70°C. *J. Atmos. Sci.*, 61, 514–544, https://doi.org/10.1175/1520-0469(2004)061<0514:GRAHOI>2.0.CO;2.

——, and ——, 2012: Ice crystal linear growth rates from -20° to -70°C: Confirmation from wave cloud studies. *J. Atmos. Sci.*, 69, 390–402, https://doi.org/10.1175/JAS-D-11-035.1.

Baker, M. B., 1997: Cloud microphysics and climate. *Science* (80-.)., 276, 1072–1078, https://doi.org/10.1126/science.276.5315.1072.

Barry, K. R., and Coauthors, 2021a: Observations of Ice Nucleating Particles in the Free Troposphere From Western US Wildfires. *J. Geophys. Res. Atmos.*, 126, 1–17, https://doi.org/10.1029/2020JD033752.

——, T. C. J. Hill, C. Jentzsch, B. F. Moffett, F. Stratmann, and P. J. DeMott, 2021b: Pragmatic protocols for working cleanly when measuring ice nucleating particles. *Atmos. Res.*, 250, 105419, https://doi.org/10.1016/j.atmosres.2020.105419.

Bartels-Rausch, T., X. Kong, F. Orlando, L. Artiglia, A. Waldner, T. Huthwelker, and M. Ammann, 2021: Interfacial supercooling and the precipitation of hydrohalite in frozen NaCl solutions as seen by X-ray absorption spectroscopy. *Cryosph.*, 15, 2001–2020, https://doi.org/10.5194/tc-15-2001-2021.

Berkemeier, T., M. Shiraiwa, U. Pöschl, and T. Koop, 2014: Competition between water uptake and ice nucleation by glassy organic aerosol particles. *Atmos. Chem. Phys.*, 14, 12513–12531, https://doi.org/10.5194/acp-14-12513-2014.

Berresheim, H., F. L. Eisele, D. J. Tanner, L. M. McInnes, D. C. Ramsey-Bell, and D. S. Covert, 1993: Atmospheric sulfur chemistry and cloud condensation nuclei (CCN) concentrations over the northeastern Pacific Coast. *J. Geophys. Res.*, 98, 12701, https://doi.org/10.1029/93JD00815.

Bertram, T. H., R. E. Cochran, V. H. Grassian, and E. A. Stone, 2018: Sea spray aerosol chemical composition: Elemental and molecular mimics for laboratory studies of heterogeneous and multiphase reactions. *Chem. Soc. Rev.*, 47, 2374–2400, https://doi.org/10.1039/c7cs00008a.

Bian, H., and Coauthors, 2019: Observationally constrained analysis of sea salt aerosol in the marine atmosphere. *Atmos. Chem. Phys.*, 19, 10773–10785, https://doi.org/10.5194/acp-19-10773-2019.

Bigg, E. K., 1953: The formation of atmospheric ice crystals by the freezing of droplets. *Q. J. R. Meteorol. Soc.*, 79, 510–519, https://doi.org/10.1002/qj.49707934207.

Bird, R. B.; Stewart, W. E.; Lightfoot, E. N. *Transport Phenomena*; Wiley India Pvt. Ltd., 2014.

Boose, Y., and Coauthors, 2016: Ice nucleating particles in the Saharan Air Layer. *Atmos. Chem. Phys.*, 16, 9067–9087, https://doi.org/10.5194/acp-16-9067-2016.

Boucher, O., and Coauthors, 2013: Clouds and aerosols. *Climate Change 2013 the Physical Science Basis: Working Group I Contribution to the Fifth Assessment Report of the Intergovernmental Panel on Climate Change*, Cambridge University Press, 571–658.

Bowdle, D. A., P. V. Hobbs, and L. F. Radke, 1985: Particles in the lower troposphere over the High Plains of the United States. Part III: ice nuclei. *J. Clim. Appl. Meteorol.*, 24, 1370–1376, https://doi.org/10.1175/1520-0450(1985)024<1370:PITLTO>2.0.CO;2.

Brock, C. A., and Coauthors, 2019: Aerosol size distributions during the Atmospheric Tomography Mission (ATom): Methods, uncertainties, and data products. *Atmos. Meas. Tech.*, 12, 3081–3099, https://doi.org/10.5194/amt-12-3081-2019.

Campbell, J. M., F. C. Meldrum, and H. K. Christenson, 2017: Observing the formation of ice and organic crystals in active sites. *Proc. Natl. Acad. Sci. U. S. A.*, 114, 810–815, https://doi.org/10.1073/pnas.1617717114.

Carlson, T. N., and J. M. Prospero, 1972: The Large-Scale Movement of Saharan Air Outbreaks over the Northern Equatorial Atlantic. *J. Appl. Meteorol.*, 11, 283–297, https://doi.org/10.1175/1520-0450(1972)011<0283:TLSMOS>2.0.CO;2.

Charnawskas, J. C., and Coauthors, 2017: Condensed-phase biogenic–anthropogenic interactions with implications for cold cloud formation. *Faraday Discuss.*, 200, 165–194, https://doi.org/10.1039/C7FD00010C.

Chen, Y., S. M. Kreidenweis, L. M. McInnes, D. C. Rogers, and P. J. DeMott, 1998: Single particle analyses of ice nucleating aerosols in the upper troposphere and lower stratosphere. *Geophys. Res. Lett.*, 25, 1391–1394, https://doi.org/10.1029/97GL03261.

Christner, B. C., R. Cai, C. E. Morris, K. S. McCarter, C. M. Foreman, M. L. Skidmore, S. N. Montross, and D. C. Sands, 2008: Geographic, seasonal, and precipitation chemistry influence on the abundance and activity of biological ice nucleators in rain and snow. *Proc. Natl. Acad. Sci. U. S. A.*, 105, 18854–18859, https://doi.org/10.1073/pnas.0809816105.

Collins, D. B., and Coauthors, 2014: Direct aerosol chemical composition measurements to evaluate the physicochemical differences between controlled sea spray aerosol generation schemes. *Atmos. Meas. Tech.*, 7, 3667–3683, https://doi.org/10.5194/amt-7-3667-2014.

Conen, F., C. E. Morris, J. Leifeld, M. V. Yakutin, and C. Alewell, 2011: Biological residues define the ice nucleation properties of soil dust. *Atmos. Chem. Phys.*, 11, 9643–9648, https://doi.org/10.5194/acp-11-9643-2011.

Connolly, P. J., O. Möhler, P. R. Field, H. Saathoff, R. Burgess, T. Choularton, and M. Gallagher, 2009: Studies of heterogeneous freezing by three different desert dust samples. *Atmos. Chem. Phys.*, 9, 2805–2824, https://doi.org/10.5194/acp-9-2805-2009.

Cooper, W. A., and G. Vali, 1981: The Origin of Ice in Mountain Cap Clouds. *J. Atmos. Sci.*, 38, 1244–1259, https://doi.org/10.1175/1520-0469(1981)038<1244:TOOIIM>2.0.CO;2.

Cotton, W. R., and Coauthors, 2003: RAMS 2001: Current status and future directions. *Meteorol. Atmos. Phys.*, 82, 5–29, https://doi.org/10.1007/s00703-001-0584-9.

Crawford, I., and Coauthors, 2012: Ice formation and development in aged, wintertime cumulus over the UK: Observations and modelling. *Atmos. Chem. Phys.*, 12, 4963–4985, https://doi.org/10.5194/acp-12-4963-2012.

Cziczo, D. J., and J. P. D. Abbatt, 2000: Infrared Observations of the Response of NaCl, MgCl2, NH4HSO4, and NH4NO3 Aerosols to Changes in Relative Humidity from 298 to 238 K. *J. Phys. Chem. A*, 104, 2038–2047, https://doi.org/10.1021/jp9931408.

——, D. M. Murphy, P. K. Hudson, and D. S. Thomson, 2004: Single particle measurements of the chemical composition of cirrus ice residue during CRYSTAL-FACE. *J. Geophys. Res. Atmos.*, 109, D04201, https://doi.org/10.1029/2003jd004032.

——, and Coauthors, 2013: Clarifying the dominant sources and mechanisms of cirrus cloud formation. *Science* (80-.)., 340, 1320–1324, https://doi.org/10.1126/science.1234145.

——, and K. D. Froyd, 2014: Sampling the composition of cirrus ice residuals. *Atmos. Res.*, 142, 15–31, https://doi.org/10.1016/j.atmosres.2013.06.012.

Dahneke, B. (1983) Simple kinetic theory of Brownian diffusion in vapors and aerosols, in Theory of Dispersed Multiphase Flow, *R. E. Meyer, ed.*, Academic Press, New York, pp. 97-133.

David, R. O., and Coauthors, 2019: Pore condensation and freezing is responsible for ice formation below water saturation for porous particles. *Proc. Natl. Acad. Sci. U. S. A.*, 116, 8184–8189, https://doi.org/10.1073/pnas.1813647116.

DeMott, P. J., M. P. Meyers, and W. R. Cotton, 1994: Parameterization and Impact of Ice initiation Processes Relevant to Numerical Model Simulations of Cirrus Clouds. *J. Atmos. Sci.*, 51, 77–90, https://doi.org/10.1175/1520-0469(1994)051<0077:PAIOII>2.0.CO;2.

——, D. C. Rogers, and S. M. Kreidenweis, 1997: The susceptibility of ice formation in upper tropospheric clouds to insoluble aerosol components. *J. Geophys. Res. Atmos.*, 102, 19575–19584, https://doi.org/10.1029/97jd01138.

——, D. C. Rogers, S. M. Kreidenweis, Y. Chen, C. H. Twohy, D. Baumgardner, A. J. Heymsfield, and K. R. Chan, 1998: The role of heterogeneous freezing nucleation in upper tropospheric clouds: Inferences from SUCCESS. *Geophys. Res. Lett.*, 25, 1387–1390, https://doi.org/10.1029/97GL03779.

——, D. J. Cziczo, A. J. Prenni, D. M. Murphy, S. M. Kreidenweis, D. S. Thomson, R. Borys, and D. C. Rogers, 2003a: Measurements of the concentration and composition of nuclei for cirrus formation. *Proc. Natl. Acad. Sci.*, 100, 14655–14660, https://doi.org/10.1073/pnas.2532677100.

——, K. Sassen, M. R. Poellot, D. Baumgardner, D. C. Rogers, S. D. Brooks, A. J. Prenni, and S. M. Kreidenweis, 2003b: African dust aerosols as atmospheric ice nuclei. *Geophys. Res. Lett.*, 30, 26–29, https://doi.org/10.1029/2003GL017410.

——, M. D. Petters, A. J. Prenni, C. M. Carrico, S. M. Kreidenweis, J. L. Collett, and H. Moosmüller, 2009a: Ice nucleation behavior of biomass combustion particles at cirrus temperatures. *J. Geophys. Res. Atmos.*, 114, D16205, https://doi.org/10.1029/2009JD012036.

——, K. Sassen, M. R. Poellot, D. Baumgardner, D. C. Rogers, S. D. Brooks, A. J. Prenni, and S. M. Kreidenweis, 2009b: Correction to "African dust aerosols as atmospheric ice nuclei." *Geophys. Res. Lett.*, 36, https://doi.org/10.1029/2009GL037639.

——, and Coauthors, 2010: Predicting global atmospheric ice nuclei distributions and their impacts on climate. *Proc. Natl. Acad. Sci.*, 107, 11217–11222, https://doi.org/10.1073/pnas.0910818107.

——, and Coauthors, 2015: Integrating laboratory and field data to quantify the immersion freezing ice nucleation activity of mineral dust particles. *Atmos. Chem. Phys.*, 15, 393–409, https://doi.org/10.5194/acp-15-393-2015.

——, and Coauthors, 2017: Comparative measurements of ambient atmospheric concentrations of ice nucleating particles using multiple immersion freezing methods and a continuous flow diffusion chamber. *Atmos. Chem. Phys.*, 17, 11227–11245, https://doi.org/10.5194/acp-17-11227-2017.

——, and Coauthors, 2018: The Fifth International Workshop on Ice Nucleation phase 2 (FIN-02): laboratory intercomparison of ice nucleation measurements. *Atmos. Meas. Tech.*, 11, 6231–6257, https://doi.org/10.5194/amt-11-6231-2018.

——, and Coauthors, 2023: Atmospheric oxidation impact on sea spray produced ice nucleating particles. *Environ. Sci. Atmos.*, https://doi.org/10.1039/d3ea00060e.

Eidhammer, T., and Coauthors, 2010: Ice initiation by aerosol particles: Measured and predicted ice nuclei concentrations versus measured ice crystal concentrations in an orographic wave cloud. *J. Atmos. Sci.*, 67, 2417–2436, https://doi.org/10.1175/2010JAS3266.1.

Ezhova, E., V.-M. Kerminen, K. E. J. Lehtinen, and M. Kulmala, 2018: A simple model for the time evolution of the condensation sink in the atmosphere for intermediate Knudsen numbers. *Atmos. Chem. Phys.*, 18, 2431–2442, https://doi.org/10.5194/acp-18-2431-2018.

Field, P. R., and Coauthors, 2001: Ice nucleation in orographic wave clouds: Measurements made during INTACC. *Q. J. R. Meteorol. Soc.*, 127, 1493–1512, https://doi.org/10.1002/qj.49712757502.

——, and Coauthors, 2017: Chapter 7. Secondary Ice Production - current state of the science and recommendations for the future. *Meteorol. Monogr.,* https://doi.org/10.1175/amsmonographs-d-16-0014.1.

Fitzgerald, J. W., 1991: Marine aerosols: A review. *Atmos. Environ. Part A*, Gen. Top., 25, 533–545, https://doi.org/10.1016/0960-1686(91)90050-H.

Fletcher, N., 1962: Physics of Rain Clouds. Cambridge University Press, 386 pp.

Froyd, K. D., S. M. Murphy, D. M. Murphy, J. A. De Gouw, N. C. Eddingsaas, and P. O. Wennberg, 2010: Contribution of isoprene-derived organosulfates to free tropospheric aerosol mass. *Proc. Natl. Acad. Sci. U. S. A.*, 107, 21360–21365, https://doi.org/10.1073/pnas.1012561107.

Gantt, B., and N. Meskhidze, 2013: The physical and chemical characteristics of marine primary organic aerosol: A review. *Atmos. Chem. Phys.*, 13, 3979–3996, https://doi.org/10.5194/acp-13-3979-2013.

Gasparini, B., A. Meyer, D. Neubauer, S. Münch, and U. Lohmann, 2018: Cirrus cloud properties as seen by the CALIPSO satellite and ECHAM-HAM global climate model. *J. Clim.*, 31, 1983–2003, https://doi.org/10.1175/JCLI-D-16-0608.1.

Gierens, K., 2003: On the transition between heterogeneous and homogeneous freezing. *Atmos. Chem. Phys.*, 3, 437–446, https://doi.org/10.5194/acp-3-437-2003.

Haag, W., B. Kärcher, J. Ström, A. Minikin, U. Lohmann, J. Ovarlez, and A. Stohl, 2003: Freezing thresholds and cirrus cloud formation mechanisms inferred from in situ measurements of relative humidity. *Atmos. Chem. Phys.*, 3, 1791–1806, https://doi.org/10.5194/acp-3-1791-2003.

Hallett, J., and S. C. Mossop, 1974: Production of secondary ice particles during the riming process. *Nature*, 249, 26–28.

Harrison, A. D., and Coauthors, 2022: The ice-nucleating activity of African mineral dust in the Caribbean boundary layer. *Atmos. Chem. Phys.*, 22, 9663–9680, https://doi.org/10.5194/acp-22-9663-2022.

Heymsfield, A. J., C. A. Knight, and J. E. Dye, 1979: Ice Initiation in Unmixed Updraft Cores in Northeast Colorado Cumulus Congestus Clouds. *J. Atmos. Sci.*, 36, 2216–2229, https://doi.org/10.1175/1520-0469(1979)036<2216:IIIUUC>2.0.CO;2.

——, and Coauthors, 2017: Cirrus Clouds. *Meteorol. Monogr.*, 58, 2.1-2.26, https://doi.org/10.1175/AMSMONOGRAPHS-D-16-0010.1.

Hill, T. C. J., B. F. Moffett, P. J. DeMott, D. G. Georgakopoulos, W. L. Stump, and G. D. Franc, 2014: Measurement of ice nucleation-active bacteria on plants and in precipitation by quantitative PCR. *Appl. Environ. Microbiol.*, 80, 1256–1267, https://doi.org/10.1128/AEM.02967-13.

——, P. J. Demott, Y. Tobo, J. Fröhlich-Nowoisky, B. F. Moffett, G. D. Franc, and S. M. Kreidenweis, 2016: Sources of organic ice nucleating particles in soils. *Atmos. Chem. Phys.*, 16, 7195–7211, https://doi.org/10.5194/acp-16-7195-2016.

——, and Coauthors, 2023: Resolving the controls over the production and emission of ice-nucleating particles in sea spray. *Environ. Sci. Atmos.*, 3, 970–990, https://doi.org/10.1039/D2EA00154C.

Hiranuma, N., and Coauthors, 2014: A comprehensive parameterization of heterogeneous ice nucleation of dust surrogate: laboratory study with hematite particles and its application to atmospheric models. *Atmos. Chem. Phys.*, 14, 13145–13158, https://doi.org/10.5194/acp-14-13145-2014.

——, and Coauthors, 2015: A comprehensive laboratory study on the immersion freezing behavior of illite NX particles: A comparison of 17 ice nucleation measurement techniques. *Atmos. Chem. Phys.*, 15, 2489–2518, https://doi.org/10.5194/acp-15-2489-2015.

Hoose, C., and O. Möhler, 2012: Heterogeneous ice nucleation on atmospheric aerosols: a review of results from laboratory experiments. *Atmos. Chem. Phys.*, 12, 9817–9854, https://doi.org/10.5194/acp-12-9817-2012.

Huang, Y., and Coauthors, 2022: Microphysical processes producing high ice water contents (HIWCs) in tropical convective clouds during the HAIC-HIWC field campaign: Dominant role of secondary ice production. *Atmos. Chem. Phys.*, 22, 2365–2384, https://doi.org/10.5194/acp-22-2365-2022.

Ickes, L., and Coauthors, 2020: The ice-nucleating activity of Arctic sea surface microlayer samples and marine algal cultures. *Atmos. Chem. Phys.*, 20, 11089–11117, https://doi.org/10.5194/acp-20-11089-2020.

Ignatius, K., and Coauthors, 2016: Heterogeneous ice nucleation of viscous secondary organic aerosol produced from ozonolysis of α-pinene. *Atmos. Chem. Phys.,* 16, 6495–6509, https://doi.org/10.5194/acp-16-6495-2016.

Jensen, E. J., S. Kinne, and O. B. Toon, 1994: Tropical cirrus cloud radiative forcing: Sensitivity studies. *Geophys. Res. Lett.*, 21, 2023–2026, https://doi.org/10.1029/94GL01358.

Kaluarachchi, C. P., and Coauthors, 2022a: Size-Dependent Morphology, Composition, Phase State, and Water Uptake of Nascent Submicrometer Sea Spray Aerosols during a Phytoplankton Bloom. *ACS Earth Sp. Chem.*, 6, 116–130, https://doi.org/10.1021/acsearthspacechem.1c00306.

——, and Coauthors, 2022b: Effects of Atmospheric Aging Processes on Nascent Sea Spray Aerosol Physicochemical Properties. *ACS Earth Sp. Chem.*, 6, 2732–2744, https://doi.org/10.1021/acsearthspacechem.2c00258.

Kanji, Z. A., L. A. Ladino, H. Wex, Y. Boose, M. Burkert-Kohn, D. J. Cziczo, and M. Krämer, 2017: Overview of Ice Nucleating Particles. *Meteorol. Monogr.,* 58, 1.1-1.33, https://doi.org/10.1175/amsmonographs-d-16-0006.1.

——, R. C. Sullivan, M. Niemand, P. J. DeMott, A. J. Prenni, C. Chou, H. Saathoff, and O. Möhler, 2019: Heterogeneous ice nucleation properties of natural desert dust particles coated with a surrogate of secondary organic aerosol. *Atmos. Chem. Phys.*, 19, 5091–5110, https://doi.org/10.5194/acp-19-5091-2019.

Kärcher, B., and U. Lohmann, 2003: A parameterization of cirrus cloud formation: Heterogeneous freezing. *J. Geophys. Res.*, 108, 4402, https://doi.org/10.1029/2002JD003220.

Kasparoglu, S., and Coauthors, 2022: Experimental Determination of the Relationship Between Organic Aerosol Viscosity and Ice Nucleation at Upper Free Tropospheric Conditions. *J. Geophys. Res. Atmos.*, 127, 1–20, https://doi.org/10.1029/2021JD036296.

Kaufman, Y. J., 2005: Dust transport and deposition observed from the Terra-Moderate Resolution Imaging Spectroradiometer (MODIS) spacecraft over the Atlantic Ocean. J. *Geophys. Res.*, 110, D10S12, https://doi.org/10.1029/2003JD004436.

Keinert, A., D. Spannagel, T. Leisner, and A. Kiselev, 2020: Secondary ice production upon freezing of freely falling drizzle droplets. *J. Atmos. Sci.*, 77, 2959–2967, https://doi.org/10.1175/JAS-D-20-0081.1.

Knopf, D. A., P. A. Alpert, and B. Wang, 2018: The Role of Organic Aerosol in Atmospheric Ice Nucleation: A Review. *ACS Earth Sp. Chem.*, 2, 168–202, https://doi.org/10.1021/acsearthspacechem.7b00120.

Kong, X., and Coauthors, 2018: A continuous flow diffusion chamber study of sea salt particles acting as cloud nuclei: deliquescence and ice nucleation. *Tellus, Ser. B Chem. Phys. Meteorol.*, 70, 1–11, https://doi.org/10.1080/16000889.2018.1463806.

Koop, T., B. Luo, A. Tsias, and T. Peter, 2000b: Water activity as the determinant for homogeneous ice nucleation in aqueous solutions. *Nature*, 406, 611–614, https://doi.org/10.1038/35020537.

——, A. Kapilashrami, L. T. Molina, and M. J. Molina, 2000b: Phase transitions of sea-salt/water mixtures at low temperatures: Implications for ozone chemistry in the polar marine boundary layer. *J. Geophys. Res. Atmos.*, 105, 26393–26402, https://doi.org/10.1029/2000JD900413.

——, J. Bookhold, M. Shiraiwa, and U. Pöschl, 2011: Glass transition and phase state of organic compounds: dependency on molecular properties and implications for secondary organic aerosols in the atmosphere. *Phys. Chem. Chem. Phys.*, 13, 19238, https://doi.org/10.1039/c1cp22617g.

Korolev, A., and G. A. Isaac, 2006: Relative Humidity in Liquid, Mixed-Phase, and Ice Clouds. *J. Atmos. Sci.*, 63, 2865–2880, https://doi.org/10.1175/JAS3784.1.

——, 2007: Limitations of the Wegener-Bergeron-Findeisen mechanism in the evolution of mixed-phase clouds. *J. Atmos. Sci.*, 64, 3372–3375, https://doi.org/10.1175/JAS4035.1.

——, E. F. Emery, J. W. Strapp, S. G. Cober, G. A. Isaac, M. Wasey, and D. Marcotte, 2011: Small ice particles in tropospheric clouds: Fact or artifact? Airborne icing instrumentation evaluation experiment. *Bull. Am. Meteorol. Soc.*, 92, 967–973, https://doi.org/10.1175/2010BAMS3141.1.

——, and Coauthors, 2017: Mixed-Phase Clouds: Progress and Challenges. *Meteorol. Monogr.*, 58, 5.1-5.50, https://doi.org/10.1175/amsmonographs-d-17-0001.1.

——, and T. Leisner, 2020: Review of experimental studies of secondary ice production. *Atmos. Chem. Phys.*, 20, 11767–11797, https://doi.org/10.5194/acp-20-11767-2020.

——, and Coauthors, 2020: A new look at the environmental conditions favorable to secondary ice production. *Atmos. Chem. Phys.*, 20, 1391–1429, https://doi.org/10.5194/acp-20-1391-2020.

——, P. J. Demott, I. Heckman, M. Wolde, E. Williams, D. J. Smalley, and M. F. Donovan, 2022: Observation of secondary ice production in clouds at low temperatures. *Atmos. Chem. Phys.*, 22, 13103–13113, https://doi.org/10.5194/acp-22-13103-2022.

——, and Heckman, I., 20AD: SPICULE: Ka-Band Probe Radar (KPR) profile data. Version 1.0. https://doi.org/10.26023/Z36H-G1VR-F300.

Krämer, M., and Coauthors, 2009: Ice supersaturations and cirrus cloud crystal numbers. *Atmos. Chem. Phys.*, 9, 3505–3522, https://doi.org/10.5194/acp-9-3505-2009.

——, and Coauthors, 2016: A microphysics guide to cirrus clouds – Part 1: Cirrus types. *Atmos. Chem. Phys.*, 16, 3463–3483, https://doi.org/10.5194/acp-16-3463-2016.

——, and Coauthors, 2020: A microphysics guide to cirrus - Part 2: Climatologies of clouds and humidity from observations. *Atmos. Chem. Phys.*, 20, 12569–12608, https://doi.org/10.5194/acp-20-12569-2020.

Ladino, L. A., and Coauthors, 2016: Addressing the ice nucleating abilities of marine aerosol: A combination of deposition mode laboratory and field measurements. *Atmos. Environ.*, 132, 1–10, https://doi.org/10.1016/j.atmosenv.2016.02.028.

——, A. Korolev, I. Heckman, M. Wolde, A. M. Fridlind, and A. S. Ackerman, 2017: On the role of ice-nucleating aerosol in the formation of ice particles in tropical mesoscale convective systems. *Geophys. Res. Lett.*, 44, 1574–1582, https://doi.org/10.1002/2016GL072455.

Lasher-Trapp, S., D. C. Leon, P. J. DeMott, C. M. Villanueva-Birriel, A. V. Johnson, D. H. Moser, C. S. Tully, and W. Wu, 2016: A multisensor investigation of rime splintering in tropical maritime cumuli. *J. Atmos. Sci.*, 73, 2547–2564, https://doi.org/10.1175/JAS-D-15-0285.1.

Lauber, A., A. Kiselev, T. Pander, P. Handmann, and T. Leisner, 2018: Secondary ice formation during freezing of levitated droplets. *J. Atmos. Sci.,* 75, 2815–2826, https://doi.org/10.1175/JAS-D-18-0052.1.

Lawson, P., B. A. Baker, C. G. Schmitt, and T. L. Jensen, 2001: An overview of microphysical properties of Arctic clouds observed in May and July 1998 during FIRE ACE. *J. Geophys. Res. Atmos.*, 106, 14989–15014, https://doi.org/10.1029/2000JD900789.

——, S. Woods, and H. Morrison, 2015: The Microphysics of Ice and Precipitation Development in Tropical Cumulus Clouds. *J. Atmos. Sci.*, 72, 2429–2445, https://doi.org/10.1175/JAS-D-14-0274.1.

——, C. Gurganus, S. Woods, and R. Bruintjes, 2017: Aircraft observations of cumulus microphysics ranging from the tropics to midlatitudes: Implications for a “new” secondary ice process. *J. Atmos. Sci.*, 74, 2899–2920, https://doi.org/10.1175/JAS-D-17-0033.1.

——, R. Bruintjes, S. Woods, and C. Gurganus, 2022: Coalescence and Secondary Ice Development in Cumulus Congestus Clouds. *J. Atmos. Sci.*, 79, 953–972, https://doi.org/10.1175/JAS-D-21-0188.1.

——, S. Woods, and R. Bruintjes, 2022: SPEC Learjet 35 Instrument Data. Version 2.0. https://doi.org/10.26023/NHSC-AC8Y-9W09.

——, Q. Mo, and R. Bruintjes, 2022: SPICULE: SPEC Learjet 35 Flight Videos. Version 1.0. https://doi.org/10.26023/G9FD-6NXX-5Y0P.

——, R. Bruintjes, and Q. Mo, 2022: SPEC Learjet Hawkeye-CPI Cloud Particle Images. Version 1.0. https://doi.org/10.26023/SFPD-T4AD-7Y03.

——, and Coauthors, 2023: The Secondary Production of Ice in Cumulus Experiment (SPICULE). *Bull. Am. Meteorol. Soc.*, 104, E51–E76, https://doi.org/10.1175/BAMS-D-21-0209.1.

Leung, G. R., S. M. Saleeby, G. A. Sokolowsky, S. W. Freeman, and S. C. Van Den Heever, 2023: Aerosol-cloud impacts on aerosol detrainment and rainout in shallow maritime tropical clouds. *Atmos. Chem. Phys.*, 23, 5263–5278, https://doi.org/10.5194/acp-23-5263-2023.

Levin, E. J. T., and Coauthors, 2019: Characteristics of Ice Nucleating Particles in and Around California Winter Storms. *J. Geophys. Res. Atmos.*, 124, 11530–11551, https://doi.org/10.1029/2019JD030831.

Liou, K.-N., 1986: Influence of Cirrus Clouds on Weather and Climate Processes: A Global Perspective. *Mon. Weather Rev.*, 114, 1167–1199.

Liu, S., and Coauthors, 2021: Sea spray aerosol concentration modulated by sea surface temperature. *Proc. Natl. Acad. Sci. U. S. A.*, 118, e2020583118, https://doi.org/10.1073/pnas.2020583118.

Luebke, A. E., and Coauthors, 2016: The origin of midlatitude ice clouds and the resulting influence on their microphysical properties. *Atmos. Chem. Phys.*, 16, 5793–5809, https://doi.org/10.5194/acp-16-5793-2016.

Lynch, D. K., 1996: Cirrus clouds: Their role in climate and global change. *Acta Astronaut.*, 38, 859–863, https://doi.org/10.1016/S0094-5765(96)00098-7.

Mahrt, F., K. Kilchhofer, C. Marcolli, P. Grönquist, R. O. David, M. Rösch, U. Lohmann, and Z. A. Kanji, 2020: The Impact of Cloud Processing on the Ice Nucleation Abilities of Soot Particles at Cirrus Temperatures. *J. Geophys. Res. Atmos.*, 125, 1–23, https://doi.org/10.1029/2019JD030922.

Marcolli, C., 2014: Deposition nucleation viewed as homogeneous or immersion freezing in pores and cavities. *Atmos. Chem. Phys.*, 14, 2071–2104, https://doi.org/10.5194/acp-14-2071-2014.

Martin, S. T., 2000: Phase transitions of aqueous atmospheric particles. *Chem. Rev.*, 100, 3403–3453, https://doi.org/10.1021/cr990034t.

Mayer, K. J., J. S. Sauer, J. Dinasquet, and K. A. Prather, 2020a: CAICE Studies: Insights from a Decade of Ocean-Atmosphere Experiments in the Laboratory. *Acc. Chem. Res.*, 53, 2510–2520, https://doi.org/10.1021/acs.accounts.0c00504.

——, X. Wang, M. V. Santander, B. A. Mitts, J. S. Sauer, C. M. Sultana, C. D. Cappa, and K. A. Prather, 2020b: Secondary Marine Aerosol Plays a Dominant Role over Primary Sea Spray Aerosol in Cloud Formation. *ACS Cent. Sci.*, 6, 2259–2266, https://doi.org/10.1021/acscentsci.0c00793.

McCluskey, C. S., and Coauthors, 2014: Characteristics of atmospheric ice nucleating particles associated with biomass burning in the US: Prescribed burns and wildfires. *J. Geophys. Res. Atmos.*, 119, 10458–10470, https://doi.org/10.1002/2014JD021980.

——, and Coauthors, 2018a: A Mesocosm Double Feature: Insights into the Chemical Makeup of Marine Ice Nucleating Particles. *J. Atmos. Sci.*, 75, 2405–2423, https://doi.org/10.1175/JAS-D-17-0155.1.

——, and Coauthors, 2018b: Observations of Ice Nucleating Particles Over Southern Ocean Waters. *Geophys. Res. Lett.*, 45, 11,989-11,997, https://doi.org/10.1029/2018GL079981.

Meyers, M. P., P. J. DeMott, and W. R. Cotton, 1992: New Primary Ice-Nucleation Parameterizations in an Explicit Cloud Model. *J. Appl. Meteorol.*, 31, 708–721, https://doi.org/10.1175/1520-0450(1992)031<0708:NPINPI>2.0.CO;2.

——, R. L. Walko, J. Y. Harrington, and W. R. Cotton, 1997: New RAMS cloud microphysics parameterization. Part II: The two-moment scheme. *Atmos. Res.*, 45, 3–39, https://doi.org/10.1016/S0169-8095(97)00018-5.

Möhler, O., and Coauthors, 2008: The effect of organic coating on the heterogeneous ice nucleation efficiency of mineral dust aerosols. *Environ. Res. Lett.*, 3, https://doi.org/10.1088/1748-9326/3/2/025007.

Moore, K. A., Hill, T. J. C., McCluskey, C. S., and Coauthors, 2023: Characterizing Ice Nucleating Particles over the Southern Ocean using Simultaneous Aircraft and Ship Observations. *ESS Open Archive*. https://doi.org/10.22541/essoar.168889890.00880378/v1

Mossop, S. C., 1978: The influence of drop size distribution on the production of secondary ice particles during graupel growth. *Q. J. R. Meteorol. Soc.*, 104, 323–330, https://doi.org/10.1002/qj.49710444007.

Mülmenstädt, J., O. Sourdeval, J. Delanoë, and J. Quaas, 2015: Frequency of occurrence of rain from liquid-, mixed-, and ice-phase clouds derived from A-Train satellite retrievals. *Geophys. Res. Lett.*, 42, 6502–6509, https://doi.org/10.1002/2015GL064604.

Murphy, D. M., D. S. Thomson, and M. J. Mahoney, 1998: In Situ Measurements of Organics, Meteoritic Material, Mercury, and Other Elements in Aerosols at 5 to 19 Kilometers. *Science* (80-.)., 282, 1664–1669, https://doi.org/10.1126/science.282.5394.1664.

——, and Coauthors, 2019: The distribution of sea-salt aerosol in the global troposphere. *Atmos. Chem. Phys.*, 19, 4093–4104, https://doi.org/10.5194/acp-19-4093-2019.

Murray, B. J., and Coauthors, 2010: Heterogeneous nucleation of ice particles on glassy aerosols under cirrus conditions. *Nat. Geosci.*, 3, 233–237, https://doi.org/10.1038/ngeo817.

——, D. O'sullivan, J. D. Atkinson, and M. E. Webb, 2012: Ice nucleation by particles immersed in supercooled cloud droplets. *Chem. Soc. Rev.*, 41, 6519–6554, https://doi.org/10.1039/c2cs35200a.

Niemand, M., and Coauthors, 2012: A particle-surface-area-based parameterization of immersion freezing on desert dust particles. *J. Atmos. Sci.*, 69, 3077–3092, https://doi.org/10.1175/JAS-D-11-0249.1.

O'Dowd, C. D., and G. De Leeuw, 2007: Marine aerosol production: A review of the current knowledge. Philos. Trans. *R. Soc. A Math. Phys. Eng. Sci.*, 365, 1753–1774, https://doi.org/10.1098/rsta.2007.2043.

——, M. H. Smith, I. E. Consterdine, and J. A. Lowe, 1997: Marine aerosol, sea-salt, and the marine sulphur cycle: A short review. *Atmos. Environ.*, 31, 73–80, https://doi.org/10.1016/S1352-2310(96)00106-9.

——, and Coauthors, 2004: Biogenically driven organic contribution to marine aerosol. *Nature*, 431, 676–680, https://doi.org/10.1038/nature02959.

Pandis, S. N., L. M. Russell, and J. H. Seinfeld, 1994: The relationship between DMS flux and CCN concentration in remote marine regions. *J. Geophys. Res.*, 99, 16945, https://doi.org/10.1029/94JD01119.

Patade, S., and Coauthors, 2021: Empirical formulation for multiple groups of primary biological ice nucleating particles from field observations over Amazonia. *J. Atmos. Sci.*, 2195–2220, https://doi.org/10.1175/JAS-D-20-0096.1.

——, and Coauthors, 2022: The influence of multiple groups of biological ice nucleating particles on microphysical properties of mixed-phase clouds observed during MC3E. *Atmos. Chem. Phys.*, 22, 12055–12075, https://doi.org/10.5194/acp-22-12055-2022.

Patnaude, R. J., M. Diao, X. Liu, and S. Chu, 2021a: Effects of Thermodynamics, Dynamics and Aerosols on Cirrus Clouds Based on In Situ Observations and NCAR CAM6 Model. *Atmos. Chem. Phys.*, 21, 1835–1859, https://doi.org/10.5194/acp-21-1835-2021.

——, R. J. Perkins, S. M. Kreidenweis, and P. J. DeMott, 2021b: Is Ice Formation by Sea Spray Particles at Cirrus Temperatures Controlled by Crystalline Salts? *ACS Earth Sp. Chem.*, 5, 2196–2211, https://doi.org/10.1021/acsearthspacechem.1c00228.

Pazmany, A. L., and S. J. Haimov, 2018: Coherent power measurements with a compact airborne Ka-band precipitation radar. *J. Atmos. Ocean. Technol.*, 35, 3–20, https://doi.org/10.1175/JTECH-D-17-0058.1.

Peckhaus, A., A. Kiselev, T. Hiron, M. Ebert, and T. Leisner, 2016a: A comparative study of K-rich and Na/Ca-rich feldspar ice-nucleating particles in a nanoliter droplet freezing assay. *Atmos. Chem. Phys.*, 16, 11477–11496, https://doi.org/10.5194/acp-16-11477-2016.

——, ——, R. Wagner, D. Duft, and T. Leisner, 2016b: Temperature-dependent formation of NaCl dihydrate in levitated NaCl and sea salt aerosol particles. *J. Chem. Phys.*, 145, https://doi.org/10.1063/1.4972589.

Peng, Z., and J. L. Jimenez, 2020: Radical chemistry in oxidation flow reactors for atmospheric chemistry research. *Chem. Soc. Rev.*, 49, 2570–2616, https://doi.org/10.1039/C9CS00766K.

Petters, M. D., and T. P. Wright, 2015: Revisiting ice nucleation from precipitation samples. *Geophys. Res. Lett.*, 42, 8758–8766, https://doi.org/10.1002/2015GL065733.

Phillips, V. T. J., A. M. Blyth, P. R. A. Brown, T. W. Choularton, and J. Latham, 2001: The glaciation of a cumulus cloud over New Mexico. *Q. J. R. Meteorol. Soc.*, 127, 1513–1534, https://doi.org/10.1256/smsqj.57502.

——, P. J. DeMott, and C. Andronache, 2008: An empirical parameterization of heterogeneous ice nucleation for multiple chemical species of aerosol. *J. Atmos. Sci.*, 65, 2757–2783, https://doi.org/10.1175/2007JAS2546.1.

——, J. I. Yano, and A. Khain, 2017: Ice multiplication by breakup in ice-ice collisions. Part I: Theoretical formulation. J. *Atmos. Sci.*, 74, 1705–1719, https://doi.org/10.1175/JAS-D-16-0224.1.

——, S. Patade, J. Gutierrez, and A. Bansemer, 2018: Secondary ice production by fragmentation of freezing drops: Formulation and theory. *J. Atmos. Sci.*, 75, 3031–3070, https://doi.org/10.1175/JAS-D-17-0190.1.

Prather, K. A., and Coauthors, 2013: Bringing the ocean into the laboratory to probe the chemical complexity of sea spray aerosol. *Proc. Natl. Acad. Sci. U. S. A.*, 110, 7550–7555, https://doi.org/10.1073/pnas.1300262110.

Prenni, A. J., and Coauthors, 2007: Examinations of ice formation processes in Florida cumuli using ice nuclei measurements of anvil ice crystal particle residues. *J. Geophys. Res. Atmos.*, 112, 1–16, https://doi.org/10.1029/2006JD007549.

Price, H. C., and Coauthors, 2018: Atmospheric Ice-Nucleating Particles in the Dusty Tropical Atlantic. *J. Geophys. Res. Atmos.*, 123, 2175–2193, https://doi.org/10.1002/2017JD027560.

Pruppacher, K., and J. D. Klett, 1997: Microphysics of Clouds and Precipitation. Kluwer Academic Publishers,.

Qu, Z., and Coauthors, 2022: The impacts of secondary ice production on microphysics and dynamics in tropical convection. *Atmos. Chem. Phys.*, 22, 12287–12310, https://doi.org/10.5194/acp-22-12287-2022.

Quinn, P. K., D. B. Collins, V. H. Grassian, K. A. Prather, and T. S. Bates, 2015: Chemistry and Related Properties of Freshly Emitted Sea Spray Aerosol. *Chem. Rev.*, 115, 4383–4399, https://doi.org/10.1021/cr500713g.

Richardson, M., 2009: Making Real Time Measurements of Ice Nuclei Concentrations at Upper Tropospheric Temperatures: Extending the Capabilities of the Continuous Flow Diffusion. Colorado State University, 274 pp.

Rogers, D. C., 1988: Development of a continuous flow thermal gradient diffusion chamber for ice nucleation studies. *Atmos. Res.,* 22, 149–181, https://doi.org/10.1016/0169-8095(88)90005-1.

——, P. J. DeMott, S. M. Kreidenweis, and Y. Chen, 1998: Measurements of ice nucleating aerosols during SUCCESS. *Geophys. Res. Lett.*, 25, 1383–1386, https://doi.org/10.1029/97GL03478.

——, P. J. DeMott, S. M. Kreidenweis, and Y. Chen, 2001: A continuous-flow diffusion chamber for airborne measurements of ice nuclei. *J. Atmos. Ocean. Technol.*, 18, 725–741, https://doi.org/10.1175/1520-0426(2001)018<0725:ACFDCF>2.0.CO;2.

Rowe, J. P., A. T. Lambe, and W. H. Brune, 2020: Technical Note: Effect of varying the λ = 185 and 254 nm photon flux ratio on radical generation in oxidation flow reactors. *Atmos. Chem. Phys.*, 20, 13417–13424, https://doi.org/10.5194/acp-20-13417-2020.

Saleeby, S. M., and W. R. Cotton, 2008: A Binned Approach to Cloud-Droplet Riming Implemented in a Bulk Microphysics Model. *J. Appl. Meteorol. Climatol.*, 47, 694–703, https://doi.org/10.1175/2007JAMC1664.1.

——, and S. C. Van den Heever, 2013: Developments in the CSU-RAMS aerosol model: Emissions, nucleation, regeneration, deposition, and radiation. *J. Appl. Meteorol. Climatol.*, 52, 2601–2622, https://doi.org/10.1175/JAMC-D-12-0312.1.

——, S. C. Heever, P. J. Marinescu, S. M. Kreidenweis, and P. J. DeMott, 2016: Aerosol effects on the anvil characteristics of mesoscale convective systems. *J. Geophys. Res. Atmos.*, 121, 3446–3464, https://doi.org/10.1002/2016JD025082.

Saliba, G., and Coauthors, 2020: Seasonal Differences and Variability of Concentrations, Chemical Composition, and Cloud Condensation Nuclei of Marine Aerosol Over the North Atlantic. *J. Geophys. Res. Atmos.*, 125, 1–24, https://doi.org/10.1029/2020JD033145.

Sanchez, K. J., and Coauthors, 2021: Measurement report: Cloud processes and the transport of biological emissions affect southern ocean particle and cloud condensation nuclei concentrations. *Atmos. Chem. Phys.*, 21, 3427–3446, https://doi.org/10.5194/acp-21-3427-2021.

Sassen, K., W. P. Arnott, D. O. C. Starr, G. G. Mace, Z. Wang, and M. R. Poellot, 2003a: Midlatitude cirrus clouds derived from hurricane Nora: A case study with implications for ice crystal nucleation and shape. *J. Atmos. Sci.*, 60, 873–891, https://doi.org/10.1175/1520-0469(2003)060<0873:MCCDFH>2.0.CO;2.

——, P. J. DeMott, J. M. Prospero, and M. R. Poellot, 2003b: Saharan dust storms and indirect aerosol effects on clouds: CRYSTAL-FACE results. *Geophys. Res. Lett.*, 30, 1–4, https://doi.org/10.1029/2003GL017371.

——, Z. Wang, and D. Liu, 2008: Global distribution of cirrus clouds from CloudSat/cloud-aerosol lidar and infrared pathfinder satellite observations (CALIPSO) measurements. *J. Geophys. Res. Atmos.*, 113, D00A12, https://doi.org/10.1029/2008JD009972.

Saunders, C. P. R., and A. S. Hosseini, 2001: A laboratory study of the effect of velocity on Hallett–Mossop ice crystal multiplication. Atmos. Res., 59–60, 3–14, https://doi.org/10.1016/S0169-8095(01)00106-5.

Schill, G. P., and M. A. Tolbert, 2014: Heterogeneous ice nucleation on simulated sea-spray aerosol using Raman microscopy. *J. Phys. Chem. C*, 118, 29234–29241, https://doi.org/10.1021/jp505379j.

——, and Coauthors, 2020: Widespread biomass burning smoke throughout the remote troposphere. *Nat. Geosci.*, 13, 422–427, https://doi.org/10.1038/s41561-020-0586-1.

Schneider, J., and Coauthors, 2021: High homogeneous freezing onsets of sulfuric acid aerosol at cirrus temperatures. *Atmos. Chem. Phys.*, 21, 14403–14425, https://doi.org/10.5194/acp-21-14403-2021.

Schwarz, J. P., B. Weinzierl, B. H. Samset, M. Dollner, K. Heimerl, M. Z. Markovic, A. E. Perring, and L. Ziemba, 2017: Aircraft measurements of black carbon vertical profiles show upper tropospheric variability and stability. *Geophys. Res. Lett.*, 44, 1132–1140, https://doi.org/10.1002/2016GL071241.

Seifert, A., and K. D. Beheng, 2006: A two-moment cloud microphysics parameterization for mixed-phase clouds. Part 1: Model description. *Meteorol. Atmos. Phys.*, 92, 45–66, https://doi.org/10.1007/s00703-005-0112-4.

Seinfeld, J. H., and S. N. Pandis, 2006: Atmospheric Chemistry and Phyisics: From Air Pollution to Climate Change. 2nd Edition. Second. F. Herbert, Ed.

——, and Coauthors, 2016: Improving our fundamental understanding of the role of aerosol-cloud interactions in the climate system. *Proc. Natl. Acad. Sci. U. S. A.*, 113, 5781–5790, https://doi.org/10.1073/pnas.1514043113.

Shingler, T., and Coauthors, 2012: Characterisation and airborne deployment of a new counterflow virtual impactor inlet. *Atmos. Meas. Tech.*, 5, 1259–1269, https://doi.org/10.5194/amt-5-1259-2012.

Sjogren, S., and Coauthors, 2007: Hygroscopic growth and water uptake kinetics of two-phase aerosol particles consisting of ammonium sulfate, adipic and humic acid mixtures. *J. Aerosol Sci.*, 38, 157–171, https://doi.org/10.1016/j.jaerosci.2006.11.005.

Sotiropoulou, G., E. Vignon, G. Young, H. Morrison, S. J. O'Shea, T. Lachlan-Cope, A. Berne, and A. Nenes, 2021: Secondary ice production in summer clouds over the Antarctic coast: An underappreciated process in atmospheric models. *Atmos. Chem. Phys.*, 21, 755–771, https://doi.org/10.5194/acp-21-755-2021.

Stith, J. L., D. A. Burrows, and P. J. DeMott, 1994: Initiation of ice: comparison of numerical model results with observations of ice development in a cumulus cloud. *Atmos. Res.*, 32, 13–30, https://doi.org/10.1016/0169-8095(94)90048-5.

Stokes, M. D., G. B. Deane, K. Prather, T. H. Bertram, M. J. Ruppel, O. S. Ryder, J. M. Brady, and D. Zhao, 2013: A Marine Aerosol Reference Tank system as a breaking wave analogue for the production of foam and sea-spray aerosols. *Atmos. Meas. Tech.*, 6, 1085–1094, https://doi.org/10.5194/amt-6-1085-2013.

Sullivan, S., C. Hoose, A. Kiselev, T. Leisner, and A. Nenes, 2018a: Initiation of secondary ice production in clouds. *Atmos. Chem. Phys.*, 18, 1593–1610, https://doi.org/10.5194/acp-18-1593-2018.

——, C. Barthlott, J. Crosier, I. Zhukov, A. Nenes, and C. Hoose, 2018b: The effect of secondary ice production parameterization on the simulation of a cold frontal rainband. *Atmos. Chem. Phys.*, 18, 16461–16480, https://doi.org/10.5194/acp-18-16461-2018.

Suski, K. J., T. C. J. Hill, E. J. T. Levin, A. Miller, P. J. DeMott, and S. M. Kreidenweis, 2018: Agricultural harvesting emissions of ice-nucleating particles. *Atmos. Chem. Phys.*, 18, 13755–13771, https://doi.org/10.5194/acp-18-13755-2018.

Tang, I. N., and H. R. Munkelwitz, 1993: Composition and temperature dependence of the deliquescence properties of hygroscopic aerosols. *Atmos. Environ. Part A, Gen. Top.*, 27, 467–473, https://doi.org/10.1016/0960-1686(93)90204-C.

——, A. C. Tridico, and K. H. Fung, 1997: Thermodynamic and optical properties of sea salt aerosols. *J. Geophys. Res. Atmos.,* 102, 23269–23275, https://doi.org/10.1029/97jd01806.

Testa, B., and Coauthors, 2021: Ice Nucleating Particle Connections to Regional Argentinian Land Surface Emissions and Weather During the Cloud, Aerosol, and Complex Terrain Interactions Experiment. *J. Geophys. Res. Atmos.*, 126, 1–26, https://doi.org/10.1029/2021JD035186.

Tobo, Y., and Coauthors, 2013: Biological aerosol particles as a key determinant of ice nuclei populations in a forest ecosystem. *J. Geophys. Res. Atmos.*, 118, 10,100-10,110, https://doi.org/10.1002/jgrd.50801.

——, and Coauthors, 2019: Glacially sourced dust as a potentially significant source of ice nucleating particles. *Nat. Geosci.*, 12, 253–258, https://doi.org/10.1038/s41561-019-0314-x.

Twohy, C. H., and M. R. Poellot, 2005: Chemical characteristics of ice residual nuclei in anvil cirrus clouds: Evidence for homogeneous and heterogeneous ice formation. *Atmos. Chem. Phys.*, 5, 2289–2297, https://doi.org/10.5194/acp-5-2289-2005.

——, A. J. Schanot, and W. A. Cooper, 1997: Measurement of Condensed Water Content in Liquid and Ice Clouds Using an Airborne Counterflow Virtual Impactor. *J. Atmos. Ocean. Technol.*, 14, 197–202, https://doi.org/10.1175/1520-0426(1997)014<0197:MOCWCI>2.0.CO;2.

——, and Coauthors, 2010: Relationships of biomass-burning aerosols to ice in orographic wave clouds. *J. Atmos. Sci.*, 67, 2437–2450, https://doi.org/10.1175/2010JAS3310.1.

Twomey, S., 1977: The Influence of Pollution on the Shortwave Albedo of Clouds. *J. Atmos. Sci.,* 34, 1149–1152, https://doi.org/10.1175/1520-0469(1977)034<1149:tiopot>2.0.co;2.

UCAR/NCAR-Earth Observing Laboratory, 2021: SPICULE: Low Rate (LRT - 1 sps) Navigation, State Parameter, and Microphysics Flight-Level Data. Version 1.0. https://doi.org/10.26023/SXJ1-0JC5-0Y0V.

Vali, G., 1971: Quantitative Evaluation of Experimental Results an the Heterogeneous Freezing Nucleation of Supercooled Liquids. *J. Atmos. Sci.*, 28, 402–409, https://doi.org/10.1175/1520-0469(1971)028<0402:QEOERA>2.0.CO;2.

——, P. J. DeMott, O. Möhler, and T. F. Whale, 2015: Technical Note: A proposal for ice nucleation terminology. *Atmos. Chem. Phys.*, 15, 10263–10270, https://doi.org/10.5194/acp-15-10263-2015.

Wagner, R., O. Möhler, and M. Martin Schnaiter, 2012: Infrared optical constants of crystalline sodium chloride dihydrate: Application to study the crystallization of aqueous sodium chloride solution droplets at low temperatures. *J. Phys. Chem. A*, 116, 8557–8571, https://doi.org/10.1021/jp306240s.

——, and O. Möhler, 2013: Heterogeneous ice nucleation ability of crystalline sodium chloride dihydrate particles. *J. Geophys. Res. Atmos.*, 118, 4610–4622, https://doi.org/10.1002/jgrd.50325.

——, J. Kaufmann, O. Möhler, H. Saathoff, M. Schnaiter, R. Ullrich, and T. Leisner, 2018: Heterogeneous Ice Nucleation Ability of NaCl and Sea Salt Aerosol Particles at Cirrus Temperatures. *J. Geophys. Res. Atmos.*, 123, 2841–2860, https://doi.org/10.1002/2017JD027864.

——, and Coauthors, 2021: Heterogeneous ice nucleation ability of aerosol particles generated from Arctic sea surface microlayer and surface seawater samples at cirrus temperatures. *Atmos. Chem. Phys.*, 21, 13903–13930, https://doi.org/10.5194/acp-21-13903-2021.

Walko, R. L., W. R. Cotton, M. P. Meyers, and J. Y. Harrington, 1995: New RAMS cloud microphysics parameterization part I: the single-moment scheme. *Atmos. Res.*, 38, 29–62, https://doi.org/10.1016/0169-8095(94)00087-T.

Waman, D., S. Patade, A. Jadav, A. Deshmukh, A. K. Gupta, V. T. J. Phillips, A. Bansemer, and P. DeMott, 2022: Dependencies of four mechanisms of secondary ice production on cloud top temperature in a continental convective storm. *J. Atmos. Sci.*, 1–66, https://doi.org/10.1175/JAS-D-21-0278.1.

Weis, D. D., and G. E. Ewing, 1999: Water content and morphology of sodium chloride aerosol particles. *J. Geophys. Res. Atmos.*, 104, 21275–21285, https://doi.org/10.1029/1999JD900286.

Welti, A., K. Müller, Z. L. Fleming, and F. Stratmann, 2018: Concentration and variability of ice nuclei in the subtropical maritime boundary layer. *Atmos. Chem. Phys.*, 18, 5307–5320, https://doi.org/10.5194/acp-18-5307-2018.

Wernli, H., M. Boettcher, H. Joos, A. K. Miltenberger, and P. Spichtinger, 2016: A trajectory-based classification of ERA-Interim ice clouds in the region of the North Atlantic storm track. *Geophys. Res. Lett.*, 43, 6657–6664, https://doi.org/10.1002/2016GL068922.

Wex, H., and Coauthors, 2014: Kaolinite particles as ice nuclei: Learning from the use of different kaolinite samples and different coatings. *Atmos. Chem. Phys.*, 14, 5529–5546, https://doi.org/10.5194/acp-14-5529-2014.

Wildeman, S., S. Sterl, C. Sun, and D. Lohse, 2017: Fast Dynamics of Water Droplets Freezing from the Outside In. *Phys. Rev. Lett.*, 118, 084101, https://doi.org/10.1103/PhysRevLett.118.084101.

Wilson, T. W., and Coauthors, 2012: Glassy aerosols with a range of compositions nucleate ice heterogeneously at cirrus temperatures. *Atmos. Chem. Phys.*, 12, 8611–8632, https://doi.org/10.5194/acp-12-8611-2012.

——, and Coauthors, 2015: A marine biogenic source of atmospheric ice-nucleating particles. *Nature*, 525, 234–238, https://doi.org/10.1038/nature14986.

Wise, M. E., K. J. Baustian, T. Koop, M. A. Freedman, E. J. Jensen, and M. A. Tolbert, 2012: Depositional ice nucleation onto crystalline hydrated NaCl particles: A new mechanism for ice formation in the troposphere. Atmos. Chem. Phys., 12, 1121–1134, https://doi.org/10.5194/acp-12-1121-2012.

Wolf, M. J., and Coauthors, 2019: Investigating the Heterogeneous Ice Nucleation of Sea Spray Aerosols Using Prochlorococcus as a Model Source of Marine Organic Matter. *Environ. Sci. Technol.,* 53, 1139–1149, https://doi.org/10.1021/acs.est.8b05150.

——, and Coauthors, 2020a: A biogenic secondary organic aerosol source of cirrus ice nucleating particles. *Nat. Commun.*, 11, https://doi.org/10.1038/s41467-020-18424-6.

——, and Coauthors, 2020b: A link between the ice nucleation activity and the biogeochemistry of seawater. *Atmos. Chem. Phys.*, 20, 15341–15356, https://doi.org/10.5194/acp-20-15341-2020.

Woods, S., R. P. Lawson, E. Jensen, T. P. Bui, T. Thornberry, A. Rollins, L. Pfister, and M. Avery, 2018: Microphysical Properties of Tropical Tropopause Layer Cirrus. *J. Geophys. Res. Atmos.*, 123, 6053–6069, https://doi.org/10.1029/2017JD028068.

Yano, J., V. T. J. Phillips, and V. Kanawade, 2016: Explosive ice multiplication by mechanical break-up in ice–ice collisions: a dynamical system-based study. *Q. J. R. Meteorol. Soc.*, 142, 867–879, https://doi.org/10.1002/qj.2687.

Zhang, Y., A. MacKe, and F. Albers, 1999: Effect of crystal size spectrum and crystal shape on stratiform cirrus radiative forcing. *Atmos. Res.*, 52, 59–75, https://doi.org/10.1016/S0169-8095(99)00026-5.

——, and Coauthors, 2019: The Cooling Rate- And Volatility-Dependent Glass-Forming Properties of Organic Aerosols Measured by Broadband Dielectric Spectroscopy. *Environ. Sci. Technol.*, 53, 12366–12378, https://doi.org/10.1021/acs.est.9b03317.

Zieger, P., and Coauthors, 2017: Revising the hygroscopicity of inorganic sea salt particles. *Nat. Commun.*, 8, https://doi.org/10.1038/ncomms15883.

Zobrist, B., C. Marcolli, D. A. Pedernera, and T. Koop, 2008: Do atmospheric aerosols form glasses? *Atmos. Chem. Phys.*, 8, 5221–5244, https://doi.org/10.5194/acp-8-5221-2008.

Zuberi, B., A. K. Bertram, C. A. Cassa, L. T. Molina, and M. J. Molina, 2002: Heterogeneous nucleation of ice in (NH4)2SO4-H2O particles with mineral dust immersions. *Geophys. Res. Lett.*, 29, https://doi.org/10.1029/2001gl014289.

APPENDICES

Appendix 1, Reproduced from Patnaude et al. (2021b), Supplemental Material

A1.1 Flow Calculation Introduction

Flow profile calculations in CFDC instruments are necessary to determine the conditions that sample aerosols are exposed to when ice nucleation occurs. Prior CFDC instruments utilized calculations detailed by Rogers (1988). These calculations have several approximations in them that are not applicable at the very low temperature and corresponding supersaturation conditions accessed in these experiments. To complete the work described in the main manuscript, it was necessary to adjust these calculations to produce more accurate estimates of the aerosol temperature and supersaturation conditions in the CFDC lamina. We review the more rigorous derivation and resulting equations here. The revised calculations produce essentially identical results for typical operating conditions of CFDC instruments, indicating that no corrections to past CFDC data are required.

A1.2 Annular Forced Flow

An important approximation used in the prior calculations is that the annular region into which sample is introduced can be approximated by parallel plates. Here, we derive equations for the temperature and vapor profiles in the actual cylindrical geometry. Flow profiles through an annular region with walls of differing temperatures can be calculated in two parts and combined. The first calculation is for an annular region where the walls are the same temperature. This is a classic Hagan-Poiseuille flow problem, and has been solved many places, including in Bird et al (2014). The solution takes the form:

$$V(r) = \frac{G}{4\mu}\left({R_1}^2 - r^2\right) + \frac{G}{4\mu}\left({R_2}^2 - {R_1}^2\right)\frac{\ln\left(r/R_1\right)}{\ln\left(R_2/R_1\right)} \qquad \text{Eq. A1.1}$$

where G is the pressure gradient, R_1 is the inner column radius, R_2 is the outer column radius, and μ is the dynamic viscosity. This can be solved in terms of average flow by integrating across the annulus, dividing that by the cross-sectional area, and solving that term for G:

$$G = \frac{8\mu Q}{\pi\left(R_2{}^4 - R_1{}^4 - \frac{\left(R_1{}^2 - R_2{}^2\right)^2}{\ln\left(R_2/R_1\right)}\right)} \qquad \text{Eq. A1.2}$$

This can be substituted back into Eq. A1.1 to yield:

$$V(r) = \frac{2Q\left[r^2 - R_1{}^2 + \left(R_1{}^2 - R_2{}^2\right)\frac{\ln\left(r/R_1\right)}{\ln\left(R_2/R_1\right)}\right]}{\pi\left(R_1{}^4 - R_2{}^4 - \frac{\left(R_1{}^2 - R_2{}^2\right)^2}{\ln\left(R_2/R_1\right)}\right)} \qquad \text{Eq. A1.3}$$

where Q is the mean volumetric flow through the column. It should be noted that Q is generally not the same as the volumetric total flow measured (and controlled) outside the column. The appropriate units: Q should be in m^3/s and r in meters for V(r) in m/s.

A1.3 Annular Convective Flow

In addition to the forced flow, there is also convective flow that is due to the temperature gradient within the anulus. This is solved for independently using a similar procedure to that found in Bird et al (2014), but accounting for the annular shape, rather than assuming parallel plates as was done in the original version of our custom software.

First, the change of temperature between the two walls is calculated. This is slightly different for the annular shape than for a parallel plate approximation. First, an energy balance is constructed, with the only contributions coming from conduction from the walls as a function of radius, yielding the equation:

$$-\frac{1}{r}\frac{d}{dr}(rq_r) = 0 \qquad \text{Eq. A1.4}$$

where r is radius and q_r is the conducted heat, described by Fourier's law as:

$$q_r = -k\frac{dT}{dr} \quad \text{Eq. A1.5}$$

where k is the thermal conductivity. This results in the differential equation:

$$\frac{k}{r}\frac{dT}{dr} + k\frac{d^2T}{dr^2} = 0 \quad \text{Eq. A1.6}$$

With the boundary conditions of $T(R_1)=T_1$ and $T(R_2)=T_2$, the solution takes the form:

$$T(r) = \frac{T_2 \ln(R_1) - T_1 \ln(R_2) + (T_1 - T_2)\ln(r)}{\ln(R_1) - \ln(R_2)} \quad \text{Eq. A1.7}$$

As the R_1 and R_2 become much greater in magnitude than their difference, this solution produces essentially the same results as the linear solution for parallel plates. For the CFDC column however, the temperature differences between the two solutions are significant. The table below shows the differences for a cold wall temperature of -40 °C and warm wall of -20 °C and approximate radii of the columns used in our instrument. The maximum air temperature difference is about 0.6 °C. It should be noted that these differences do not directly translate into measured CFDC conditions as they do not account for aerosol lamina position.

r	linear	curved	dif
1.5625	-40	-40	0
1.60625	-38	-37.7627	0.237313321
1.65	-36	-35.5855	0.414499561
1.69375	-34	-33.4653	0.534706113
1.7375	-32	-31.3992	0.60083953
1.78125	-30	-29.3844	0.615589487
1.825	-28	-27.4186	0.581449841
1.86875	-26	-25.4993	0.500737181
1.9125	-24	-23.6244	0.37560725
1.95625	-22	-21.7919	0.208069491
2	-20	-20	0

From the radial dependence of temperature, the flow caused by the temperature gradient can be calculated. For the zero net flow case, the momentum balance can be written as:

$$\frac{d}{dr}(r\tau_{rz}) = \left(\frac{dP}{dz} + \rho g\right) r \qquad \text{Eq. A1.8}$$

where P is the pressure, z is the along-flow direction, ρ is the fluid density, and g is the gravitational constant. T_{rz} is the shear stress tensor, and in this case can be rewritten as:

$$\tau_{rz} = -\mu \frac{dV_z}{dr} \qquad \text{Eq. A1.9}$$

where μ is the dynamic viscosity. Substitution results in the differential equation:

$$-\frac{\mu}{r}\frac{dV_z}{dr} - \mu\frac{d^2V_z}{dr^2} = \frac{dP}{dz} + \rho g \qquad \text{Eq. A1.10}$$

Density of the fluid (air) is not constant, and varies with temperature. To account for this, a Taylor expansion in density is made about an undefined reference temperature, T^0:

$$\rho = \rho|_{T^0} + \left.\frac{\partial \rho}{\partial T}\right|_{T^0} (T - T^0) + \cdots = \rho^o - \rho^o \beta^0 (T - T^0) + \cdots \qquad \text{Eq. A1.11}$$

where ß is the coefficient of volume expansion. The first two terms are kept, and substituted into Eq. A1.10 to yield:

$$-\frac{\mu}{r}\frac{dV_z}{dr} - \mu\frac{d^2V_z}{dr^2} = \frac{dP}{dz} + \rho^0 g - \rho^o \beta^0 g (T - T^0) \qquad \text{Eq. A1.12}$$

For the zero-flow case, we can simplify this equation because the only pressure differential is due to the net gravitational force on the system. This causes the first two terms on the right hand side of the equation to balance, leaving:

$$-\frac{\mu}{r}\frac{dV_z}{dr} - \mu\frac{d^2V_z}{dr^2} = -\rho^o \beta^0 g (T - T^0) \qquad \text{Eq. A1.13}$$

At this point, the Eq. A1.7 for T(r) is substituted in, yielding a differential equation with complex constants but a relatively simple form:

$$-\frac{1}{r}\frac{dV_z}{dr}-\frac{d^2V_z}{dr^2}=A+B*\ln(r) \quad \text{Eq. A1.14}$$

$$A=\frac{\rho^o\beta^0 g}{\mu}\left(\frac{T_1\ln(R_2)-T_2\ln(R_1)}{\ln(R_1)-\ln(R_2)}+T^0\right) \quad \text{Eq. A1.15}$$

$$B=\frac{\rho^o\beta^0 g}{\mu}\left(\frac{T_1-T_2}{\ln(R_1)-\ln(R_2)}\right) \quad \text{Eq. A1.16}$$

The constant term in A and B are calculated assuming an ideal gas for density and thermal expansion, and a parameterized equation for μ as follows:

$$\rho^o=\frac{P*MW_{air}}{R*T^0} \quad \text{Eq. A1.17}$$

$$\beta^0=\frac{1}{T^0} \quad \text{Eq. A1.18}$$

$$\mu=\frac{(T-273.15)0.005+1.718}{1000} \quad \text{Eq. A1.19}$$

where T is temperature in K, P is pressure, MW_{air} is the mean molecular weight of air, and R is the gas constant. We note that μ varies with temperature across the annular region, but the variance is relatively small, about 10% across a 20 °C temperature gap. Currently T^0 is used for solving μ, but it is possible and more accurate to include the temperature dependence. Temperature dependence of viscosity will become more important as the convective flow dominates, at low forced flow, and large temperature differences.

The differential equation (Eq. A1.14) is solved with no-slip boundary conditions, i.e. $V_z(R_1) = V_z(R_2) = 0$. The solution takes the form:

$$V_z(r)=\frac{-(A+B)}{4}r^2+\frac{B}{4}r^2\ln(r)+C_1\ln(r)+C_0 \quad \text{Eq. A1.20}$$

$$C_0 = \frac{-(A+B)R_1^2 Ln(R_2) + Ln(R_1)\left((A+B)R_2^2 + B\,(R_1^2 - R_2^2)Ln(R_2)\right)}{4\left(Ln(R_1) - Ln(R_2)\right)} \quad \text{Eq. A1.21}$$

$$C_1 = \frac{(A+B)(R_1^2 - R_2^2) - B\,R_1^2 Ln(R_1) + B\,R_2^2 Ln(R_2)}{4\left(Ln(R_1) - Ln(R_2)\right)} \quad \text{Eq. A1.22}$$

The constants in these equations are messy, but not computationally difficult to calculate. The last piece of the solution is arriving at a better definition for the T^0 constant that the fluid density Taylor series was expanded around. This is done by invoking the constraint that the net volume flow is zero:

$$\int_{R_1}^{R_2} 2\pi V(r) r dr = 0 \quad \text{Eq. A1.23}$$

The solution yields an equation in the form:

$$T^0 = k_1(R_1, R_2)T_1 + k_2(R_1, R_2)T_2 \quad \text{Eq. A1.24}$$

where the constants are:

$$k_1 = \frac{(3\,R_2^2(R_1^2 - R_2^2)LN(R_2) - 8\,R_1^4 LN(R_1)LN(R_2) + 4\,R_1^4 LN(R_2)^2)}{4\,(R_1^2 - R_2^2)\left(LN(R_1) - LN(R_2)\right)\left(-R_1^2 + R_2^2 + (R_1^2 + R_2^2)LN(R_1) - (R_1^2 + R_2^2)LN(R_2)\right)} + \frac{4\,(R_1^2 - R_2^2)^2 + 7\,R_1^2(-R_1^2 + R_2^2)LN(R_1) + 3\,R_2^2(-R_1^2 + R_2^2)LN(R_1) + 4\,R_1^4 LN(R_1)^2 + 7\,R_1^2(R_1^2 - R_2^2)LN(R_2)}{4\,(R_1^2 - R_2^2)\left(LN(R_1) - LN(R_2)\right)\left(-R_1^2 + R_2^2 + (R_1^2 + R_2^2)LN(R_1) - (R_1^2 + R_2^2)LN(R_2)\right)} \quad \text{Eq. A1.25}$$

$$k_2 = \frac{(-4\,(R_1^2 - R_2^2)^2 - 3\,R_1^2(-R_1^2 + R_2^2)LN(R_1) - 7\,R_2^2(-R_1^2 + R_2^2)LN(R_1) - 4\,R_2^4 LN(R_1)^2)}{4\,(R_1^2 - R_2^2)\left(LN(R_1) - LN(R_2)\right)\left(-R_1^2 + R_2^2 + (R_1^2 + R_2^2)LN(R_1) - (R_1^2 + R_2^2)LN(R_2)\right)} + \frac{-3\,R_1^2(R_1^2 - R_2^2)LN(R_2) - 7\,R_2^2(R_1^2 - R_2^2)LN(R_2) + 8\,R_2^4 LN(R_1)LN(R_2) - 4\,R_2^4 LN(R_2)^2}{4\,(R_1^2 - R_2^2)\left(LN(R_1) - LN(R_2)\right)\left(-R_1^2 + R_2^2 + (R_1^2 + R_2^2)LN(R_1) - (R_1^2 + R_2^2)LN(R_2)\right)} \quad \text{Eq. A1.26}$$

The final combined velocity profile equation, including the Hagan-Poiseuille flow (Eq. A1.3) and the convective flow due to the cross-gap temperature differential (Eq. A1.20) is thus:

$$V_z(r) = \frac{-(A+B)}{4} r^2 + \frac{B}{4} r^2 \ln(r) + C_1 \ln(r) + C_0 + \frac{2Q\left[r^2 - {R_1}^2 + \left({R_1}^2 - {R_2}^2\right)\frac{\ln(r/R_1)}{\ln(R_2/R_1)}\right]}{\pi\left({R_1}^4 - {R_2}^4 - \frac{\left({R_1}^2 - {R_2}^2\right)^2}{\ln(R_2/R_1)}\right)} \quad \text{Eq. A1.27}$$

where A, B, C_0, and C_1 are all constants that depend on R_1, R_2, T_1 and T_2 as described in Eq. A1.15, 16, 21, and 22 above.

A1.4 Volume to Mass Flow Conversion

A remaining problem, however, is that all of the calculations so far have solved for volumetric flow. The column volumetric flow is not the same, however, as the volume flow through the mass flow controllers (MFCs). The mass flow is the same, and can be used to calculate the volume flow inside the column, although that will depend on the temperatures, radii, and the flow rate through the column. The standard flow can be calculated using the equation:

$$\int_{R_1}^{R_2} 2\pi V_z(r) \frac{T^*}{T(r)} \frac{P}{P^*} r dr = V_{t,s} \quad \text{Eq. A1.28}$$

where T* and P* are standard temperature and pressure, 273.15 K and 1 bar respectively. $V_{t,s}$ is the total standard flow through the column. This equation is difficult to solve analytically; however, an equivalent "standard velocity profile" V(r) can also be constructed such that:

$$\int_{R_1}^{R_2} 2\pi V_s(r) r dr = V_{t,s} \quad \text{Eq. A1.}$$

In the approach taken here for software programming purposes, this is similar to determination of the normal velocity profile, and the two profiles are calculated concurrently.

In the program, the velocity profile for only the forced part of the flow is found using an initial volumetric flow rate assuming the effective column temperature is T^0. The total standard

flow of this profile is compared with the input standard flow, and used to calculate an effective column temperature, T_{eff}. This correction takes the form:

$$Q\frac{T^*}{T_{eff}}\frac{P}{P^*} = V_{t,s} \qquad \text{Eq. A1.29}$$

This correction is somewhat approximate due to the non-linear radial dependence on temperature inside the column. The approximation is essentially another Taylor expansion around T^0 keeping only the linear term (similar to the method going from Eq. A1.10-12). T^0 (Eq. A1.24) is chosen largely out of convenience, because its calculation is already required, rather than forcing a calculation of a new reference point. The error introduced by this treatment is very small and appears to be less than ~0.2 % for all reasonable operating conditions of the CFDC. This error gets larger with colder temperatures and large temperature gaps between the two walls, but even at extreme conditions (T_1 = -100, T_2 = 0, $V_{t,s}$ = 10 SLM) it only reaches about 6 %.

For CFDC operation, the lamina position of the sample flow must be determined. In the parallel plate framework, it was assumed that half of the sheath mass flux (or volume flux) is on either side of the sample lamina. The CFDC inlet is designed such that there are the same number of identical sheath flow holes on each side of the sample inlet, and that the volume above each set of holes is the same. This means the assumption that half of the mass flow is on either side of the sample flow should be valid for the annular geometry. Thus, the following should hold:

$$\int_{R_1}^{R_{S1}} 2\pi V_s(r) r dr = \int_{R_{S2}}^{R_2} 2\pi V_s(r) r dr = \frac{V_{sheath}}{2} \qquad \text{Eq. A1.30}$$

where V_{sheath} is the sheath flow rate, R_1 and R_2 are the inner and outer annulus radii, and R_{s1} and R_{s2} are the sample lamina beginning and end radii. Eq. A1.31 is solved numerically using

calculated standard flow velocity profiles (Eq. A1.29), with R_{s1} and R_{s2} being essentially independent from one another.

A1.5 Annular Water Vapor Profiles

Determination of supersaturation in the CFDC requires calculation of the water vapor profiles within the annulus. This problem is similar to the calculation of temperature profiles, as both are governed by Fick's second law of diffusion, which states:

$$\nabla^2 e = 0 \qquad \text{Eq. A1.31}$$

where here e is vapor pressure, and ∇^2 is the Laplacian. In cylindrical coordinates this yields:

$$\frac{1}{r}\frac{de}{dr} + \frac{d^2e}{dr^2} = 0 \qquad \text{Eq. A1.32}$$

as seen in Eq. A1.6 for temperature. Eq. A1.33 can be solved using the boundary conditions:

$$e(R_1) = e_i(T_1) \qquad \text{Eq. A1.33}$$
$$e(R_2) = e_i(T_2) \qquad \text{Eq. A1.34}$$

where R_1, R_2, T_1 and T_2 are the inner and outer radii and temperatures as before. e_i denotes equilibrium vapor pressure of ice. Values for vapor pressure can be calculated at given temperatures using various fits for water vapor pressures over ice, such as that proposed by Murphy and Koop (2005) which is used for the CFDC. The final equation for the radial dependence of the water vapor pressure takes the same form as Eq. A1.7 for temperature across the annular region:

$$e(r) = \frac{e_i(T_2)\ln(R_1) - e_i(T_1)\ln(R_2) + (e_i(T_1) - e_i(T_2))\ln(r)}{\ln(R_1) - \ln(R_2)} \qquad \text{Eq. A1.35}$$

Supersaturation profiles across the annulus are calculated as:

$$SS_i\%\,(r) = 100 * \frac{e(r)}{e_i(T(r))} \qquad \text{Eq. A1.36}$$

$$SS_w\%\,(r) = 100 * \frac{e(r)}{e_w(T(r))} \qquad \text{Eq. A1.37}$$

where e(r) is the vapor pressure at the radial position r, for the selected set of column conditions. The vapor pressure for e(r) depends only on the wall temperatures and column geometry, not the temperature at the radius where supersaturation is calculated. However, e_i or e_w is the equilibrium vapor pressure for the computed temperature within the annulus, and has no dependence on the vapor pressure at the walls.

Uncertainties in measurements of RH_i and RH_w are assumed to be similar to calculated uncertainties from a previous study using a similar CFDC arrangement at temperatures < 233 K (Richardson, 2009). In general, uncertainties in RH_w increase with decreasing temperature, but we assume an average uncertainty of ~4% RH_w for this study. Temperature uncertainties are relatively insensitive to wall temperature and are approximately ±0.5 K. In general, uncertainties vary with the width of the lamina, which is determined by the flow rates, and the location of the particles in the lamina.

A1.6 Comparisons to Previous Calculations

Comparison of these calculations with the previous parallel plate calculations was done for a variety of temperatures, for selected water supersaturation (SS_w) conditions of -5, 0 and 5%. The comparisons are shown in Figure A1.1.

Data are shown as differences between the previously-calculated value and the new calculated value; positive numbers mean that the previous calculations produced a larger number. The calculations shown are for total flow of 15 LPM volumetric and sheath flow of 13.5 LPM volumetric. Conditions are calculated as the center of the aerosol lamina in the previous calculations, and the average conditions across the aerosol lamina in the new calculation. While these are slightly different criteria, the comparisons are valid as the variability across the entire

lamina is small at this high sheath flow rates. When the inner wall is the cold wall (bottom two graphs), the comparisons show minimal differences. The temperatures are up to 0.3 °C warmer in the new calculations, and the supersaturations change by less than 0.2%, which is generally not significant given other noise in the measurements. When the walls are switched, however, and the outer wall is the cold wall, larger differences are observed. The new calculations produce temperatures about 1 °C colder, and supersaturations approaching 2 % lower.

This behavior likely arises because the difference between the flat and curved assumptions are either canceled out or exacerbated by the temperature gradient, depending on configuration. The previous, parallel plate calculations essentially assume equal air masses near each plate, which is more valid when the lower radius plate is cold.

The comparisons show generally the same trends at lower flow rates, although the previous calculations break down sooner and fail to produce reasonable results at colder temperatures. The breakdown happens sooner with the outer wall as the cold wall as well. Results for 10 LPM total flow (8.5 LPM sheath) are shown in Figure A1.2.

For the 5 LPM (3.5 LPM sheath) case, the previous calculations fail for most conditions, indicated by either off scale values, or large differences between the calculation, as shown in Figure A1.3.

A1.7 Additional Figures

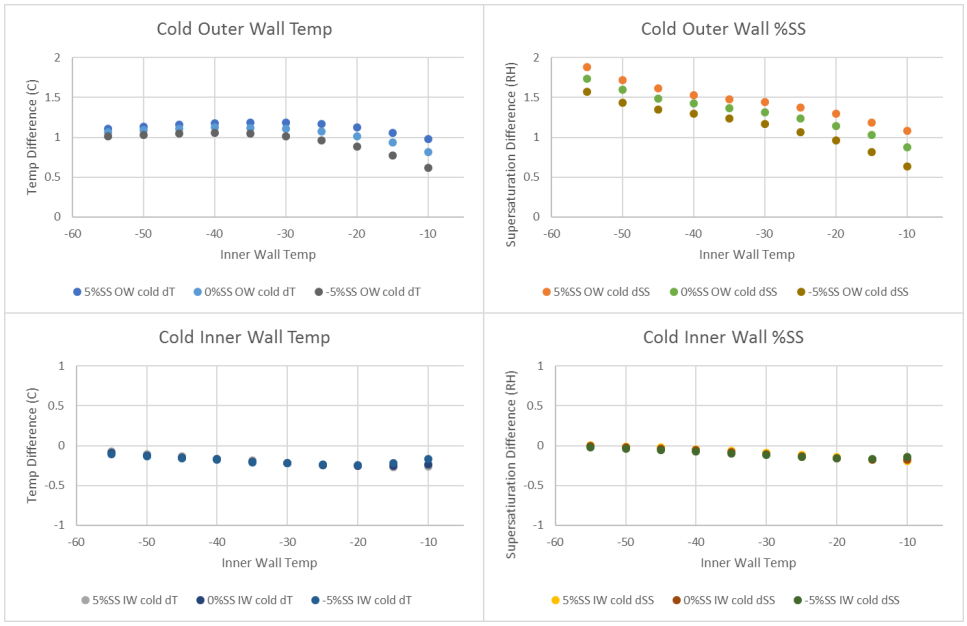


Figure A1.1. Comparison between previous and current flow calculations in lamina temperature (left) and water supersaturation (right) for different wall configurations and operating temperatures at 15 LPM total and 13.5 LPM sheath flows.

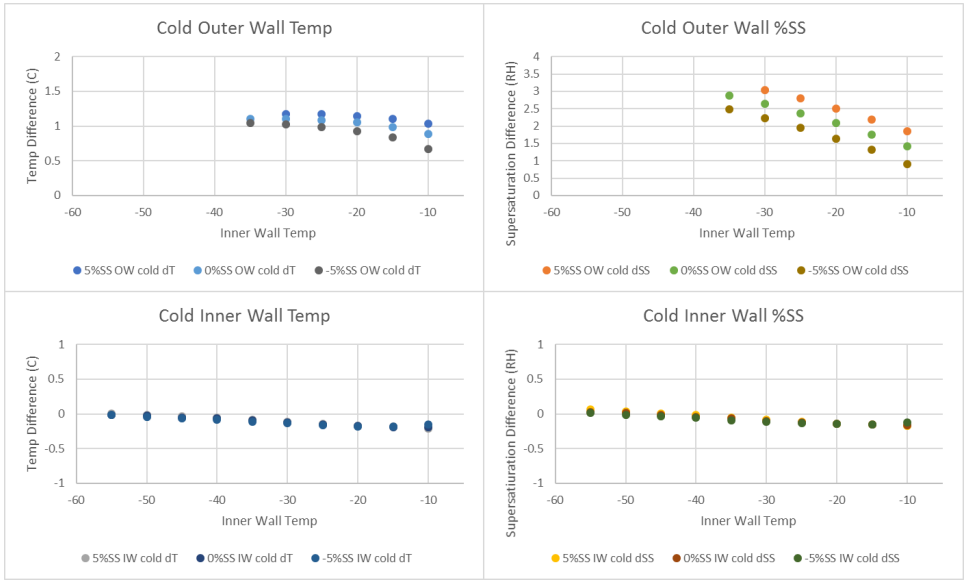


Figure A1.2. Comparison between previous and current flow calculations in lamina temperature (left) and water supersaturation (right) for different wall configurations and operating temperatures at 10 LPM total and 8.5 LPM sheath flows.

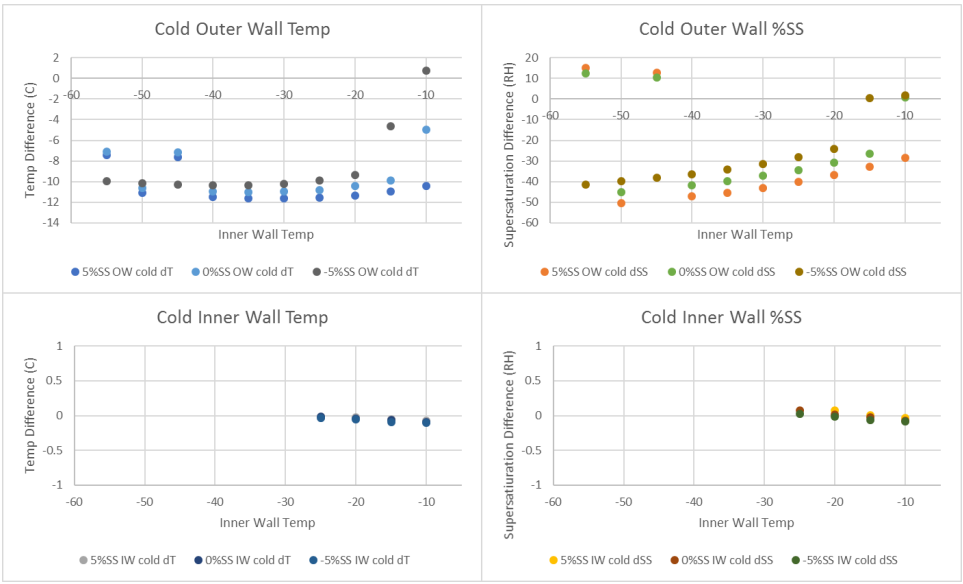


Figure A1.3. Comparison between previous and current flow calculations in lamina temperature (left) and water supersaturation (right) for different wall configurations and operating temperatures at 5 LPM total and 3.5 LPM sheath flows.

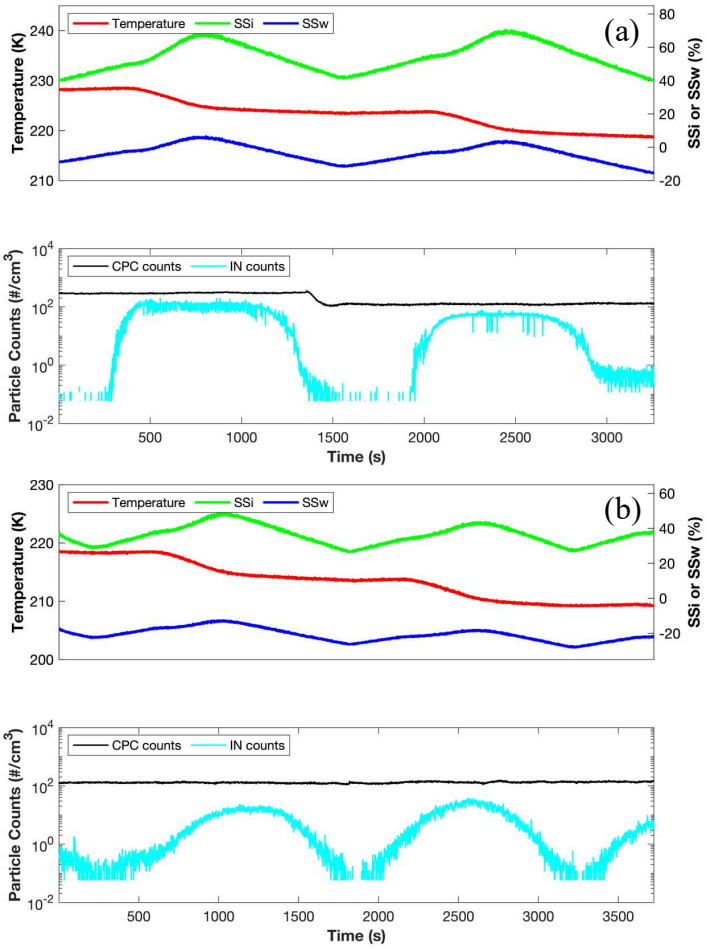


Figure A1.4. CFDC time series for SSA experiments starting at (a) ~228 K and 223 K, and experiments starting at (b) ~218 K and 214 K. Red line indicates temperature and blue and green lines indicate water and ice supersaturations, respectively. Black and cyan lines indicate the number concentrations measured by the CPC and counted as ice nucleating particles, respectively.

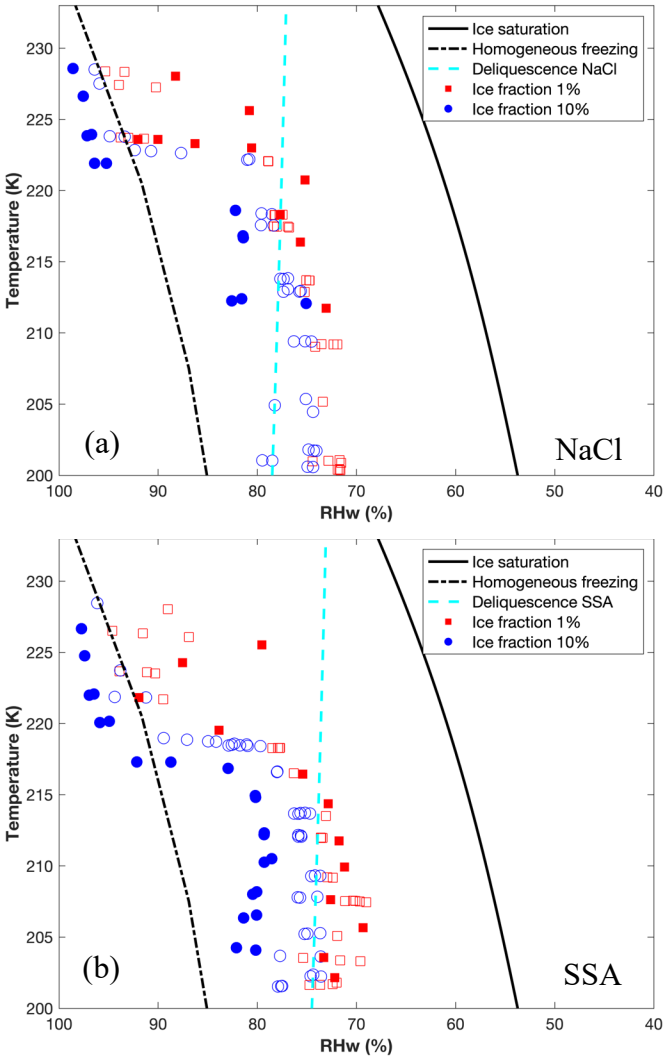


Figure A1.5. Ice fractions for (a) NaCl and (b) SSA generated particles. Blue and red markers denote 10% and 1% frozen fraction, respectively, where filled markers represent 600 nm particles and open markers for 150 nm particles. The dashed cyan line represents the predicted deliquescence for NaCl[3]. Black solid and dashed lines denote ice saturation and expected homogeneous freezing (Koop et al. 2000a), respectively. Ice fractions are calculated by dividing the number of ice particles by the total aerosol counts from the OPC.

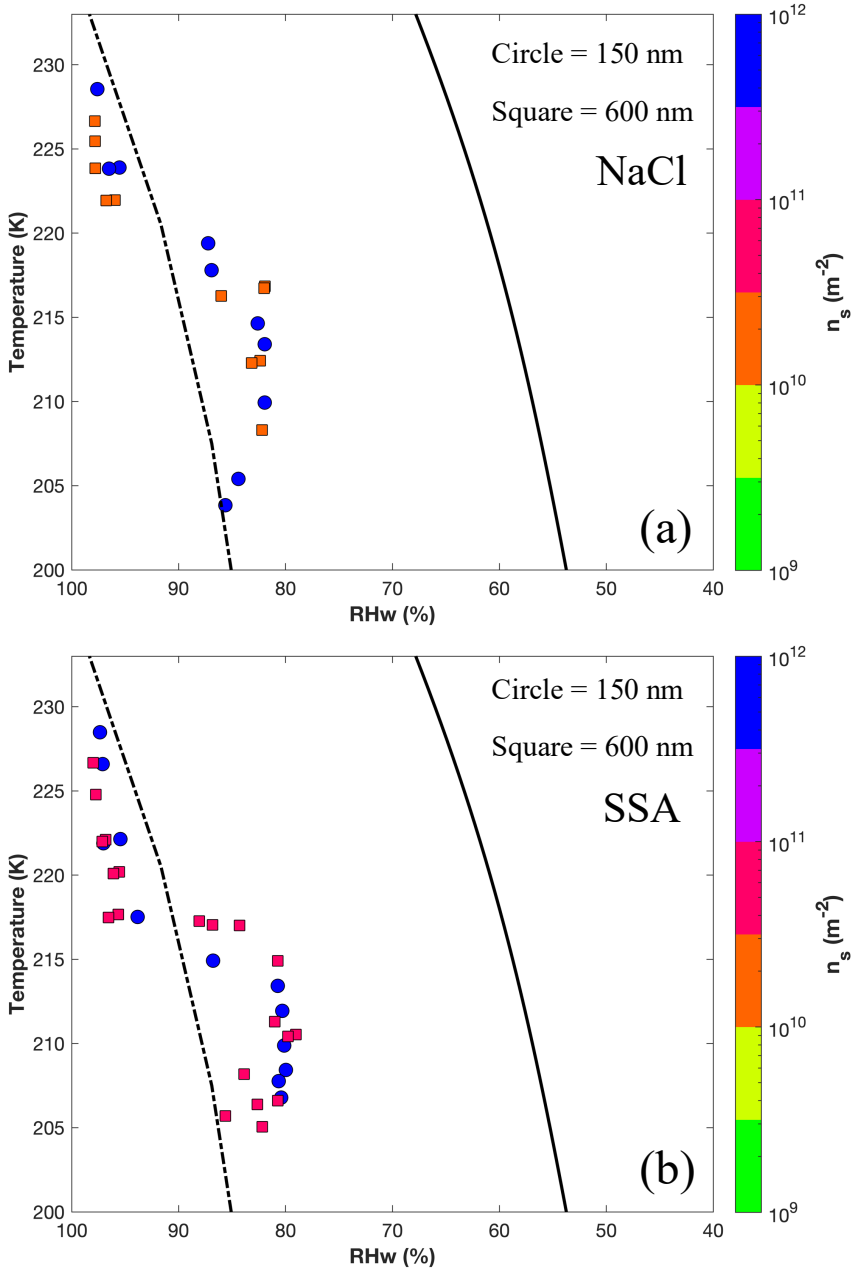


Figure A1.6. Ice active surface site density (n_s) magnitudes for a given RH_w and temperature for (a) NaCl and (b) SSA at 10% ice fraction. Circle and square markers indicate 150 nm and 600 nm particles, respectively. The black solid line indicates ice saturation and the dashed line represents expected homogeneous freezing conditions (Koop et al. 2000a).

Appendix 2, Reproduced from Patnaude et al. (2023), Supplemental Material

A2.1. Estimate of condensation sinks in OFR

In this section, we estimate the ability of vapors to condense onto aerosol particles for determination of the dominant condensation sinks during the MART experiments. The pSSA and the newly formed SMA particles will compete for the available condensable vapors produced in the MART. The formula to compute the condensation sink CS (s^{-1}), assuming a constant flux correction factor β, is shown in equation (A2.1):

$$CS = \frac{\partial M}{\partial t} = 2\pi\, D_v\, \beta \int D_p\, n\left(D_p\right) dD_p \qquad \text{(Eq. A2.1)}$$

where D_v (cm s^{-1}) is the diffusivity coefficient of the condensing vapor. The integral is simplified into:

$$N\overline{D_p} \qquad \text{(Eq. A2.2)}$$

where N is the total aerosol concentrations and $\overline{D_p}$ is the number mean diameter of the aerosol population. For SMA, N = 10^5 and for pSSA, N= 150 cm^{-3}. $\overline{D_p}$ was calculated using the geometric mean diameter Dp_g using:

$$\overline{D_p} = Dp_g * \exp\left(0.5 \ln \sigma_g\right)^2) \qquad \text{(Eq. A2.3)}$$

where Dp_g is assumed to be 160 nm and 20 nm, and σ_g is 3.2 and 1.6 for the pSSA and SMA particles, respectively. These lognormal parameters were determined by approximate fitting of lognormal distributions to the aerosol size distributions (see Figure A2.6). We assume a D_v of 0.1 $cm^2\ s^{-1}$ and the formula for β is due to Dahneke (1983) as reported in Seinfeld and Pandis (2006), and given by:

$$\beta = \frac{1+Kn}{1+2\,Kn\,(1+Kn)/_{\alpha}} \qquad \text{(Eq. A2.4)}$$

where the accommodation coefficient α is set to 1, and the Knudsen number (*Kn*) is computed as $2\lambda/\overline{D_p}$ with an assumed λ = 120 nm (Ezhova et al. 2018). Finally, the timescale of condensation for each particle type is determined by taking the inverse of equation A2.1. This results in estimated condensation sink timescales of ~3 and 11 minutes for the SMA and pSSA, respectively.

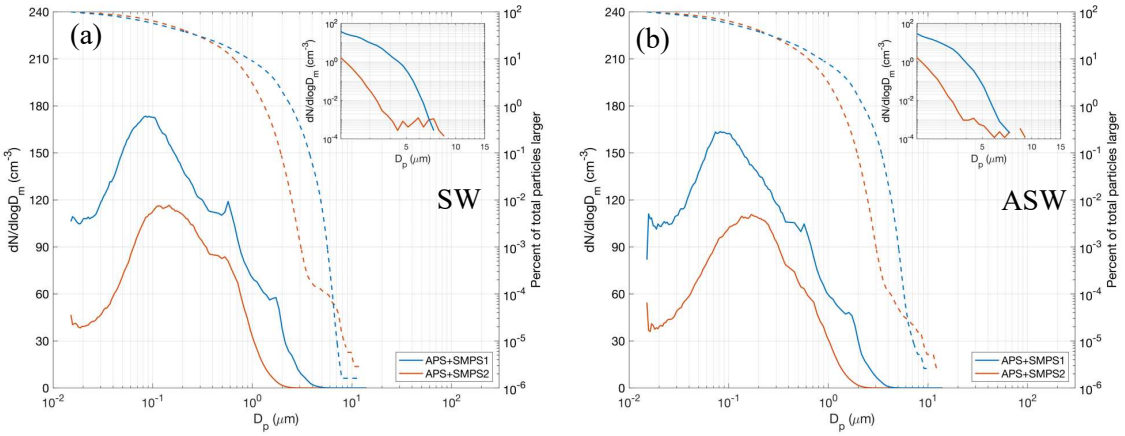


Figure A2.1. Merged size distributions from the SMPS and APS for the upstream (blue solid line) and downstream (red solid line) set of sizing instruments generated from (a) real and (b) artificial seawater. The dashed lines represent the percent of total particles larger than a given particle diameter and the colors match the size distribution they are referring to. The panels in the upper right of both figures denote the size distributions zoomed in a logarithmic scale for particles > 2 μm.

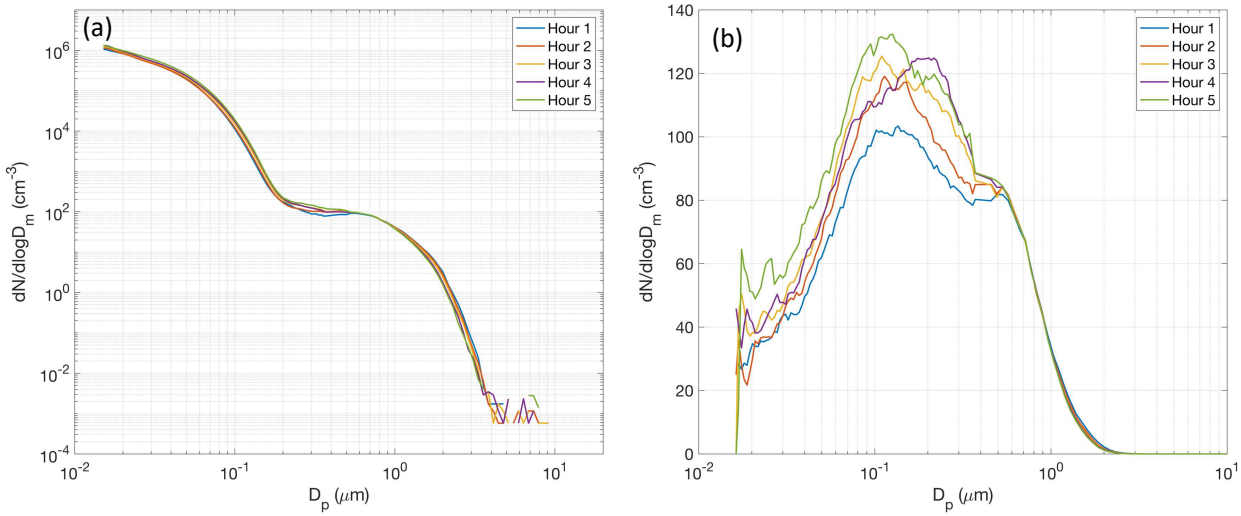


Figure A2.2. Size distributions of (a) aSSA+SMA and (b) pSSA color-coded by hours of each experiment.

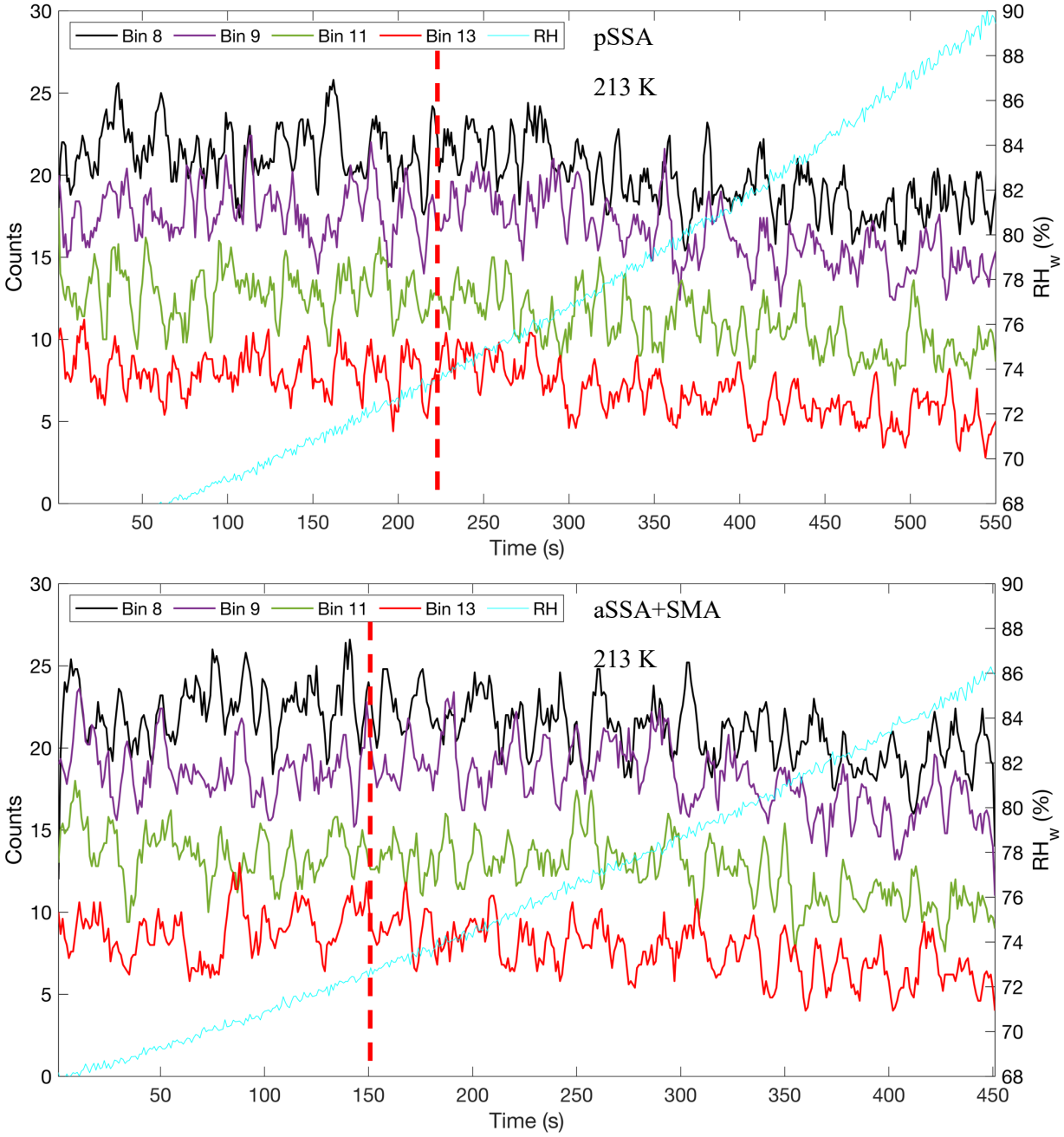


Figure A2.3. Time series of particle counts for four different OPC size channels for (a) pSSA and (b) aSSA+SMA at 213 K. The cyan line represents the RH_w and the dashed red line represents the RH_w where the particle counts begin to decrease, indicating transfer to larger channels and hence growth by water uptake.

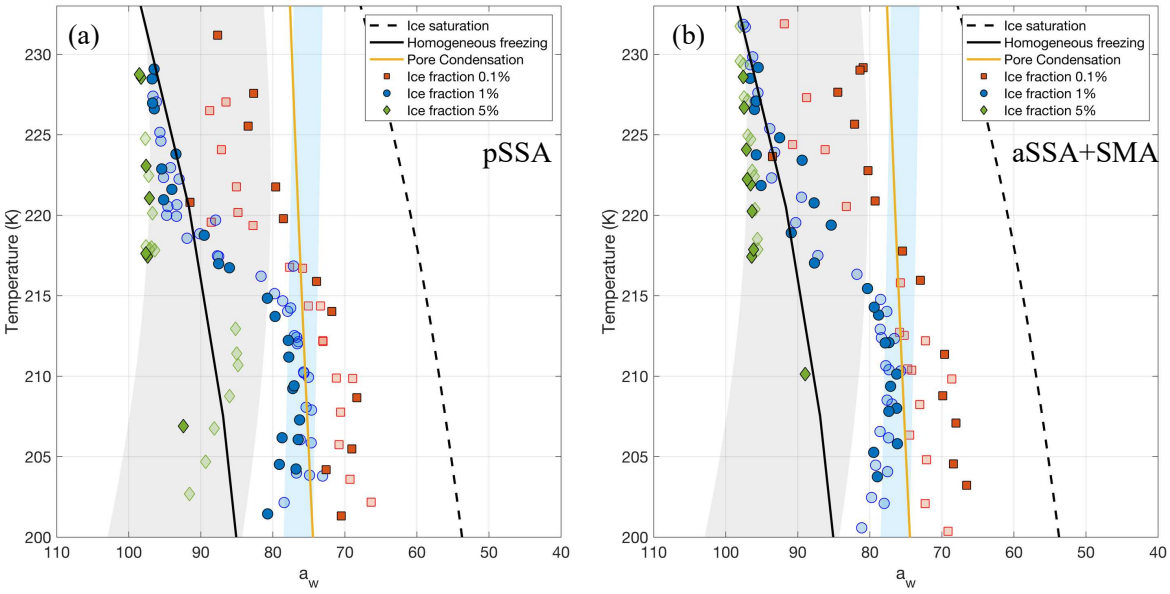


Figure A2.4. Fraction of frozen particles for (a) pSSA and (b) aSSA+SMA particles. The filled markers denote particles generated from real seawater and the open markers from artificial seawater. The red, blue and green markers indicate 0.1%, 1%, and 5% frozen fractions, respectively. The reference lines indicate ice saturation (black dashed), the parameterized RH_w for pore condensation in an 11 nm pore (Marcolli 2014) (solid yellow), and the expected threshold for the onset of homogeneous freezing (Koop et a., 2000a) (solid black). The blue shaded region represents the range of possible deliquescence RHs for NaCl and SSA, using the parameterization from Tang and Munkelwitz (1993) for NaCl extrapolated to colder temperatures as the upper bound and shifting it down 4% RH for SSA following Wagner et al. (2018). The gray shaded region represents the range of uncertainty for the aqueous sulfuric acid particle homogeneous freezing parameterization as presented in Schneider et al. (2021).

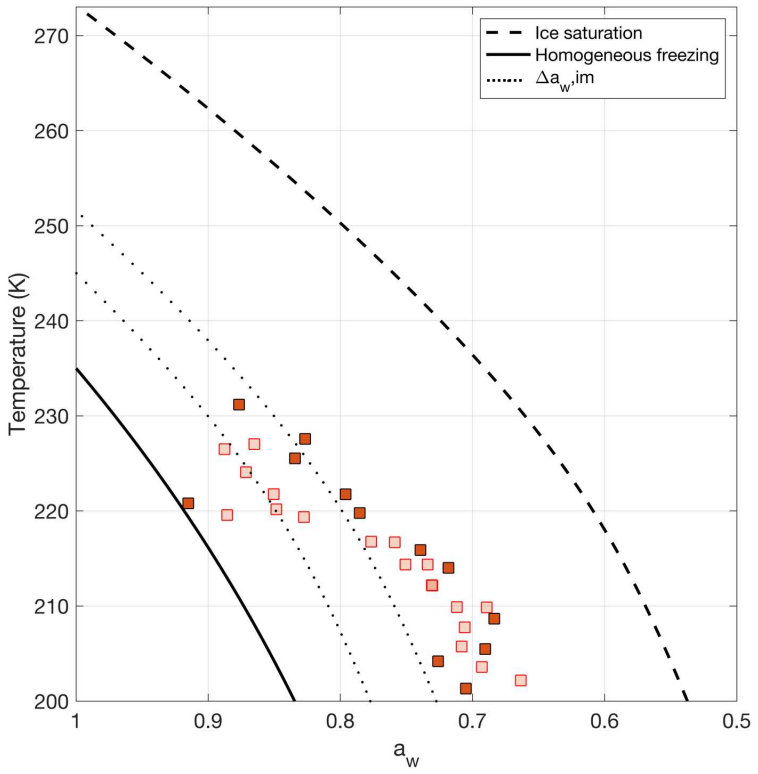


Figure A2.5. The same 0.1 % frozen fraction shown from Figure A2.4, but for a given temperature and water activity (a_w). We assume the larger particles would nucleate ice first difference leading to a negligible difference between the RH_w and a_w. The reference lines indicate ice saturation (black dashed), the expected threshold for the onset of homogeneous freezing (Koop et al. 2000a) (solid black), and the dotted lines indicates a constant water activity offset (Δa_w) fitted to the 0.1 % data to resemble immersion freezing.

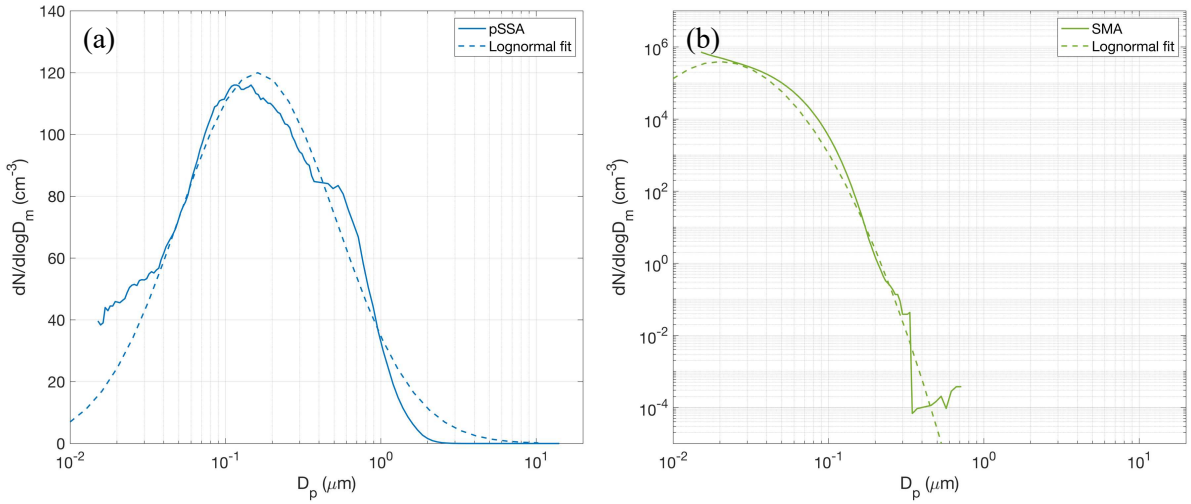


Figure A2.6. Particle size distributions of (a) pSSA and (b) SMA denoted by the solid lines and are the same as Figure 3.2. The dashed lines represent the lognormal fits with geometric mean diameters and σ_g for (a) 160 nm and 3.2 and (b) 20 nm and 1.6, respectively.

Appendix 3, Supplemental Material from Chapter 4

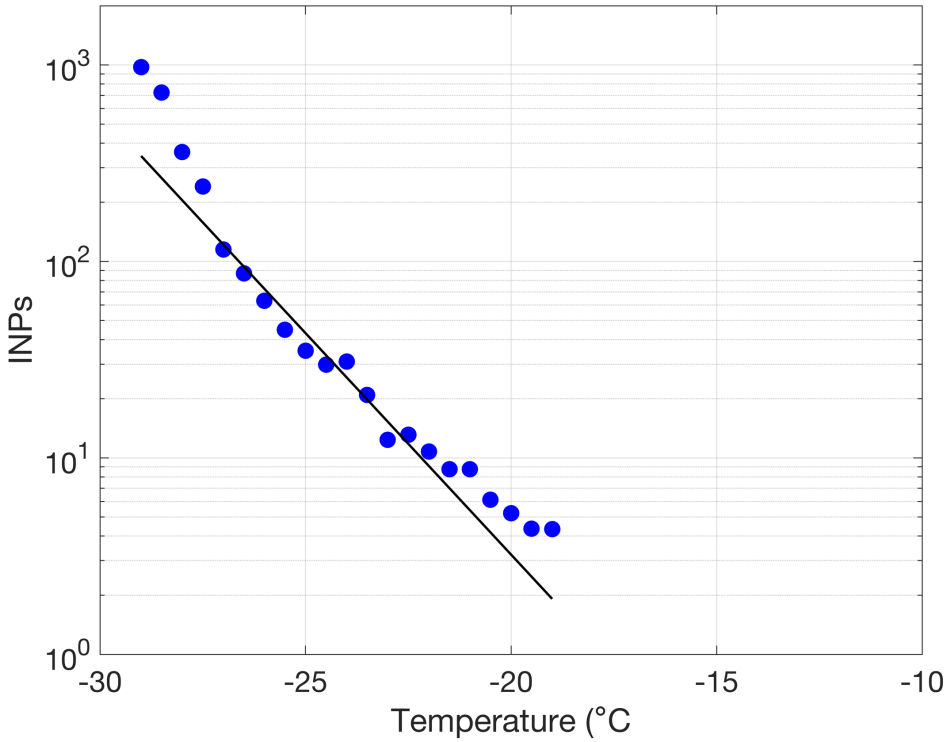


Figure A3.1. The number INPs per blank filter versus temperature, averaged from all the blank filters collected during SPICULE. The black line represents the best fit line that is applied to the sample filters. In general, the blank correction reduced the INP number by ~2% at -20 ºC.

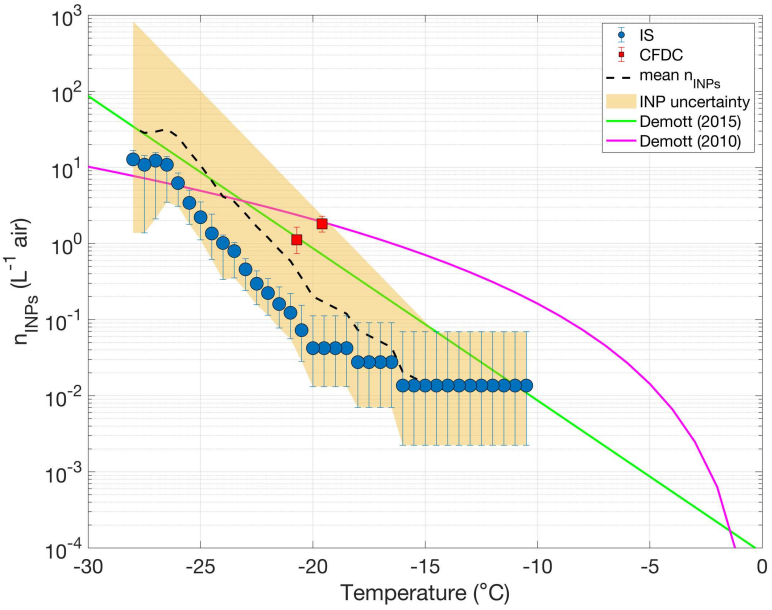


Figure A3.2. INP numbers and uncertainty versus temperature for the CFDC (red markers) and IS (blue markers). The green and pink solid lines represent the number of INPs predicted for a

constant aerosol number concentration of 2.5 cm^{-3}, using the DeMott et al. (2015) and DeMott et al. (2010) parameterizations, respectively.

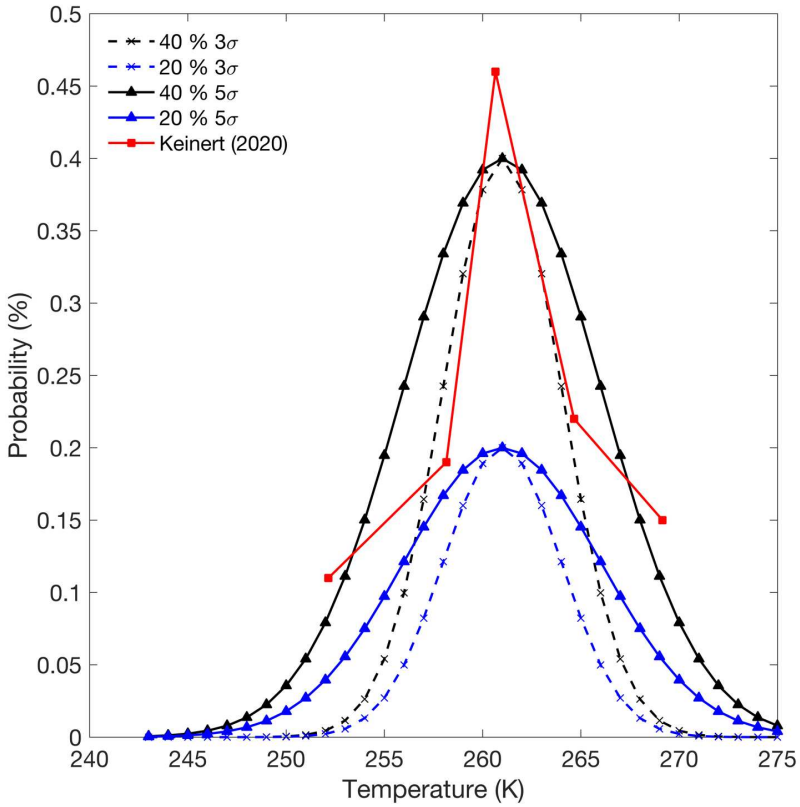


Figure A3.3. Probability distributions for droplet fragmentation as a function of temperature for various maximum probabilities and standard deviations (σ). The red solid line represents the probability of breakup of pure water droplets in moist airflow from Keinert et al. (2020).

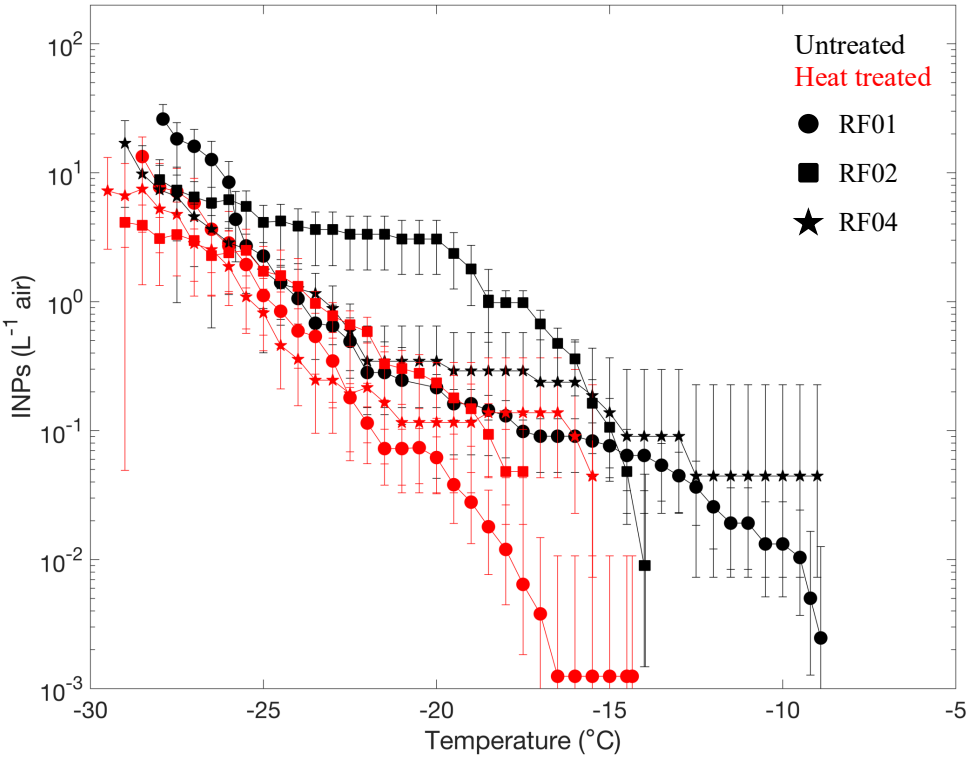


Figure A3.4. INP numbers versus temperature for untreated (black) and heat treated (red) filters. The circle, square, and star markers represent filters collected from RF01, RF02 and RF04, respectively.

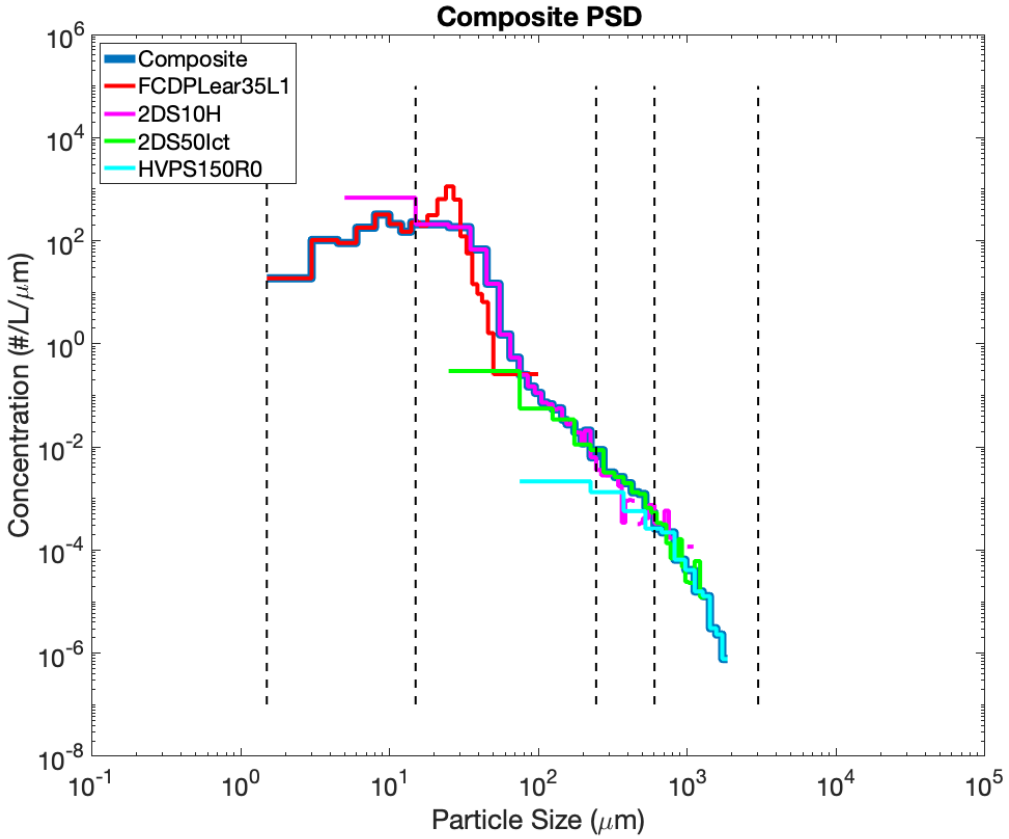


Figure A3.5. Composite size distribution selected from the different cloud probes. The color of the distribution denotes which cloud probe that portion of the distribution was measured.

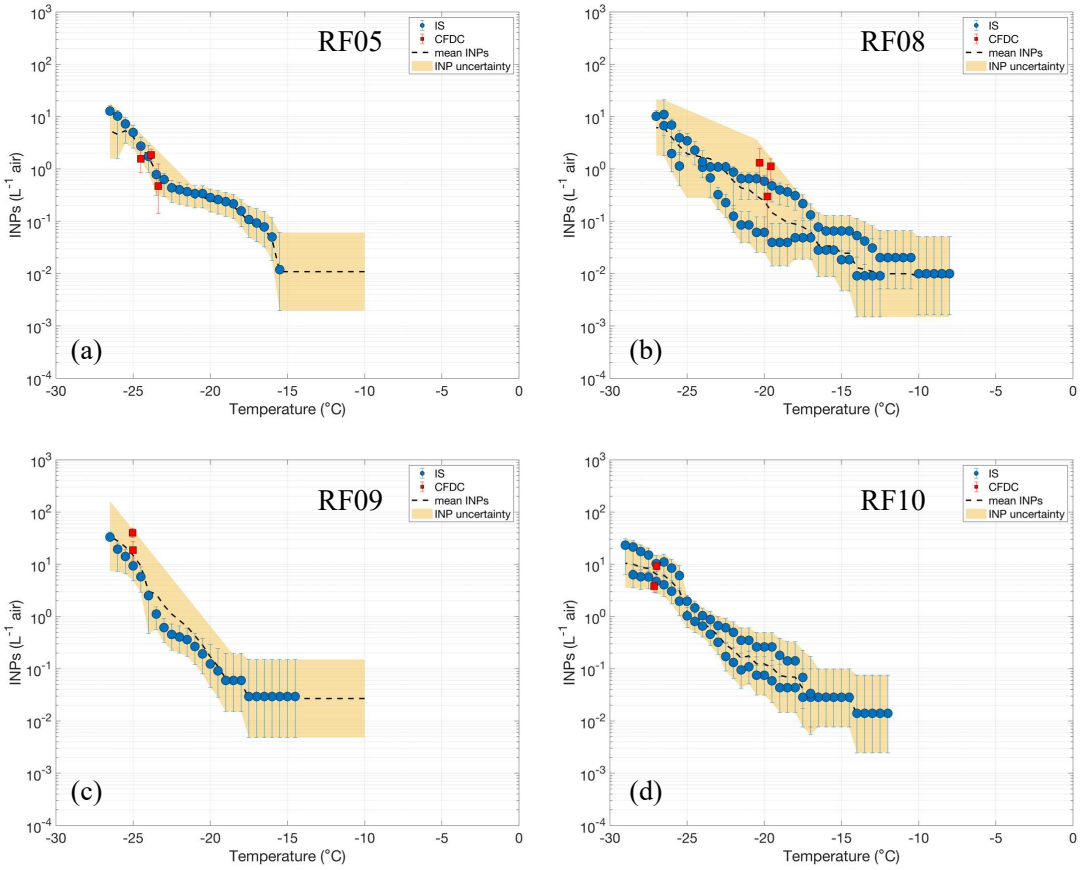


Figure A3.6. INP numbers and uncertainty (shaded tan region) versus temperature for the CFDC (red markers) and IS (blue markers) for RFs 5, 8, 9, and 10. The black dashed line represents the average number of INPs within the uncertainty range.